

Supercritical Water Oxidation of Hazardous Waste: Process Enhancement and Reactor Design

AMMAR Al-ATTA, MSc.

Thesis submitted to the University of Nottingham

for the degree of

DOCTOR OF PHILOSOPHY

June 2018

Abstract

The work presented in this thesis is focused on two specific areas of supercritical water oxidation (SCWO). Firstly, the design and testing of an innovative anti-corrosive reactor design that can be used for the SCWO of hazardous organic waste. Secondly, exploiting the merits of counter current mixing reactor in combining two processes; Supercritical water oxidation (SCWO) and supercritical water hydrothermal synthesis (SCWHS) in one reactor.

In Chapter 1, an introduction to supercritical fluid and supercritical water oxidation is given, followed by a brief account of the main problems associated with SCWO. This includes a review of the experience to date, with different reactor designs for corrosion control. This Chapter also provide an introduction to hydrothermal methodology and continuous flow reactor design for nanoparticle production, along with the aims and objective of this PhD.

Chapter 2 details the components and construction of the experimental rigs used in this thesis. Additionally, this Chapter presents the principles behind the main analytical techniques used throughout this work, along with the definition of some important parameters.

Chapter 3 reports the use of a physical modelling approach to assess mixing dynamics inside three different types of reactor where supercritical water is mixed with a second colder, waste containing, effluent flow. Physical or 'pseudo' modelling was used to simulate the general flow patterns and mixing regimes in transparent pseudo reactors (to allow visualization). Towns water was used

to simulate the supercritical water flow and 40% w/w aqueous sucrose solution to simulate the cold aqueous effluent flow. This visual technique allowed the quantification of mixing efficiency, as well as identification of issues such as flow recycling, stagnant zones, and other inconsistencies in the mixing dynamics. An upwards co-current protected wall reactor arrangement provided the 'best' mixing i.e. with minimal wall contact during the downstream oxidation process.

A combined process of SCWO and SCWHS in a continuous counter current reactor is the focus of Chapter 4. Acrylic acid was chosen as a model compound to represent an organic wastewater and the effects of the reaction temperature, residence time, oxidant ratio and acrylic acid concentration on chemical oxygen demand (COD) were all investigated. Two different experimental configurations for oxidant delivery were carried out in 'pre-heated' and 'non-preheated' oxidant configurations. With a stoichiometric excess of 100% oxygen, COD reduction levels of 80% (non-preheated) and 15% (preheated) were achieved with very short residence times. SCWHS was achieved through the addition of small amounts of various soluble metal salts in the cold upflow resulted in nanoparticles forming which increased the reaction rate and hydrothermal oxidation efficiency. The addition of small amounts of chromium nitrate (>5mM) results in nearly 100% COD reduction at 380°C and residence times of 0.75 seconds. The potential economic benefits of combining the two processes together, in the different configurations, were also evaluated.

In Chapter 5, The results of the catalytic oxidation in supercritical water of a non-biodegradable and highly toxic organic compound (phenol) are presented. The reactions were studied in a continuous counter current reactor through the in-

situ formation of Fe_2O_3 catalyst. The preliminary results showed that catalytic non-preheated oxidant configuration resulted in increased COD removal when compared to other oxidant delivery methods. It was shown that temperatures below 400°C could be used to decompose these compounds into final product and that complete conversion of COD could likely be expected within less than 1 second. It was demonstrated that SCWO combined with SCWHS is a feasible and cost-effective alternative for the destruction of contaminants in water.

In Chapter 6, A laboratory-scale protected wall reactor rig was designed, constructed, tested, and operated to validate the pseudo modelling for application to SCWO. SEM, SEM/EDS, and XRD results showed that 1 meter long protected wall reactor was divided into two regions. 25% of the reactor length was protected by the flow of clean supercritical water. Near complete removal of the organic content of 2,4-DCP was obtained at mild operating conditions.

To conclude, a summary of the work detailed in this thesis is delivered in Chapter 7. The most pertinent findings from this work are put forward, followed by a discussion of future work which could lead on from this thesis.

Acknowledgements

I wish to express my gratitude to some people and organisations for their support and assistance during the time spent on this thesis. Firstly, I would like to express my sincere thanks to my main supervisor, Prof. Ed Lester for all the support and patience over the years. Without his technical advice and management this thesis would not have reached its full potential. However, his guidance often went beyond the purely technical aspects and covered areas as diverse as presentation and writing skills, personal development, team working and more. Thus, it is clear to me that without his input I would not have transitioned from a hesitant student to a self-sufficient researcher.

Special thanks to my co-supervisors Dr. Thomas Huddle and Dr. Rachel Gomes for their advice, discussions on the work, and their invaluable support.

This research was sponsored by the Iraqi Council of Representatives with additional funding from the SHYMAN project- huge thanks go to them. I would also like to thank all the members of staff at Iraqi Cultural Attachè for supporting me to pursue my studies.

Still, I would like to thank the outstanding contributions of all of the staff and postgraduate research students in the Faculty of Engineering who have helped to make my time at Nottingham so enjoyable.

My wholeheartedly thanks also go to my family and friends for their love and assistance in making my PhD time balanced and enjoyable.

Finally, a special word of thanks to my wife, Doha Al-Mosawe, who not only helped with the overall design and layout of the present document but also read and listened to most of its contents, providing always key feedback with a smile in her face. Experiments failed and instruments broke but no matter how long or bad a day was, she was always there for me, keeping me levelled and focused. She believed in me even when I doubted, so it is safe to say that this thesis was completed because of her.

Affirmation

The work reported in this Thesis has not been published elsewhere, with the exception of the following publications:

Journal and Book Chapter Publications

1. Huddle T, **Al-Atta A**, Moran S, Lester E. Pseudo fluid modelling used in the design of continuous flow supercritical water oxidation reactors with improved corrosion resistance. *The Journal of Supercritical Fluids*. 2017; 120:355-65, DOI: http://dx.doi.org/10.1016/j.supflu.2016.06.004.

2. **Al-Atta A**, Huddle T, Rodrguez Y.G, Mato F, Garca-Serna J, Cocero M.J, Gomes R, Lester E. A techno-economic assessment of the potential for combining supercritical water oxidation with insitu hydrothermal synthesis of nanocatalysts using a counter current mixing reactor. *Chemical Engineering Journal*. 2018; 344:431-440,

   DOI: https://doi.org/10.1016/j.cej.2018.03.058.

3. Lester E, Dunne P, Chen Y, **Al-Atta A** 2018, 'The engineering of continuous hydrothermal/solvothermal synthesis of nanomaterials, in A Hunt, T Attard (ed.), Supercritical and other high-pressure solvent systems: for extraction, reaction and material processing, *Royal society of chemistry*, London.

Presentations, Posters and Awards

1. **Al-Atta A**, Huddle T, Moran S, Lester E, Understanding Mixing Regimes and Flow Dynamics in Supercritical Water Reactors through Pseudo Fluid Modelling for the Design of Corrosion-Resistant SCWO Reactors, *11th International Symposium on Supercritical Fluids* (ISSF), Seoul, South Korea, October 2015.

2. **Al-Atta A**, Huddle T, Moran S, Lester E, pseudo fluid modelling for supercritical water oxidation reactor design, *Engineering Showcase*, Nottingham, UK, May 2016; Poster-Runner Up.

3. **Al-Atta A**, Huddle T, Lester E, Supercritical water oxidation of hazardous waste: Process enhancement and reactor design, *3 minute thesis*: Engineering Showcase, Nottingham, UK, May 2017; Finalist.

Contents

Contents viii

List of Figures xiv

List of Tables xxvii

1 BACKGROUND 1

1.1 Introduction 1

1.2 Supercritical Fluids (SCF) 2

1.2.1 Properties of supercritical water (SCW) 4

1.2.2 Supercritical Water Oxidation (SCWO) 7

1.2.3 Other applications of supercritical water 11

1.3 Reaction mechanisms and kinetics of SCWO 12

1.3.1 Model compounds 14

1.3.2 Industrial wastewater 21

1.4 Operational problems in SCWO systems 23

1.4.1 Corrosion 23

1.4.2 Salt deposition 25

1.4.3 Economics aspects 26
1.5 Existing SCWO reactor designs 27
1.5.1 Tubular reactor 27
1.5.2 Cooled wall reactor (CWR) 28
1.5.3 Transpiring Wall Reactor (TWR) 31
1.5.4 Current status of commercial SCWO facilities around the world 34
1.6 Catalytic supercritical water oxidation 36
1.6.1 Homogeneous catalytic reactions 38
1.6.2 Heterogeneous catalytic reactions 39
1.7 Hydrothermal synthesis of nanomaterials 41
1.7.1 Pseudo fluid modelling 43
1.7.2 Counter current mixing reactor 45
1.8 Aims and objectives of this PhD 49

2 EXPERIMENTAL APPARATUS AND ANALYTICAL TECHNIQUES 53

2.1 General description of experimental set-up 53
2.1.1 Pseudo fluid modelling 54
2.1.2 Counter current mixing reactor system 55
2.1.3 Protected wall reactor system 61
2.2 Safety considerations 66
2.3 Analysis techniques 67
2.3.1 Chemical Oxygen Demand (COD) 68
2.3.2 Gas chromatography - Mass spectroscopy (GC-MS) 69

2.3.3 X-Ray Diffraction (XRD) 70
2.3.4 Transmission Electron Microscopy (TEM) 73
2.3.5 Scanning Electron Microscopy (SEM) and Energy Dispersive X-ray (EDX) Spectroscopy 74
2.4 Calculation of parameters 77
2.4.1 Residence time 77
2.4.2 Reynolds number 78
2.4.3 Concentration of reagents at reaction conditions 79
2.4.4 Oxidant ratio 80

3 PSEUDO FLUID MODELLING OF SCWO REACTORS 81

3.1 Introduction 81
3.2 Modified pseudo fluid modelling 83
3.2.1 Selection and preparation of pseudo fluids 83
3.2.2 Pseudo reactor design 84
3.2.2.1 Counter current mixing model 86
3.2.2.2 Co-current mixing model 87
3.2.2.3 Co-current "protected wall" model 88
3.2.3 Inlet Reynolds numbers and flowrates 90
3.2.4 Experimental stage 92
3.2.5 Fully automated calibration stage 92
3.3 Modified pixel image analysis 96
3.3.1 Calibration of concentration gradient 96
3.3.2 Processing of experimental images 102

3.4 Evaluating different reactor designs using pseudo fluid modelling . 104
3.4.1 Counter current mixing reactor 104
3.4.2 Co-current mixing reactor 107
3.4.3 Co-current protected wall reactor 111
3.5 Quantification and identification of ideal mixing 114
3.5.1 The wall zone 116
3.5.2 The mixing zone 116
3.6 Overall reactor efficiency definition 117
3.7 Conclusions 120

4 SUPERCRITICAL WATER OXIDATION OF ACRYLIC ACID IN COUNTER CURRENT REACTOR 123

4.1 Introduction 123
4.2 Experimental set-up 127
4.2.1 Experiments with oxidant preheating 128
4.2.2 Experiments without oxidant preheating 129
4.3 Effect of operational parameters on reduction of COD 129
4.3.1 Effect of reaction temperature 132
4.3.2 Effect of residence time and Reynolds number 133
4.3.3 Effect of oxidant ratio 134
4.3.4 Effect of acrylic acid concentration 135
4.4 Effect of in-situ catalyst formation 136
4.4.1 Titania (TiO_2) 137
4.4.2 Cobalt oxide (Co_3O_4) 141
4.4.3 Hematite (Fe_2O_3) 146

4.4.4 Chromium based particles 148
4.4.5 Mixed catalyst 154
4.5 Initial economic considerations 161
4.6 Conclusions 166

5 CATALYTIC SUPERCRITICAL WATER OXIDATION OF PHENOL IN COUNTER CURRENT REACTOR 169

5.1 Introduction 169
5.2 Phenol 170
5.2.1 Initial experiments and configurations assessment 172
5.2.2 Non-preheated oxidant configuration 174
5.2.3 Catalytic non-preheated oxidant configuration 178
5.3 Conclusions 183

6 SUPERCRITICAL WATER OXIDATION OF 2,4-DCP IN PROTECTED WALL REACTOR 185

6.1 Introduction 185
6.2 Protected wall reactor rig 187
6.3 Protected wall reactor results 190
6.4 Conclusions 196

7 CONCLUSIONS AND FUTURE WORK 199

7.1 Conclusions 199
7.2 Future work 202

BIBLIOGRAPHY 205

Appendices **227**

A Pseudo fluid calculator **227**

B Chromatographic information of phenol samples **231**

List of Figures

1.1 Pressure temperature phase diagram with the triple point, critical point, and supercritical region of water (Kamler and Soria, 2012). 5

1.2 A graph showing changes in the properties of water with increasing temperature at 24 Mpa, adopted from (Kritzer et al., 1999). . . . 6

1.3 Process schematic diagram for conventional SCWO process. . . . 11

1.4 Variation of selected phenol oxidation product at (380°C, 278 atm, 250 ppm phenol, and 250% excess oxygen, adopted from (Thornton and Savage, 1990). 16

1.5 Reaction pathways for thermal oxidative decomposition of acrylic acid, adopted from (Shende and Levec, 2000). 18

1.6 Diagram showing the main problems that may occur in the various parts of a conventional SCWO plant, adopted from (Vadillo et al., 2013). 23

1.7 Tubular reactor with oxidant multiple injections. 28

1.8 The performance of the cooled-wall reactor refrigerated with the waste feed flow (Bermejo et al., 2009). 30

1.9 The performance of a cooled wall reactor refrigerated with cooling water flow, adopted from (Bermejo et al., 2011). 31

1.10 The basic design of a transpiring wall reactor, adopted from (Xu et al., 2014). 32

1.11 Results of pseudo fluid modelling studies on the mixing dynamics of T-piece mixer (Blood et al., 2004). 44

1.12 Comparison between different techniques for investigating mixing within a T-piece mixer. (a) Pseudo fluid modelling (Blood et al., 2004), (b) CFD (Sierra-Pallares et al., 2011), (c) Direct observation using optical cell (Aizawa et al., 2007) and (d) Neutron beam (Takami et al., 2012). 46

1.13 Diagram of the counter-current mixing reactor used for the synthesis of nanoparticles. The cold aqueous metal salt flows upwards from the base of the reactor and mixes counter currently with a superheated water stream 47

2.1 Simplified schematic diagram for visualisation system. (a) Experimental stage set-up and (b) Light and camera position. 56

2.2 A process flow diagram of the counter current reactor system. . . 58

2.3 A process flow diagram of the co-current protected wall reactor system. 64

2.4 A diagram showing the basis of XRD analysis. 71

2.5 The basic layout of a transmission electron microscope (TEM). . . 74

2.6 The basic layout of a scanning electron microscope (SEM). 76

2.7 Main interactions involved in scanning electron microscopy. 76

2.8 Measurement of jetting distance in transparent PFA counter-current mixing reactor using pseudo fluids. (a) before run and (b) after run. Flow ratio is 2:1. 78

3.1 Comparing pseudo fluid combinations with flow rates adjusted to match Reynolds numbers (a) Methanol vs. Sucrose, (b) Water vs. Sucrose. The pseudo reactor used was only half of the full cross-sectional slice; the images above have been mirror duplicated for visualization. 85

3.2 (a) Standard configuration of counter-current mixing reactor. (b) Cross sectional slice of the counter-current reactor and (c) Pseudo reactor made up of rubber (6 mm thick) sandwiched between two polycarbonate sheets to replicate the mixing geometry in the counter-current reactor. 87

3.3 Cross sectional counter current pseudo reactor used for pseudo fluid modelling and its right side. Thickness of rubber used was 6 mm. 88

3.4 (a) Standard configuration of cocurrent mixing reactor. (b) Cross sectional slice of the co-current reactor and (c) Pseudo reactor made up of rubber (6 mm thick) sandwiched between two polycarbonate sheets to replicate the mixing geometry in the co-current reactor. 89

3.5 (a) Cross sectional co-current mixing pseudo reactor used for pseudo fluid modelling and (b) Inner across (inner tube). Thickness of rubber is 6mm. 89

3.6 (a) Standard configuration of co-current protected wall mixing reactor. (b) Cross sectional slice of the co-current protected wall reactor and (c) Pseudo reactor made up of rubber (6 mm thick) sandwiched between two polycarbonate sheets to replicate the mixing geometry in the co-current protected wall reactor. 90

3.7 (a) Cross sectional co-current protected wall pseudo reactor used for pseudo fluid modelling and (b) Inner across (inner tube). Thickness of rubber is 6 mm. 91

3.8 Schematic diagram of the automated calibration system as a part of pseudo fluid modelling process. 94

3.9 Flowsheet showing the calibration and processing steps. 97

3.10 Illustration representing the effect of combine process as a part of calibration stage of pixel image analysis. 98

3.11 Illustration showing the creating of a mask image from calibration image. Calibration was only conducted within black region of the mask. 100

3.12 illustration of a three-dimensional array as used during calibration and processing stages. Array dimensions=$a \times b \times n$. (n) is the total number of calibration images. 21 calibration images in this work. 101

3.13 Relationship between red pixel value and dye concentration for a single pixel of a calibration image. Each point represents a single calibration image at known dye concentration. 102

3.14 Image analysis concentration maps of counter current pseudo reactor (half side). (a) Using Beer-Lambert law for dye concentration calculations (b) without the combine process applied (c) with the combine process and linear interpolation applied to produce an accurate concentration map. 103

3.15 Cross sectional counter current mixing geometry. 105

3.16 Actual experimental image and Concentration map for the pseudo reactor. Flowrates: pseudo SCW downward flow, inner tube: 995 $mLmin^{-1}$ and pseudo wastewater upward flow, outer tube from base of reactor: 150 $mLmin^{-1}$. This is a simulation of 5:5 flow rate ratio used for actual SCWO process. The pseudo reactor used was only half of the full cross-sectional slice; the images above have been mirror duplicated for visualization. 105

3.17 Concentration maps for counter current mixing rector. The numbers in the lower image represent the flow rates of hydrothermal solution and wastewater (in $mLmin^{-1}$) being simulated, respectively. 106

3.18 Comparison between the CFD results obtained from several studies for the counter current mixer and the pseudo fluid simulation experiments at different flow rate ratios (SCW:cold flow), (a) 10:5 (Sierra-Pallares et al., 2011), (b) 20:20 (Sierra-Pallares et al., 2016a), (c) 40:20 (Zielke et al., 2016), and (d) 5:5 this work. . . . 107

3.19 Cross sectional co-current mixing geometry. 108

3.20 Actual experimental image and Concentration map for the co-current mixing pseudo reactor. Flowrates: pseudo SCW upward flow, inner cross: 995 $mLmin^{-1}$ and pseudo cold wastewater upward flow, outer cross: 128 $mLmin^{-1}$. This is a simulation of a 5:5 flow rate ratio under conditions typically used for SCWO. . . 109

3.21 Concentration maps for co current mixing rector. The numbers in the lower image represent the flow rates of hydrothermal solution and wastewater $mLmin^{-1}$ being simulated, respectively. 110

3.22 Simulation of mixing in co-current reactor, the color code indicates the precursor tracer concentration: red: feed precursor mixture, blue: feed SCW, other colors indicate degree of mixture between precursor and SCW. flow rate ratio: 20:20 (Zielke et al., 2016) . . 110

3.23 Cross sectional co-current protected wall reactor geometry. 111

3.24 Actual experimental image and Concentration map for the co-current protected wall pseudo reactor. Flowrates: pseudo hydrothermal solution upward flow, outer cross: 4412 $mLmin^{-1}$ and pseudo cold wastewater upward flow, inner cross: 632 $mLmin^{-1}$. This is a simulation of a 50:10 flow rate ratio under conditions typically used for SCWO. 112

3.25 Concentration maps for co current protected wall rector. The numbers in the lower image represent the flow rates of hydrothermal solution and wastewater (in $mLmin^{-1}$) being simulated, respectively. 113

3.26 Zones and bucket allocation used for application of the traffic light system. Bucket size: 15×15 pixels. 115

3.27 Co-current protected wall pseudo reactor.(a) Original image as captured by camera. (b) Concentration map applied to dye concentration data after processing stage. Red indicates maximum concentration of dye and dark blue is a zero concentration of dye. (c) Color coded buckets for the wall zones of the reactor; green buckets are those with an average dye concentration of 0 ppm, red bucket are those with a detected concentration of dye. 117

3.28 Co-current protected wall pseudo reactor.(a) Original image as captured by camera. (b) Concentration map applied to dye concentration data after processing stage. Red indicates maximum concentration of dye and dark blue is a zero concentration of dye. (c) Color coded buckets for the mixing zone indicating mixing efficiency; green buckets are those with an average concentration of within the range of the target concentration (the global average concentration of the mixing zone) +/- 33%; red buckets are those with average concentrations above this range, and blue are those below. 118

3.29 Concentration of dye in co-current protected wall pseudo reactor area. 118

3.30 Efficiency ratings for co-current protected wall reactor for various combinations of inlet flow Reynolds numbers. 120

4.1 Simplified flow diagram of the continuous SCWO system. (a) Preheated oxidant configuration and (b) Non-preheated oxidant configuration. T_1 measures immediately after the heater. T_2 is the post mixed flow.T_3 is the temperature prior to the back pressure regulator (see Table 4.2 for temperatures measurements) 130

4.2 The effect reaction temperature on %COD removal. All experiments were carried out at 250 *bar*, a residence time of 1.5 *sec*, an initial AA concentration of 10 mM and an oxidant ratio of 1. . . . 132

4.3 Experimental results for the effect of residence time on %COD removal at 380°C, 250 *bar*, an initial AA concentration of 10 mM and an oxidant ratio of 1. 135

4.4 The effect of oxidant ratio on %COD removal efficiency at 380°C, 250 *bar* and 10 mM of AA. 136

4.5 Experimental results for the effect of initial organic concentration on %COD removal efficiency at 380°C, 250 *bar* and oxidant ratio of 1. 137

4.6 A schematic diagram showing the reaction arrangement for synthesis of TiO_2. (a) Preheated oxidant and (b) Non-preheated oxidant scenario 138

4.7 Catalytic effect of titania nanoparticles on %COD removal at 380°C, 250 *bar*, oxidant ratio of 1.5, and initial acrylic acid concentration of 10 mM 139

4.8 XRD patterns of TiO_2 nanoparticles obtained obtained at 380°C, 250 *bar*, oxidant ratio of 1.5 and 20 mM of metal salt concentration. The red lines at the bottom are the expected peak positions for anatase (PDF 00-064-0863). (a) Preheated oxidant and (b) Non-preheated oxidant scenario. 140

4.9 TEM images of TiO_2 nanoparticles obtained from (a)Preheated oxidant and (b) Non-preheated oxidant scenario 142

4.10 A schematic diagram showing the reaction arrangement for synthesis of Co_3O_4. (a) Preheated oxidant and (b) Non-preheated oxidant scenario 144

4.11 Catalytic effect of cobalt oxide nanoparticles on %COD removal at 380°C, 250 *bar*, oxidant ratio of 1.5, and initial acrylic acid concentration of 10 mM 144

4.12 XRD patterns of Co_3O_4 nanoparticles obtained obtained at 380°C, 250 *bar*, oxidant ratio of 1.5 and 20 mM of metal salt concentration. The red lines at the bottom are the expected peak positions for Co_3O_4 (PDF 01-073-1701). (a) Preheated oxidant and (b) Non-preheated oxidant scenario. 145

4.13 TEM images of Co_3O_4 nanoparticles obtained from (a)Preheated oxidant and (b) Non-preheated oxidant scenario 147

4.14 A schematic diagram showing the reaction arrangement for synthesis of Fe_2O_3. (a) Preheated oxidant and (b) Non-preheated oxidant scenario 148

4.15 Catalytic effect of hematite nanoparticles on %COD removal at 380°C, 250bar, oxidant ratio of 1.5, and initial acrylic acid concentration of 10 mM 149

4.16 XRD patterns of hematite nanoparticles obtained obtained at 380°C, 250 bar, oxidant ratio of 1.5 and 20 mM of metal salt concentration. The red lines at the bottom are the expected peak positions for Co_3O_4 (PDF 01-071-5088). (a) Preheated oxidant and (b) Non-preheated oxidant scenario. 150

4.17 TEM images of Fe_2O_3 nanoparticles obtained from (a)Preheated oxidant and (b) Non-preheated oxidant scenario 151

4.18 A schematic diagram showing the reaction arrangement for synthesis of chromium based particles. (a) Preheated oxidant and (b) Non-preheated oxidant scenario 152

4.19 Catalytic effect of chromium based nanoparticles on %COD removal at 380°C, 250 bar, oxidant ratio of 1.5, and initial acrylic acid concentration of 10 mM 153

4.20 Photo showing a beam path of laser light passing through the chromium based particles sample- indicative of particles being present in sample. 154

4.21 XRD of chromium based nanoparticles obtained at 380°C, 250 bar, oxidant ratio of 1.5 and 20 mM of metal salt concentration. (a) Preheated oxidant and (b) Non-preheated oxidant scenario. 155

4.22 TEM images of chromium based nanoparticles obtained from (a)Preheated oxidant and (b) Non-preheated oxidant scenario 156

4.23 A schematic diagram showing the reaction arrangement for synthesis of TiO_2 and Fe_2O_3. (a) Preheated oxidant and (b) Non-preheated oxidant scenario 157

4.24 Catalytic effect of mixed catalyst of TiO_2 and Fe_2O_3 nanoparticles on %COD removal at 380°C, 250 *bar*, oxidant ratio of 1.5, and initial acrylic acid concentration of 10 mM 158

4.25 The effect of adding TiO_2 on the settlement of Fe_2O_3 for effluent taken from supercritical preheated oxidant experiments 159

4.26 TEM images of mixed catalyst of TiO_2 and Fe_2O_3 nanoparticles obtained from (a)Preheated oxidant and (b) Non-preheated oxidant scenario 160

4.27 Flow diagram of the industrial scale process (Aspen Plus® software) 163

4.28 Energy calculation for energy demand for the three scenarios . . . 163

5.1 Experimental set up for phenol oxidation. (a) preheated oxidant scenario and (b) Non-preheated oxidant scenario 173

5.2 The effect oxidant ratio on phenol and COD removal. All experiments were carried out at 380°C, 250*bar*, a residence time of 0.75 *sec* and an initial phenol concentration of 5 mM. 176

5.3 Total ion current traces (TIC) for phenol samples treated non-preheated oxidant configuration at oxidant ratio of (a) 1.0 and (b) 1.5. 176

5.4 The effect oxidant ratio on phenol and COD removal. All experiments were carried out at 380°C, 250*bar*, a residence time of 0.75 *sec*, an initial phenol concentration of 5 mM and $Fe(NO_3)_3.9H_2O$ concentration of 10 mM. 179

5.5 Total ion current traces (TIC) for phenol samples treated catalytic non-preheated oxidant configuration at oxidant ratio of (a) 1.0 and (b) 1.5. 179

5.6 The effect in-situ formed catalyst on COD removal. All experiments were carried out at 380°C, 250 *bar*, a residence time of 0.75 *sec*, an initial phenol concentration of 5 mM and oxidant ratio of 1.0. 181

6.1 Schematic diagram of protected wall reactor system 189

6.2 Diagram of a reactor tube 191

6.3 Cross-sectional photographs of reactor tube pieces. (a) piece number (2) representing region one in the reactor tubing, (b) piece number (5) showing the end of region one and beginning of region two and (c) piece number (7) representing region two in the reactor tubing. 192

6.4 Surface morphologies of the oxide layer grown on region one of the reactor tubing. 192

6.5 Surface morphologies of the oxide layer grown on region two of the reactor tubing. 193

6.6 Cross-sectional view of the oxide film layer formed on (a) region one and (b) region two of SS316L reactor tubing during SCWO process (380°C and 25 MPa). 194

6.7 EDS line scans of oxide film layer formed on (a) region one and (b) region two of SS316L reactor tubing during SCWO process (380°C and 25 MPa). 195

6.8 XRD patterns of scales form on SS316L tubing through SCWO process (380°C and 25 MPa): (a) $FeO_{0\cdot 64}NiO_{0\cdot 36}$ oxide scale on region one and (b) $Cr_{12}Fe_{22}Mo_4Ni_{10}Si_9$ mixture on region two. . . 197

6.9 The effect of oxidant ratio on COD removal efficiency at 380°C and 25 MPa and 1 mM 2,4-DCP. 198

B.1 Calibration curves for phenol (a) entire dataset and (b) lower phenol concentrations. 232

B.2 Extracted ion current traces (EIC) for target m/z 94.06 - molecular ion of phenol. (a) Preheated oxidant and (b) Catalytic preheated oxidant scenario 233

List of Tables

1.1 Conventional methods for hazardous waste treatment. 3

1.2 Critical constant for several SCF solvents (LaGrega et al., 2010). . 4

1.3 End products of SCWO process. 9

1.4 Inactive full-scale SCWO plants (Marrone, 2013). 35

1.5 Summary of studies on homogeneous catalytic SCWO 39

1.6 Summary of studies on heterogeneous catalytic SCWO 41

2.1 Schematic legend of counter current reactor system. 60

2.2 Oxidant delivery scenarios used in the counter current reactor system. 61

2.3 Schematic legend of co-current protected wall reactor system. . . . 65

2.4 Summary of analytical techniques. 68

2.5 Chromatography and MS ion source conditions. 70

3.1 The properties of pseudo fluids at 25 °C and 1bar. 85

3.2 Supercritical water oxidation and pseudo fluid modelling key temperatures and resultant fluid density and dynamic viscosity properties. System pressure taken to be 240 and 1 bar for SCWO and Pseudo fluid modelling, respectively. 91

3.3 labelled Calibration images resulting during the calibration stage of the physical modelling process. 95

4.1 Properties of acrylic acid. 127

4.2 Reaction temperatures in °C calculated from temperatures at different locations. Flow ratio is 2:1. 131

4.3 Experiments with different residence times and the subsequent impact on mixing dynamics. 134

4.4 Cost of preheated, non-preheated and catalytic non-preheated oxidant configurations 165

5.1 Properties of phenol. 171

5.2 The range of concentration of phenol in wastewater of different industries. 172

5.3 Initial experimental conditions for phenol oxidation. 173

5.4 Preliminary test results for phenol oxidation. 174

5.5 Operational conditions and conversions for various phenol oxidation experiments. 177

5.6 Operational conditions and conversions for various phenol catalytic oxidation experiments. 182

6.1 Properties of 2,4-DCP. 187

6.2 Chemical composition of the SS316L reactor tubing. 189

A.1 summarised stream properties for counter current reactor system and pseudo fluid modelling. 228

A.2 summarised stream properties for co-current reactor system and pseudo fluid modelling. 229

A.3 summarised stream properties for co-current protected wall reactor system and pseudo fluid modelling. 230

1 BACKGROUND

1.1 Introduction

The rate of public consumption of resources and industrial products increases concurrently with social welfare and the level of development of societies (Bolla et al., 2009). Production of these industrial compounds, apart from being an important contributor to the economy of numerous countries, inevitably generates polluting byproducts. As a result, the amount of waste generated continues to increase in response to accelerated urbanization and industrialization.

In general, the chemical compositions of the generated waste are very complex, and they may contain hazardous compounds, such as inorganic substances, phenols, halogenated organic compounds, carboxylic acids, and ammonia. In order to prevent the harmful effect of these compounds on the biosystem and on surface and ground water, the mentioned compounds should be effectively and safely removed before they contaminate the biosphere. The waste management hierarchy in the UK places disposal at the bottom; below prevention, reuse, and recycling (Al-Duri et al., 2015). However, hazardous organic wastes cannot be directly reused or easily recycled, so they are subject to disposal using the best

available techniques.

Various technologies have been tested for the treatment of toxic and hazardous waste substances to remove organic and inorganic pollutants. The main techniques that have been utilized to destroy hazardous waste or convert it into non-hazardous materials, including their disadvantages, are presented in Table 1.1. These methods have been found to be limited in their applicability, since they often involve high capital and operational costs and may also be associated with the generation of secondary wastes that can often be more toxic than the original substance (LaGrega et al., 2010; Fang, 2014).

1.2 Supercritical Fluids (SCF)

Consider a mixture of liquid and gas at equilibrium conditions. When the temperature is increased, the liquid phase becomes less dense due to thermal expansion, whereas increasing the pressure would increase the density of the gas phase. As the pressure and temperature are elevated, a point is reached at which there is no longer a distinction between the two phases. In a pressure-temperature phase diagram, this is called the "critical point". Above the critical point, a single homogeneous phase fluid is described as a supercritical fluid (SCF) (LaGrega et al., 2010). Accordingly, SCF is defined as any fluid exceeding its critical temperature and pressure. The critical parameters of water and some SCFs are given in Table 1.2. In particular, carbon dioxide and water are the most frequently used SCFs in industrial applications due to their unique properties. They are "greener" than organic solvents, non-flammable, non-toxic, and relatively easy to use. A typical thermodynamic phase diagram for water can be found in

Table 1.1: Conventional methods for hazardous waste treatment.

Technology	Disadvantages
Carbon adsorption	The regeneration is expensive and results in the loss of adsorptive capacity, non-destructive process, useful only for waste with dilute organic content, result in new waste generation (Foo and Hameed, 2009).
Coagulation and flocculation	Large amount of chemicals required, sludge generation and disposal problems.
Membrane separation	High capital cost, degradation and fouling of membrane (Richardson and Harker, 2002).
Incineration	High capital and operational cost (Lin and Ma, 2012). Additional fuel in case of low organic content, hazardous stack gas emissions such as NO_x, dioxin and furan (Heimbuch and Wilhelmi, 1985).
Biological methods	Poisonous metabolites may kill the bacteria, limited to low concentration waste, non-sustainable waste treatment method for long term use (Weber et al., 2011).
Wet air oxidation	99% conversion rate is seldom achieved (Kolaczkowski et al., 1999), slow oxidation rate of low molecular weight oxygenated compounds, (Luck, 1999), colored and toxic effluent, relatively long residence time and large reactor volumes (Kritzer and Dinjus, 2001).
Supercritical water oxidation	Corrosion, salt deposition and high operational cost (Vadillo et al., 2013).

Table 1.2: Critical constant for several SCF solvents (LaGrega et al., 2010).

Solvent	Temperature, °C	Pressure, atm	Density, g/cm^3
Water	374.15	218.4	0.323
Carbon dioxide	31.1	73.0	0.460
Ammonia	132.4	111.5	0.235
Benzene	288.5	47.7	0.304
Toluene	320.6	41.6	0.292

Figure 1.1. As shown, the critical point (Tc, Pc) represents the highest values at which the equilibrium between liquid and gas can exist. The substance in the red area called "Supercritical Water" is neither a gas nor a liquid. For instance, a SCF can be liquefied (immediately converted to a liquid) if the temperature is reduced at a constant pressure. Similarly, an SCF can be gasified (immediately converted to a gas) if the pressure is decreased at a constant temperature. Therefore, an SCF is a single homogeneous phase that shares the properties of both the liquid and gas phases.

1.2.1 Properties of supercritical water (SCW)

The properties of water at supercritical conditions differ completely from the properties at ambient conditions. SCW properties lie between those of the liquid and gas phases. Therefore, SCW can be considered to be a high-density gas. The typical correlation between the properties of water at 24 MPa is represented in Figure 1.2. As the temperature increases, the density of water decreases gradually

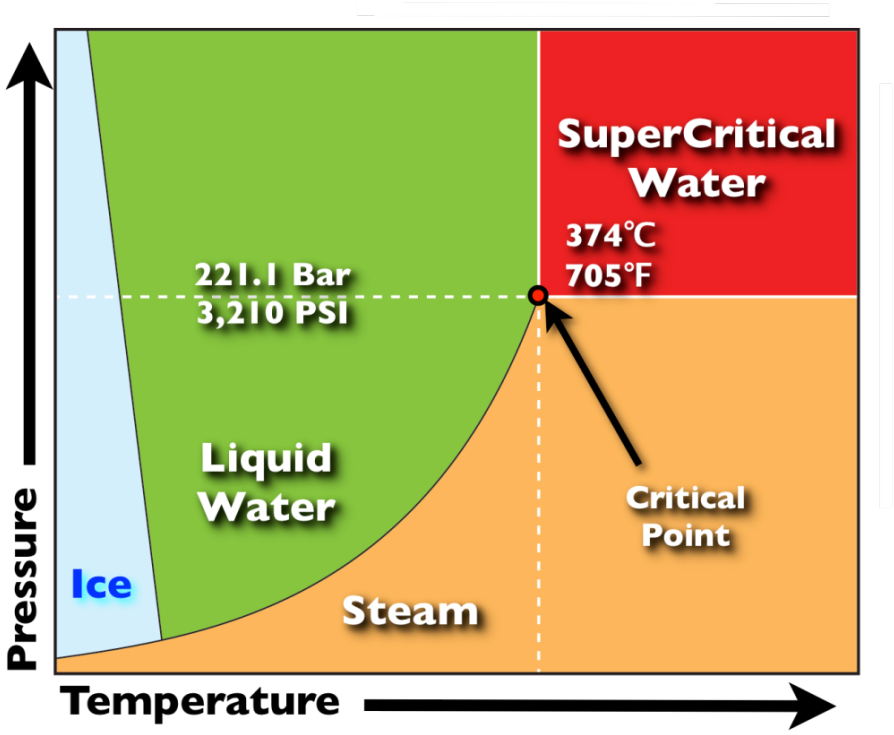


Figure 1.1: Pressure temperature phase diagram with the triple point, critical point, and supercritical region of water (Kamler and Soria, 2012).

due to thermal expansion. Near the critical temperature of water, the rate of density decrease varies very rapidly with relatively small changes in temperature. The solubility property of SCW depends primarily on its density, which is a function of temperature and pressure in the critical region. Therefore, SCW can be regulated by tuning the temperature and pressure.

As a result of the decrease in density, the dielectric constant of the water decreases and the dissociation constant (K_w) increases due to hydrogen bonds being broken. It is found that the number of hydrogen bonds in SCW is about one-third that of water at normal conditions (Cochran et al., 1992). The dielectric constant of water at normal conditions is about 80. This relatively high value is due to strong hydrogen bonding. As the temperature increases, the number of available hydrogen bonds, and consequently the value of dielectric constant,

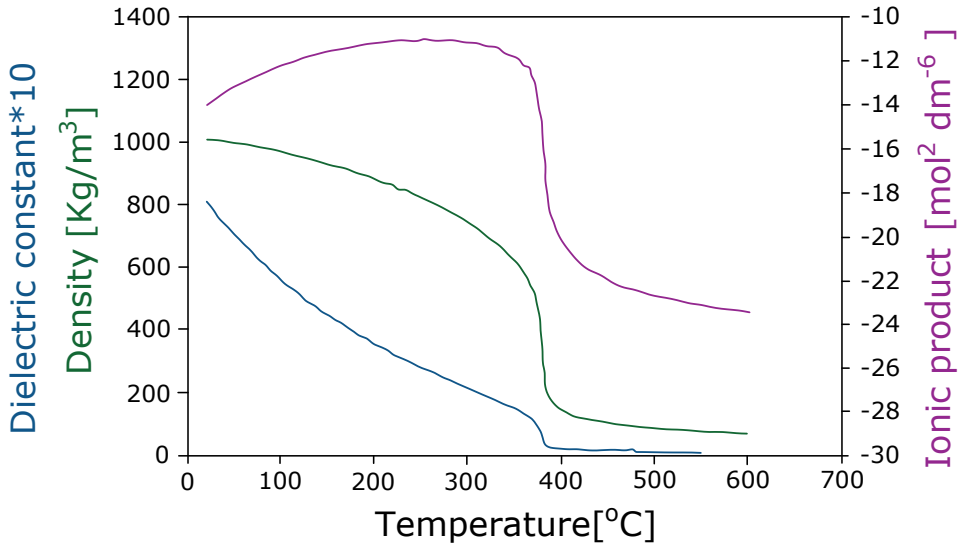


Figure 1.2: A graph showing changes in the properties of water with increasing temperature at 24 Mpa, adopted from (Kritzer et al., 1999).

decreases. For example, at a temperature of 130°C, the dielectric constant falls to 50, while at 200°C the figure drops to around 25 before reaching 5 at the water's critical point (Kritzer et al., 1999; Yesodharan et al., 2002).

Due to a high dielectric constant, water is a good solvent for ionic inorganic substances at ambient conditions. However, the solvation property of water to inorganic salt is reversible in SCW. Consequently, salts tend to precipitate out of the SCW phase. To highlight this, we see that the solubility of NaCl at ambient conditions increases with temperature and reaches its maximum value at sub-critical conditions with 400,000 mg/l. At supercritical conditions, the solubility declines very sharply by almost 4 orders of magnitude to about 100 mg/l (Armellini et al., 1994). Thus, water under supercritical conditions loses its dissolving power for inorganic salts and acts as a weakly-polar solvent.

In contrast, non-polar organic compounds such as alkanes and aromatics; and permanent gases like oxygen, are essentially miscible with water at supercritical conditions (Yesodharan et al., 2002; Bermejo and Cocero, 2006b). This is



because the corresponding value of the dielectric constant of SCW and of most polar organic solvents under normal conditions. To highlight this, we see that the solubility of benzene in water at ambient temperature and pressure is only about 1700 mg/l; but the compound shows a complete miscibility with SCW in all proportions. Other hydrocarbons can also exhibit similar solubility behaviour. All these special characteristics make SCW an ideal medium for oxidation of organic substances. The well dissolved organic compounds and oxygen in a single homogeneous SCW phase, can rapidly react with each other because of the fast thermal reaction rate in correlation with elevated system temperatures. Additionally, the absence of phase boundaries and surface tension in supercritical water medium, minimizes the interface transport limitations and facilitates a speedy chemical reactions.

1.2.2 Supercritical Water Oxidation (SCWO)

SCWO also known as Hydrothermal Oxidation (HTO) is the rapid oxidation of oxidizable materials in one homogeneous phase at temperature above 374°C and pressure above 22.1 MPa (supercritical conditions) by using an oxidizing agent like oxygen, air or hydrogen peroxide (Modell et al., 1992).

The process is well-known through its potential to breakdown a wide range of model compounds with persistent organic pollutants (POPs) such as polychlorinated biphenyls (PCBs) (Hatakeda et al., 1999; Kawasaki et al., 2006; Marulanda and Bolaños, 2010), phenol and halogenated phenol (Martino and Savage, 1999b; Lee et al., 2005; García Jarana et al., 2010), nitrogen-containing hydrocarbon compounds like aniline (Ma et al., 2012), hydrazine (Plugatyr et al., 2011), quino-

line (Pinto et al., 2006; Angeles-Hernández et al., 2008), ammonia (Bermejo et al., 2008; Cabeza et al., 2014), real waste like pesticide wastewater (Xu et al., 2015b), municipal solid waste leachate (Zou et al., 2013), laboratory waste (Dong et al., 2014) and pharmaceutical waste (Stavbar et al., 2017) that cannot be treated by conventional treatment technologies. In addition, there is a long standing convention of using SCWO as an alternative to combustion based technologies for disposing of military waste (Veriansyah et al., 2005) and radioactive waste (Leybros et al., 2010) which have the potential to produce a noxious by-product if not completely treated.

As a treatment technology, SCWO presents important advantages over other conventional treatment processes and even some modern processes such as wet air oxidation and incineration (Al-Duri et al., 2015). These advantages arise from the outstanding physical-chemical properties of SCW that make it an effective medium for oxidation reactions. SCW has shared properties between liquid and gas phases of water. The low viscosity approaching that of the gaseous phase, enhances mass transfer. The density approaching that of the liquid phase, enhances solvation. The high supercritical temperature increases the reaction rate and low dielectric constant enhances dissolution of non-polar organic materials. These properties provide a medium for the oxidation reaction in which non-polar organic materials mix, dissolve, and react quickly with oxygen.

Supercritical water oxidation is a destructive process. Thus, organic compounds are broken down rather than removed. Table 1.3 shows the end products for the SCWO process. A shortened reactor residence time is required to complete the oxidation reaction enabling a high output of waste compounds. Reaction

times ranging from a few seconds to a minute can sufficiently destroy more than 99.99% of most inorganic and organic materials (Bermejo and Cocero, 2006b). Moreover, benign and low molecular weight compounds are produced as products which are less toxic than the original waste. The operating temperature is not sufficient to produce partial oxidation products. Thus, NOx, dioxins, or CO have not been detected (Yesodharan et al., 2002). Recently, there has been an initiative to recover energy produced by the oxidation process to preheat reactants and maintain reactor conditions. This has resulted in a self-sustained energy process (Cabeza et al., 2015) while making it economically viable (Benjumea et al., 2016).

Table 1.3: End products of SCWO process.

Initial chemical	End product
Carbon	Carbon dioxide
Hydrogen	Water
Nitrogen	Nitrogen gas or Nitrate
Heteroatom (e.g., Cl, Br, S)	Oxyacid (HCl, HBr, H_2SO_4)

On the other hand, the unique properties of SCW as a reaction medium have a problematic effect on the process if aqueous feeds being treated contain heteroatoms (atoms rather than C, H). Halogens, sulphur, and phosphorus are generally converted to their corresponding inorganic acids (HCl, HBr, H_2SO_4, H_3PO_4) during the SCWO process, potentially causing severe corrosion problems (Vadillo et al., 2013). This is greatly applicable during heating-up and cooling-

down sections when conditions are at subcritical levels (Marrone and Hong, 2009). Another challenge arises from ionic salts which either exist in the aqueous feed or are formed during the acid neutralization stage in the SCWO process. These salts are insoluble in SCW and tend to precipitate onto the reactor surfaces which cause blockages. This phenomenon is termed as salt deposition. These problems and their mitigation actions are discussed in Section 1.4.

Process description:

In supercritical water oxidation, two feed streams were prepared by dissolving either hydrogen peroxide or oxygen, and organic contaminate separately in different vessels. The two streams were pressurized in two separated lines by high pressure metering pumps and preheated separately (Fang, 2014). The reactants were preheated to 400°C where the residence time in preheaters was long enough for all of the H_2O_2 to decompose into supercritical H_2O and O_2 (Garcia-Verdugo et al., 2004). After preheating, the two streams were mixed at the reactor entrance. Figure 1.3 shows a schematic of the process. The oxidation of many organic compounds in the reactor took place in a very short residence time at temperatures ranging from 600 to 650°C (Bermejo and Cocero, 2006b). From the reactor, the effluent was cooled rapidly through a heat exchanger and afterwards, the system pressure was reduced using a back pressure regulator (BPR). Then, the product passed through a gas-liquid separator to separate gases (mainly CO_2 and N_2 from effluent water). The typical heating resources to be used for the process of this sort are a sand bath, a molten salt bath, or an electric furnace (Al-Duri et al., 2015).

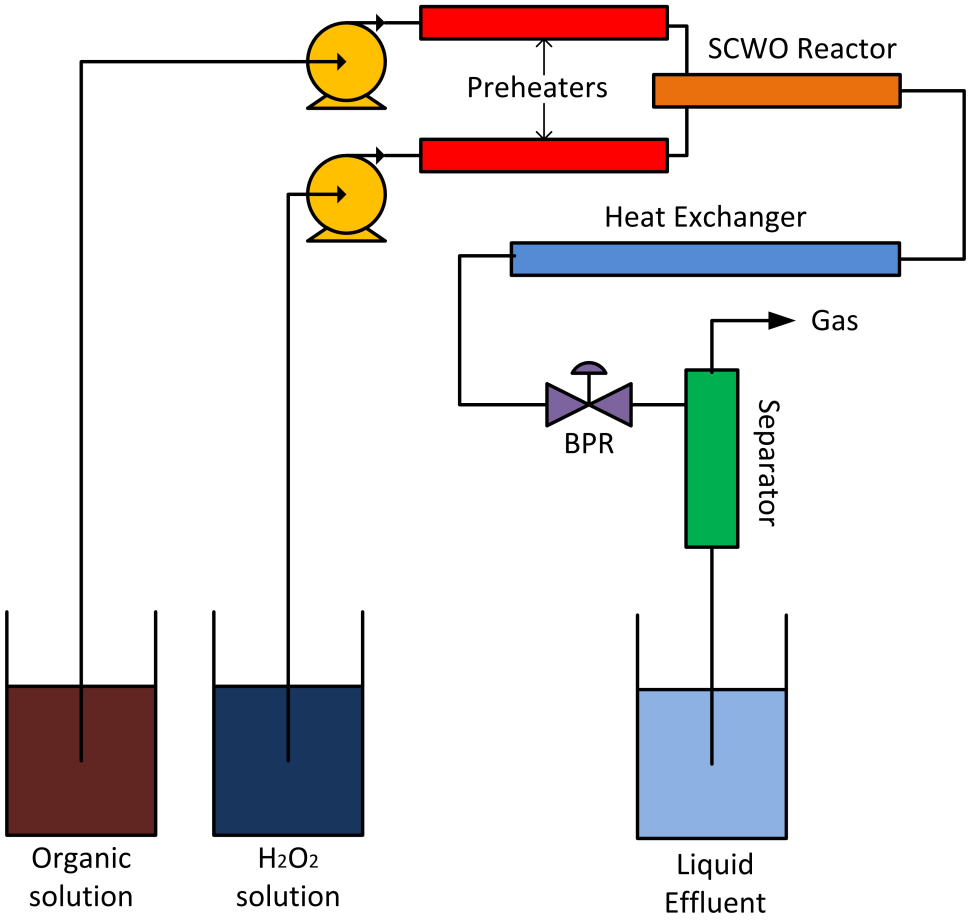


Figure 1.3: Process schematic diagram for conventional SCWO process.

1.2.3 Other applications of supercritical water

The properties of SCW described in Section 1.2.1 make it a solvent of interest for applications other than the oxidation of organic compounds.

One of the major applications of SCW is the synthesis of nanoparticles. Due to the non-polar nature of SCW, it has relatively low solubility for inorganic ionic salts. This principle forms the basis for the synthesis of fine inorganic particles in SCW. Due to this principle, and the interesting properties of SCW, it has been increasingly used in recent years as a reaction medium for the production of nanoscale metals and metal oxides (Dunne et al., 2015; Lester et al., 2012; Caramazana-Gonzalez et al., 2017). Because the main reaction media is water,

rather than noxious solvents, the technology has received a tremendous amount of interest as a sustainable or green technology. More details on the hydrothermal synthesis of nanoparticles are given in Section 1.7.

Sub and supercritical water have also reportedly been used in chemical recycling, bio-oil upgrading and supercritical water gasification. Compared to other established processes, again, this process technology has advantages in its inherent greenness and potential higher energy efficiency (Piñero-Hernanz et al., 2008; Remón et al., 2016).

1.3 Reaction mechanisms and kinetics of SCWO

The destruction of organic compounds in SCWO is primarily based upon radical reaction mechanisms rather than ionic reactions due to very low values of ionic product of water at supercritical conditions (Kritzer, 2004). The organic molecules are attacked by free radicals which are produced during the oxidation of organic compounds in SCW. The major radical reactions taking place during the SCWO process can be summarized in the following equations (Fang, 2014):

Hydroxyl generation:

$$H_2O_2 \longrightarrow 2\,HO^{\bullet}$$

Hydrogen removal and generation of organic radical ($R^{\bullet}$):

$$RH + HO^{\bullet} \longrightarrow R^{\bullet} + H_2O$$

Production of peroxy radical ($ROO^{\bullet}$):

$$R^{\bullet} + O_2 \longrightarrow ROO^{\bullet}$$

Then, peroxy radical ($ROO^{\bullet}$) extracts a hydrogen atom to form an organic peroxide (ROOH) and a new organic radical ($R^{\bullet}$):



$RH + ROO^{\bullet} \longrightarrow ROOH + R^{\bullet}$

The organic peroxide (ROOH) is relatively unstable and often decomposes into lower molecular weight compounds. These reactions will proceed until the termination of the radical reaction occurs and the final products are formed.

In the SCWO process, some organic compounds are readily oxidized into final degradation products, whereas others are transformed into refractory rate-limiting intermediate products such as acetic acid and ammonia. The simplification of the hydrocarbon SCWO mechanism is shown in the following equations:

$A + O_2 \longrightarrow Product$

$A + O_2 \longrightarrow B$

$B + O_2 \longrightarrow Product$

where A and B represent the initial organic and intermediate product, respectively. However, the detailed mechanism during the reaction is more complicated. A molecule will not be converted into a final product upon collision with the oxidant. The reaction proceeds through a series of reversible elementary reactions. For simple hydrocarbons, these elementary steps are fully understood. Whereas, for more complex compound, the proposed mechanism is quite ambiguous.

Due to the wide variety of organic species in the mixture, the concentration of A and B can be expressed in bulk as Total Organic Carbon (TOC) or Chemical Oxygen Demand (COD). Therefore, the oxidation of organic compounds in SCW can be expressed in the form of a global rate equation as:

$$\frac{-d[COD]}{dt} = \mathrm{K}[COD]^{\mathrm{a}}[O_2]^{\mathrm{b}}[H_2O]^{\mathrm{c}} = \mathrm{A}e^{-\mathrm{E/RT}}[COD]^{\mathrm{a}}[O_2]^{\mathrm{b}}[H_2O]^{\mathrm{c}} \qquad (1.1)$$

where K is the reaction constant, A is a pre-exponential term, E is the activation energy ($kJmol^{-1}$), R is the gas constant ($Jmol^{-1}K^{-1}$), T is the reaction temperature (K); a, b and c are the order of each reactant.

Global kinetic parameters have been determined by extensive kinetic studies undertaken for a large number and variety of compounds ranging from simple model compounds to complex industrial wastes.

1.3.1 Model compounds

The potential of the SCWO process has been investigated for a wide range of model compounds ranging in complexity from simple to more complex hydrocarbons respectively. Studies have been performed into the oxidation of non-nitrogenated, nitrogenated, and heteroatom containing compounds. Most studies identify the effects of reaction parameters on the destruction efficiency of the process in terms of TOC, COD and investigated compound removal, with some also studying oxidation kinetics and the reaction pathway. In a majority of cases, it was found that hydrocarbons conversions are positively correlated with temperatures, residence time and oxidant dose.

Investigations into oxidation of phenol as a model pollutant have been carried out by different researchers in both batch (Koo et al., 1997) and continuous reactor configurations (Thornton and Savage, 1990) since phenol is ubiquitous in industrial wastewaters; and the oxidation of aromatic compounds often proceeds through a phenol intermediate (Martino and Savage, 1999a).

Thornton and Savage (1990) investigated the effect of reaction conditions; namely temperature, pressure, residence time and reactant concentrations on the



oxidation of phenol in sub and supercritical water. The oxidation experiments employed covered a variety of phenol conversions ranging from 0-100%. Variations in oxidation conditions resulted in varying conversions between these extremes. When the pressure was subcritical, the residence time was short and the temperature reached 380°C. Under these conditions, the phenol conversions did not exceed 11%. Whereas, this conversion rate approached its maximum value at supercritical pressure, long residence time and excess concentration of oxidant. These effects in term of temperature and residence time are consistent with measurements by Pérez et al. (2004). They concluded that phenol concentration and excess oxygen of more than 10% had little effect on phenol conversion. However, both Thornton and Savage (1990); Koo et al. (1997) found that conversions increased with increasing feed and oxygen concentrations.

Thornton and Savage (1990) identified the formation of a large number of intermediate compounds ranging in complexity from low to high molecular weight products. Some of these products (e.g., 4-phenoxyphenol, dibenzofuran, and 2,2-biphenol) are more complex than the original phenol itself. This indicate that oxidation of phenol in supercritical water proceed through a set of multiple reaction pathways. To resolve these reaction pathways, variations of some intermediates with residence time were given as shown in Figure 1.4. The fact that the concentration of phenol steadily decreased while the concentration of intermediates increased, reached its maximum and then decreased; indicates the presence of a parallel set of series reactions. Martino and Savage (1997) proposed a parallel pathway for phenol to be converted into multi-ring substances and phenol dimers. Secondary decomposition of dimers led to ring-opening intermediates, whereby

these intermediates were eventually converted to carbon oxides.

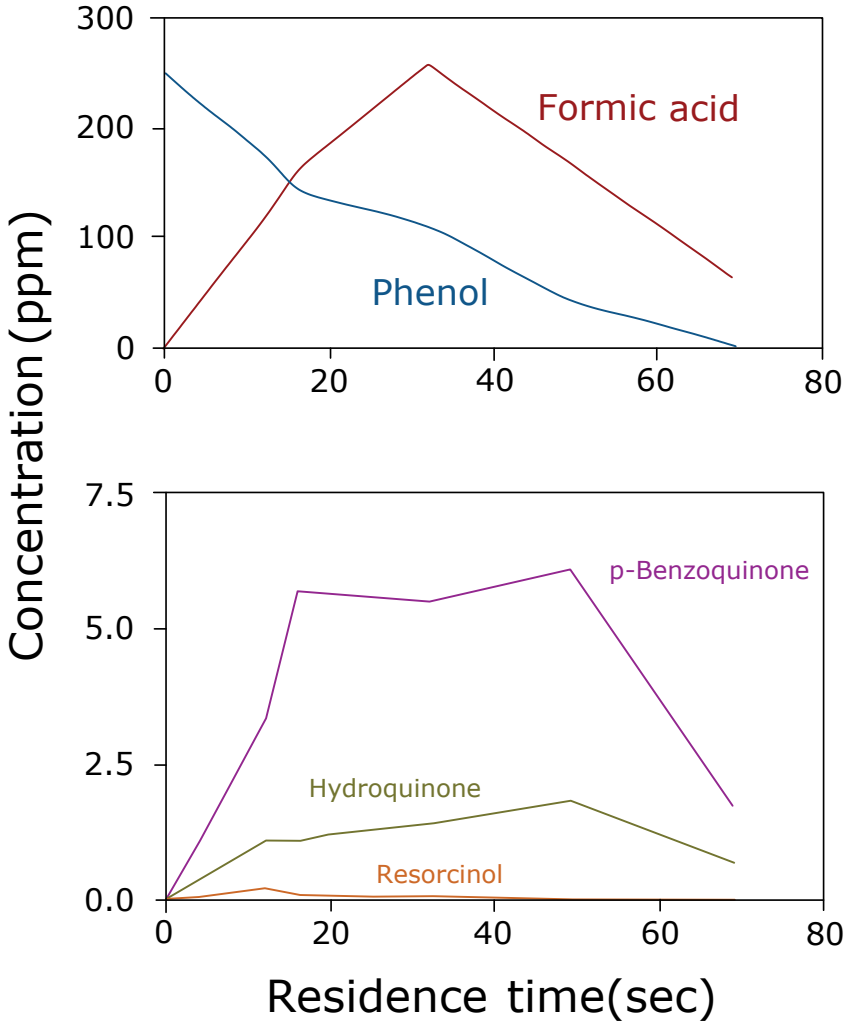


Figure 1.4: Variation of selected phenol oxidation product at (380°C, 278 atm, 250 ppm phenol, and 250% excess oxygen, adopted from (Thornton and Savage, 1990).

In order to increase the hydrothermal oxidation rate of phenol at mild conditions, free radical promoters were used in both WAO and SCWO processes. Compared to oxygen, the addition of hydrogen peroxide as a source of free radicals to WAO systems has shown the ability to enhance the reaction rate, leading to higher conversions at shorter residence times (Kolaczkowski et al., 1997; Rivas et al., 1999). The positive effect of hydrogen peroxide addition is due to the thermal decomposition of hydrogen peroxide to give two hydroxyl radicals $HO^{\bullet}$,

which is an extremely reactive oxidant. The rate of initiation of organic radicals by hydroxyl radicals is considered to be much faster as compared to oxygen at the same operating conditions. It is also believed that the existence of hydroxyl radicals can impede the formation of dimers and toxic aromatic species by expediting the formation of ring-opening intermediates (Rubalcaba et al., 2007; Quintanilla et al., 2010).

Shende and Levec (2000) investigated the oxidation kinetics of acrylic acid which has been observed as an intermediate product in hydrothermal oxidation of phenols. Oxidation experiments were conducted in a titanium reactor at subcritical conditions. It was found that hydrothermal degradation of acrylic acid can be neglected at a temperature range of 180-280°C. Conversely, 72% of acrylic acid was converted to CO_2 and other intermediates at 290°C. The HPLC analysis showed that formic and acetic acid are the main intermediates in the oxidation of acrylic acid. It was speculated that formic acid was formed from oxalic and glyoxalic acids but this was not confirmed analytically. The reaction pathways for the hydrothermal oxidation of acrylic acid is presented in Figure 1.5.

Investigations into SCWO of nitrogen-containing hydrocarbons have been reported in recent years. Al-Duri and her research group conducted a series of studies on the continuous SCWO of dimethyl formamide (DMF) and 1,8-Diazabicyclo[5.4.0]undec-7-ene (DBU) (Al-Duri et al., 2008; García-Jarana et al., 2013; Al-Duri et al., 2016; Al-Duri and Alsoqyani, 2017). The first study was carried out using a conventional SCWO process in a plug flow coiled reactor. It was found that complete conversion of DBU was achieved at 450°C; however TOC reduction approached 98% at temperatures just above 600°C. They also found

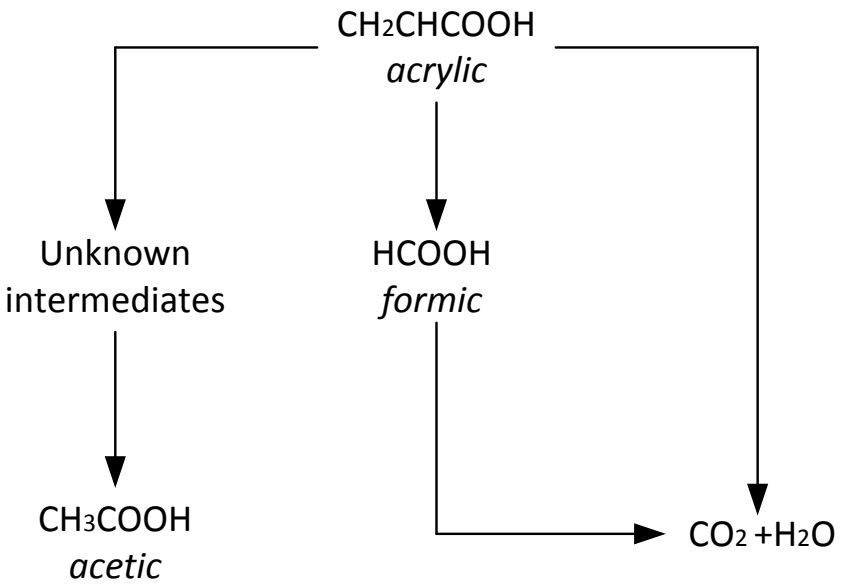


Figure 1.5: Reaction pathways for thermal oxidative decomposition of acrylic acid, adopted from (Shende and Levec, 2000).

that around 20% of inorganic carbon remained un-oxidized and 60% of NH_4^+ remained in solution even at temperatures exceeding 650°C. With sufficient oxidant concentration, the conversion of TC to CO_2 become more significant when the reaction temperature increased from 450 to 500°C. However, the presence of ammonia was still detected at 650°C. Due to the recalcitrant nature of ammonia, a catalyst is essential in achieving a high conversion in the SCWO process. The effect of pressure on DBU conversion was obvious in the near critical region due to high sensitivity of fluid density to pressure changes in this region.

García-Jarana et al. (2013) studied the advantages of the SCWO process with oxidant multi-injection over a conventional oxidant single entry in treating DMF. Experiments were conducted by splitting the initial oxidant feed into two points. The first point occurred at the reactor inlet and the second injection at one of the three different locations along the reactor. It was found that multi oxidant injection experiments resulted in increased DMF and TOC removal when compared

to single oxidant entry experiments. The best position for the second injector was halfway along the reactor length with 75% of the total deliverable oxidant at the first injection point, and 25% at the second injection point. The use of this configuration resulted in enhancement in TOC reduction of 89.2% compared to 79.8% achieved at single oxidant injection. However, splitting the oxidant over more than one feeding point had no beneficial effect on NH_4^+ removal.

Al-Duri et al. (2016) investigated the effect of addition of a co-fuel on the destruction of DBU in the SCWO process. Isopropyl alcohol (IPA) was chosen as a co-fuel because it is readily oxidized in SCW and has an important heat of reaction value $\triangle H_{\mathrm{r}}$ (-1908 $kJmol^{-1}$)(Abelleira et al., 2013). The beneficial effect of co-fuel on the reaction rate was attributed to the release of vigorous free radicals and extra heat by fuel. The result showed that addition of IPA enhanced TOC removal at moderate temperatures. TOC removal improved by 9.5% at 400°C, 2 *sec* and an IPA/DBU ratio of 4. They also found that the addition of IPA can be beneficial for the oxidation of ammonia. The yield percentage of NH_4^+ in the liquid phase reduced by 9% at 400°C and a stoichiometric amount of oxygen. Similar conclusions were reached by Oe et al. (2007); Ploeger et al. (2007) where they used methanol and ethanol as a co-fuels in oxidation of ammonia respectively. They also stated that addition of co-fuels enhanced the conversion of ammonia to nitrogen gas.

The presence of heteroatoms in organic compounds has become a concern to the SCWO system. The oxidation of atoms like chlorine, sulfur and phosphorus into their corresponding acids is the main problem inhibiting the industrialization of the process. Therefore, the investigation into such hydrocarbons has been an

important aspect in assessing the entire SCWO technology as a waste treatment process. A commonly investigated organo-heteroatom is chlorine, e.g. in the form of chlorophenol and polychlorinated biphenyls.

The sub and SCWO of 2,4-dichlorophenoxyacetic acid (2,4-D) was investigated by Hashimoto et al. (2010). The results indicate that although almost complete degradation of 2,4-D was obtained at subcritical temperatures, TOC reductions were very slow compared to those in supercritical water. 2,4 DCP and acetic acid are the main intermediates in both sub and supercritical water. TOC conversions and dechlorination were significantly enhanced (95 and 91% respectively) at 400°C and a reaction time of 60 min.

Lee et al. (1990) compared the oxidation rate of 2,4-dichlorophenol and acetic acid using oxygen and hydrogen peroxide in a series of premixed, batch experiments at 450°C to 500°C. At comparable operating conditions, they found that the conversions of both compounds was higher by using hydrogen peroxide as an oxidation agent. A more recent study on the effect of hydrogen peroxide was performed by Hatakeda et al. (1999). The efficiencies of hydrogen peroxide and oxygen as oxidants for the destruction of polychlorinated biphenyls (PCBs) were compared under SCW conditions in the range of 200°C to 450°C using a batch-reactor system. The highest conversion using hydrogen peroxide was 99.999%, while the conversion using oxygen was less than 15% under the same reaction conditions. This indicates that hydrogen peroxide is a far more powerful oxidizing agent than oxygen and the oxidation reaction was initiated by a different chain initiation step. In other words, hydrogen peroxide is readily decomposed into the hydroxyl radicals $HO^{\bullet}$ which are more reactive than $HO_2^{\bullet}$ generated in

SCWO using oxygen (Gopalan and Savage, 1994). Hatakeda et al. (1999) also used hydrogen peroxide as an oxidant for PCB oxidation in a flow-reactor system. The oxidation was carried out at 30 MPa and 400°C in a range of residence times from 10.7 to 101.7 *sec*. A high conversion rate of 99% was achieved in all runs. Although the preheating temperature in this system was set to 150°C, this may retard the complete decomposition of hydrogen peroxide and be advantageous to the generation of hydroxyl radicals.

1.3.2 Industrial wastewater

As well as research into the suitability of the SCWO process for model compounds, there have also been lab- and pilot scale researches into the capability of the process to treat multi-component real industrial wastewater.

The SCWO of two types of coking wastewater has been investigated using a continuous flow reactor and H_2O_2 as an oxidant (Du et al., 2013). This waste contained high amounts of NH_3−N, phenol, COD and inorganic salts. Due to a high concentration of inorganic salts in coking wastewater which may cause plugging during the SCWO process, a salt separator was used between the preheater and the reactor. Subsequently, the efficiency of the salt separator was also investigated. The authors found that both phenol and COD can be easily destroyed at moderate temperatures, whereas NH_3−N was very stable even at 500°C. However, as the temperature exceeds 650°C, the conversion of all pollutants is above 99.94%. They also found that the pressure has a negligible effect on pollutants destruction and a pressure just above the critical point of water is enough to maintain supercritical condition for the process. As regards to the salt separator,

a high separation of salts was obtained by maintaining the inner temperature and pressure at 600°C and 25 MPa, respectively. An increase in the efficiency of the salt separator with increasing temperature was observed which can be attributed to a decrease in the solubility of salts under supercritical conditions (Hodes et al., 2004).

The co-detoxification of two inevitable secondary waste streams: municipal solid waste leachate and fly ash has been done by Zou et al. (2013) under SCWO conditions. MSW leachate is a highly polluted type of wastewater, difficult to treat by conventional methods and containing large amounts of organic and inorganic contaminates (Renou et al., 2008). Fly ash generated from incineration of MSW is contaminated with numerous toxic substances like heavy metals, polychlorinated dibenzo-p-dioxins (PCDDs) and polychlorinated dibenzofurans (PCDFs) that if not treated properly, can cause adverse effects to human health and the environment. The MSW leachate was contained several complex organic compounds with a relatively high concentration of COD: 34600 mg/l; TOC; 8172 mg/l; NH_3−N; 1615 mg/l; some trace metals and sand. It was found that temperature and concentration of the oxidant has an important role in stimulating conversion while residence time has surprisingly little effect on COD% removal. Almost complete removal of COD was obtained with operating conditions of 500°C, residence time of 2 min and 300% of excess oxidant. The addition of fly ash enhanced COD and PCDDs/Fs reduction efficiency. The promoting effect of adding 6g of fly ash increased COD conversion from 87.4 to 91.6% at 400°C. The catalytic effect of fly ash on COD degradation may be attributed to small contents of heavy metals as a catalytic resource.

1.4 Operational problems in SCWO systems

Technically, widespread industrial use of the SCWO process is impeded by some engineering challenges. These challenges, in particular corrosion and precipitation arise when complex waste mixtures frequently containing heteroatoms, are introduced to the system. Additionally, the rigorous operating conditions of high temperature and pressure with high oxygen concentration can result in a highly aggressive environment for the SCWO system. Figure 1.6 indicate the main problems that can occur in the various parts of a SCWO plant.

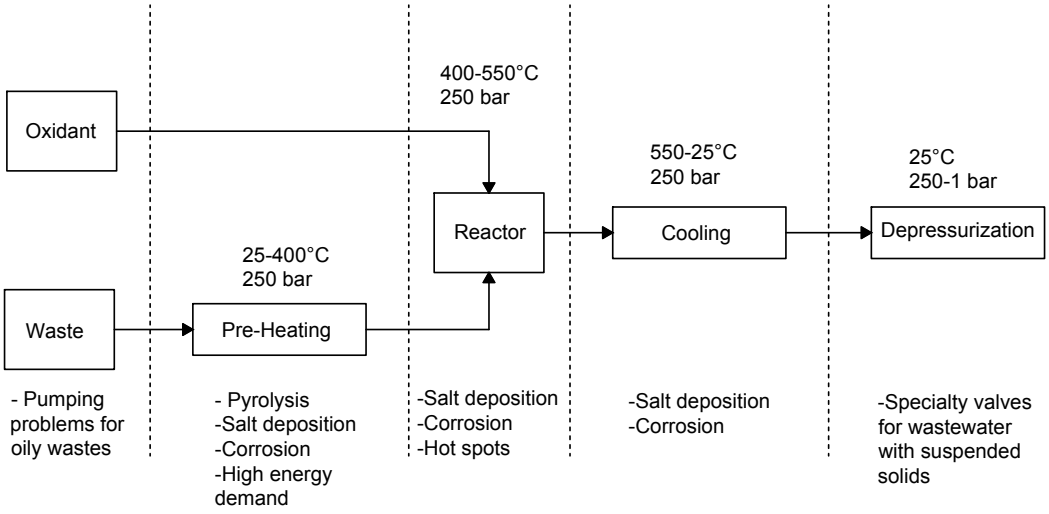


Figure 1.6: Diagram showing the main problems that may occur in the various parts of a conventional SCWO plant, adopted from (Vadillo et al., 2013).

1.4.1 Corrosion

Corrosion is the first main challenge of the SCWO process. It happens when the wastewater being treated, contains aggressive heteroatoms such as halogens. The corresponding acids generated from decomposition of these heteroatoms are quite dangerous to the system, especially in the subcritical region where the tempera-

ture ranges from 250-350°C and the dissociation constant of these acids is very high. Surprisingly, at supercritical conditions, the severity of corrosion is lower by order of magnitude due to non-polar solvent character of water at low densities. In fact, the region near critical point exhibits a maximum point of corrosion when the temperature is high enough to encourage a fast reaction rate, concentration of corrosive species; and their corresponding dissociation constant being sufficiently high for a corrosion reaction to occur. This implies that the tubing used to pre-heat the solution or cool down the product is more susceptible to corrosion than the reactor. Nevertheless, it is absolutely true that corrosion will happen in any part of the SCWO system especially in the presence of heteroatoms and absence of any mitigating actions. As a result, a number of potential strategies for corrosion control in the process have been developed. The main methodologies used for corrosion mitigation in a SCWO system can be divided into four categories:

1. Use of corrosion resistance materials for short or long-term application, e.g. stainless steel, nickel-base alloy.

2. Optimize process operating conditions to prevent or minimize corrosion, e.g. neutralization, cold feed injection.

3. Protect underlying structures by forming a corrosion-resistance solid barrier, e.g. coating, lining.

4. Keep corrosive species away from the reactor wall surface by innovative reactor design, e.g. transpiring wall reactor.

1.4.2 Salt deposition

As mentioned earlier, the solubility of most salts decrease dramatically when water becomes low density SCW. These salts are either present in the organic feed or are released during the process as a result of acid neutralization, which may precipitate and deposit onto the internal surface resulting in fouling. This process can significantly reduce the heat transfer efficiency of the system. Therefore, salt deposition is one of the main problems that has postponed the large-scale commercial application of SCWO. Control methods for salt deposition in SCWO can be summarised into special operation techniques and reactor designs. Xu et al. (2015a) state the following concepts as potential solutions to this problem:

1. Minimizing the salt content of wastewater prior to the reactor using a salt separator.

2. Increasing the pressure which can enhance salt solubility.

3. Reducing fluid velocity to achieve sedimentation by gravity.

4. Introduction of fluidized particles, thereby providing a large surface area for salt to adhere.

5. Adoption of a rotating scraper or transport mechanical brusher to remove sticky salt from the inner surface of the reactor.

6. Introduction of cool water or an acid solution to dissolve salts and prevent scaling on the reactor surface.

7. Novel reactor design through which salts are not permitted to deposit on

the wall or agglomerate e.g., reverse flow reactor, transpiring wall reactor, and cool wall reactor.

A detailed list of patents pertaining to specific operation techniques and reactor design to overcome reactor plugging induced by salt deposition, can be found in Xu(2015)'s paper. Nevertheless, the appropriate means to control or eliminate salt deposition in SCWO requires a combination of special operation techniques and specific reactor form. Innovative reactor configuration design combined with more than one operation technique before and during the reactor stage forms a complete control unit to treat the given wastewater.

1.4.3 Economics aspects

The scarcity of actual data about investment, capital and operational costs of full-scale SCWO technology complicates the economic analysis of the process. Furthermore, operational costs for SCWO are greatly influenced by the choice of oxidant, the flammable content of the waste and the energy integration of the process.

The own nature and characteristics of the SCWO process implies high capital investment costs. Firstly, a high energy cost is necessary to get high reaction temperature and pressure whereby these rigorous reaction conditions lead to high equipment cost and potential safety issues. Secondly, the problem of corrosion and deposition results in the use high corrosion resistant alloy and more a sophisticated reactor design. Therefore, initial investment is high and the process can not be economically feasible unless an auto thermal regime is reached in the reactor or catalysts are applied to the process.



Marulanda and Bolaños (2010) predicted the treatment price of a SCWO mobile plant capable of treating 1 l/h of PCB-contaminated mineral transformer oils to be $75/l. This value is close to the treatment cost of same organic waste by incineration. They also estimated that the reactor cost represents 7% of overall equipment cost. Gidner and Stenmark (2001) estimated the operating cost for a SCWO plant treating 1 dry ton/h of sewage sludge, to be about £70/dry ton. They found that oxygen consumption computes roughly 75% of the total operational cost.

1.5 Existing SCWO reactor designs

1.5.1 Tubular reactor

Tubular reactors are the most widely used in SCWO because of its simplicity and reliability. It is the most common type of reactor encountered in the laboratory to obtain kinetics or to assess the viability of new SCWO applications. Furthermore, most full-scale commercial SCWO plants constructed so far use this type of reactor (Sloan et al., 2008; Marrone, 2013). However, tubular reactors suffer from significant drawbacks. They tend to plug and erode due to high salt accumulation and highly corrosive feedstock and the formation of uncontrolled hot spots inside the reactor due to the exothermic character of the oxidation reaction. Another important inconvenience is that the cost of these reactors can be exorbitant. The effects of temperature and pressure are directly encountered in a tubular reactor, thus a expensive material (like nickel based alloy) and a reactor having thicker wall may be necessary to withstand the harsh oxidation conditions inside the reactor (Fang, 2014).

To optimize the reaction temperature and avoid the formation of hot spots as a consequence of the exothermic reaction between the oxidant and high organic loads, an oxidant multi injection system is very desirable in SCWO with a tubular reactor. A schematic of this type of reactor is given in Figure 1.7. The oxidant multi-injection system has some advantages over the oxidant single-injection system by avoiding the rapid increase of reactor temperature due to energy released by the exothermic oxidation reaction; especially at mixing the point of wastewater and oxidant. In addition, this modification aims at promoting different reaction kinetics that can enhance the efficiency of the overall oxidation process (Portella et al., 2007). Alternative temperature control systems that have been discussed in several patents, consist of carefully dosed feed and/or quenching water through multiple injection points (Eller et al., 1998; Cansell, 2005).

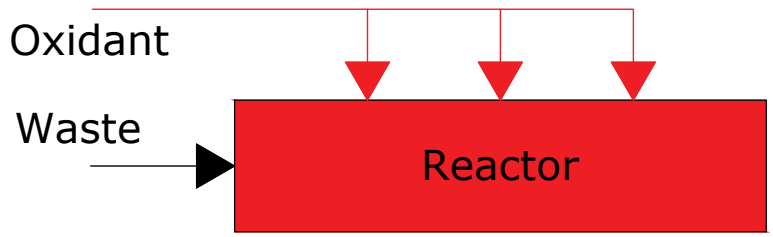


Figure 1.7: Tubular reactor with oxidant multiple injections.

1.5.2 Cooled wall reactor (CWR)

The cooled wall reactor was invented and developed by the High Pressure Processes Group (HPPG) at the University of Valladolid. It is specifically designed to isolate the thermal and mechanical effects within the SCWO system. This has been achieved by using two concentric tubes: an inner and outer one respectively. The outer tube, which holds up the pressure, is kept at a temperature lower than

400°C by the action of the feed stream or cooling water flowing down between the outer pressure shell and the inner tube. Therefore, this lowers the thermal stress and enhance the solubility of solid formed. The pressure vessel, cooled wall, can be made from relatively cheap materials such as stainless steel because it does not come in contact with an oxidant environment. The inner tube (reaction chamber) is where the reagents are mixed and the oxidation reaction takes place. It is constructed from a high corrosion resistance material to withstand the oxidizing atmosphere at temperatures as high as 800°C.

In the first construction design tested by Kritzer and Dinjus (2001), the aqueous feed was circulated between the internal and external walls; and preheated by the huge amount of heat transmitted from the exothermic reaction. To avoid back-mixing and ensure a high surface area for heat exchange, the reactor was packed with alumina sphere as a new configuration design for SCWO reactors. The applicability of this model has been tested in a pilot plant with different concentrations of pollutant feed. Outstanding results in organic waste degradation have been obtained using this technique.

An alternative design has been developed by Bermejo et al. (2009) to provide more protection to the pressure wall and solve the problem of salt precipitation inside the reaction chamber. The reactor is composed of three concentric tubes with a salt precipitation chamber located at the bottom of the reactor working at temperatures around the critical point of water. This was primarily done to precipitate salts from the feed before flowing upward to the mixer. A scheme of this reactor is presented in Figure 1.8. Despite its effectiveness in collecting a certain amount of salt, blockage of the mixer and reaction chamber occurred

when working with high salt content waste. Plugging in the injector caused high pressure drops that made oxidant delivery difficult. Consequently a complete collapse of internal components of the reactor happened due to high pressure inside the reactor. Another modification of a cooled wall reactor comprises the creation

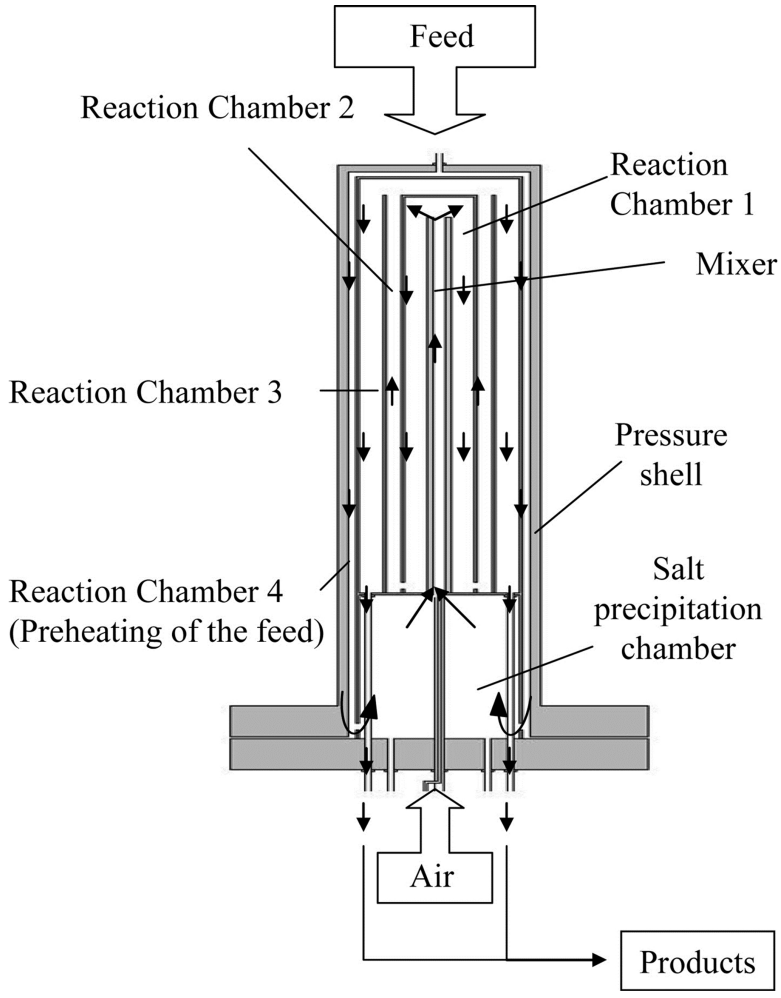


Figure 1.8: The performance of the cooled-wall reactor refrigerated with the waste feed flow (Bermejo et al., 2009).

of a hydrothermal flame as an internal source of heat allowing reduction of the reactor size (Bermejo et al., 2011). The main difference between the previous cooled wall reactor and the new design is that pressurized water at room temperature circulated between the reaction chamber and the pressure vessel as shown in Figure 1.9. The cooling water entered the reaction chamber from the top of

the reactor to mix with reaction products and leave the reactor from its lower part. Another difference is that the reagent (feed and oxidant) injected cold in the reactor over the hydrothermal flame. This model has been tested successfully with wastewater sludge and high salt content feeds (Cabeza et al., 2013).

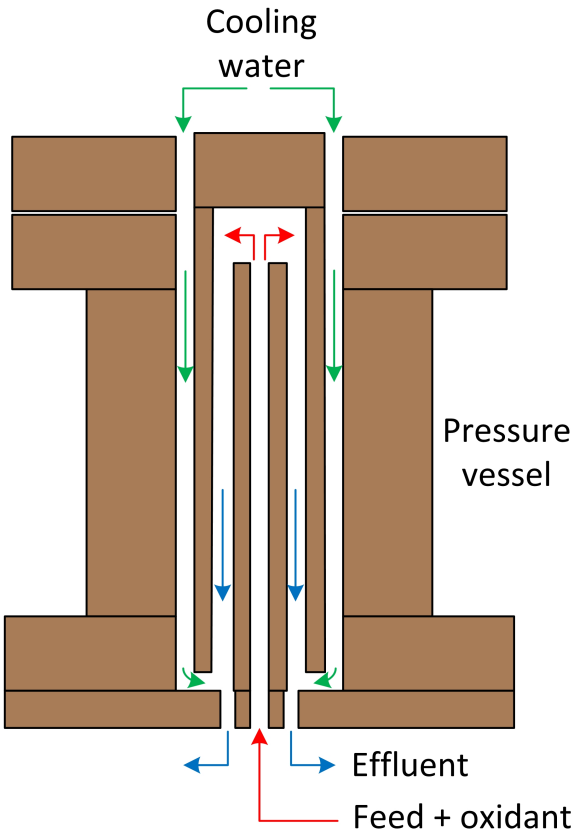


Figure 1.9: The performance of a cooled wall reactor refrigerated with cooling water flow, adopted from (Bermejo et al., 2011).

1.5.3 Transpiring Wall Reactor (TWR)

The transpiring wall reactor was invented by McGuinness T. of Turbosystems Engineering Inc. in 1994 (McGuinness, 1994). The TWR has been successfully introduced as a suitable alternative for dealing with corrosion and salt deposition by forming a cool, protective film of solute-free water. The reactor consists of a reaction chamber as a porous, transpiring wall surrounded by a pressure-bearing

wall as presented in Figure 1.10. Clean water is circulated outside the transpiring wall which then goes through the liner creating a protective layer against corrosive agents, salt and high temperatures on the inner surface of the reaction chamber. The subcritical water will dissolve and/or sweep away the precipitated salt particles during SCWO process. Therefore, both the transpiring wall and the pressure-bearing wall can be made from relatively cheap material. The transpiring wall can be divided into two forms, a liner consisting of many platelets or thin layers bound together; or a porous wall consisting of sintered metal or porous alumina ceramic (Xu et al., 2010).

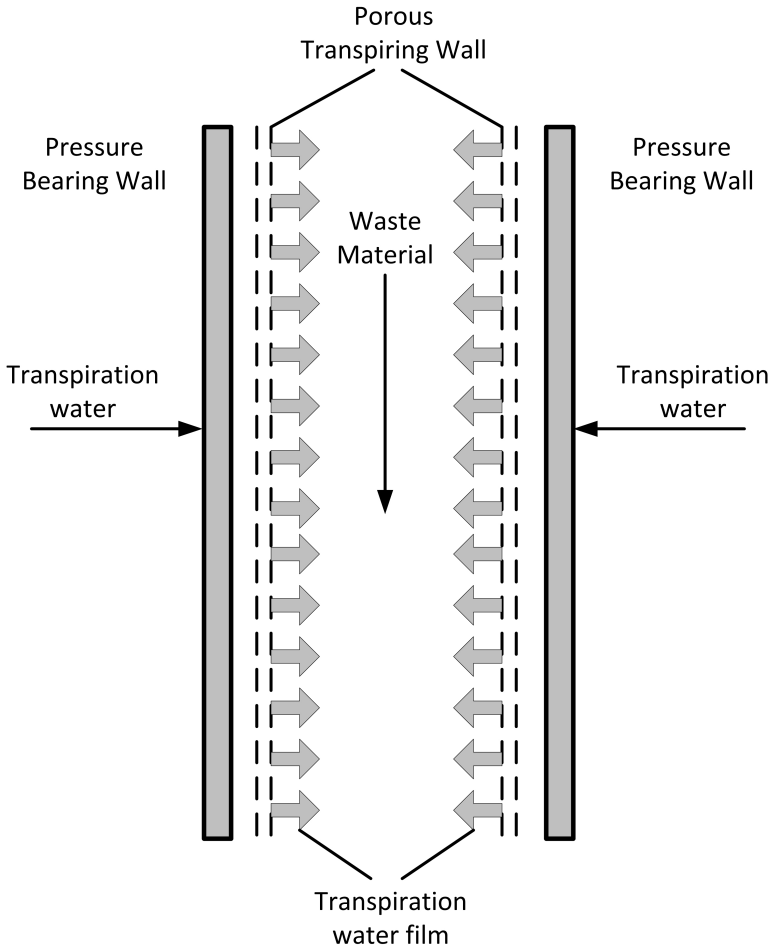


Figure 1.10: The basic design of a transpiring wall reactor, adopted from (Xu et al., 2014).

Heat recovery is the main drawback to be considered in TWR. The hot reaction fluid is cooled and diluted by mixing it with the transpiration water which can be subcritical water; to re dissolve precipitated salt particles and transfer them away from the internal reactor surface. This may evidently reduce the reactor effluent temperature, thereby making heat recovery less efficient.

From the perspective of the oxidation reaction, the data obtained with this type of reactors show interesting results in contaminate destruction. Bermejo and Cocero (2006a) have successfully treated industrial waste containing acetic acid as a main compound with a TWR. In their study, they showed that the reactor can reach removal efficiencies higher than 99.9% using isopropanol as a co-fuel. Interior inspections did not reveal either corrosion or salt deposition. Another study revealed that contaminate removal from landfill leachate in TWR was achieved at a low supercritical temperature of 430°C which led to a reduction in energy consumption (Gong and Duan, 2010).

A new engineering design has been developed by Chen et al. (2014, 2015) to overcome the demerits of TWRs. A dynamic gas seal wall reactor (DGSWR) has the same structure as a TWR with an essential difference being is the former, air flows between the external pressure bearing wall and internal transpiring wall, working as an oxidant and transpiring fluid. Chen et al. (2015) utilized feed-multi injection technology to handle the problems that may arise from waste preheating. The system has been successfully tested for sewage sludge treatment with COD removal reaching 99.15%. However, some shortcomings were observed in the new SCWO system such as solid precipitation.

1.5.4 Current status of commercial SCWO facilities around the world

Since the potential of SCWO was first realized in the 1980s, a number of companies have been established for commercializing this process. However as yet, the technology has not reached the expected level of commercial development. Some SCWO industrial plants have been closed after a few months of operation because of the technical difficulties related with extreme operating conditions inside the equipment. Table 1.4 indicates the inactive plants involved in commercializing SCWO technology.

However, as of early 2012, there are six companies around the world that are still currently involved in the commercialization of the SCWO process. Each active company has at least one full-scale facility either in operation, in construction or in the design stage. These six are: General Atomics, SRI International, SuperWater Solutions, Hanwha Chemical, SuperCritical Fluids International (SCFI), and Innoveox. Among them, there are three currently operating full-scale SCWO plants (Marrone, 2013).

The number of full-scale commercial SCWO plants that are still in operation is less than what it was in the past. However, companies operating at present have plans to install up to nine further plants. Each SCWO company has at least one unique mechanism for handling corrosion and salt deposition and/or limiting the operation to non-corrosive feeds. While not without its challenges, SCWO technology commercialization remains an area of great interest and activity.

Table 1.4: Inactive full-scale SCWO plants (Marrone, 2013).

Company	Feed	Dates	Reason for shutdown
EcoWaste Technologies	Oxygenated hydrocarbons, amines	1994 - 2000	Corrosion and plugging
Foster Wheeler	Dyes	1998 - 2002	Liner mechanical problems
Organo (MODAR)	Semiconductor manufacture wastes	1998 - 2002	Location was sold
Shinko Pantec (EcoWaste)	Waste sludge	2000 - 2004	Material durability
HydroProcessing	Wastewater sludge	2001 - 2002	Heat exchanger corrosion
Chematur	Spent catalyst	2002 - 2007	Loss of contract by JM for catalyst recovery
HOO	Food industry waste water	2004 - 2006	HOO went out of business
Hanwha Chemical	TPA process waste water	2006 - 2007	Oxygen feed compressor problems

1.6 Catalytic supercritical water oxidation

Although conventional SCWO can rapidly convert organic compounds into innocuous products with a conversion rate of 99.99%, waste sometimes includes very stable organic compounds which are partially oxidised or lead to formation of some particularly recalcitrant compounds such as ammonia and acetic acid. These intermediates need high temperatures and a longer residence time to be completely oxidised. In addition, the free-radical reactions in non-catalytic SCWO can sometimes form undesired by products. Accordingly, catalytic oxidation in supercritical water has received considerable attention in academic research. Applying catalysts to SCWO process aims to expedite the oxidation rate at lower processing temperature and increase the selectivity to complete oxidation products (i.e., CO_2 and H_2O). Therefore, process economics can be enhanced by reducing the reactor volume and lowering the energy requirement (SAVAGE* et al., 2006). Additional advantage of using a catalyst in the SCWO process is avoiding problems associated with severe operating conditions like high corrosion rate, low densities, low reactant concentrations and salt depositions.

Application of catalysts as either homogeneous or heterogeneous to SCWO is not new and has been the main topic of research in many studies. Ding et al. (1996) conducted a review study on catalytic enhancement and technology in relation to SCWO. They considered topics such as the selection of useful catalysts for SCWO, characterizing them on the basis activity and stability when exposed to the SCWO environment. The selection of catalyst depends on correlation of catalytic activity with physicochemical properties. The catalyst can be active



for the reaction but not selective; and in the worse case lose its activity within a short period of operation. Therefore, the selection of an appropriate catalyst relies on three important aspects, namely activity, selectivity and stability. The latter is the most difficult to achieve at the operating conditions of the process where an oxidant atmosphere, the presence of mineral acids at high pressure and temperature are always present.

A novel process for the simultaneous treatment of two blended streams of organic and inorganic wastewater was proposed by Shin et al. (2009a). Acrylonitrile wastewater was mixed with copper plating wastewater to study the synergetic effect of simultaneous SCWO treatment. TOC reduction of acrylonitrile wastewater was accelerated due to the in-situ formation of Cu, Cu_2O and CuO nanocatalyst during SCWO, while the exothermic reaction from organic waste degradation provide enough energy for copper and copper oxide recovery. All experimental parameters, except temperature, were kept constant to investigate the synergetic effect of wastewater treatment. For example, the maximum catalytic effect of copper plating wastewater was found at 450°C, where the TOC reduction increased from 17.6% to 67.3% at a residence time of 2 *sec*. However at temperatures above 550°C, the catalytic reaction lacked any influence upon the TOC reduction. Another study conducted (Veriansyah et al., 2005) showed the in situ formation of chromium oxide nanoparticle during the decomposition of LCD manufacturing wastewater by SCWO. However, the researchers do not mention any catalytic effect of nanosized particles produced during the process.

1.6.1 Homogeneous catalytic reactions

Transition metal salts have been used as homogeneous catalysts for SCWO. An early study done by Yang and Eckert (1988) for the oxidation of *p*-chlorophenol proved the ability of copper and manganese salts as homogeneous catalysts to enhance the reaction rate by 40%. They also found that further addition of metal salts did not enhance the oxidation rate. Gizir et al. (2003) carried out the oxidation of phenol and chlorophenol over metallic sulfate salts of Cu, V, Fe, Mn, Ni and Co. They demonstrated that salts of copper and vanadium were the most effective for the destruction of phenol and chlorophenols. However, the reaction rate gain was not 40% higher the uncatalyzed reaction. Both nickel and manganese salts did not show any catalytic effect on phenol disappearance. Some other researchers investigated that effect of alkali, NaOH and heteropolyacids as homogeneous catalysts in SCWO. Table 1.5 shows a summary of homogeneous catalytic reactions done on organic compound oxidation.

However, the key step of the homogeneously catalyzed reaction is the removal or recovery of the metal ion from the treated effluent due to its toxicity. At supercritical conditions, the separation can be done by utilizing the unique characteristic of supercritical water's salt solubility, opening the opportunity to develop more research in homogeneous catalytic oxidation. Since the utilization of homogeneous catalysts is always restricted by difficulties, heterogeneous catalysis is the preferred route when both are available.

Table 1.5: Summary of studies on homogeneous catalytic SCWO

Compound	Catalyst	Reference
Aniline	$FeSO_4$, $MnSO_4$	(Qi et al., 2002)
Pharmaceutical wastewater	$CuSO_4 \cdot {}_5H_2O$	(Falamarzian et al., 2014)
o-Chlorophenol	NaOH, KOH	(Sun et al., 2007)
Nitrobenzne	$H_4SiW_{12}O_{40}$	(Arslan-Alaton and Ferry, 2002)

1.6.2 Heterogeneous catalytic reactions

The complete oxidation of organic materials by heterogeneous catalysts is a subject that has achieved significant interest in the last two decades. Some studies have been devoted to identifying materials that are catalytically active for hydrothermal oxidation, maintain their activity for a long time and are sable at severe supercritical water environment. For example, Yu and Savage (2001) studied the activity of three different catalysts (bulk MnO_2, bulk TiO_2, and supported CuO/Al_2O_3) on oxidising phenol in supercritical water at 380-450°C and 219-300 *atm* in a tubular flow reactor. As expected, the catalyst accelerated the destruction of phenol. Among the three catalysts, supported CuO/Al_2O_3 caused the fastest disappearance of phenol on mass of catalyst basis whereas MnO_2 provided the fastest elimination on an areal basis. Although a huge reduction in surface area was recorded after exposure to SCWO conditions, e.g. 95% for CuO/Al_2O_3, all three catalysts largely maintained their activities for phenol disappearance and selectivity for CO_2 production throughout more than 100 h of continuous

use. The atomic absorption analysis of the process effluent revealed that no Mn or Ti was detected which indicated that MnO_2 and TiO_2 maintained their stability for over 120h of continuous operation. On the other hand, the CuO/Al_2O_3 catalyst was not stable given that both Cu and Al were detected in the effluent. Bulk MnO_2 was considered the best one of the three catalysts for SCWO of phenol because it remained stable under reaction conditions, providing high activity and good activity maintenance. According to Yu and Savage (1999, 2000b), the existence of CuO/Al_2O_3 led to an approximate three-fold reduction in the concentration of undesired phenol dimers compared to non-catalytic SCWO. However, the bulk MnO_2 catalyst could not affect the selectivity to produce CO_2 or dimers. The role of MnO_2 was to accelerate the rate of generation of phenoxy radicals which in turn react in the fluid phase by the same mechanism for non-catalytic SCWO of phenol.

Angeles-Hernández et al. (2008) investigated the effect of operating conditions namely temperature, pressure, oxidant concentration and initial organic concentration on SCWO of quinoline over a MnO_2/CuO mixed catalyst. The results showed that as long as conditions close to the critical point of water were reached, increasing the operating temperature did not have any effect on the removal of TOC and quinoline. The closeness values for TOC and quinoline reductions indicated that existence of the catalyst lowered the formation of undesired intermediates. They also found that excess oxygen concentration had a positive effect on organic degradation. As well as investigations on the activity of transition metal oxides for organic compound oxidation, there have also been some other heterogeneous catalysts like alkali carbonates and activated carbon that have

been studied. Table 1.6 summarizes heterogeneous catalysts explored in SCWO of organic compounds.

Table 1.6: Summary of studies on heterogeneous catalytic SCWO

Compound	Catalyst	Reference
Phenol	V_2O_5, MnO_2/CeO	(Ding et al., 1995)
Phenol	MnO_2	(Tomita and Oshima, 2004)
Phenol	TiO_2	(Yu and Savage, 2001)
Phenol	Activated carbon	(Matsumura et al., 2002)
p-nitrophenol	Mn_2O_3/Ti−Al	(Dong et al., 2015)
o-chlorophenol	Na_2CO_3, K_2CO_3	(Sun et al., 2007)
Acetonitrile	MnO_2	(Youngprasert et al., 2010)
Coal Wastewater	Mn_2O_3, Co_2O_3	(Wang et al., 2012)
Sewage sludge	Red mud	(Chen et al., 2016)

1.7 Hydrothermal synthesis of nanomaterials

Hydrothermal synthesis has been described as the use of aqueous solvents in conditions of high temperature and pressure to dissolve and recrystallise materials which, under standard conditions, are relatively insoluble (Tang, 2014). Because the main reaction media is water, rather than noxious solvents, the technology attracts a lot of interest as a sustainable or green technology. Furthermore, the diverse research devoted to hydrothermal synthesis has shown a wide range of nanomaterials can be produced via this route.

In the early 90s, Arai and Adschiri group were the first to take advantage of the unique properties of SCW, namely the decreased dielectric constant and increased dissociation to H^+ and OH^-; to synthesis metal oxide particles in a continuous manner, including different morphologies of aluminium oxide, cobalt oxide, magnetite, nickel oxide and titania (Adschiri et al., 1992). This research was extended, making remarkable contributions to the field of continuous SCW synthesis of nanomaterials, including the detailed assessment of reaction conditions for tunable product compositions, morphology and functionality (Byrappa and Adschiri, 2007).

In supercritical water hydrothermal synthesis of metal oxide nanoparticles, the reagent stream which typically consist of an inorganic metal salt (ML_x), is brought into contact with a separate stream of water pre-heated to a near critical or supercritical state. The high K_w value and high concentration of OH^- species in near critical water leads to the immediate hydrolysis of metal salt without addition of any base. The metal hydroxide consequently experiences a dehydration step which results in the formation of metal oxide nanoparticles as described by the following equations:

$$\text{Hydrolysis: } ML_x + xOH^- \longrightarrow M(OH)_x + xL^-$$

$$\text{Dehydration: } M(OH)_x \longrightarrow MO_{x/2} + x/_2H_2O$$

These metal oxide nanoparticles are then carried further downstream through an additional heating zone to promote growth (Dunne et al., 2015).

It is generally understood that the way of mixing metal salt and supercritical water streams in continuous hydrothermal reactors, plays an important role on determining the quality and quantity of the product (Blood et al., 2004; Takami

et al., 2012). As such, several groups have built and experimented with different mixer/reactor designs for the hydrothermal synthesis of nanomaterials. Several researchers used a T-piece fitting to mix the reagent flows. In many cases, the T-piece was placed upright with the supercritical water feed entering through the side arm and the cold metal salt flowing down; the bottom arm of the Tee-piece then formed the product outlet. While this simple reactor configuration allowed the rapid heating of precursor streams and has proven successful in the synthesis of a variety of materials, it is prone to blockages because of particle build-up in the metal salt feed arm. At the University of Nottingham, studies were conducted to investigate the flow dynamics and mixing regime within a T-piece mixer using pseudo fluid modelling (Blood et al., 2004). This modelling technique was developed and used for the work described in this thesis, the details of which will be described in the Chapter 3.

1.7.1 Pseudo fluid modelling

Since 2002, Lester's Group at the University of Nottingham applied a new modelling technique to optimize and develop the process and highlight any inconsistencies in the mixing dynamics within a T-piece reactor. Although some researchers used Computational Fluid Dynamics (CFD) to model the mixing scenario (Adschiri et al., 2003), Blood *et al* developed a pseudo fluid modelling-method based on the absorption of light by a dyed solution to quantify the mixing pattern of two modelling fluids in a perspex modelling reactor at ambient conditions. The modelling fluids were carefully selected to simulate the conditions in a SCW Tee reactor and to physically recreate the mixing regime in a perspex mod-

elling reactor. Methanol represented the pseudo SCW stream whilst 40% w/w aqueous sucrose solution was used to model the metal salt stream. These modelling fluids were chosen because they have similar density and viscosity ratios to those between supercritical water and pressurized metal salt solution. Methylene blue dye (12 ppm) was used to colour the sucrose solution and visualise mixing. Reynolds numbers for the SCW and aqueous metal salt streams entering the system were used to calculate the corresponding flow rates in the pseudo reactor. Image analysis result, shown in Figure 1.11, indicated that T-piece reactor geometry would lead to poor mixing conditions and suffer from undesirable issues such as flow recycling, stagnant zones and back mixing which in turn resulted in particle build up and blockages; a problem regularly observed within experimental work.

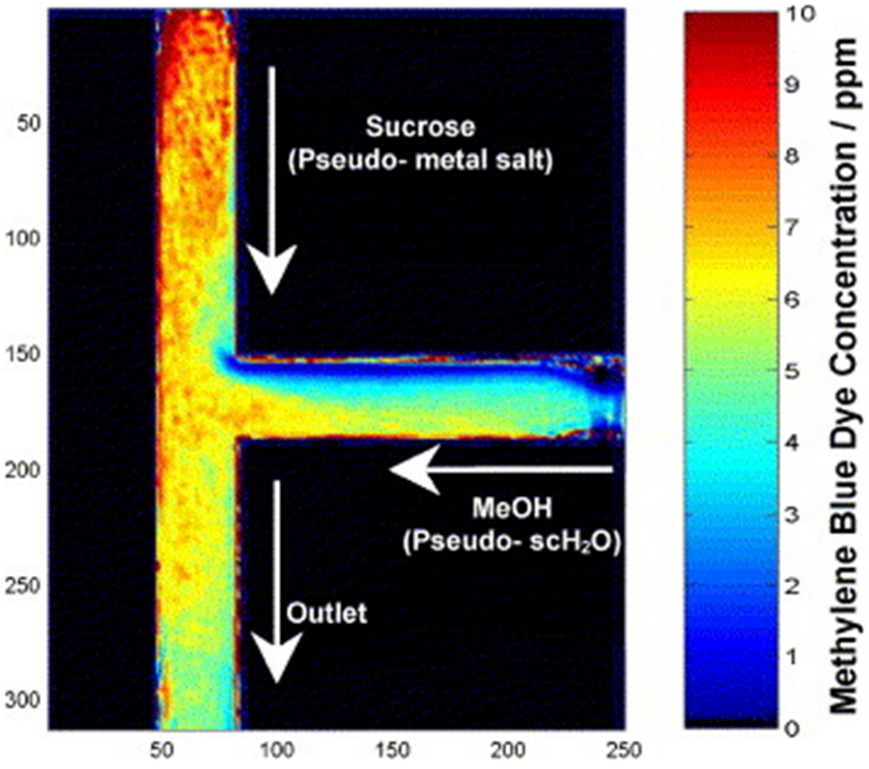


Figure 1.11: Results of pseudo fluid modelling studies on the mixing dynamics of T-piece mixer (Blood et al., 2004).



Whilst pseudo fluid modelling operates at ambient temperatures and pressures, it has been validated by computational modelling. CFD results also predicted improper mixing of reagent streams within the T-piece mixer (Sierra-Pallares et al., 2011). Direct observations of mixing behaviour within a T-piece mixer using a newly designed optical cell has been done by (Aizawa et al., 2007). Mixing of preheated water and dyed room temperature water was directly observed on enforcing a different mixing direction. A good agreement was found between pseudo fluid modelling and this direct visualisation method. More recently, Adschiri group published an article, describing the use of neutron radiography to visualise the flows of water inside their mixing point (Takami et al., 2012). Again, as shown in Figure 1.12, good correlation has been demonstrated between pseudo fluid modelling, CFD, direct observation and neutron beam measurement techniques.

Continuing on from the work of Blood *et al*, researchers within the University of Nottingham used pseudo fluid images combined with CFD results to assess the best possible design for a supercritical water reactor. As a result of these investigations, a novel counter current mixing reactor design was patented by Lester and Azzopardi (2005). This reactor exploited strong buoyancy forces to induce turbulent mixing and prevented the undesirable mixing conditions associated with the more basic T-piece reactor.

1.7.2 Counter current mixing reactor

The counter current mixing reactor design used in a part of this work is shown in Figure 1.13. A tube-in-tube configuration was constructed using Swagelok® high

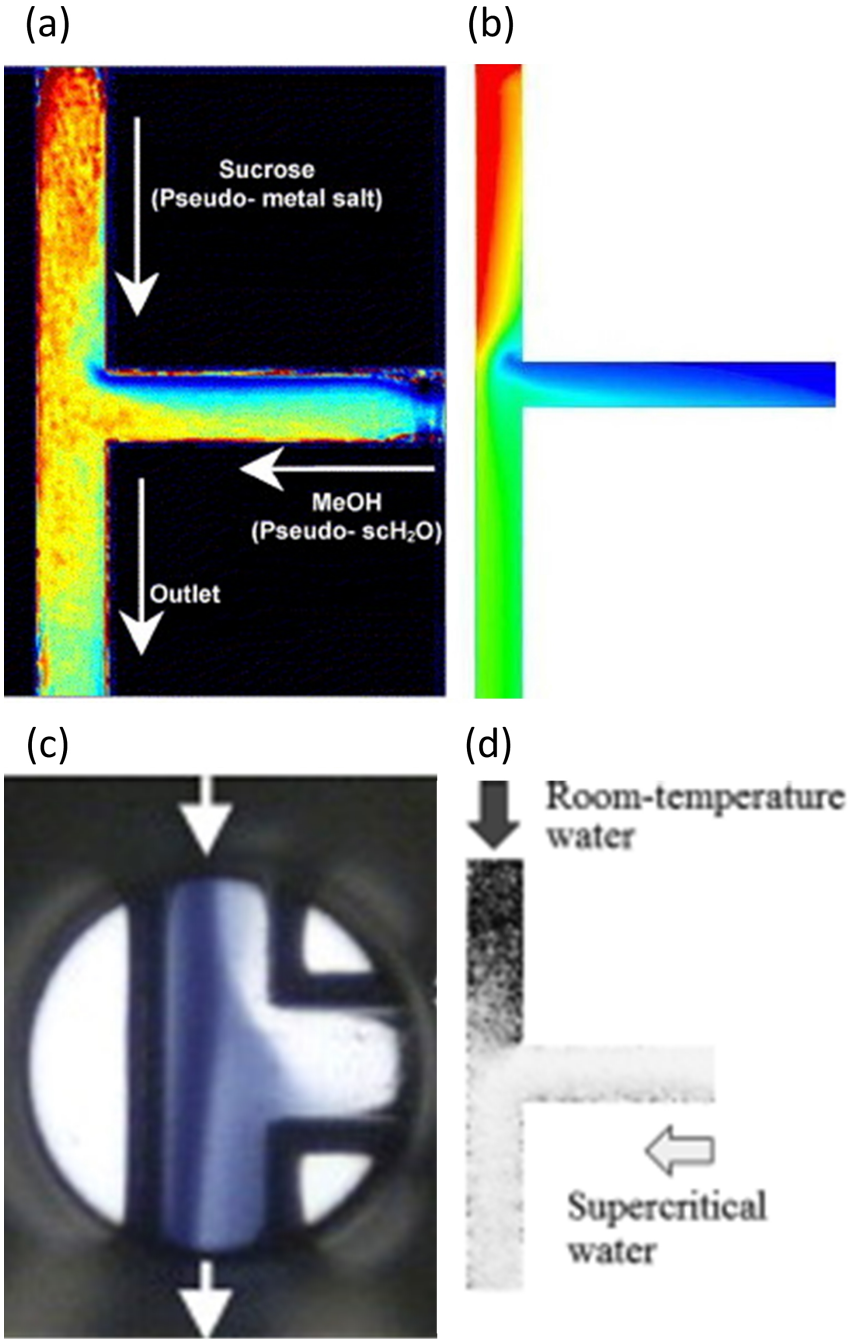


Figure 1.12: Comparison between different techniques for investigating mixing within a T-piece mixer. (a) Pseudo fluid modelling (Blood et al., 2004), (b) CFD (Sierra-Pallares et al., 2011), (c) Direct observation using optical cell (Aizawa et al., 2007) and (d) Neutron beam (Takami et al., 2012).

pressure fitting; where the preheated water is fed downward through the thinner inner tube (1/8" diameter, with a wall thickness of 0.028"), and a cool metal salt stream is fed counter-currently in the outer tube (3/8" diameter, with a wall thickness of 0.065")(Lester et al., 2006). Mixing and nano metal oxide particle formation occurs at the interface, after which the product travels upwards and leaves via the side branch of the reactor before being cooled at the heat exchanger. Since the development of this innovative reactor, a wide range of nanomaterials have been successfully produced which include metal oxides such as Co_3O_4 (Lester et al., 2012), TiO_2 (Caramazana-Gonzalez et al., 2017), Fe_2O_3 (Dunne et al., 2015), ZrO_2:Eu^{3+} (Hobbs et al., 2009)), metals such as Ag (Aksomaityte et al., 2013), phosphates such as hydroxapatite $Ca_{10}(PO_4)_6(OH)_2$ (Lester et al., 2013), and metal organic frameworks like ZIF-8 (Munn et al., 2015).

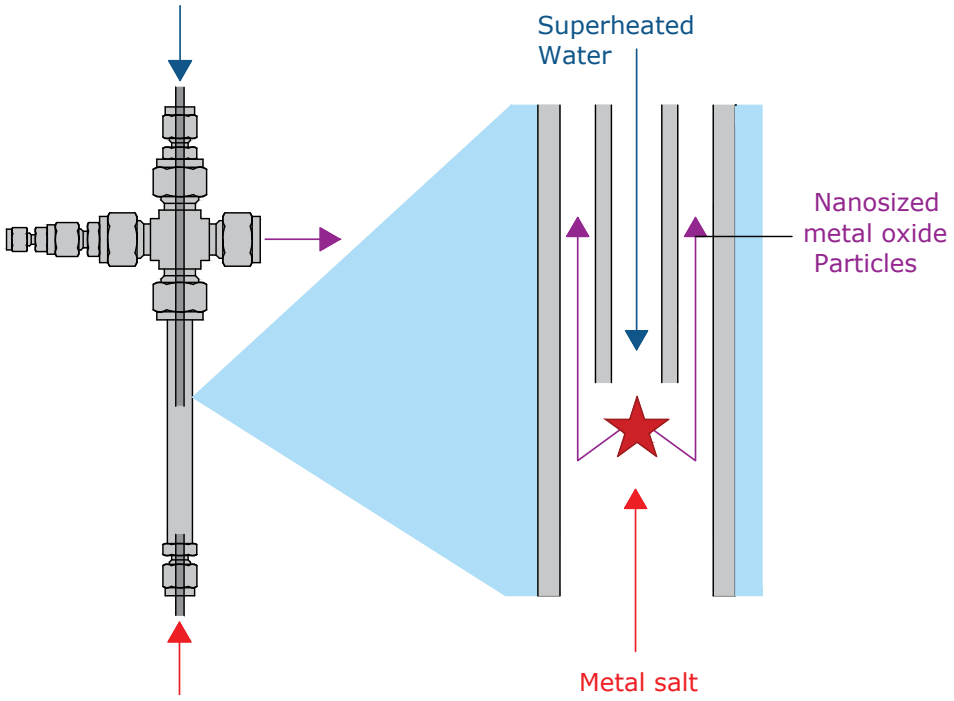


Figure 1.13: Diagram of the counter-current mixing reactor used for the synthesis of nanoparticles. The cold aqueous metal salt flows upwards from the base of the reactor and mixes counter currently with a superheated water stream

In process engineering, mixing and flow regimes in the reactor have a significant effect on the performance of the process. Phenix et al. (2002) studied the effect of mixing of organic feed and oxidant on kinetics of reaction during the SCWO process. They found that reactor configuration and flow conditions have an influence on the measured induction time required to establish the free-radical pool. They conducted a series of experiments varying a Reynolds number from the laminar to turbulent region and stated the importance of the mixing parameter when the Reynolds number is low. Moreover, extensive reports have been focused on the optimisation of parameters such as residence time, reaction temperature, oxidant excess but comparatively little discussion has been focussed on reactor geometry and its effect on process performance. This needs to be rectified because related work on selective oxidation of para-xylene in sub and supercritical water underlined the importance of the reactor configuration in order to control product distribution (Pérez et al., 2016). Consequently, the unique characteristics of counter current mixing reactor can be exploited for oxidation of organic compounds in supercrtitical water. Unlike other SCWO reactor designs, counter current mixing reactor offers the following advantages:

1. Cool feed injection of organic compounds may prevent damage of components and/or piping used to heat up feed due to hetero atoms that may be present in the organic compound stream causing severe corrosion to the equipment.

2. Immediate and rapid heating of the organic compounds upon contact with supercritical water within the reactor. Fast heating may avoid charring or organic pyrolysis compounds formation.



3. Strong downstream eddies which may prevent any particle accumulation on the reactor surface.

4. Combined process of organic materials oxidation and metal oxides production (in nanometre scale) which could speed up the oxidation rate through catalytic activities.

5. A mobile, large surface area is provided by nanoparticles so that any salt present in the waste stream will more likely adhere to the particle rather than the reactor walls or other components.

1.8 Aims and objectives of this PhD

Through the course of this Chapter, the physical and chemical advantages of using SCWO over other waste treatment protocols have been described for a wide range of hazardous organic compounds. Although numerous studies on SCWO were published in the last three decades, its emergence into industrial application remains in its infancy. The scale-up commercialization development of the process is subject to technical difficulties related to corrosion and salt deposition. Furthermore, high investment that is necessary to build an SCWO plant and its high operating costs, increase the burden of implementing the technology.

In addition to solution-dependent and material-dependent factors, mixing is one of the key factors affecting the corrosion phenomena in the SCWO process. It is essential to know exactly what happens inside the reactor in terms of fluid dynamics and mixing regime. Thus, being able to model it physically may provide means to solve the technical difficulties associated with the SCWO process.



However, supercritical water cannot be directly visualized easily. Pseudo fluid modelling offers a cheap, rapid and effective approach to quantify mixing efficiency and highlight any potential inconsistencies in a design of the reactor.

The merits of counter current mixing reactor for SCW application technologies like SCWO and SCWHS have been highlighted in this Chapter. While counter current mixing reactor has been widely used for metal oxide nanoparticles production, the applicability of using counter current mixing reactor as a SCWO reactor remains uncharted territory. Moreover, combining of two processes; SCWO and SCWHS in one reactor would be of even greater novelty which opens up a wide range of future possibilities comprising the oxidation of organic compounds, synthesis of nanomaterials, optimisation of the reaction condition, and application testing.

The aims of this research and the steps to tackle these aims can be summarized as follows:

- Design a new anti-corrosive reactor that can account for oxidation of halogenated organic compounds in supercritical water at different operational conditions.

    1. Using the pseudo fluid modelling technique at ambient conditions to quantify mixing in different SCWO reactors.
    2. Designing and constructing a new SCWO reactor based on data collected from (1).
    3. Investigating the morphology of the oxide layers formed on the internal surface of the new reactor during SCWO of halogenated organic



compound.

- Conduct a combined process of organic materials oxidation and metal oxides production in the novel counter current mixing reactor.

    1. Study the effect of pre-heated and non-preheated oxidant on destruction of various organic compounds in counter current mixing reactor.
    2. Study the catalytic effect of different metal oxide produced in situ on oxidation of acrylic acid.
    3. Study the catalytic effect of Fe_2O_3 produced in-situ on oxidation of phenol.

2

EXPERIMENTAL APPARATUS AND ANALYTICAL TECHNIQUES

This Chapter will describe the general set-up of experimental rigs used in Chapter 3, 4, 5 and 6. For each procedure, a detailed schematic of the rig used for each set of experiments and the respective safety considerations, will be presented. Furthermore, the main analytical methods employed in Chapter 4, 5 and 6 for analysing the liquid sample and characterising the structural properties of nanoparticles, will be introduced. This will be in addition to the principle of each technique and the data that can be obtained from it.

2.1 General description of experimental set-up

The experimental procedure for modelling and oxidation work adopted during this research will be outlined in this section. The initial sub-section will describe the pseudo fluid modelling technique used to provide information on mixing dynamics within a supercritical water reactor. The following sub-section will describe the supercritical water oxidation rig equipped with a counter current mixing reactor; widely used for the production of nanoparticles through supercritical water hydrothermal synthesis. The final sub-section will describe the supercritical water

oxidation rig equipped with a protected wall reactor. This step is used to validate the pseudo fluid modelling presented in this research work.

2.1.1 Pseudo fluid modelling

Pseudo fluid modelling (conducted at ambient conditions) was developed to provide an indication of fluid dynamics and hence mixing inside three different types of supercritical water reactor. The technique uses pseudo fluids, transparent pseudo reactors and image analysis to simulate the general flow patterns within the reactor volume. This section describes the general set up of the process. The technique development including calibration and image processing is fully described in Chapter 3.

A simplified schematic diagram of a pseudo reactor modelling set-up is displayed in Figure 2.1. This model is based on the counter current mixing reactor design (Lester et al., 2006) which is used as a basis for alternative configuration and reactor design in the research.

A 500 Watt halogen spotlight was positioned and diffused directly behind a cross sectional Perspex pseudo reactor. All experimental and calibration processes were conducted in a dark room to ensure that a constant level of illumination was maintained throughout a working day. One fluid (town water) was introduced to the system from a tap, while the other (dyed sucrose solution) was introduced using a positive displacement pump. These were connected to flexible PVC tubing which in turn was attached to an ultrasonic, transit-time flow meter, a device that utilizes ultrasound measurements to record data. Any sonically reflective materials such as air bubbles or solid particles suspended in the fluid, should

be minimized in order to ensure a high accuracy level of the flow measurement. The flow meters were connected to the pseudo reactor inlets using similar PVC tubing. Flow rate of the sucrose solution was controlled by a manual bypass valve arrangement, due to which flow in excess of a set flow rate returns to the inlet supply vessel through a bypass (recycle) line. The town water flow was controlled using a constrictive (pinch valve) on the flexible PVC tubing.

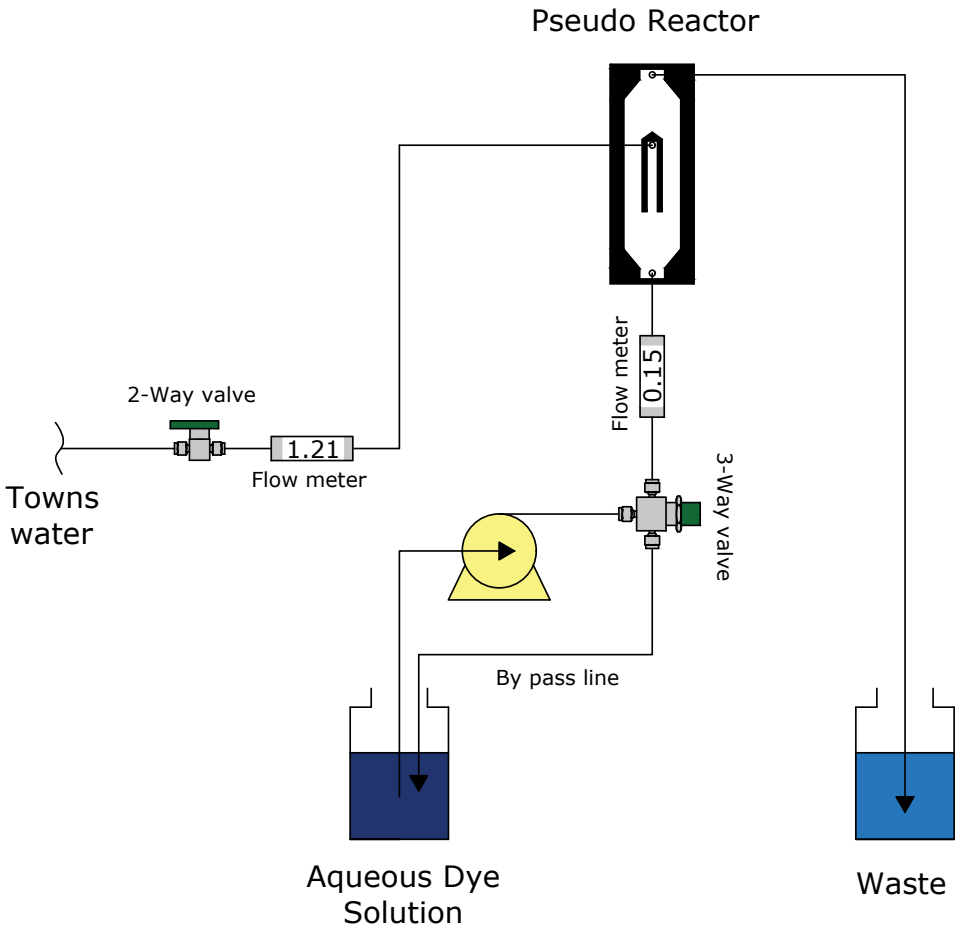
A similar tubing set-up was applied to the pseudo reactor outlet which is located at the top of the pseudo reactor, feeding into a large vessel for safe disposal. Hose clips were used to attach and seal the tubing into fittings.

High resolution video footage (50 frames per second, 1080×1920 pixels) were recorded using a Panasonic video camera recorder. It is important to note that the position of the camera was not altered between the experimental and calibration stages. Video footage was transferred to a computer for image processing using MATLAB®.

2.1.2 Counter current mixing reactor system

The equipment set-up that was used to conduct the majority of oxidation experimental work was constructed at the University of Nottingham for the continuous production of nanoparticles. A process flow diagram representing the supercritical water oxidation rig equipped with a counter current mixing reactor is given in Figure 2.2 with the CAD schematic legend in Table 2.1. All system components, including the counter current reactor, tubing and fitting, were entirely constructed from 316 stainless steel (Swagelok®). Pressure in the system was maintained by a back pressure regulator, BPR (manufactured by Pressure

(a)



(b)

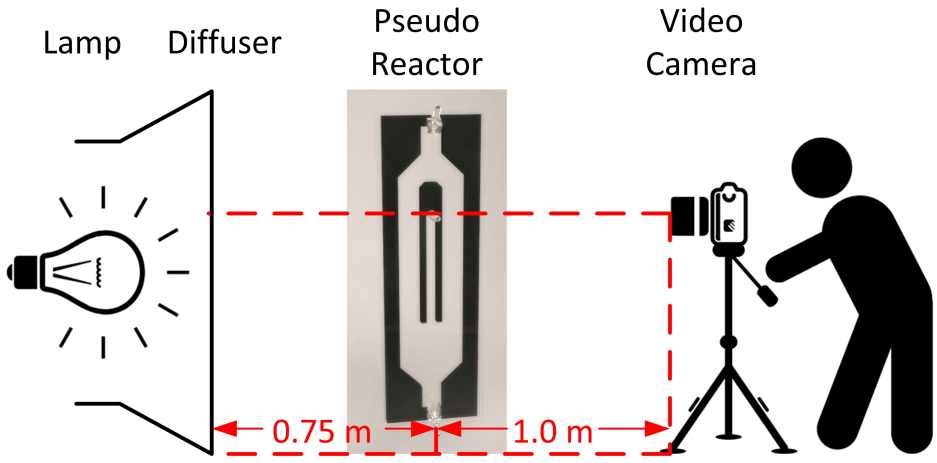


Figure 2.1: Simplified schematic diagram for visualisation system. (a) Experimental stage set-up and (b) Light and camera position.



Tech, UK). Temperature in the process was monitored and recorded using Picolog software connected to a personal computer. Depending on the oxidant delivery method and the subsequent use of catalysts, different set of experiments were carried out to investigate the effect of using a counter current reactor to conduct the SCWO process. These scenarios are summarised in Table 2.2.

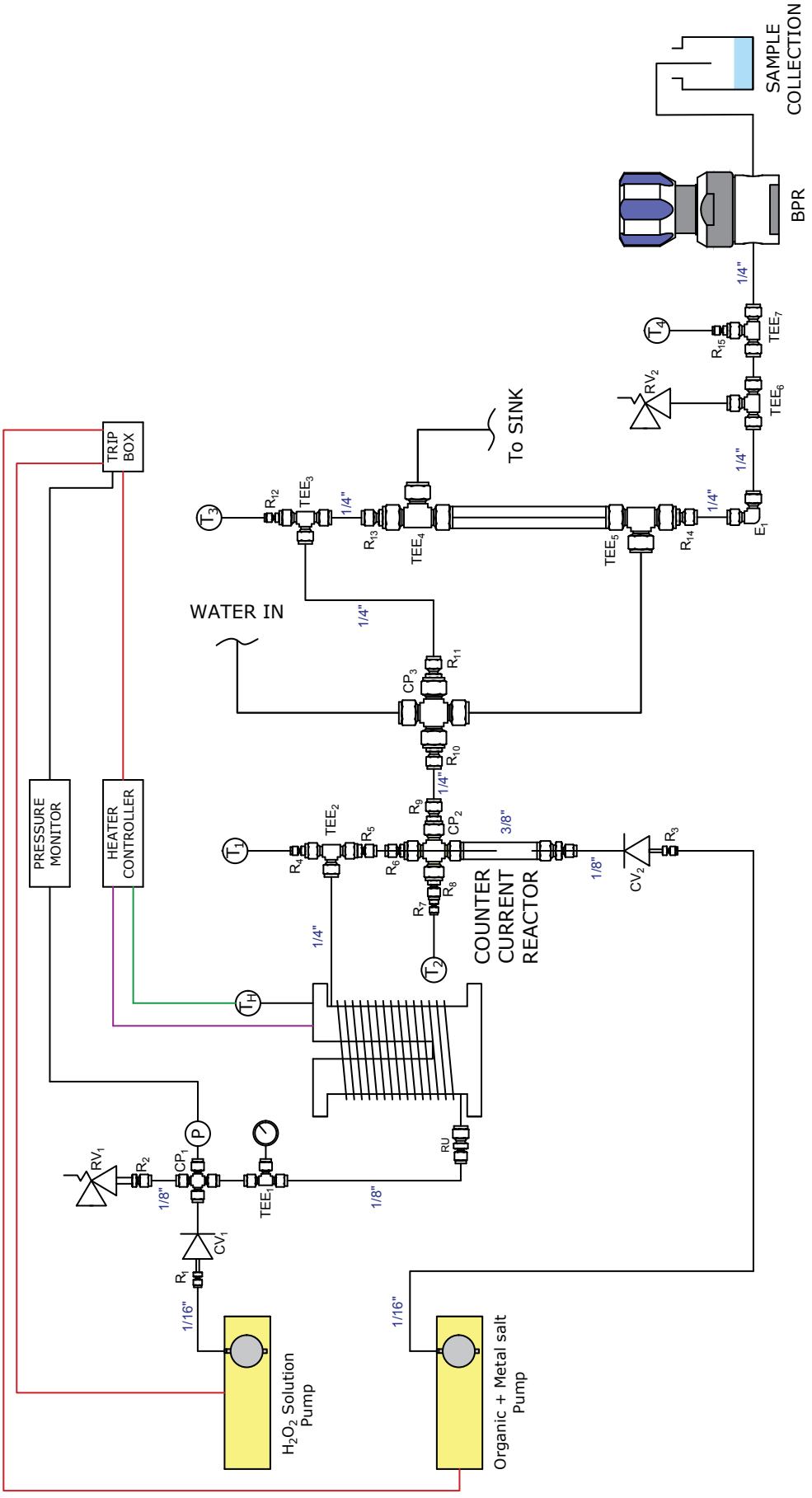


Figure 2.2: A process flow diagram of the counter current reactor system.



For the supercritical water oxidation experiment, an organic material solution was introduced to the system at a pre-set flow rate of up to 12 $mLmin^{-1}$, using a Gilson HPLC pump equipped with a 25 SC pump head. The stream flowed through a check valve before entering the counter current reactor from the inlet at the base as an upward flow without any preheating. In some cases, involving a non-preheated oxidant, an additional Gilson HPLC pump was used to deliver a feed stream containing H_2O_2 solution. This feed stream was pressurized and mixed with an organic feed stream at a mixing tee and introduced to the reactor from the bottom.

Meanwhile, a distilled water stream which may or not contain H_2O_2 depending on the oxidant delivery scenario, was pumped into the system with a maximum flow of 24 $mLmin^{-1}$ using a Gilson HPLC pump equipped with a 25 SC pump head. This then proceeded to flow through a check valve before flowing through a pressure relief valve and piezoelectric pressure transducer, which in turn was connected to a digital pressure monitor. The stream passed through an analogue pressure gauge before entering a 6m length of 1/4" tubing coiled around an 2KW electric heater. A thermocouple within the heater block acted as a feedback control. After the heater, the water feed flowed past a thermocouple before entering the top of the reactor as a down flow.

Upon exiting the reactor, the oxidised product, including any gases formed during the oxidation process, was partially cooled by a primary vertical cooling loop. The product was then flowed through a Tee shaped union at which a thermocouple was mounted on the perpendicular port, allowing the initial cooling temperature to be monitored. The product was subsequently cooled by a counter

Table 2.1: Schematic legend of counter current reactor system.

Schematic Code	Description
Cross Pieces	
CP1	1/8” Union Cross
CP2	3/8” Union Cross
CP3	1/2” Union Cross
Tees	
TEE 1	1/8” Union Tee
TEE 2,3,6, and 7	1/4” Union Tee
TEE 4 and 5	1/2” Union Tee
Reducers	
R1, R3 and R7	1/16” × 1/8” Reducer
R2 and R5	1/8” × 1/4” Reducer
R6 and R8	1/8” × 3/8” Reducer
R4, R12 and R15	1/16” × 1/4” Reducer
R9	1/4” × 3/8” Reducer
R10, R11, R13, and R14	1/4” × 1/2” Reducer
RU	1/8” × 1/4” Reducing Union
Unions	
E1	1/4” Union Elbow
Pressure	
CV1 and 2	1/8” Poppet Check Valve, 6000 psi
P	Pressure Transducer, 0-5000 psig
Temperature	
T_H	K type thermocouple, 3 × 150 mm (1/8”)
T_1,2, 3, 4, and 5	K type thermocouple, 1.5 × 150 mm (1/16”)
Electrical Cables	
	Power cable special controller to heater
	Thermocouple cable
	Power cables to trip box (To be tripped)

current heat exchanger which brought the temperature down to ambient conditions approximately. The product stream continued to flow through a pressure relief valve before passing through the BPR, resulting in the collection of the product at ambient pressure.

Table 2.2: Oxidant delivery scenarios used in the counter current reactor system.

Scenario	Down flow 1/8" tubing	Up flow 3/8" tubing
Preheated oxidant	H_2O_2 solution	model compound solution
Non-preheated oxidant	Distilled water	model compound and H_2O_2 solution
Catalytic preheated oxidant	H_2O_2 solution	model compound and metal salt solution
Catalytic non preheated oxidant	Distilled water	model compound, H_2O_2 and metal salt solution

2.1.3 Protected wall reactor system

A full flow diagram, including external thermocouple positions, representing the supercritical water oxidation rig equipped with a protected wall reactor; is given in Figure 2.3 with a CAD schematic legend in Table 2.3. Based on the pseudo fluid modelling results (Chapter 3), the protected wall reactor system was designed and built at the University of Nottingham. Similar to the counter current reactor system, the protected wall reactor system was entirely constructed from SS316L (Swagelok®). System pressure was controlled using a BPR.

Two Gilson HPLC pumps, exhibiting a maximum combined capacity of 50



$mLmin^{-1}$, were connected in parallel for delivering distilled water to the system. Each stream flowed through a check valve and a number of safety constraints before entering into a 6m length of 1/4" tubing coiled around an electrical pre-heater block. After the preheating step, the two water streams were combined in a tee shaped union and passed through a thermocouple. Finally, they were split again, entering the reactor via the left and right ports of the cross union.

A model halogenated compound, 2,4-Dichlorophenol (2,4-DCP), was introduced to the system using a Gilson HPLC pump with a maximum flow rate of 10 $mLmin^{-1}$. The stream passed through a check valve, an analogue pressure gauge and a pressure relief valve before entering the reactor via the south port of the cross union. The reactor was placed in an electrical tube furnace (SFL, model 75/7.5) to maintain and control the reaction temperature. The tube furnace had three heating zones with overall power of 2.7 kW and an internal bore diameter of 75mm. Heat resistant steel wool (grade 4) was placed in the annulus between the furnace bore and reactor tubing to enhance heat transfer in the tubular furnace. The end of the reactor was attached to a tee shaped union, to the perpendicular port of which was connected a thermocouple for post reaction temperature monitoring. The 1/4" tubing between cross and tee shaped unions was defined as the reactor length because after the tee shaped union, the product stream was quenched and neutralized. A fourth Gilson HPLC pump was used to introduce diluted NaOH straight after the reactor to neutralize the HCl produced after the oxidation reaction.

Like the counter current reactor system, the product stream subsequently flowed through two cooling loops; a primary vertical and a secondary horizontal



counter current heat exchanger respectively. Thermocouples were installed before and after each cooling loop, allowing temperatures to be monitored. The resulting product stream flowed through a pressure relief valve and BPR before collection at ambient conditions.

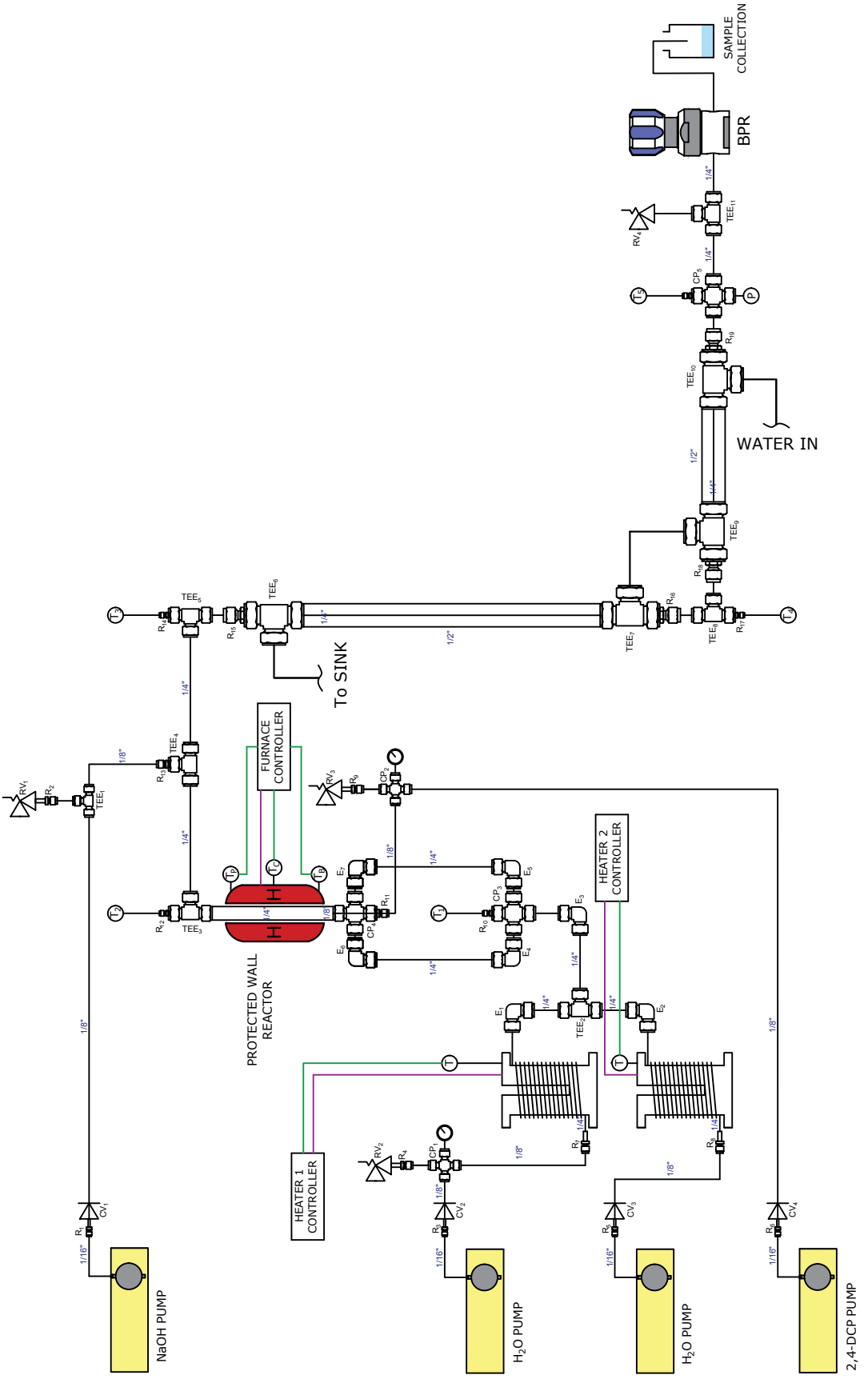


Figure 2.3: A process flow diagram of the co-current protected wall reactor system.

Table 2.3: Schematic legend of co-current protected wall reactor system.

Schematic Code	Description
Cross Pieces	
CP 1 and 2	1/8" Union Cross
CP 3-5	1/4" Union Cross
Tees	
TEE 1	1/8" Union Tee
TEE 2-5 and TEE 8-9 and 11	1/4" Union Tee
TEE 6, 7, 9 and 10	1/2" Union Tee
Reducers	
R1, R3, R5 and R6	1/16" × 1/8" Reducer
R2, R4, R7-R9, R11, and R13	1/8" × 1/4" Reducer
R10, R12, R14, R17 and R20	1/16" × 1/4" Reducer
R15, R16, R18 and R19	1/4" × 1/2" Reducer
Unions	
E 1-7	1/4" Union Elbow
Pressure	
CV 1-4	1/8" Poppet Check Valve, 6000 psi
P	Pressure Transducer, 0-5000 psig
Temperature	
T, T_P, T_C, T_B	K type thermocouple, 3 × 150 mm (1/8")
$T_1 - T_5$	K type thermocouple, 1.5 × 150 mm (1/16")
Electrical Cables	
	Power cable special controller to heater
	Thermocouple cable



2.2 Safety considerations

Due to the nature of supercritical water (T_c= 374.1°C; P_c= 221 *bar*), the following safety precautions have been put in place to ensure the safety of system operators in addition to protecting the BPR:

- ***Fume hood.*** The entire rig was located in a Lexan box, within a fume hood in case of release of harmful fumes during experiments.

- ***LEXAN Shielding*** totally surrounded the high pressure apparatus and protected persons in the vicinity of the rig from projectiles thrown due to excess pressure or escaping reactants due to a sudden loss of pressure.

- ***Piezoelectric pressure transducers.*** These output the pressure of the water stream electronically to digital pressure monitors. In the unlikely event of an excess pressurisation an electrical trip has been set at 4000 psi (276 bar) which will cut the power to the water heater.

- ***Pressure relief valves*** were installed to open in the event of excess pressure, preventing further increases in pressure. Pressure relief valves are set at a bleed pressure of 3900 psi (269 bar).

- ***A Bourdon Pressure Gauge (0-400*** *bar**)*** was included so that system pressure can continue to be monitored in the event of a loss of electrical power.

- ***Gilson pumps*** do not have integrated pressure transducers. In the event of excess pressure, pressure will be released from the release valves first



and if pressure continues to increase, the trip system will cut power to all pumps.

- ***The BPR*** used was controlled by manually adjusting spring tension. In the event of a power failure, the ability of the BPR to hold pressure within the system will remain unaffected.

- ***Temperature*** was continuously monitored online by computer via the TC-08 Pico logger software.

- ***Emergency Shutdown.*** In the highly unlikely event that all of the above safety features fail, there is an emergency shutdown button (located on the trip box) which can be hit in the event of an excess pressure, higher than normal temperature or system error. This cuts power to the band heaters, water and organic material pumps respectively.

2.3 Analysis techniques

An analysis of liquid samples was conducted in order to assess and quantify the extent of degradation of the organic compounds within each experimental set-up. Solid particles were analysed in order to identify and characterise the structural properties of nanomaterials developed in Chapter 4. On the other hand, the internal surface of the protected wall reactor tubing was examined to identify the extent of the protected zone within the reactor. Table 2.4 describes the analytical techniques used during the research project.

Table 2.4: Summary of analytical techniques.

Analytical technique	Analysis or Species Quantified
COD	Acrylic acid, phenol and 2,4-DCP
GC-MS	Phenol
XRD	Metal oxide nanoparticles
TEM	Metal oxide nanoparticles
SEM and SEM/EDS	Internal surface of reactor tubing

2.3.1 Chemical Oxygen Demand (COD)

Chemical oxygen demand (COD) of organic content in water samples was monitored for each experiment in order to investigate the effect of changing various operational parameters on the removal of COD.

The COD test involved oxidising the organic content of liquid samples under acidic conditions for 2h at 148°C. The organic matter was oxidized by a strong oxidizing agent of potassium dichromate and sulphuric acid in the presence of silver sulphate as catalyst. These compounds are all present in the sample cuvettes LCI400 (HACH LANGE LTD, Manchester, UK) used for COD measurement. The 2 mL organic compound sample in COD cuvettes was digested in a LT 200 COD reactor. The end products were water, carbon dioxide and trivalent chromium. The detection of the trivalent chromium was measured at 605 nm wavelength using a visible spectrum spectrophotometer.

The DR 2800 spectrophotometer automatically reads the bar codes on the



sample cuvettes to detect the appropriate test procedure via laser identification. As the cuvette rotated, it was measured 10 times within 5 seconds for an average value that eliminates any abnormal results.

The reduction in COD is calculated based on the following equation:

$$\%COD\,reduction = \frac{COD_{initial} - COD_{\circ}}{COD_{initial}} \times 100 \tag{2.1}$$

Where $COD_{initial}$ and $COD_{\circ}$ are the initial and final concentrations of COD in mgL^{-1}.

Two separated streams of distilled water and known concentration of acrylic acid in a ratio of 2:1, were flowed through the experimental rig at the beginning of operation without any pressurising or preheating, see Figure 2.2. The resultant mixed solution stream was further diluted to a factor of 0.2. This 'double diluted' product represents the initial concentration of COD. The collection effluent from SCWO were diluted in the same manner.

2.3.2 Gas chromatography - Mass spectroscopy (GC-MS)

As well as assessing the COD content in order to quantify how the organic compounds decompose on a global scale, liquid samples arising from the oxidation of phenol were also analysed using gas chromatography with a mass spectrometer. This was done in order to quantify the removal of phenol and track the evolution and destruction of intermediate compounds.

Analysis of a number of standard solutions of phenol resulted in the creation of a calibration curve from which the unknown phenol concentration of liquid samples collected from the experiment could be evaluated. Two calibration plots



were generated, one for the entire dataset and one focused on the more dilute solutions. This was done because the instrument is probably not linear over such a wide range of concentrations. Both calibration plots show a linear relationship between phenol concentration and peak area.

The hardware used for this analysis was a gas chromatograph Agilent 7890B (Agilent Technologies Inc, Wilmington, USA) coupled with a JEOL AccuTOF GCX (JEOL Ltd., Tokyo, Japan) mass spectrometer. The conditions at which the analysis was conducted are given in Table 2.5 below:

Table 2.5: Chromatography and MS ion source conditions.

GC column	J and W DB-5MS 30m x 0.25mm x 25um
Column temperature	40°C (2min) to 330°C @ 10°C min^{-1}
Carrier gas	Helium
Inlet temperature	200°C
Transfer line temperature	180°C
Ionisation energy	70eV @ 150°C

2.3.3 X-Ray Diffraction (XRD)

This analysis technique is used to determine phase composition, crystalline size and structure of a solid sample. As illustrated in Figure 2.4, a beam of X-ray of a known wavelength (λ) is fired at the target material, which then interacts with the electrons of atoms on each crystal plane. As a result, the X-rays are scattered from atoms and collected by the detector component of the equipment.

The crystal solid in which the atoms are arranged in a periodic array with long-range order can produce a diffraction pattern which contains information about the atomic arrangement within the crystal. However amorphous materials which do not have long-range atomic order, can not produce such a diffraction pattern.

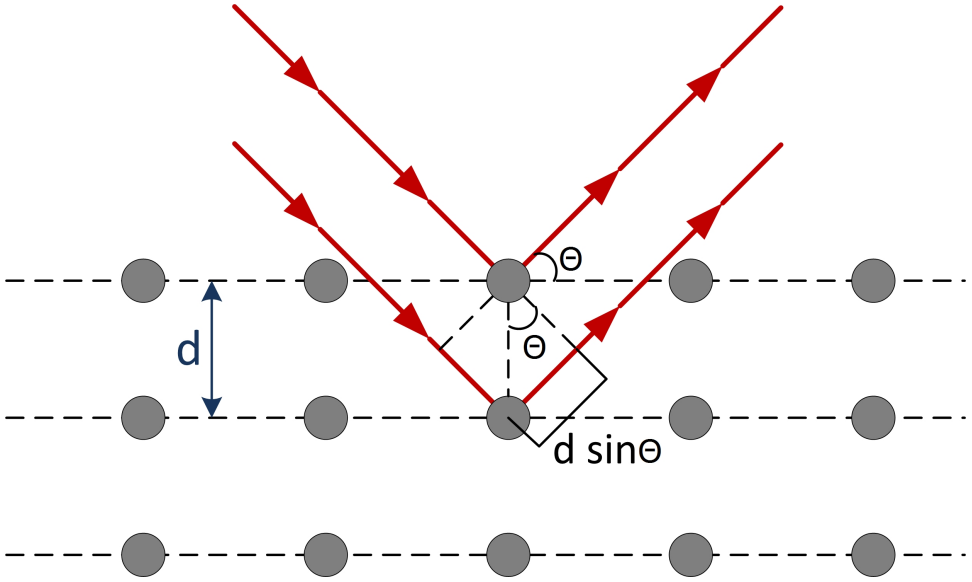


Figure 2.4: A diagram showing the basis of XRD analysis.

During analysis, an X-ray beam is directed at the target material from a range of incident angles. As the rays hit the material, they are diffracted by the lattice structure of the crystal. The sample is fixed and the detector rotates to measure the intensity of diffraction peaks at each angle. Thus, the intensity at each angle depends on the orientation and the distance between parallel planes of atoms. Braggs law calculates the angle where constructive interference from X-rays scattered by parallel planes of atoms will produce a diffraction peak.

$$n\,\lambda = 2d\,sin\theta \tag{2.2}$$



Where n is an integer, λ is the wavelength of the X-ray, d is the spacing between diffracting planes and θ is the incident angle between the X-ray source and the sample.

The diffraction pattern obtained for every crystalline phase is unique, since the position and spacing of the atoms within the crystal lattice, and the spacing between the crystal planes is specific to the material. Therefore each crystal structure gives signal peaks of different intensity at differing angles of 2θ. Thus a diffraction pattern can act as a 'fingerprint' for a given substance.

In addition to this phase identification, diffraction patterns may also yield information on the crystallite size. Crystallites smaller than 120nm create broad diffraction peaks. This peak broadening can be used to quantify the average crystallite size of nanoparticles using the Scherrer equation:

$$D = \frac{K\,\lambda}{\beta\,cos\theta} \tag{2.3}$$

Where, D is the crystallite size, K is the Scherrer constant which takes into account the shape of the crystal, λ is the X-ray wavelength, β is the full-width of the peak at half maximum (FWHM) in radians and θ is Bragg's angle.

In this work, XRD analysis was carried out on the dried metal oxide nanoparticles which were obtained by freeze drying with liquid nitrogen under low temperature vacuum (-54°C). The analysis was completed using a Bruker D8 Advance system (Bruker AXS, Germany) through Cu Kα radiation (λ=1.54056 A) in a 2θ range between 15° and 75°. The Scherrer method, assuming Gaussian peak broadening, was used to calculate the crystallite size of metal oxide nanoparticles.

2.3.4 Transmission Electron Microscopy (TEM)

TEM is a microscopy imaging technique that uses electrons as a light source to provide very high resolution images down to the scale of several Angstroms. The configuration of the TEM system is given in Figure 2.5. An electron beam which is generated from the electron gun, travels through the sample material. The transmitted electrons hit a screen located at the bottom of the microscope to form a projection of the sample where parts may appear darker than others depending on the density of material. Thus, a particle size and morphology can be determined based on the contrast difference of the electrons that have been transmitted through. The transmitted electrons generate an image of the particle, which is finally shown either on a fluorescent screen or a monitor.

In this work, TEM was used for the characerisation of metal oxide nanoparticles produced through the oxidation of acrylic acid in supercritical water. Nano-metal oxides produced in water from the oxidation experiments, were allowed to settle for a 24h. A few drops of settled nanoparticles were then sampled and suspended in acetone for examination by TEM. A drop of this suspended alcoholic solution mixture was placed on the TEM grid. Acetone was used for dispersion because it has a relatively low surface tension thereby allowing the particles to be well distributed over the TEM grid. TEM images were obtained using a JEOL 2100F system (FEGTEM) operating with an acceleration voltage of 100kV.

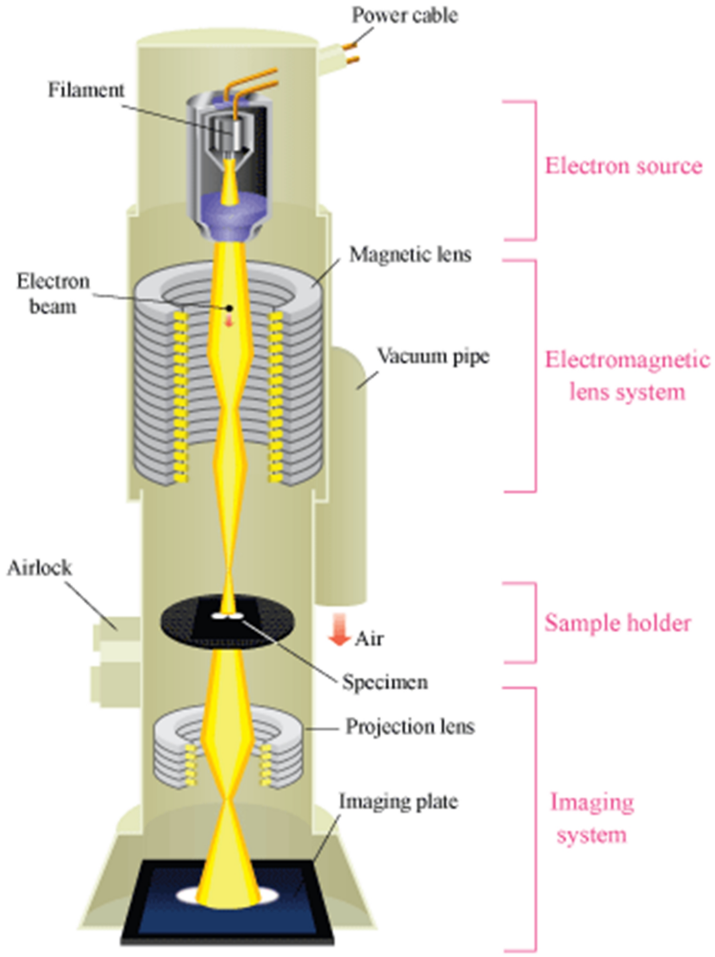


Figure 2.5: The basic layout of a transmission electron microscope (TEM).

2.3.5 Scanning Electron Microscopy (SEM) and Energy Dispersive X-ray (EDX) Spectroscopy

SEM is a surface imaging technique that uses a high energetic electron beam to examine surface morphology. Unlike typical optical microscopes which use light to create an image, the use of electrons in SEM enables higher magnification due to the shorter wavelength of electron compared to visible light and a larger depth of field compared to light microscopy.

The electron beam is generated by an electron gun and travels through a series

of condensers and lenses, see Figure 2.6, which allow focusing of the beam on the sample. On reaching the sample, several interactions can occur depending on the depth of penetration by the incident beam as shown in Figure 2.7. As a result, different signals are generated including but not limited to secondary electrons (SE), backscattered electrons (BSE) and X-rays which can all be detected using the detectors. SE are a result of the interaction between incident beam electrons and sample surface electrons. They generally have low energy and very shallow escape depths in the range of 5-50 nm. Therefore, they are used to reveal the surface structure of a material with a resolution of 10 nm or better (Postek et al., 1980). BSE are a result of the interaction between incident beam electrons and nuclei of sample atoms. BSEs have higher energies and are generated from electrons that penetrate deeper into the sample (up to several microns). Moreover, the number of BSE emitted from the sample vary depending on the particular element used since atoms with higher atomic numbers emit more BSEs. As a result, these atoms appear brighter after detection. Therefore, BSEs are used to provide an excellent compositional contrast. X-ray signals are only emitted from the sample atom when a high energy electron falls down to a lower energy level to fill the vacancy created as a result of the release of SE from the inner shells, see Figure 2.7. X-rays have a huge escape depths (larger than 50 microns) and provide a characteristic or elemental contrast. As a result, X-ray detection allows for determination of elemental analysis and provides a high resolution elemental map through EDX (energy dispersive X-ray spectroscopy) analysis.

Simple sample preparation, rapid and reliable data acquisition, high magni-

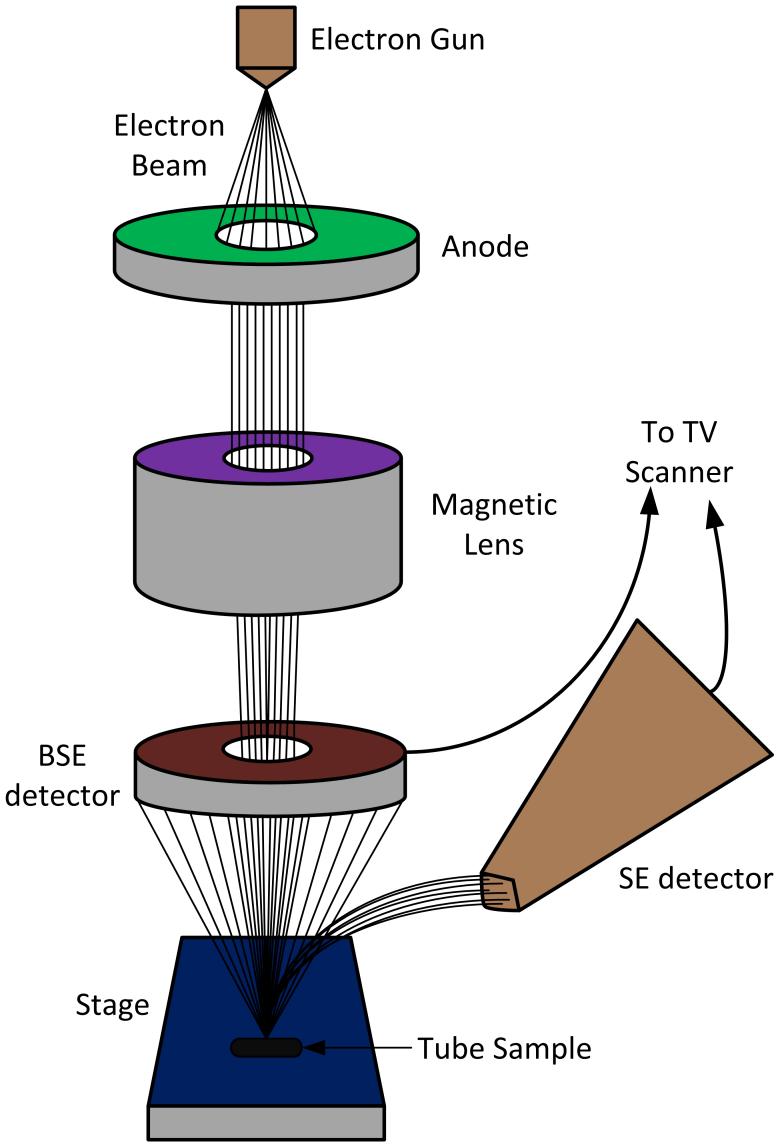


Figure 2.6: The basic layout of a scanning electron microscope (SEM).

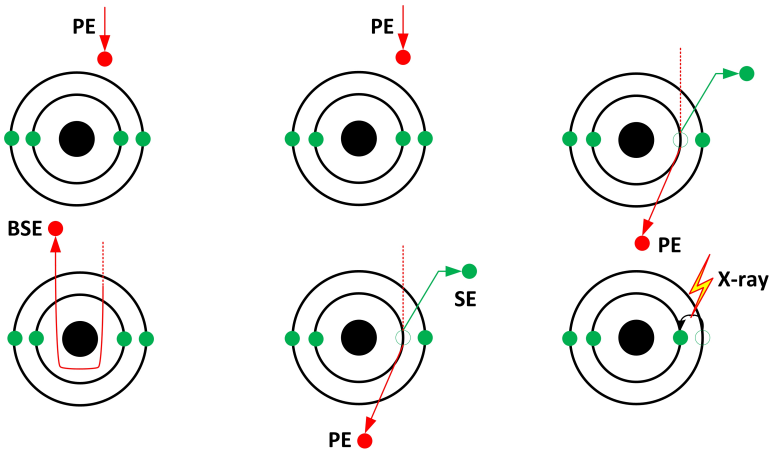


Figure 2.7: Main interactions involved in scanning electron microscopy.



fication and quality imaging make SEM a very useful tool. The SEM kit used in this study is a FEI Quanta 600 MLA with a lanthanum hexaboride (LaB_6) filament to generate an electron beam. In most cases, an accelerating voltage of 25 or 30 kV is used.

2.4 Calculation of parameters

2.4.1 Residence time

The residence time for the counter current mixing reactor and protected wall reactor was calculated from the mixing point to the first cooler. In a counter current mixing reactor, the mixing point is located somewhere below the nozzle (Lester et al., 2006; Sierra-Pallares et al., 2016b) and changed with jetting distance. In order to estimate the position of the mixing point within the counter current reactor, initial trials using a perfluoroalkoxy (PFA) pseudo reactor were conducted to visualise the jetting distance of pseudo superheated flow (dyed town water) into a body of pseudo organic aqueous solution (40%w/w aqueous sucrose solution). The results show that the jetting distance relates to the flow and flow ratios. For a flow ratio of 2:1, as shown in Figure 2.8, the mixing point position was almost at one-third the distance between the tip of the nozzle and the entry of denser flow at the base. For the protected wall reactor, the reaction volume was estimated to be from the outlet of the inner tube to the outlet of the outer tube before the NaOH injection point. The estimated residence time for the reaction is calculated in the following equation:

$$\tau = \frac{V_r}{M_T}\,\rho(P,T) \tag{2.4}$$

Where V_r is the reaction volume, which is estimated from the mixing point of two streams at the outlet of the reactor (prior to the first cooler), M_T is the total mass flow rate including the water, oxidant and the organic solution feeds into the system, ρ(P,T) is the density of fluid at reaction pressure and temperature. However, the fluid density at the reaction conditions is assumed to be that of pure water and obtained from NIST database since the investigations were performed with dilute solutions of organic compound in the water and no data was available for density of water-organic compound-oxidant mixtures at supercritical conditions. Reaction temperature is calculated (see Figure 2.2) from the average between the superheated water (T_1) and outlet mixture temperature (T_2).

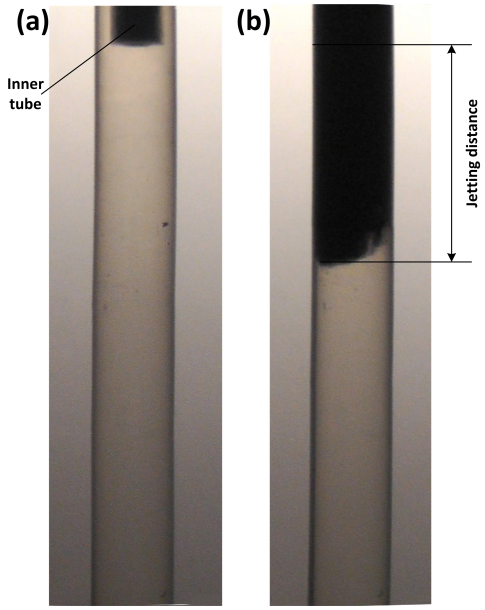


Figure 2.8: Measurement of jetting distance in transparent PFA counter-current mixing reactor using pseudo fluids. (a) before run and (b) after run. Flow ratio is 2:1.

2.4.2 Reynolds number

It is important to know whether the mixing regime occurs in a laminar or turbulent region. Reynolds number of the mixed flow at reaction conditions in counter

current and protected wall reactor was calculated as follows:

$$Re(T,P) = \frac{\rho(T,P)\, \upsilon(T,P)\, d}{\mu(T,P)} \tag{2.5}$$

2.4.3 Concentration of reagents at reaction conditions

The concentration of the reactants at reaction conditions will be different from the concentrations at which they were prepared at ambient conditions due to the temperature-dependant nature of density and consequently, volume. The following equation is used to calculate the initial concentration of the model compound at the reaction conditions (Veriansyah et al., 2007):

$$[RH] = C_{RH} \times \frac{M_{RH}}{M_T} \times \rho(P,T) \tag{2.6}$$

Where C_{RH} is the concentration of the model compound in the feed stock in $molL^{-1}$, M_{RH} is the feed mass flow rate of model compound into the reactor in $gmin^{-1}$, M_T is the total feed mass flow rate into the system in $gmin^{-1}$, ρ(P,T) is the density of water at reaction conditions.

For the initial concentration of oxidant at the reaction condition:

$$[O_2] = \frac{[H_2O_2]}{2} \times \frac{M_{H_2O_2}}{M_T} \times \rho(P,T) \tag{2.7}$$

Where $[H_2O_2]$ is the concentration of H_2O_2 in the feed stock in $molL^{-1}$, M_{H2O2} is the feed mass flow rate of H_2O_2 into the reactor in $gmin^{-1}$, M_T is the total feed mass flow rate into the system in $gmin^{-1}$, $\rho(P,T)$ is the density of water at reaction conditions. The equation is divided by two because 1 mole of H_2O_2



decomposes into 0.5 mole of O_2 and 1 mole of H_2O.

2.4.4 Oxidant ratio

The amount of oxidant required for the SCWO reaction is defined as follows

$$Oxidant\ ratio = \frac{[H_2O_2]_{initial}}{[H_2O_2]_s} \tag{2.8}$$

Where $[H_2O_2]_{initial}$ and $[H_2O_2]_s$ refer to initial and stoichiometric concentration of H_2O_2. Hence, an oxidant ratio of unity indicates that the amount of oxidant delivered was exactly equal to the amount necessary for ideal stoichiometric conversion. Consequently, an oxidant ratio greater than 1 indicates an excess of oxygen and an oxidant ratio less than 1, indicates an oxidant deficiency.

3

PSEUDO FLUID MODELLING OF SCWO REACTORS

Highlights

- Pseudo fluids were used to simulate mixing at supercritical conditions.
- A fully automated calibration method for pseudo fluid modelling was developed.
- Three potential reactor geometries for SCWO were studied.
- A visual "traffic light" system was used to visualize reactor performance.
- A co-current protected wall reactor design showed promise for minimizing corrosion.

3.1 Introduction

After more than three decades since its potential was first recognized, a considerable amount of research has been published on the reduction of SCWO technical difficulties, mainly (corrosion and salt deposition). However, these two issues are still not effectively solved and hindered general industrial implementation of the process (Marrone, 2013). Some researchers have highlighted the need for understanding flow dynamics and mixing regimes within SCWO reactor volume

(Hodes et al., 2004; Wellig et al., 2009). Therefore, investigations into the mixing behaviour would provide a path to solve problems that arise during SCWO process.

Rigorous reaction conditions of high operating temperature and pressure mean that in-situ observations are highly impractical although research groups at Tohoku university have had some success with sapphire micro reactors (Aizawa et al., 2007) and with the use of a neutron beam system (Takami et al., 2012). Therefore an alternative approach has been developed, this being a modelling technique termed "pseudo fluid modelling".

Pseudo fluid modelling simulate the general flow patterns and mixing regimes at ambient conditions through the use of pseudo fluids, transparent pseudo reactors and image analysis techniques. The selection of pseudo fluids was based on differing densities and viscosities resulting in initial immiscibility upon mixing, as is the case when mixing supercritical water with an ambient temperature wastewater stream within supercritical water mixing reactors. Therefore, heat transfer (and indeed pressure considerations) are not included in the modelling work.

Pseudo fluid modelling has been successfully used to quantify the mixing pattern of the two fluids in supercritical water hydrothermal synthesis (Blood et al., 2004). To validate this technique, a recent study was carried out to compare pseudo fluid modelling results with CFD modelling (Sierra-Pallares et al., 2011). A good agreement was found between these different approaches and, more recently, between pseudo fluids, CFD and neutron beam measurements (Sugioka et al., 2014). The continued development in processing hardware, higher resolu-



tion cameras and greater image analysis functionality have all served to improve the use of potential of pseudo fluids modelling.

3.2 Modified pseudo fluid modelling

As early mentioned, Blood and his co-workers developed a new visualisation technique to quantify the mixing patterns for two fluids in an acrylic (Tee shape) pseudo reactor at ambient conditions (Blood et al., 2004). This section will describe the general modelling process as well as the progress that have been made to original pseudo fluid modelling work.

3.2.1 Selection and preparation of pseudo fluids

As mentioned, two modelling fluids are required to ascertain the mixing regime within SCWO reactor. In the work done by (Blood et al., 2004), methanol was used as a pseudo supercritical water whereas 40% w/w aqueous sucrose solution was chosen to model the aqueous metal salt stream. The selection of these two fluids depended on the ratio of inertia to viscous forces. The density and viscosity ratio of the metal salt solution to supercritical water in actual reactor are closely resembled to this ratio of sucrose solution to methanol in pseudo reactor. In order to lower the cost of testing whilst simultaneously avoiding the production of significant amounts of waste liquor, initial trials investigated whether an alternative to methanol could be employed for the simulations. These initial tests indicated identical mixing regimes where water (containing no sucrose) was used in place of methanol. Figure 3.1 shows two tests, one carried out using methanol as the supercritical water pseudo fluid and one with just water but with adjustments in



flow rate to achieve the same Reynolds number. Several comparative experiments showed no difference. Hence, town water - 40% w/w dyed aqueous sucrose solution combination were being used to simulate the properties of SCWO streams. Town water (pseudo supercritical water) was chosen to represent hydrothermal solution whereas the aqueous wastewater stream was modelled by a 40% w/w dyed aqueous sucrose solution (pseudo-wastewater).

It is worthwhile mentioning that these fluids were selected based on differing densities and viscosities resulting in initial immiscibility upon mixing, as is the case when mixing supercritical water with an ambient temperature wastewater stream within supercritical water mixing reactors. This change enabled longer experiments to be carried out meaning more data collection and enhanced process safety, repeatability and reduced cost, and issues with waste disposal. Properties for these pseudo fluids are summarised in Table 3.1.

40% w/w sucrose solution was prepared by using commercially available caster sugar and distilled water. Nigrosin water soluble dye was chosen to color sucrose solution. A required amount was added to the sucrose solution in order to produce a suitable dye concentration of 150 *ppm*. Then, the solution was stirred until the sugar and dye were completely dissolved. Towns water was used without any purification.

3.2.2 Pseudo reactor design

The flows in the original studies were effectively 3D as a result of video footage looking through a cylindrical pipe. This was not ideal as the behaviour across the curved surfaces could potentially dilute the mixing behaviour. The new approach

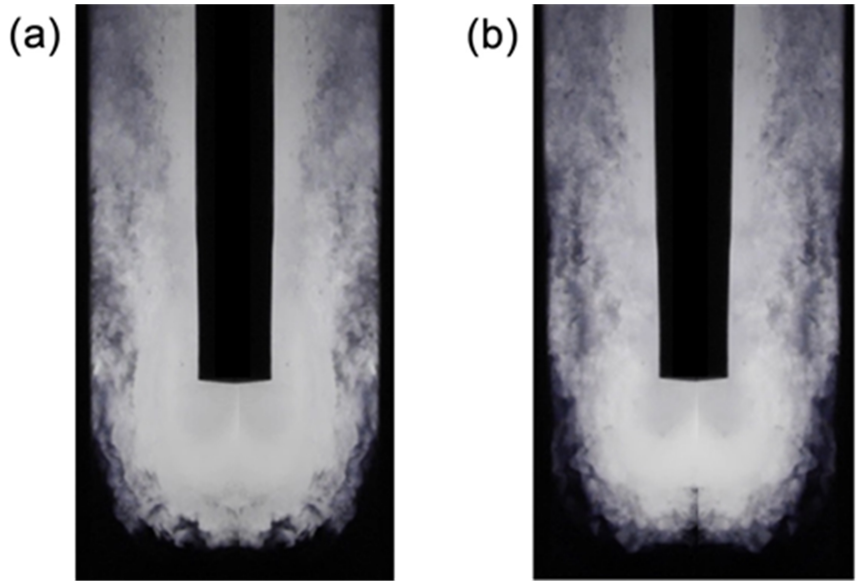


Figure 3.1: Comparing pseudo fluid combinations with flow rates adjusted to match Reynolds numbers (a) Methanol vs. Sucrose, (b) Water vs. Sucrose. The pseudo reactor used was only half of the full cross-sectional slice; the images above have been mirror duplicated for visualization.

Table 3.1: The properties of pseudo fluids at 25 °C and 1bar.

Pseudo fluid	Density, $[Kgm^{-3}]$	Viscosity, $[Kgm^{-1}s^{-1}]$
Methanol liquid	791.01	0.00059
Town water	998.21	0.00100
Aqueous sucrose 40% w/w	1176.4	0.00617

used sheets of perspex clamped with spring clamps with a custom crafted rubber inserts to create the same mixing geometries but with a restricted path length relative to the camera viewpoint.

Three different pseudo reactor models were tested using this modified pseudo fluid modelling with the specific aim of quantifying fluid dynamics that would indicate efficient mixing that might also reduce wall corrosion.

3.2.2.1 Counter current mixing model

The initial visualization experiments are based on the counter current reactor design (Lester et al., 2006) which is widely used for nanoparticle formation in supercritical water hydrothermal synthesis. A schematic diagram for this reactor along with its pseudo model is given in Figure 3.2. This model represents a tube in tube configuration where the hydrothermal solution (H_2O/H_2O_2 solution) is flowed downward through the inner tube (1/8" outer diameter), and the wastewater stream is fed upward into the outer tube (3/8" outer diameter). Mixing occurs at the interface, then the oxidation product is carried up and out of the right-side arm of the cross piece to the cooling loop. To represent this mixing scenario in pseudo fluid modelling, the pseudo hydrothermal solution (town water) was flowed downward through the inner cross (10 *mm* inner diameter) and the pseudo wastewater stream (40% dyed sucrose solution) was fed upward into the outer cross (30 *mm* inner diameter). The mixture was flowed upward to the outlet of pseudo reactor which is located at the top of the pseudo reactor, and fed into a large vessel for safe disposal. For this model, a half cross-section, as shown in Figure 3.3, was used because the full section was giving asymmetric mixing i.e.

mixed flow going up one side.

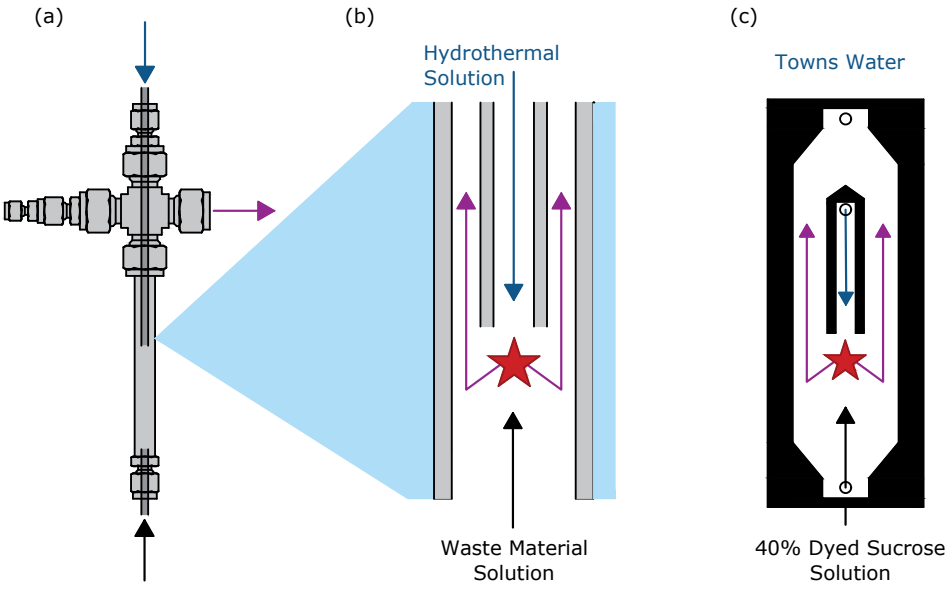


Figure 3.2: (a) Standard configuration of counter-current mixing reactor. (b) Cross sectional slice of the counter-current reactor and (c) Pseudo reactor made up of rubber (6 *mm* thick) sandwiched between two polycarbonate sheets to replicate the mixing geometry in the counter-current reactor.

3.2.2.2 Co-current mixing model

In contrast to the previous counter current design, this configuration creates a co-current mixing regime. The hydrothermal solution is fed upward through the inner tube (1/8" outer diameter) at the bottom of the reactor, whilst the waste material is pumped into the sides of the reactor cross piece (3/8" outer diameter), entering below the outlet of the hydrothermal solution. Mixing occurs at the interface, then the oxidation product is carried up to the heat exchanger. To represent this mixing scenario in pseudo fluid modelling, the pseudo hydrothermal solution (towns water) was flowed upward through the inner cross (10 *mm* inner diameter) and the pseudo wastewater stream (40% dyed sucrose solution) was fed upward through the outer cross (30 *mm* inner diameter). A schematic diagram

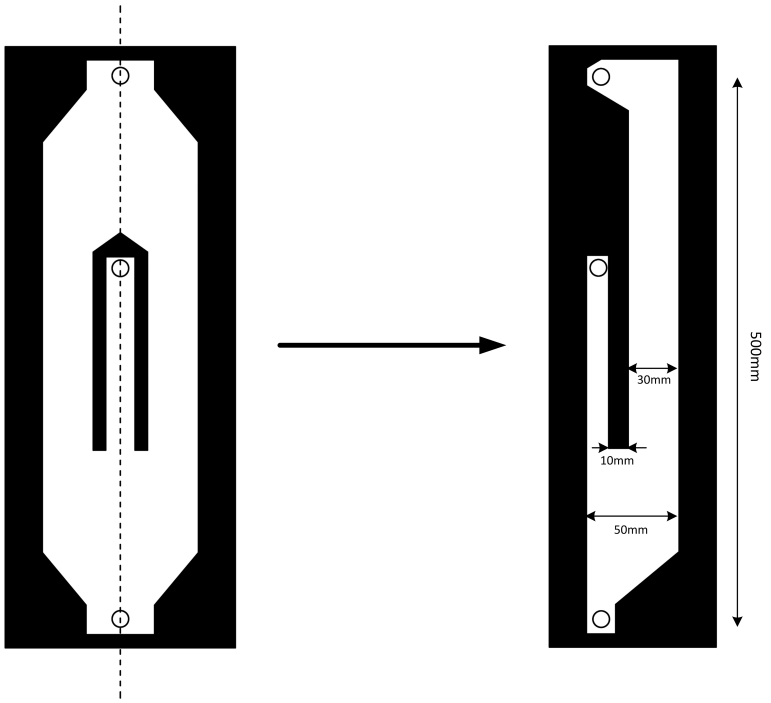


Figure 3.3: Cross sectional counter current pseudo reactor used for pseudo fluid modelling and its right side. Thickness of rubber used was 6 mm.

for this reactor along with its pseudo model dimensions are given in Figure 3.4 and Figure 3.5.

3.2.2.3 Co-current "protected wall" model

The final model quantifies the extent that the flow orientation affects the eventual mixing mechanism within the reactor. In this case, the two inlet streams were interchanged from the previous configuration, i.e. waste material was fed into the inner tube (1/8" outer diameter) and the hydrothermal solution in the outer tube (1/4" outer diameter) both flow upwards in the same direction to the outlet of the reactor. Mixing occurs at the interface, then the oxidation product is carried up to the cooling loop. To represent this mixing scenario in pseudo fluid modelling, the pseudo waste material (40% dyed sucrose solution) was flowed upward through the inner cross (40 mm inner diameter) and the pseudo hydrothermal solution

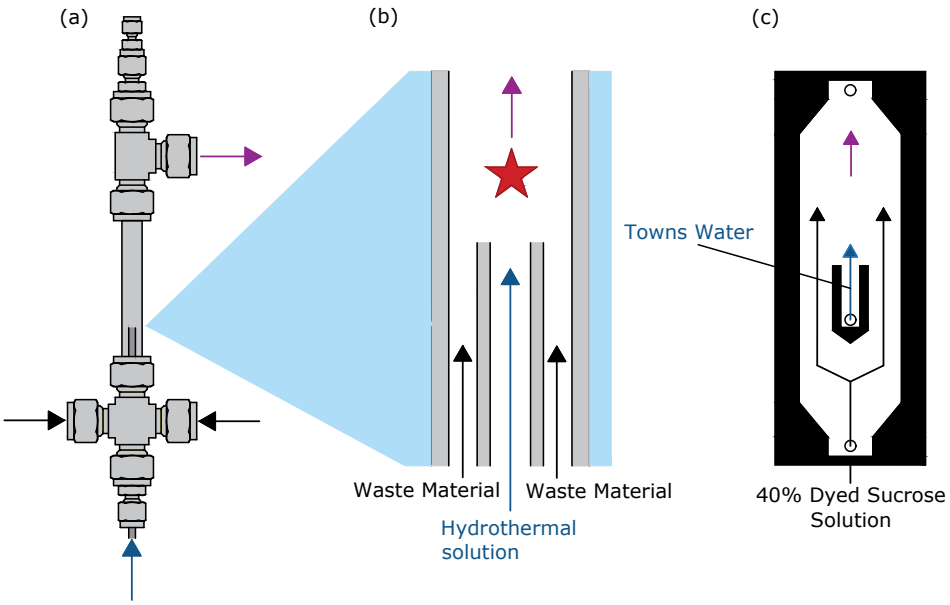


Figure 3.4: (a) Standard configuration of cocurrent mixing reactor. (b) Cross sectional slice of the co-current reactor and (c) Pseudo reactor made up of rubber (6 mm thick) sandwiched between two polycarbonate sheets to replicate the mixing geometry in the co-current reactor.

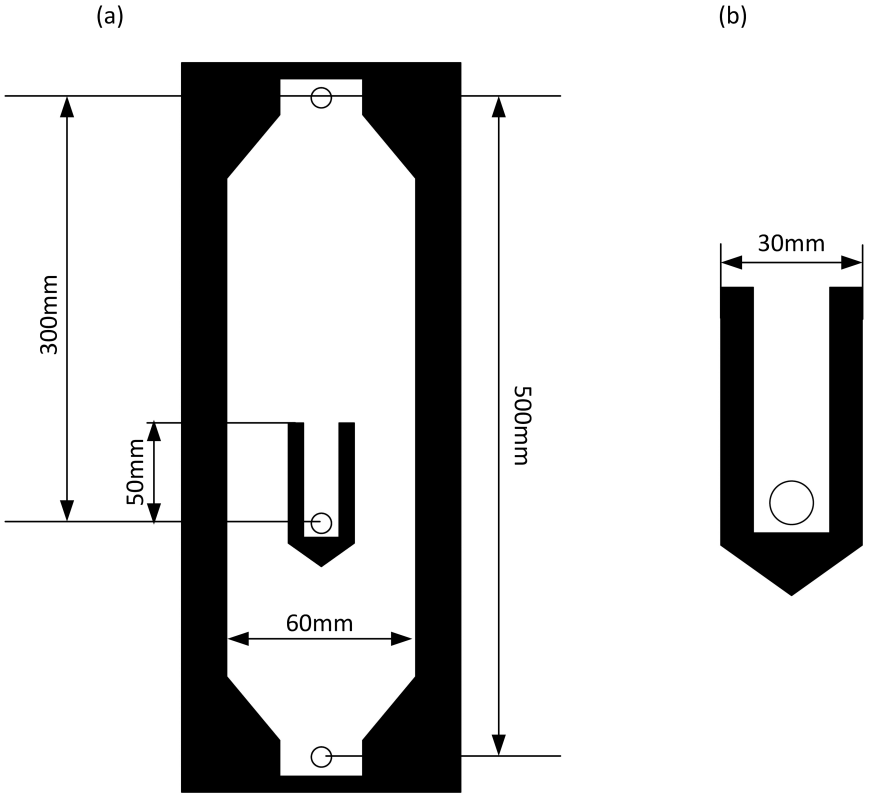


Figure 3.5: (a) Cross sectional co-current mixing pseudo reactor used for pseudo fluid modelling and (b) Inner across (inner tube). Thickness of rubber is 6mm.

(town water) was fed upward through the outer cross (75 *mm* inner diameter). A schematic diagram for this reactor along with its pseudo model dimensions are given in Figure 3.6 and Figure 3.7.

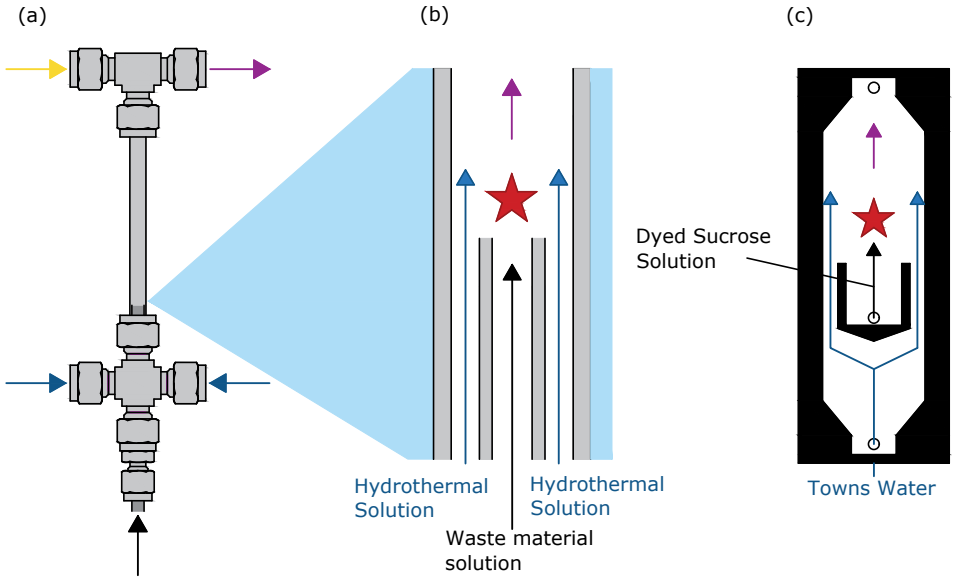


Figure 3.6: (a) Standard configuration of co-current protected wall mixing reactor. (b) Cross sectional slice of the co-current protected wall reactor and (c) Pseudo reactor made up of rubber (6 *mm* thick) sandwiched between two polycarbonate sheets to replicate the mixing geometry in the co-current protected wall reactor.

3.2.3 Inlet Reynolds numbers and flowrates

To aid initial calculations required for pseudo fluid modelling, the inlet temperatures and pressures for real fluid for SCWO process have to be known. Data were collected from hydrothermal synthesis of nanoparticles rig. System data and resultant fluid properties are presented in Table 3.2.

Equation (3.1) is used to determine the inlet Reynolds numbers (Re) exhibited by counter current mixing SCWO reactor. The inner diameters (d) for the wastewater outer tube and SCW inner tube were 6.223 and 1.7526 *mm*, respectively. Wide range of flow rates for SCW and wastewater between (5-20

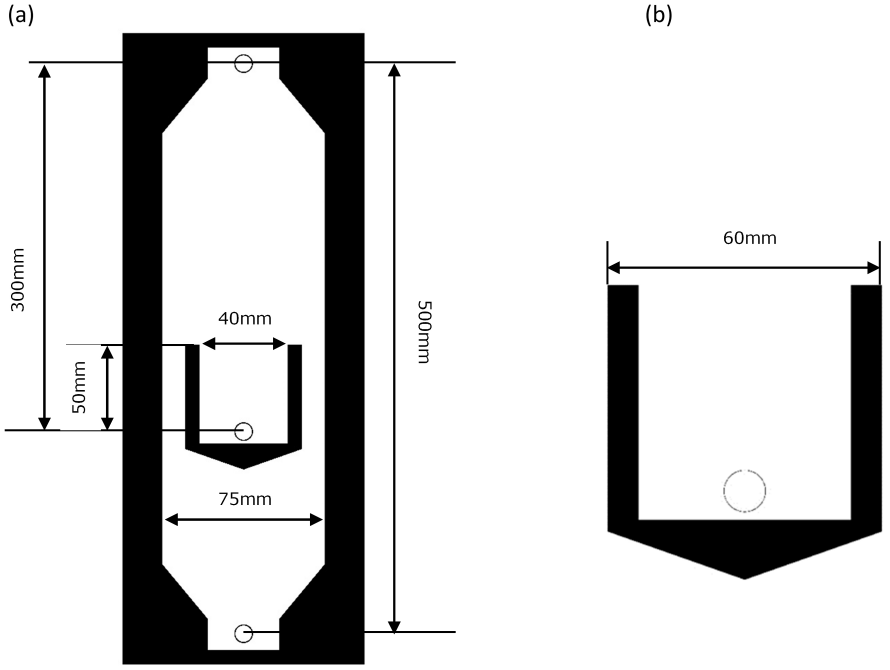


Figure 3.7: (a) Cross sectional co-current protected wall pseudo reactor used for pseudo fluid modelling and (b) Inner across (inner tube). Thickness of rubber is 6 mm.

Table 3.2: Supercritical water oxidation and pseudo fluid modelling key temperatures and resultant fluid density and dynamic viscosity properties. System pressure taken to be 240 and 1 bar for SCWO and Pseudo fluid modelling, respectively.

Conditions	$T\,^{\circ}$C	ρ, $[Kgm^{-3}]$	μ, $[Kgm^{-1}s^{-1}]$
Supercritical water oxidation			
Hydrothermal solution	390	182.14	0.0000295
Wastewater stream	20	1008.9	0.0009933
Pseudo fluid modelling			
Town water	20	998.21	0.0010016
Aqueous sucrose 40% w/w	20	1176.4	0.0061700



$mLmin^{-1}$) has been investigated.

$$Re = \frac{\rho \upsilon d}{\mu} \tag{3.1}$$

The inlet Reynold numbers obtained from Equation 3.1 were used to calculate the required volumetric flowrates of each modelling fluid needed for visualisation experiments. These values along with real and pseudo reactor dimensions are summarised in the Appendix A. This was done using a flow rate calculator which was created using Microsoft Excel to estimate required flow rates for pseudo fluid modelling.

3.2.4 Experimental stage

In experimental stage of physical modelling process, firstly, tap water was introduced to the system at constant flow (996-3983 $mLmin^{-1}$) using water supply. Then, 40% w/w dyed sucrose solution (150 ppm) was achieved at constant flow (152-610 $mLmin^{-1}$) using a positive displacement pump. Each experiment was recorded using video camera recorder to produce high resolution footage.

The original images acquired in 2004 were relatively low definition, at 480 by 640 pixels and 30 frames per second with 8 bit color. The new images are captured at a resolution of 1080 by 1960 pixels 50 frames per second, in 24 bit color, using a Panasonic video camera (HC-700) recorder.

3.2.5 Fully automated calibration stage

Previous pseudo-modelling work used six or seven pre-made concentrations of dye solution to calibrate the mixing simulations that were manually poured into the

perspex reactor model. This was labour intensive and potentially resulted in the movement of the model itself which would result in inaccuracies in the calibration. Both issues were avoided with the new process which involves automatically filling the modelling mixer with twenty one different known levels of dye concentration (0-150 *ppm*) and recording video footage for it. As illustrated in Figure 3.8, two Gilson HPLC pumps were used to mix aqueous dye solutions (150 *ppm*) with town water at various flow ratios and transfer the solution into the pseudo reactor. Equation (3.2) is used to estimate the flowrate of dyed solution feed for each calibration level.

$$F_{dye(n)} = \frac{P_{head} * Conc_{(n)}}{In_{conc} - Conc_{(n)}} \tag{3.2}$$

where, P_{head} is the maximum pump head (25 $mLmin^{-1}$), $Conc_{(n)}$ is the dye concentration for each calibration level and $In_{(conc)}$ is the initial dye concentration (150 *ppm*). It is worthwhile mentioning that using one of the pumps at its prime flow (25 $mLmin^{-1}$), see Table 3.3, saved the time required by calibration process by 25%. The two feeds were mixed at a 1/16" tee piece and homogeneity achieved by flowing through an extended length of SS316 tubing (1/16" OD) prior to the entry into the pseudo reactor from the inlet at the base. This tubing was also connected to an electromagnetic solenoid valve which, upon energizing, allowed the contents of the pseudo reactor to be emptied to a waste vessel between each dye concentration calibration step. A MATLAB® script was used to control these steps and water flushing steps between calibration levels to avoid dye contamination, providing a fully automated calibration system with no requirement for manual handling, giving increased dye concentration accuracy and eliminating

risk of the pseudo reactor changing in position. This dramatically improved the quality of the resultant images and subsequent fitting accuracy for calibration of pixel values to dye concentrations.

Additionally, the improved automated calibration system permits a dynamic and unrestricted number of calibration levels (21 employed in this case), producing near perfect calibration curves.

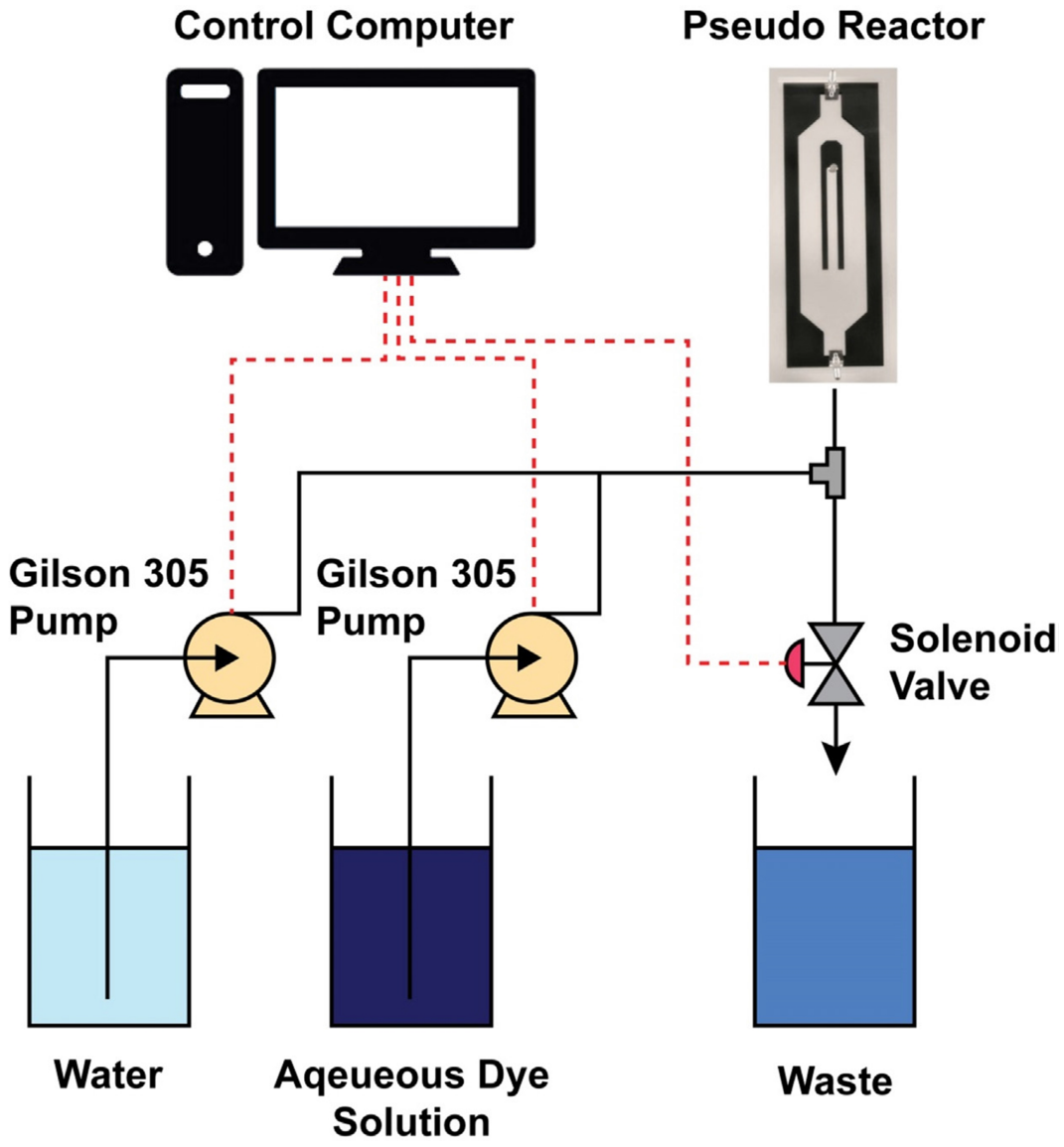


Figure 3.8: Schematic diagram of the automated calibration system as a part of pseudo fluid modelling process.

Table 3.3: labelled Calibration images resulting during the calibration stage of the physical modelling process.

Image label	Dye pump flowrate $mLmin^{-1}$	Water pump flowrate $mLmin^{-1}$	Dye concentration ppm
C-1	0	25	0
C-2	1.3158	25	7.5
C-3	2.7778	25	15
C-4	4.4118	25	22.5
C-5	6.2500	25	30
C-6	8.3333	25	37.5
C-7	10.7143	25	45
C-8	13.4615	25	52.5
C-9	16.6667	25	60
C-10	20.4545	25	67.5
C-11	25	25	75
C-12	25	20.4545	82.5
C-13	25	16.6667	90
C-14	25	13.4615	97.5
C-15	25	10.7143	105
C-16	25	8.3333	112.5
C-17	25	6.2500	120
C-18	25	4.4118	127.5
C-19	25	2.7778	135
C-20	25	1.3158	142.5
C-21	25	0	150

3.3 Modified pixel image analysis

Image analysis was used to create a coloured concentration maps which can be used to quantify mixing inside the pseudo reactor area. Pixel image analysis procedure was divided in two stages, calibration and processing stage. The calibration stage accounts for non-uniform light distribution, marks or scratches on polycarbonate which may be present during the practical experimentation. Data obtained from the calibration stage was applied to the digital footage captured during experimental stage of pseudo fluid modelling in order to produce enhanced images of dye distribution throughout a pseudo reactor. These images are individually termed "concentration map". A flow diagram representing the stages of pixel image analysis is provided in Figure 3.9. This section will describe the specific developments that have been made to the pixel image analysis beyond (Blood et al., 2004) work.

3.3.1 Calibration of concentration gradient

The first step of the calibration stage of pixel image analysis involved divide the calibration video footage into individual consecutive images (Tiff format) using Adobe After Effects software. This resulted in twenty-one folders each of them contain 200 calibration images (produced from 4 seconds of video at 50 fps) were acquired for each dye calibration level. The next step was to combine each set of calibration images to produce an individual representative image for those concentrations using MATLAB® computer software. As is shown in Figure 3.10, combining and averaging of pixel values across the 200 images minimised dynamic

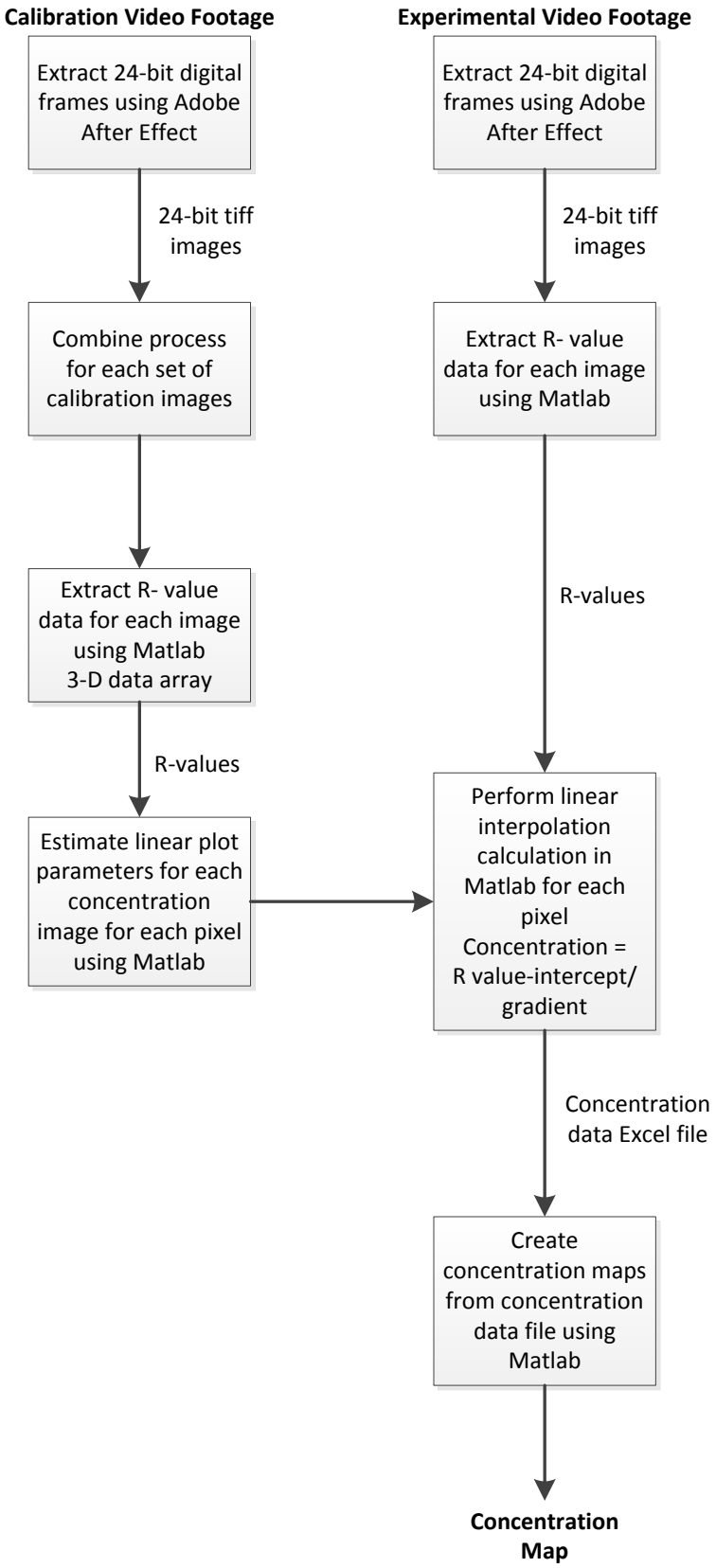


Figure 3.9: Flowsheet showing the calibration and processing steps.

noise and grain between video frames captured by the video camera at each dye concentration calibration level. The outcome was a folder containing twenty-one clean individual calibration images that were further used as a basis for next steps in calibration stage.

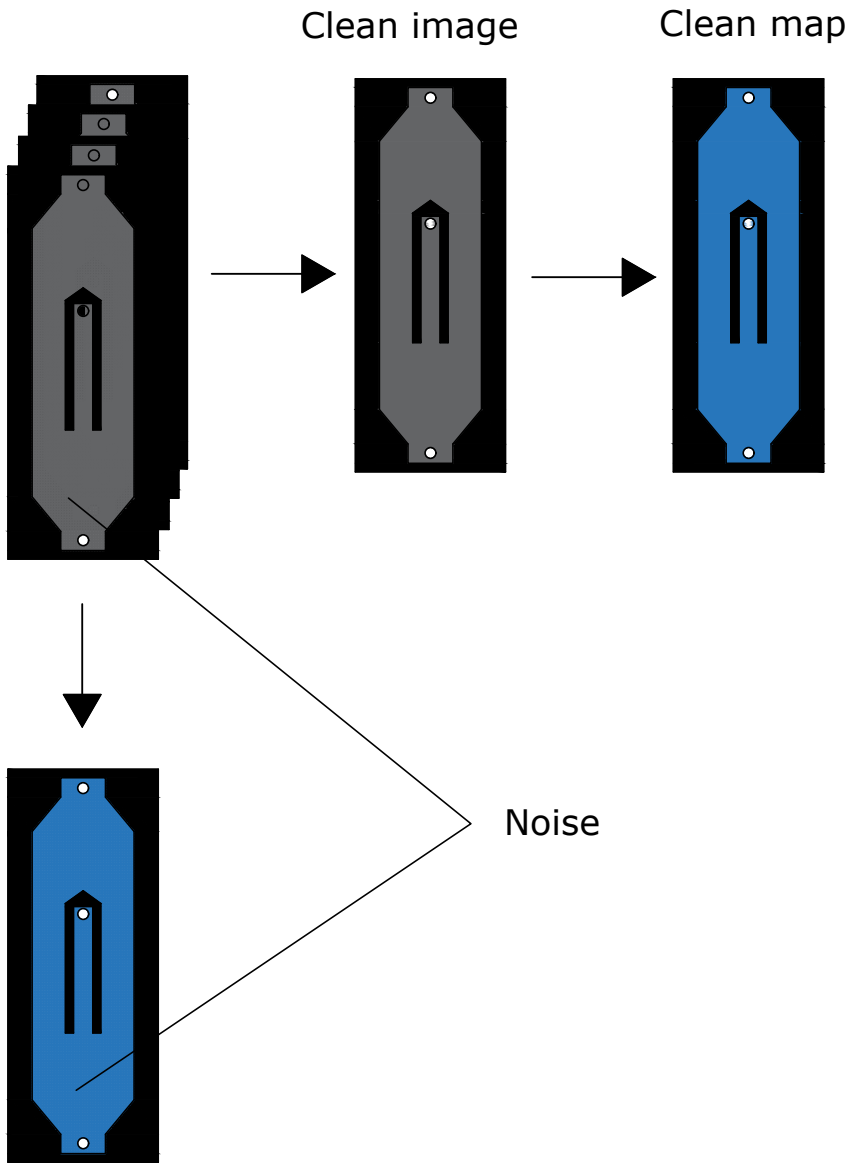


Figure 3.10: Illustration representing the effect of combine process as a part of calibration stage of pixel image analysis.

The following step of the calibration stage was to create a mask image. Adobe After Effect was used to define the edge of the investigated area of pseudo reactor.



This software was then used to fill the investigated area with black colour RGB (red, green and blue) values=0, whereas the remaining image filled with white (RGB=255). The resulting mask image, Figure 3.11, could be easily processed during the remainder of the pixel image process as a reference to pixel dimensions in calibration and experimental images. The representative dye concentration calibration images that produced from combine process were then broken down into their RGB values and analysed pixel by pixel using a MATLAB® program. As in previous work (Blood et al., 2004), initial tests showed the best range of values and reproducibility was produced for the red component of the RGB values (when using a blue dye), and thus only red value (R-value) for each pixel was considered for subsequent calibration and analysis. Therefore, each calibration image was converted from a picture (Tiff format) into a two-dimensional data array (in the form of a spreadsheet) consisting of Red pixel values using MATLAB® computer software. This software combined the individual spreadsheets to produce a three-dimensional red value array. Figure 3.12 illustrates such an array which include data for a complete set of calibration images. At this point, a curve of dye concentration against R-value could be produced for every individual pixel in the calibration image as shown in Figure 3.13.

In the work done by (Blood et al., 2004), the concentration of dye in each pixel was calculated using the Beer-Lambert law, using the coefficients determined in the calibration process. However, the new automated calibration process generated more than seventy times as much data during the calibration process and this data indicated poor exponential relationship i.e. the relationship between concentration and pixel value did not follow the Beer Lambert law. This may be

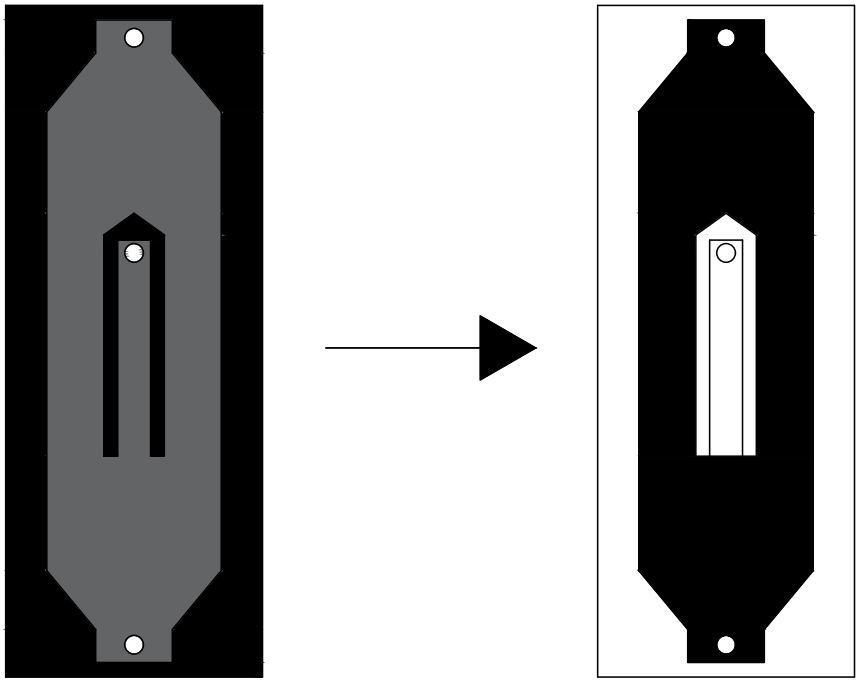


Figure 3.11: Illustration showing the creating of a mask image from calibration image. Calibration was only conducted within black region of the mask.

attributed to the unavoidable loss of contrast with the new HD camera at low concentrations. Consequently, correlating R-values against dye concentration for each pixel showed non-exponential relationship at low and high concentrations values. In this work, therefore, linear interpolation, Equation (3.3), between data points was used for calibration, which was deemed acceptable in light of the large number of calibration data points (21).

$$y = mx + c \tag{3.3}$$

where y is the pixel red value (0-255); x is the dye concentration (ppm); and m, c are the constants found for each part of the calibration curve for each individual pixel. For each pixel in each of the calibration images, three calibration values were stored: the "m" and "c" values for each straight line equation, and the

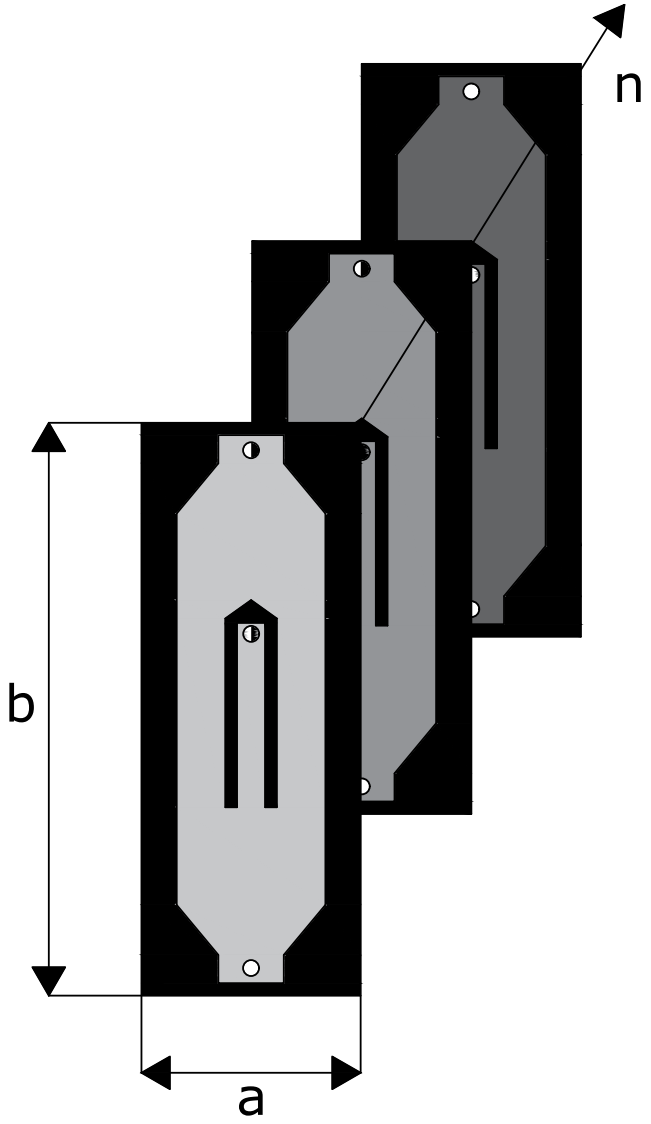


Figure 3.12: illustration of a three-dimensional array as used during calibration and processing stages. Array dimensions=$a \times b \times n$. (n) is the total number of calibration images. 21 calibration images in this work.

pixel value limit (the pixel value in each calibration image) in order to determine which straight line equation to apply when analysing. The outcome is a four-dimensional data array consisting of the following data:

- Two dimensional image (1080×1960).
- Number of calibration images (21 images).
- Linear plot parameters: m, c and pixel limit values (3 calibration value).

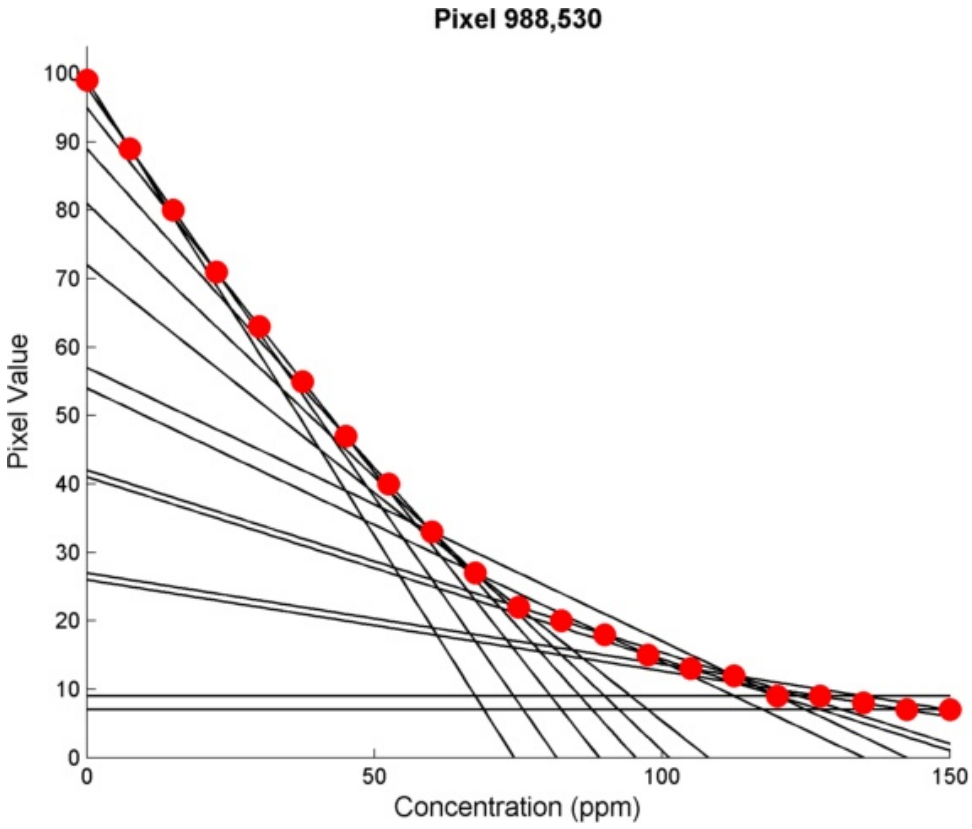


Figure 3.13: Relationship between red pixel value and dye concentration for a single pixel of a calibration image. Each point represents a single calibration image at known dye concentration.

3.3.2 Processing of experimental images

The processing stage of pixel image analysis was used to process the experimental video footage that recorded during visualization modelling. As in the calibration stage, the first step of this procedure was to convert each captured video footage into sequentially numbered images using Adobe After Effect and label them with the correct flow rate ratios. R-values of each pixel of experimental images were then extracted and combined with four-dimensional data array produced at the end of calibration stage to determine the concentration of dye in each pixel in experimental images using Equation (3.4). Pixel limit values were used to identify which a straight line equation should be followed to estimate the concentration

of dye for the corresponding pixel R-value.

$$Concentration\ of\ dye\ (ppm) = \frac{pixel\ R\ value - intercept}{gradient} \tag{3.4}$$

The pixel dye concentration values for a single experimental image was then converted into coloured dye concentration map. The effect of applying linear interpolation and combine process as a part of calibration stage on resultant concentration map is illustrated in Figure 3.14. This image analysis technique can display a variety of information such as mixing patterns, the presence of any circulation zones or mixing efficiency in specific zones within the pseudo reactor. This technique was applied to three different mixing configurations.

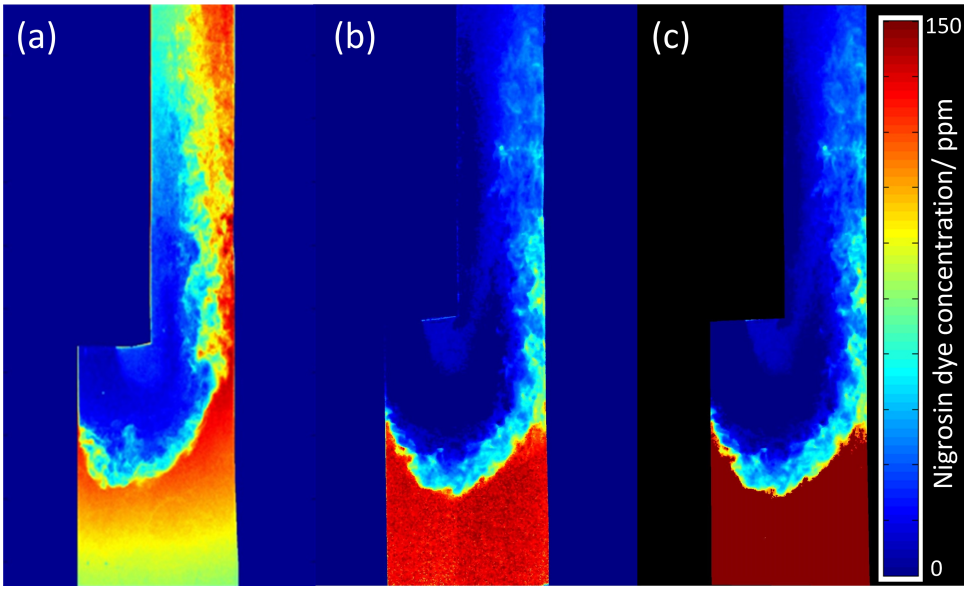


Figure 3.14: Image analysis concentration maps of counter current pseudo reactor (half side). (a) Using Beer-Lambert law for dye concentration calculations (b) without the combine process applied (c) with the combine process and linear interpolation applied to produce an accurate concentration map.

3.4 Evaluating different reactor designs using pseudo fluid modelling

Three different reactor designs were tested using this new image analysis method with the specific aim of quantifying fluid dynamics that would indicate efficient mixing that might also minimize reactor wall corrosion.

3.4.1 Counter current mixing reactor

The first reactor model was based on the nozzle reactor design (Lester et al., 2006) and used as a baseline or comparative model. This tube in tube design allows the low density, highly bouyant superheated stream to flow down the inner tube into the upflow of a cold dense aqueous stream in the outer tube as shown in Figure 3.15. As the two fluids mix, the resultant flow moves up the outer pipe and out of the reactor region. Illustrative experimental images and concentration maps are shown in Figure 3.16. The concentration map shows the distribution of the dyed sucrose solution in the pure water environment. The density difference between the two modelling fluids, i.e. buoyancy forces, induce turbulent macro mixing eddies which flow upwards towards the outlet of the reactor.

Therefore, various flow ratios were tested to investigate their effect on flow pattern in pseudo reactor and highlight any inconsistencies in the mixing dynamics. In this figure, it is possible to see the areas at the reactor wall that may be exposed to corrosion or wall deposition. In this configuration, a homogeneous mixing observed close to the outer wall and if it were to occur during the SCWO process, it would certainly result in severe corrosion in this area. Average images for different flow ratios are given in Figure 3.17. It is clear when the pseudo super-

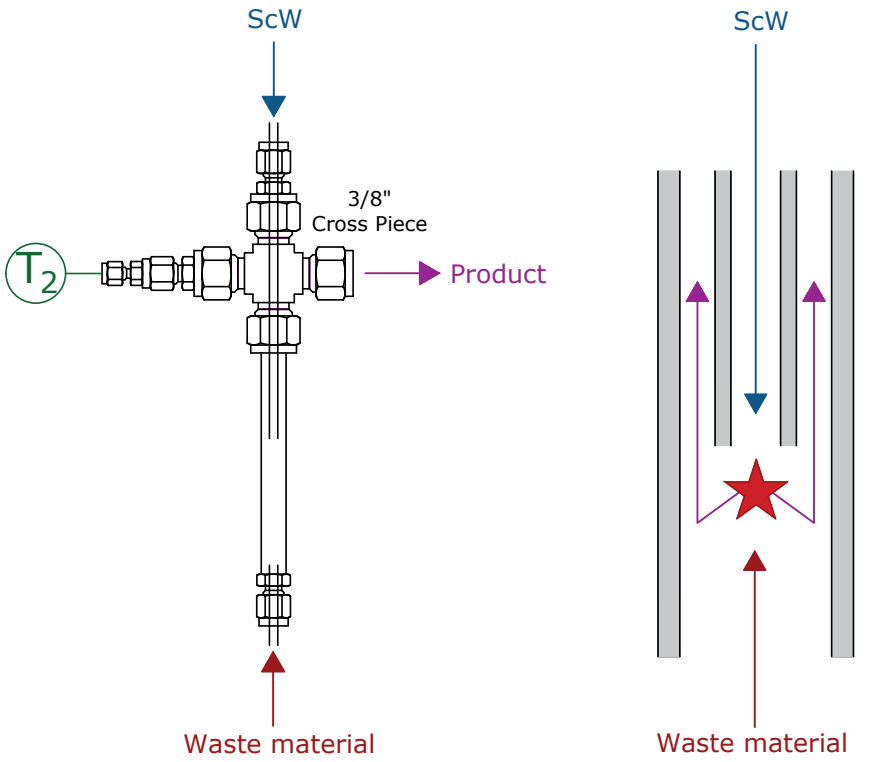


Figure 3.15: Cross sectional counter current mixing geometry.

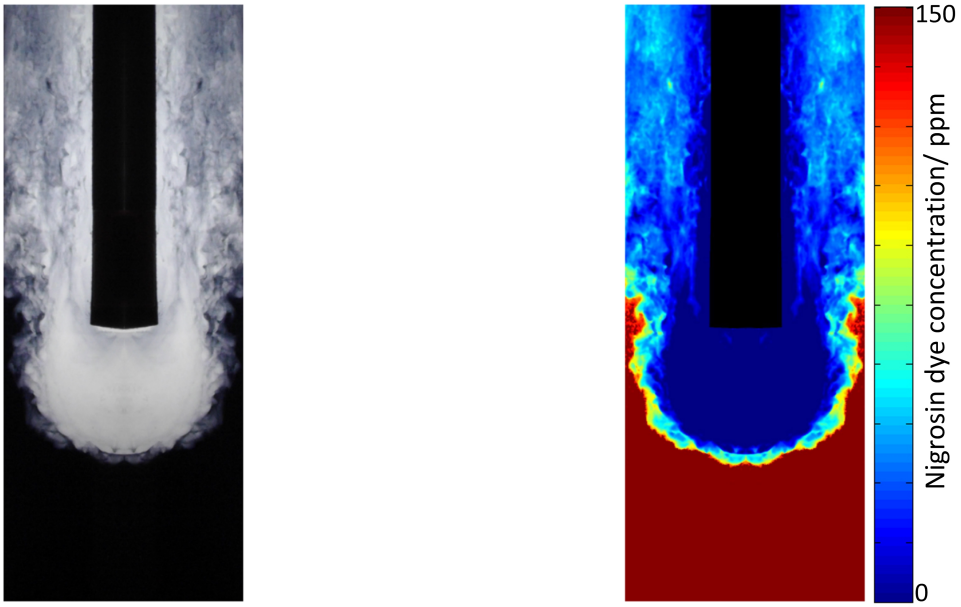


Figure 3.16: Actual experimental image and Concentration map for the pseudo reactor. Flowrates: pseudo SCW downward flow, inner tube: 995 $mLmin^{-1}$ and pseudo wastewater upward flow, outer tube from base of reactor: 150 $mLmin^{-1}$. This is a simulation of 5:5 flow rate ratio used for actual SCWO process. The pseudo reactor used was only half of the full cross-sectional slice; the images above have been mirror duplicated for visualization.

heated flow increases, the jetting distance also increases as does the recirculation area created at the outer wall, particularly in flow ratio (20:5). If this situation were prolonged, the result would probably result in corrosion in this area.

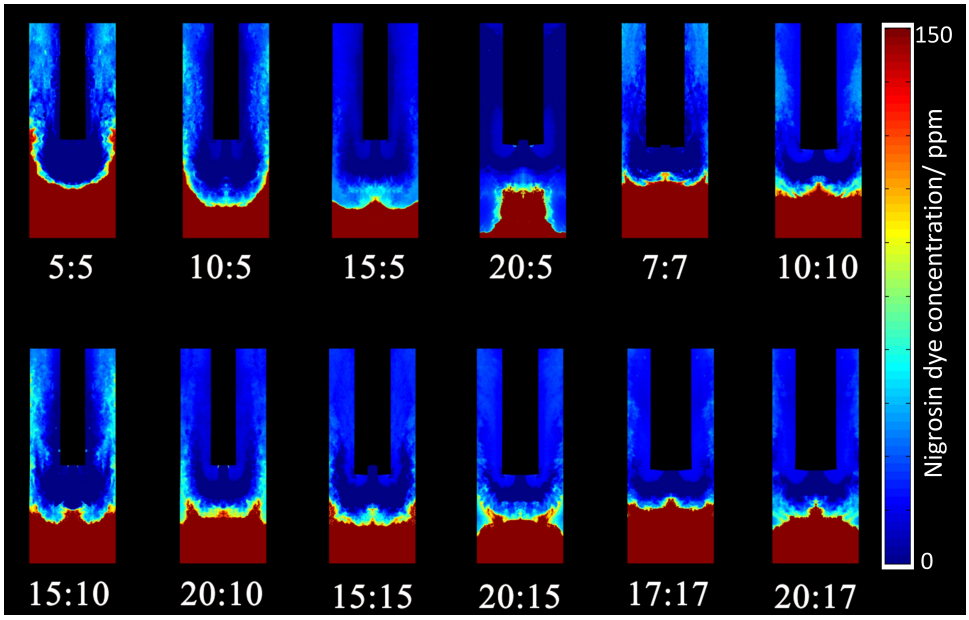


Figure 3.17: Concentration maps for counter current mixing rector. The numbers in the lower image represent the flow rates of hydrothermal solution and wastewater (in $mLmin^{-1}$) being simulated, respectively.

The results from the physical simulation experiments for counter current mixing reactor have been compared with CFD simulations presented by various research groups (Sierra-Pallares et al., 2011, 2016a; Zielke et al., 2016). The concentration map and photographs of the original papers are presented in Figure 3.18, and it is possible to say that there is a good agreement between these two different simulations techniques. It is important to remind here that this set of pseudo fluid modelling data was obtained at ambient conditions, and therefore although it may reflect the difference in density of the two fluids it cannot explain the gradients produced by temperature differences due to the heat transfer in the construction material of the mixer.

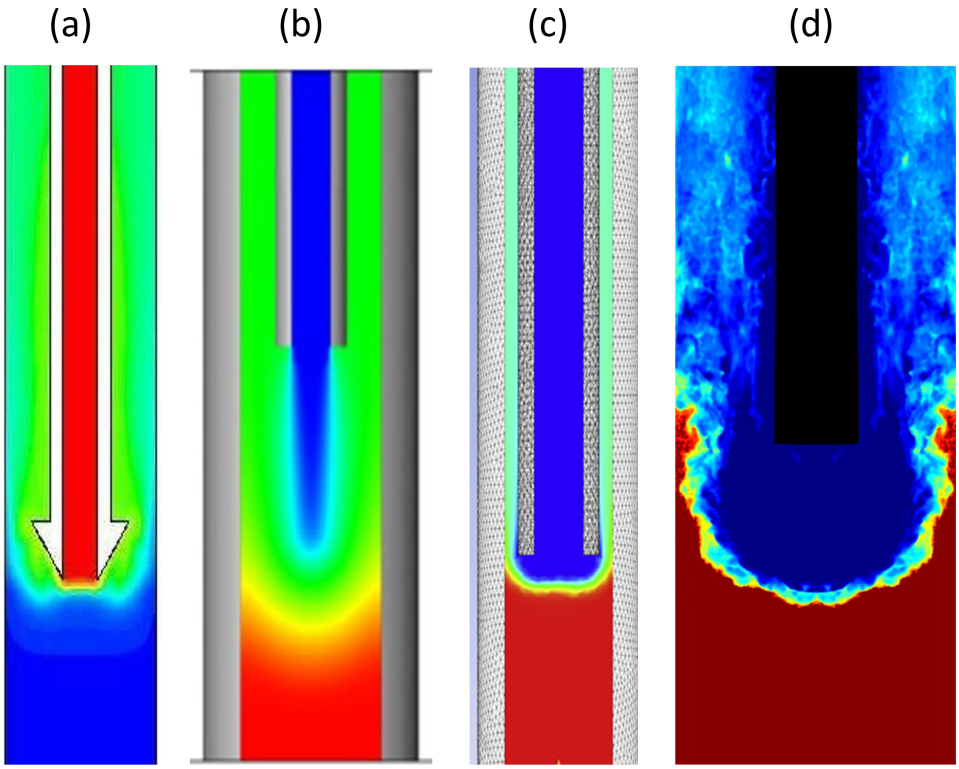


Figure 3.18: Comparison between the CFD results obtained from several studies for the counter current mixer and the pseudo fluid simulation experiments at different flow rate ratios (SCW:cold flow), (a) 10:5 (Sierra-Pallares et al., 2011), (b) 20:20 (Sierra-Pallares et al., 2016a), (c) 40:20 (Zielke et al., 2016), and (d) 5:5 this work.

Nevertheless, counter current mixing reactor exhibited some essential features to use as a SCWO reactor. Using the density difference between the two feed streams, counter current mixing reactor yields very good mixing effects. The turbulent eddies generated are able to prevent precipitation of any salt particles on walls. The wastewater stream is rapidly heated when contacting with the supercritical water, other than being preheated in conventional SCWO process. Hence the hydrolysis of wastewater prior to oxidation is avoided.

3.4.2 Co-current mixing reactor

In contrast to the previous counter current design, this configuration creates a co-current mixing regime. The hydrothermal solution is fed upward through the

inner tube into the bottom of the reactor, whilst the waste material is pumped into the sides of the reactor cross piece, entering below the outlet of the hydrothermal solution stream. The mixture then flows upward to the outlet of the reactor as shown in Figure 3.19. The actual experimental image and its concentration map for this configuration is shown in Figure 3.20.

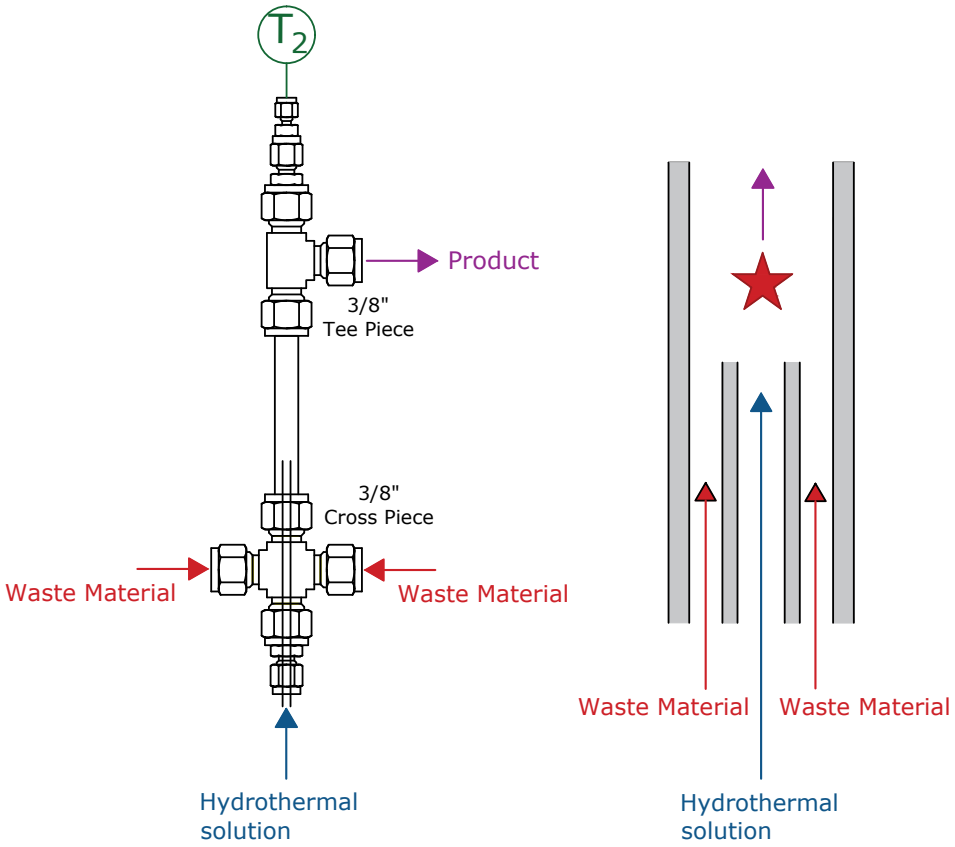


Figure 3.19: Cross sectional co-current mixing geometry.

The concentration map shows the formation of interface due density difference between two phases. When hydrothermal solution flows from inner to outer tube section, it encounters a sudden expansion in flow cross sectional area. The velocity must reduce and therefore, creating recirculation eddies at the reactor outer wall. This suggests that corrosion and salt accumulation, to some degree, could occur on the surface of the outer tube near to the interface. Moreover, the waste

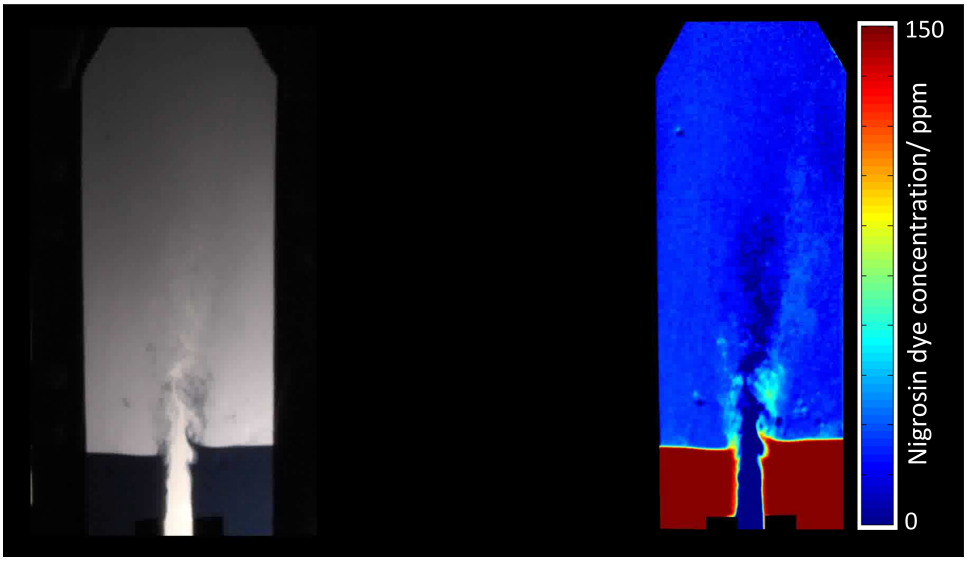


Figure 3.20: Actual experimental image and Concentration map for the co-current mixing pseudo reactor. Flowrates: pseudo SCW upward flow, inner cross: 995 $mLmin^{-1}$ and pseudo cold wastewater upward flow, outer cross: 128 $mLmin^{-1}$. This is a simulation of a 5:5 flow rate ratio under conditions typically used for SCWO.

flow appears to evenly distributed across the initial mixing area and there is no barrier preventing it from touching the inner wall of the outer channel. These findings are in agreement with results from CFD simulations by (Zielke et al., 2016). Simulation as given in Figure 3.22, showed the formation of the vortex in the co-flow geometry which is responsible for the excellent mixing properties between the two modelling fluids. Another noticeable feature of the design is the appearance of asymmetry in the outlet trajectory of the pseudo heated flow (centre) and the height of the stagnant zones either side of the heated flow outlet, see Figure 3.21. The cause could be the dynamic inertia forces acting between the two fluids (as a result of small pulses in flow and relative turbulence at the liquid - liquid interface) eventually driving the lower density flow one side of the other. More work is needed to fully understand this observation.

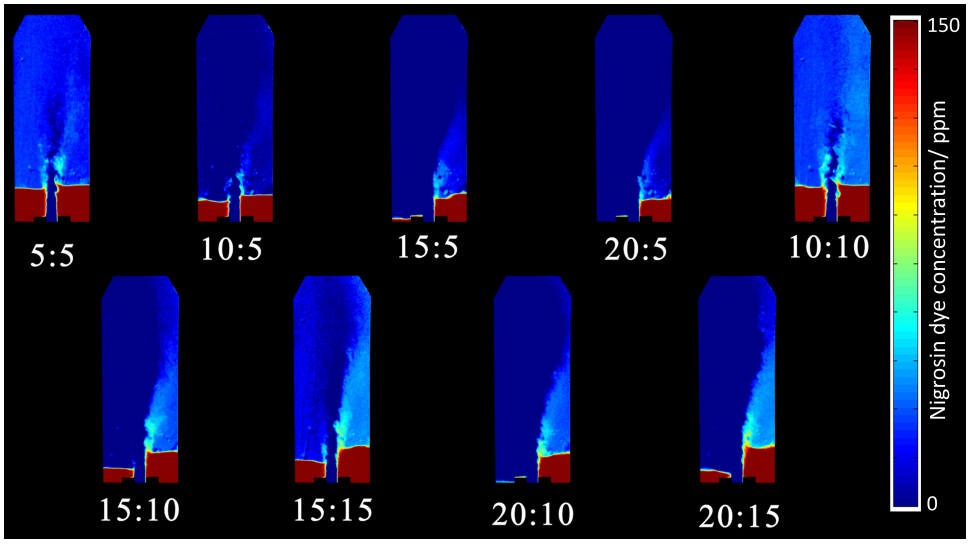


Figure 3.21: Concentration maps for co current mixing rector. The numbers in the lower image represent the flow rates of hydrothermal solution and wastewater $mLmin^{-1}$ being simulated, respectively.

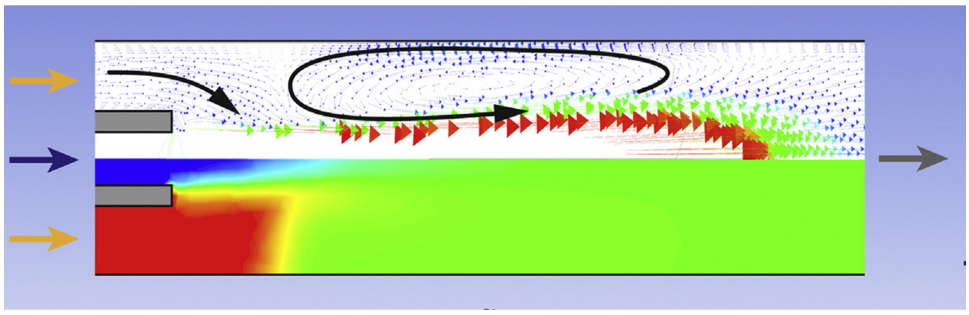


Figure 3.22: Simulation of mixing in co-current reactor, the color code indicates the precursor tracer concentration: red: feed precursor mixture, blue: feed SCW, other colors indicate degree of mixture between precursor and SCW. flow rate ratio: 20:20 (Zielke et al., 2016)

3.4.3 Co-current protected wall reactor

As discussed previously, the key factor to eliminating the corrosion of the reactor is in keeping the mixing reagents away from the surface of the reactor wall (particularly at the near-critical stage (Marrone and Hong, 2009)), whilst generating efficient mixing downstream towards the centre region of the reactor. Protected wall reactor design is similar to the previous design but the two inlet streams were interchanged i.e. the waste stream is introduced in the inner tube and the hydrothermal solution stream in the outer tube both flow upwards in the same direction to the outlet of the reactor as shown in Figure 3.23. The outer tube diameter was also decreased to potentially increase the velocity of the hydrothermal solution flow and prevent the cold flow (wastewater stream) spilling over the edge of the hot flow and sinking downwards under its own inertia.

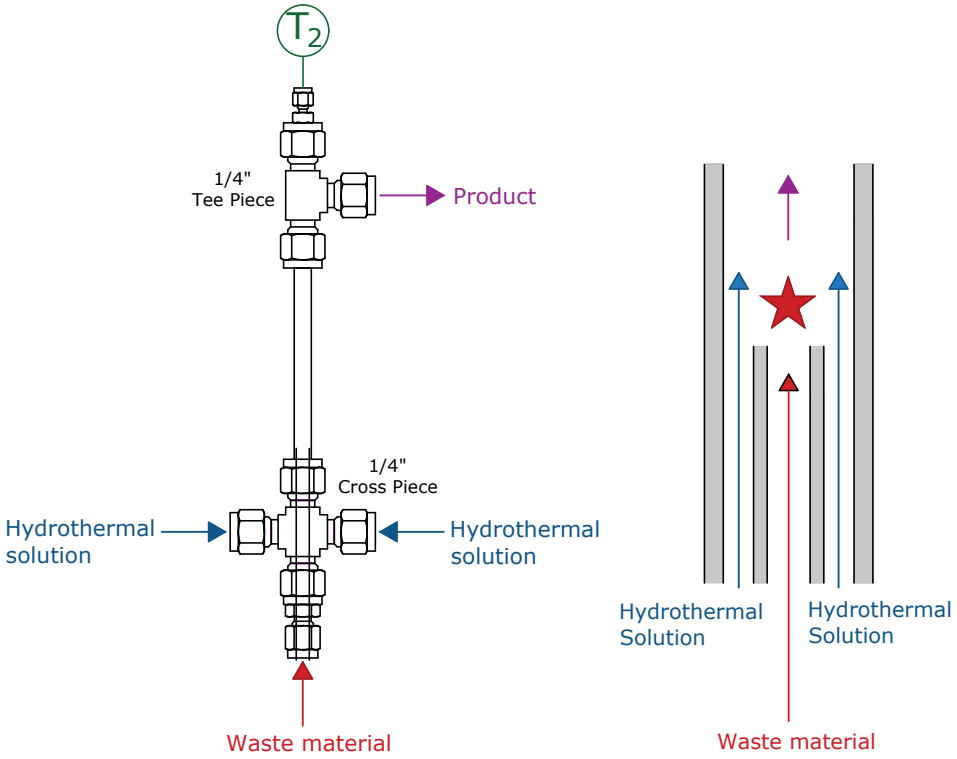


Figure 3.23: Cross sectional co-current protected wall reactor geometry.

An actual experimental images and its concentration map of this model are illustrated in Figure 3.24. The concentration map shows that the mixing zone is surrounded with a pure protecting hydrothermal solution containing very low if any concentration of dye. The density difference between the two modelling fluids prevents the pseudo waste flow reaching the reactor wall. The buoyancy forces also induce turbulent eddies which promote macro mixing as the flow travels upwards towards the outlet of the reactor (Tighe et al., 2012).

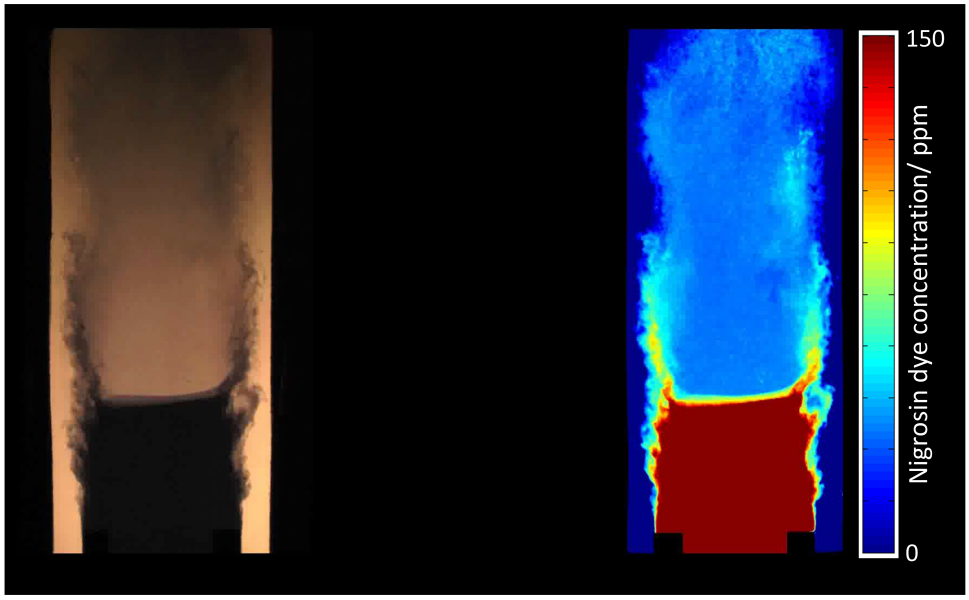


Figure 3.24: Actual experimental image and Concentration map for the co-current protected wall pseudo reactor. Flowrates: pseudo hydrothermal solution upward flow, outer cross: 4412 $mLmin^{-1}$ and pseudo cold wastewater upward flow, inner cross: 632 $mLmin^{-1}$. This is a simulation of a 50:10 flow rate ratio under conditions typically used for SCWO.

The concentration map images for a range of flow rates and ratios are shown in Figure 3.25 shows that a high pseudo hydrothermal solution flow (turbulent or transition flow regime) relative to the pseudo wastewater flow is required to control mixing and keep any attacking species and salt away from the reactor wall. Whereas the momentum of the laminar flow of the hydrothermal solution

is insufficient to avoid wall contact and recirculation zones which occur near the outer tube wall.

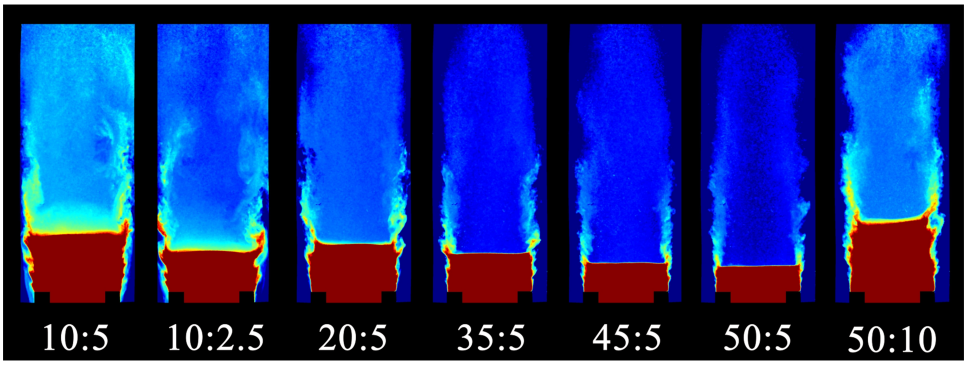


Figure 3.25: Concentration maps for co current protected wall rector. The numbers in the lower image represent the flow rates of hydrothermal solution and wastewater (in $mLmin^{-1}$) being simulated, respectively.

During SCWO, this design also avoids preheating the waste flow prior to mixing with the supercritical water flow (as with previous designs). The critical temperature of water should be achieved in reactor region rather than in the preheater (like most SCWO rig designs) (Erkonak et al., 2008; Marulanda and Bolaños, 2010; Du et al., 2013). Therefore, energy consumption of preheating can be reduced (Vadillo et al., 2013; Miller et al., 2015) and polymerization in wastewater can be avoided (Chen et al., 2015). The oxidation of any organic contaminants should occur at the turbulent shear layer when the hot flow pulls the waste materials to the reactor outlet. The energy released during the oxidation will rapidly heat the waste flow to a temperature at which the destruction of pollutants occurs. A second benefit of the reactor configuration is that the whole flow is moving upwards along with the creation of gases (during oxidation), so there should be no opportunity for dead zones or post mixing. Additional heaters can be placed around the reactor outlet which can be hotter than the initial mixing

temperature, thus creating additional buoyancy and faster oxidation rates.

3.5 Quantification and identification of ideal mixing

For the purpose of visualizing reactor performance, various process conditions were considered based on their ideality for desired features. It is possible to take the concentration maps from Figures 3.25 and simplify them further by recolouring them based on how close to ideal conditions they are. A primary aim for this research was to design a reactor that minimized potential corrosion by controlling mixing of reactants away from the reactor wall. An "ideal" SCWO reactor should be able to satisfy the following criteria:

1. Minimal (if no zero) concentration of corrosive species coming into contact with the reactor wall surfaces (to avoid corrosion).

2. Efficient mixing between the two streams (and thus effective heat transfer and contaminant destruction) in the center of the reactor at an adequate distance from the reactor walls.

A "traffic light visualization system" was applied to all image concentration data to produce maps which use color coding to indicate regional performance with respect to the above criteria. The maps can be used to visualize contaminant concentration (concerning proximity to the reactor walls) or mixing ideality in specific regions of the pseudo reactor and provide metrics for performance using different flow conditions. The acquired images showing the pseudo protected wall reactor were divided up into two primary zones as presented in Figure 3.26: the mixing zone and the wall zone. The width of each of the wall regions were

defined as 10% of the measured width of the dimension of the reactor. The zones were subsequently divided into fixed area square "buckets", which act to average out the effects of noise, grain and motion blur of the dye in the acquired images. Average dye concentrations were calculated for each bucket and the traffic light system was then applied to color each of the buckets based on selected thresholds based on the ideal concentration for each zone, producing an "ideality map". For ideality maps illustrating corrosion mitigation performance, the ideal concentration for buckets in the wall region is zero; for ideality maps illustrating mixing efficiency, the ideal average concentration for buckets (only within the mixing zone) is considered to be the average concentration of all buckets within the mixing zone.

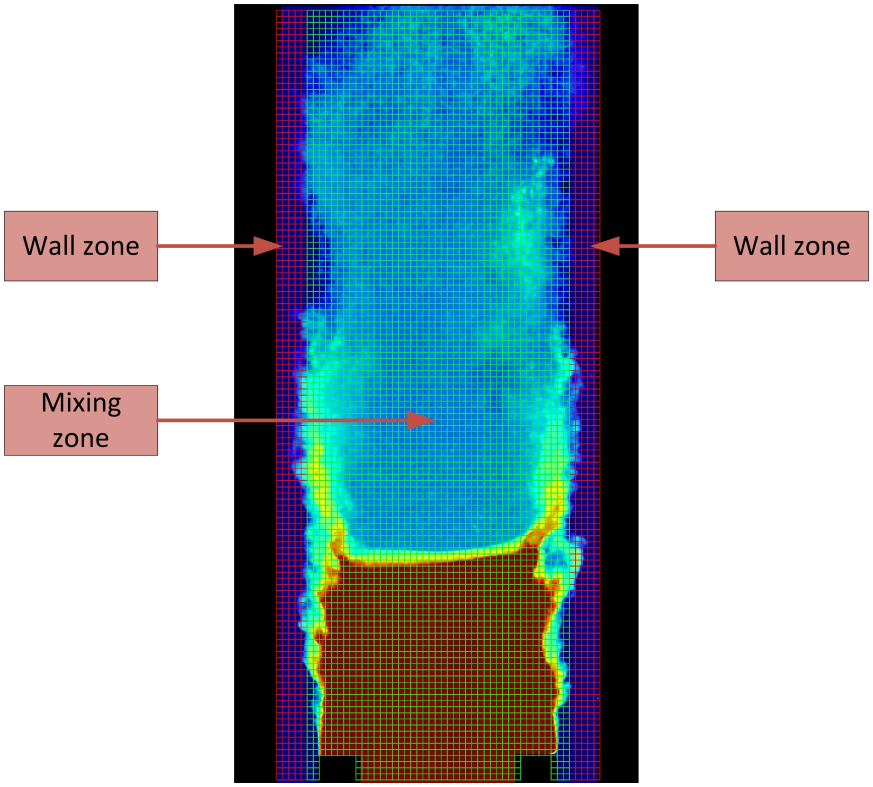


Figure 3.26: Zones and bucket allocation used for application of the traffic light system. Bucket size: 15×15 pixels.

3.5.1 The wall zone

This zone should be free from any dye and therefore the target dye concentration in this zone should be 0 *ppm* if ideal conditions are met. MATLAB® code has been used to compare the average concentration of each bucket in this zone with target concentration. The ideality of mixing in each bucket is colour coded and illustrated by the traffic light system image, as shown in Figure 3.27. For the red highlighted buckets, the average concentration of dye is higher than target concentration whilst in the green highlighted buckets; the average concentration of dye is equal to the target concentration. According to this analysis, each flow condition appears to have an optimal condition to avoid re-circulation and wall contact. However, a turbulent regime of pseudo hydrothermal solution flow has the best opportunity for avoiding corrosion.

3.5.2 The mixing zone

In the mixing zone, the target concentration, which represents the average concentration of entire mixing buckets, was quantified. Then, a percentage threshold was established to create a wide range of target concentrations where mixing is considered efficient. In this case the threshold was 33% of the target concentration. Again, the ideality of mixing in each bucket is colour coded as shown in Figure 3.28. For the red highlighted buckets, the average concentration of dye is exceeds the 33% threshold above the target concentration. In the blue highlighted buckets, the average concentration of dye is less than the 33% threshold below the target concentration. Finally the green highlighted buckets represent

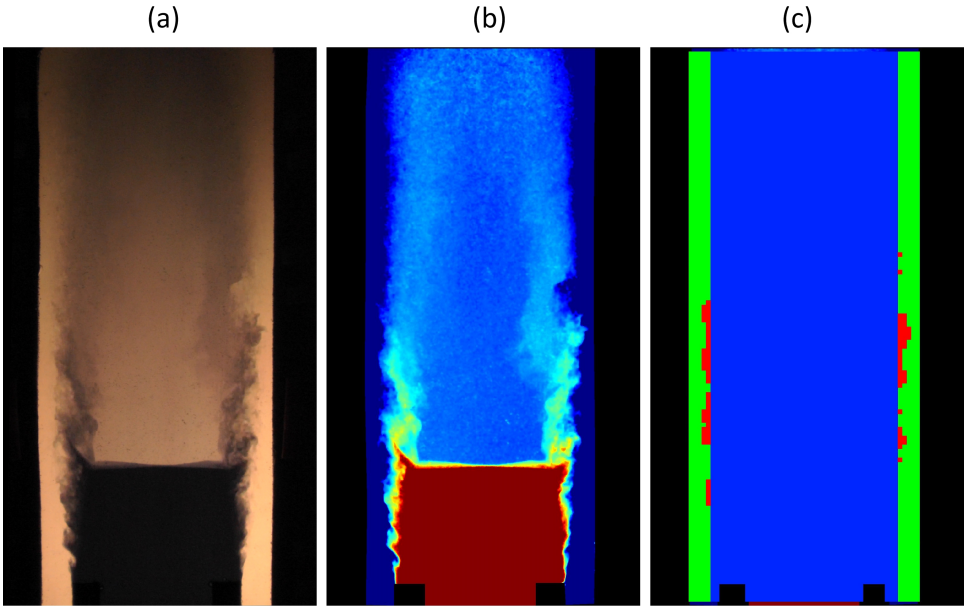


Figure 3.27: Co-current protected wall pseudo reactor.(a) Original image as captured by camera. (b) Concentration map applied to dye concentration data after processing stage. Red indicates maximum concentration of dye and dark blue is a zero concentration of dye. (c) Color coded buckets for the wall zones of the reactor; green buckets are those with an average dye concentration of 0 *ppm*, red bucket are those with a detected concentration of dye.

perfect mixing of reagents within the range of target concentrations. The average concentration of dye in each column of buckets in an experimental image is graphically shown in Figure 3.29. The broadness of peak represents how the mixing zone towards the center of the reactor and away from the reactor wall.

3.6 Overall reactor efficiency definition

Quantifying the relative ability of different operating conditions to avoid proximity between the wastewater stream and reactor wall (and this minimize corrosion) allows identification of viable process conditions when considering scale-up and potential industrial implementation. Summarizing the success of each set of conditions to a single reactor efficiency number allows direct comparison between

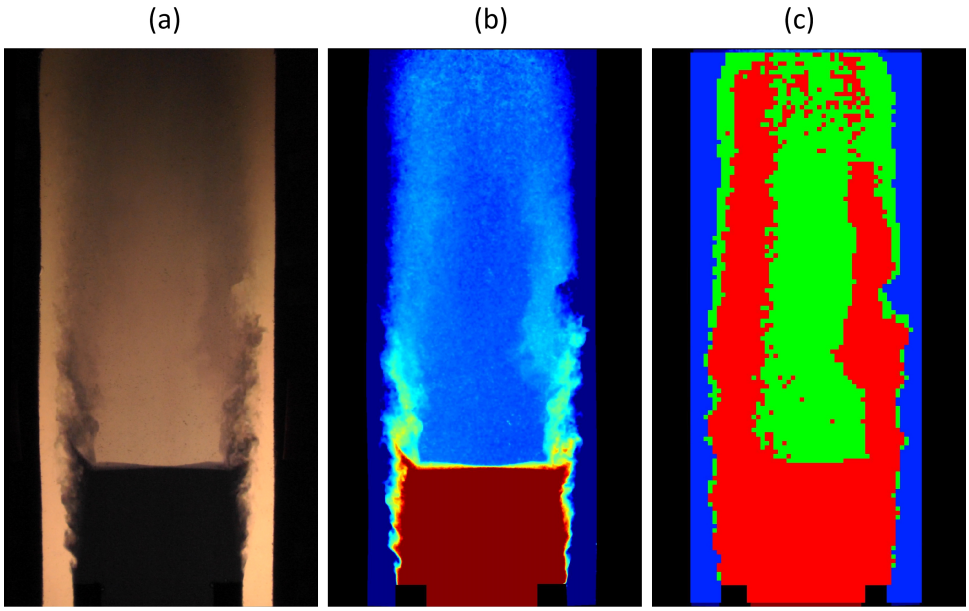


Figure 3.28: Co-current protected wall pseudo reactor.(a) Original image as captured by camera. (b) Concentration map applied to dye concentration data after processing stage. Red indicates maximum concentration of dye and dark blue is a zero concentration of dye. (c) Color coded buckets for the mixing zone indicating mixing efficiency; green buckets are those with an average concentration of within the range of the target concentration (the global average concentration of the mixing zone) +/- 33%; red buckets are those with average concentrations above this range, and blue are those below.

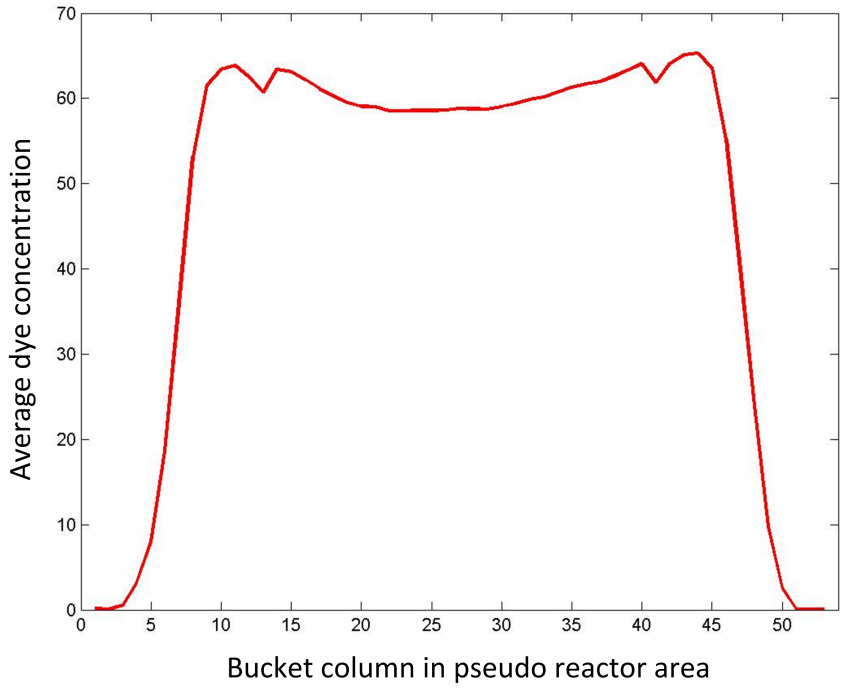


Figure 3.29: Concentration of dye in co-current protected wall pseudo reactor area.

Reynolds numbers of the inlet flows. Therefore, a technique is used to give an efficiency rating for each inlet flow rate combination. This efficiency rating reflects the average concentration of dye in the regions adjacent to the reactor walls relative to the average concentration in the entire mixing region of the reactor. This technique is based on the output data from the traffic light process or ideality indexing. A rating of 0 is used to represent 100% efficiency (i.e. an average concentration of zero dyed solution in the defined regions adjacent to the reactor walls)or no wall contact whereas a rating of 1 represents a totally non-efficient system (the average concentration at the reactor walls is the same as throughout the reactor mixing region). The efficiency rating for corrosion and salt deposition minimization is calculated from Equation (3.5):

$$E = \frac{\text{Average concentration of dye at the wall zone}}{\text{Average concentration of dye in the reactor mixing zone}} \tag{3.5}$$

Five and six increments of flow rate were used for the two pseudo fluid inlet flows, respectively, creating a matrix of thirty conditions. Inlet Reynolds numbers is used to determine the kinetic energy of pseudo hydrothermal solution stream required for avoiding wall contacts. The efficiency rating values are colour coded to give an indication of how the efficiency of the mixer varies with changes in inlet Reynolds number. As shown in Figure 3.30, in red highlighted regions, the supercritical stream (entering from the outer tube) have insufficient energy to effectively entrain of the pseudo wastewater flow away from the reactor walls and create a safe mixing zone. The green and orange highlighted regions show where there is sufficient momentum from the superheated flow to control the mixing

away from reactor wall. This characterization for mixing regime at the reactor wall helps to identify the minimum flow rate of superheated stream required to protect the wall from attacking corrosive ions.

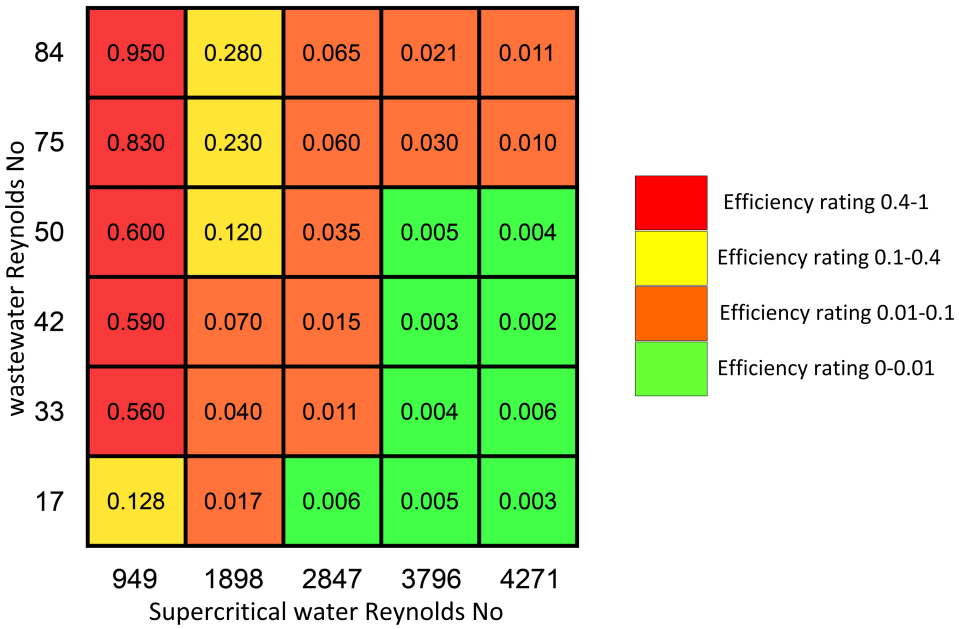


Figure 3.30: Efficiency ratings for co-current protected wall reactor for various combinations of inlet flow Reynolds numbers.

3.7 Conclusions

A visualization technique using pseudo fluids has been advanced to simulate the general flow patterns and mixing regimes of two very different fluids at ambient conditions. This technique was successfully exploited to model the condition of SCWO process and to evaluate three different reactor geometries, all of which can easily constructed using off the shelf high pressure fittings. The approach allows different flow conditions to be tested and quantified. Furthermore, a simplification of the concentration map data can be made to create a traffic light system and efficiency rating analysis were used to represent the performance of reactor in

terms of mixing efficiency and ability to keep corrosive species away from the reactor walls. From the perspective of corrosion prevention, the modelling results show that each design appears to have optimal flow conditions that reduce or avoid re-circulation and wall contact. However, the third reactor or co-current protected wall design seems to provide the best opportunity for avoiding corrosion and salt accumulation. The protecting flow of superheated stream at the reactor wall could control mixing of reagent in a safe zone. Nonetheless, pseudo fluid modelling offers a cheap, rapid and effective approach to reactor screening and desirable conditions for continuous flow supercritical hydrothermal flow processes and it is hoped this technique will be applied to study many more flow processes in the future.

4

SUPERCRITICAL WATER OXIDATION OF ACRYLIC ACID IN COUNTER CURRENT REACTOR

Highlights

- Two different experimental configurations for oxidant delivery were conducted.
- A combined oxidation/synthesis process in counter current mixing reactor was firstly reported.
- A comparison of the effectiveness of different nanocatalysts in contaminant removal.
- Addition of small amount of metal salt enhanced the removal efficiencies of COD during SCWO.
- An initial techno-economic assessment showing benefits of the process vs current standards.

4.1 Introduction

As described in Chapter 1, SCWO has been recognized as a promising technology for hazardous waste treatment. However, the industrial application of SCWO



to-date have been limited to laboratory and pilot-plant level, and few large-scale commercial applications are reported (Marrone, 2013). Besides corrosion and salt deposition, the high energy cost to get high reaction temperature ($> 550°C$) is one of the major disadvantages that inhibit the industrialization of SCWO technology. Therefore, in order to increase the efficiency of SCWO at mild temperatures, free radicals promoters were used in WAO and SCWO processes (Portela et al., 2001b). The positive effect of adding a small amount of hydrogen peroxide without any preheating, results from the thermal decomposition of hydrogen peroxide to give a highly reactive hydroxyl radicals as presented in Equation (4.1) (Rivas et al., 1999; Kolaczkowski et al., 1997). Once generated, those free radicals immediately attack all organics present in the solution as shown in Equation (4.2) (Quintanilla et al., 2010).

$$H_2O_2 \longrightarrow 2\,HO^{\bullet} \tag{4.1}$$

$$RH + HO^{\bullet} \longrightarrow R^{\bullet} + H_2O \tag{4.2}$$

However, when H_2O_2 is preheated, the generally accepted mechanism for the SCWO process is shown by Equation (4.3) (Wang et al., 2011)

$$RH + O_2 \longrightarrow R^{\bullet} + HO_2^{\bullet} \tag{4.3}$$

At moderate temperatures (e.g. $< 400°C$), the reaction (4.3) is relatively slow since ground-state oxygen does not react readily with most organic molecules because of its spin restrictions (Vogel et al., 1999). In addition, recent studies have shown that this oxygenation accelerates the corrosion of the tubing, particularly

where the H_2O_2 solution temperatures are near-critical (Sun et al., 2009; Hayward et al., 2003). Hence, oxidation with non-preheated H_2O_2 provides a more favourable approach for SCWO.

The use of catalysts could be a means to reduce these issues, either to increase the rate of reaction or to reduce the process conditions required to achieve the same efficiency as non-catalysed reactions. Under subcritical conditions, e.g. wet air oxidation (around 300°C), the COD conversion is always lower than 70% and requires a subsequent biological treatment. The use of homogeneous or heterogeneous catalyst is restricted by the maximum metal intake of the selected bacteria.

Supercritical hydrothermal synthesis (SCWHS) is another emerging technology which takes advantage of the tuneable chemical and physical properties of superheated water to produce inorganic nanoparticles by rapid nucleation (Dunne et al., 2015; Hayashi and Hakuta, 2010). A wide range of metal oxide nanoparticles, titania (TiO_2) (Kawasaki et al., 2009), cobalt oxide (Co_3O_4) (Lester et al., 2012), manganese oxide (MnO_2) (Nugroho and Kim, 2014) and hematite (Fe_2O_3) (Hao and Teja, 2003) have been commonly reported in the literature. Nano-sized catalysts have demonstrated higher efficiencies or rate of conversion than the same mass of material made up of larger particles (Chaturvedi et al., 2012). This is due to the increase in surface area to volume ratio from bulk material to nano-scale particles. For example, TiO_2 nanoparticles were shown to be more effective than larger particles in the photocatalytic degradation of pollutants (Loryuenyong et al., 2013).

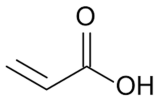
Whilst diametrically opposed as processes (one is destructive and one is for

synthesis), both processes have similarities e.g. whilst there are a significant number of research that heat the SCWO flow from ambient to supercritical conditions, using staged heating, there are others that use rapid mixing of a preheated flow (possibly containing the oxidant) with a secondary colder flow containing the contaminant (Miller et al., 2015). The latter requires a mixing design or 'reactor' geometry and these have includes tubular, co-current pipe in pipe, Y piece, cool wall, tangential swirl, transpiring wall etc. The use of a reactor to mix hot and cold flows for SCWO therefore creates the opportunity for two processes at the same time. i.e. destruction of the contaminants whilst simultaneously producing nanomaterials that can act as catalysts to increase the oxidation kinetics. Certainly catalysts could be added to the contaminant flow prior to the rapid heating and oxidation phase, but this would mean pumping particulate slurries into the system which potentially create new issues with settling (Gidner and Stenmark, 2001), poor dispersion (Pisharody et al., 1996) and pump head wear (LaGrega et al., 2010).

In order to test the principle of in-situ catalyst formation during SCWO, acrylic acid (AA) was chosen as a model unsaturated carboxylic acid contaminant. Some physical and chemical properties of AA are provided in Table 4.1. It is considered to be one of the major chemicals in a range of industries (oil additives, painting, detergents) and can cause extensive damage to the aquatic system if not being treated (Kumar et al., 2006; Shende and Levec, 2000). In these experiments COD levels were used to quantify oxidation rates rather than measuring residual acrylic acid concentration. Measuring residual contaminant levels can give a false measure of removal efficiency since partial oxidation (to produce intermediates)

is not necessarily a sufficient means of achieving COD discharge targets.

Table 4.1: Properties of acrylic acid.

Structure	
Formula	$C_3H_4O_2$
Molar mass	72.06 $gmol^{-1}$
Boiling point	114°C
Density	1.05 gcm^{-3}
Solubility in water	Miscible

In this Chapter, the advantages of the rapid mixing in the counter current mixing reactor have been exploited to produce a novel combined process of organic materials oxidation and metal oxides production (in nanometre scale) which can speed up the oxidation rate via enhanced catalytic activity. Furthermore, the effect of pre-heated (hot) and non-preheated (cold) hydrogen peroxide as an oxidant has been investigated.

4.2 Experimental set-up

All reactions were conducted at laboratory-scale. A simplified scheme of the experimental rig including the counter current mixing reactor is shown in Figure 4.1. A full flow diagram of the reactor system was given in Chapter 2. The reaction volume was estimated from the mixing point to the outlet of the reactor



and found to be 1.156 cm^3. Gilson HPLC pumps (Model 305 equipped with a 25 SC pump head) were used for feed delivery. K type thermocouples were used for temperature monitoring at different locations. All parts, fittings and tubing were made from SS316L from Swagelok®.

Two different set of experiments were carried out for investigating pre-heated and non-preheated oxidant. The methodology of reporting reaction temperature is discussed in section 4.3.

4.2.1 Experiments with oxidant preheating

A schematic diagram for this set of experiments is shown in Figure 4.1a. An aqueous solution of hydrogen peroxide was preheated through 6m length of 1/4" o.d. coiled heater at supercritical temperature. This setup enabled a complete decomposition of hydrogen peroxide to supercritical water and oxygen (Garcia-Verdugo et al., 2004). After the heater, the oxygen and supercritical water mixture flows downwards via the concentric tube in tube configuration through the thinner inner tube (1/8" outer diameter), and the cold organic solution feed enters from the bottom via an outer tube (3/8" outer diameter). Mixing and oxidation reaction occurs below down the nozzle tip (Sierra-Pallares et al., 2016a) and the product flows out of the side arm of the cross piece to the counter current heat exchanger. After cooling the product stream is brought to ambient temperature and passed through the back pressure regulator and the liquid product flowed out at ambient conditions into collection vessel.

4.2.2 Experiments without oxidant preheating

In this set of experiments, free hydrogen radicals were used as an oxidant rather than oxygen gas. This was delivered as a cold feed stream containing a H_2O_2 via a third pump. This feed stream was pressurized and mixed with organic feed stream at a mixing tee below the reactor at the base, at room temperature and without any preheating. The heated SCW flow was introduced from the top as a downward flow with just deionized water (Figure 4.1b). Upon contact with SCW, H_2O_2 was decomposed into highly reactive hydroxyl radical. Some researchers reported the interference of overall COD result from residual H_2O_2 in the effluent of the Advanced Oxidation Processes (AOPs) (Wu and Englehardt, 2012; Lee et al., 2011). Residual H_2O_2 has been found to be a problem since it will cause an overestimation of the COD. Therefore, blank tests have been carried out to ensure that all H_2O_2 has been consumed within the reactor with no residual remaining. 200% excess of H_2O_2 solutions had been mixed with supercritical water at different temperatures in non-preheated oxidant configuration and the COD tests show that there is no residual H_2O_2 remaining after hydrogen peroxide decomposition test.

4.3 Effect of operational parameters on reduction of COD

The oxidation of AA was studied by varying specific operating conditions, namely the operating temperature, residence time, oxidant ratio and feed concentration. The system pressure was kept constant at 25 MPa for all experiments. The default conditions for this process was to maintain the reaction temperature at

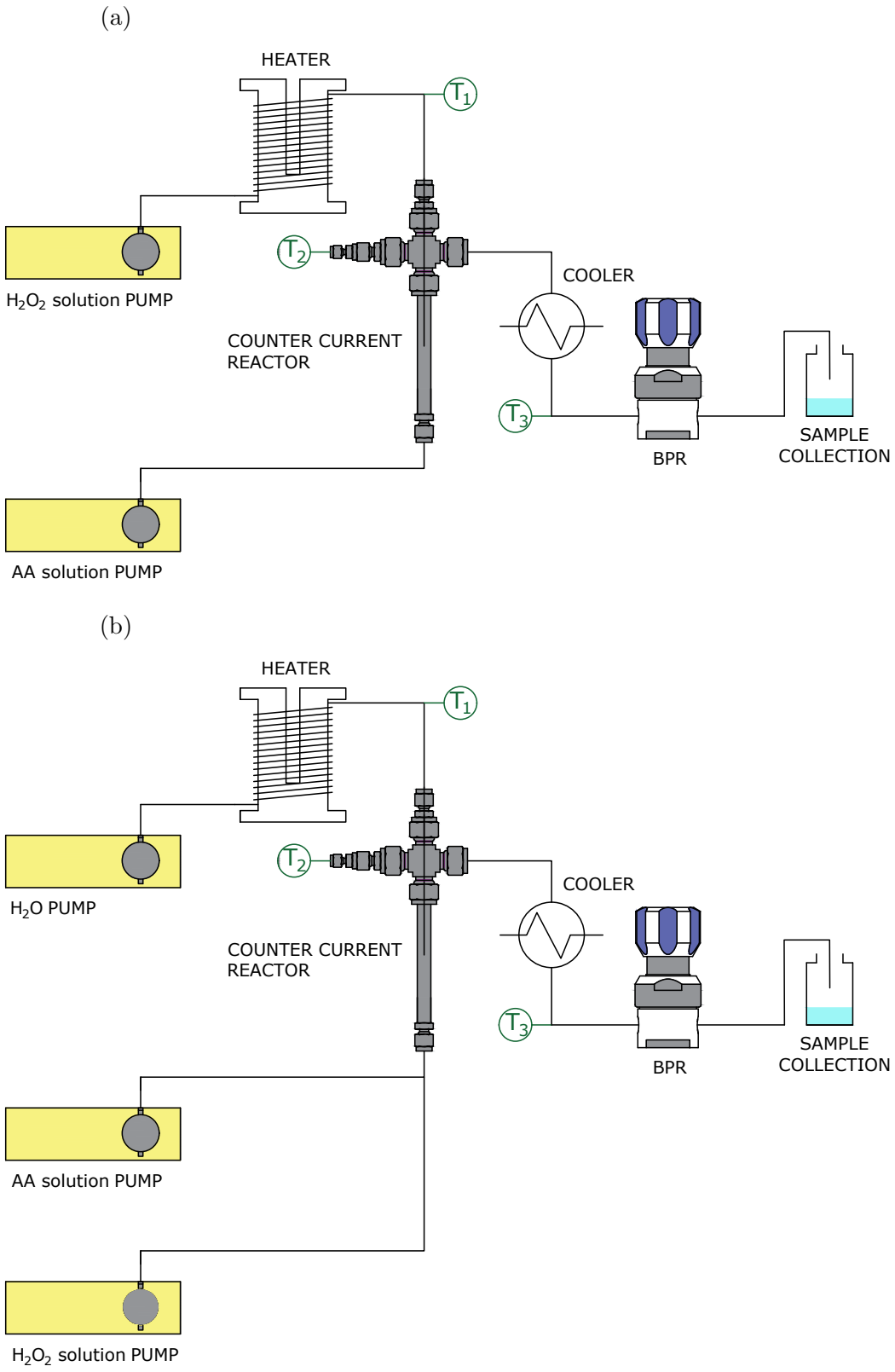


Figure 4.1: Simplified flow diagram of the continuous SCWO system. (a) Preheated oxidant configuration and (b) Non-preheated oxidant configuration. T_1 measures immediately after the heater. T_2 is the post mixed flow.T_3 is the temperature prior to the back pressure regulator (see Table 4.2 for temperatures measurements)



380°C, to make up a solution of AA of 10 mM at reaction conditions, and to deliver the stoichiometric quantity of oxidant required.

The range of temperatures that were investigated was $300-380$°C. This range was almost the largest feasible and governed by the limits of the laboratory hardware (i.e. the pump head and heater). The reaction temperatures was calculated (see Figure 4.1) from the average between the superheated water (T_1) and outlet mixture temperature (T_2) as presented in Table 4.2.

Table 4.2: Reaction temperatures in °C calculated from temperatures at different locations. Flow ratio is 2:1.

Heater set	After heater, T_1	Mixture, T_2	Reaction, T
350	345	255	300
372	363	277	320
381	370	310	340
400	388	332	360
420	395	365	380

The concentration of the AA solutions that prepared prior to each experiment were based on their concentration at reaction conditions. For example, AA concentration of 10 mM at reaction conditions of 380°C, 250 bar and flow ratio of 2:1 would correspond to a concentration of 74.84 mM in the feed stock at ambient conditions.

Residence time between (0.75-3 sec) were investigated by set the pump at flow rate ratio of (24:12-6:3 $mlmin^{-1}$) where all in laminar flow region. Oxidant

ratios of 0-3 were investigated at fixed operating conditions. The stoichiometric equation for the complete oxidation of AA is given by:

$$C_3H_4O_2 + 3O_2 \longrightarrow 3CO_2 + 2H_2O \tag{4.4}$$

4.3.1 Effect of reaction temperature

Figure 4.2 shows the effect of reaction temperature (in the range of $300-380°C$) on COD reduction at constant pressure ($25MPa$) and stoichiometric concentration of oxidant. The flow rate and initial concentrations of reactants at the feed stock were adjusted to maintain a fixed residence time of $1.5sec$.

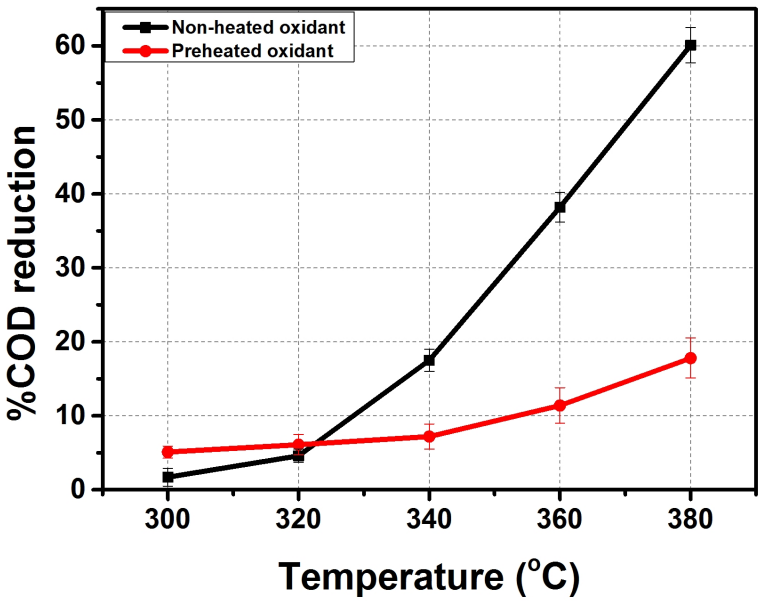


Figure 4.2: The effect reaction temperature on %COD removal. All experiments were carried out at 250 *bar*, a residence time of 1.5 *sec*, an initial AA concentration of 10 mM and an oxidant ratio of 1.

As can be seen from Figure 4.2, COD removal increased from 1 to 60% and from 5 to 18% for the non-preheated and preheated oxidant scenarios, as the

temperature was increased from 300°C to 380°C. At temperatures above 340°C, the presence of reactive free hydroxyl radicals formed in non-preheated oxidant configuration enhances the conversion efficiency. However, below 340°C, the temperature of the downward flow is well below the critical temperature of water (i.e. a down flow temperature of 345-370°C equates to a post mixed temperature of 300-340°C). Therefore, there is not enough energy to break down the organic or the oxidant mixture which result in a low COD removal for the non-preheated oxidant configuration. However, as the temperature of the heated down flow reaches the critical point, there are significant increases in COD removal. A high COD reduction of >50% at such low temperatures and residence times, particularly when compared to other studies (Gong et al., 2009; Wang et al., 2015), may be attributed to the advantages of the counter-current mixing reactor which provide an immediate and rapid heating of the organic and oxidant solution within the reactor in addition to the instantaneous strong and uniform mixing of upward and downward streams (Lester et al., 2006).

4.3.2 Effect of residence time and Reynolds number

The influence of increasing residence time on COD was evaluated whilst keeping other variables unchanged. The residence time was varied by changing the flow rate of reactants with a fixed flow ratio of (2:1), as shown in Table 4.3. Figure 4.3 shows that increasing residence time has some impact on COD reduction, depending on oxidant injection scenario. For the experiments with oxidant pre-heating, minimal effect on COD removal was observed as the residence time increased from 0.75 to 3 seconds. This minimal change could be a trade-off (or



pseudo 'compensation effect') of increased residence time vs reduced mixing intensity even though the Reynolds number all laminar. However, a steady COD reduction was achieved by increasing the residence time for the preheated oxidant configuration. This could be attributed the increased availability of the oxygen over time. It should be noted, however, that COD removal is always 3-6x less than with the non-preheated oxidant arrangement.

Table 4.3: Experiments with different residence times and the subsequent impact on mixing dynamics.

Residence time, (seconds)	Flow rate (SCW:AA solution), ($mLmin^{-1}$)	Reynolds Number
0.75	24.7:12.35	1772
1.0	18.5:9.25	1329
1.5	12.4:6.2	886
2.0	9.2:4.6	664
2.5	7.4:3.7	531
3.0	6.2:3.1	443

4.3.3 Effect of oxidant ratio

Only a 0.5% COD reduction was achieved at 380°C without the addition of an oxidant. It is therefore reasonable to assume that the effect of the hydrolysis reaction on acrylic acid was negligible, and that the oxidation reaction alone is responsible for its removal. Oxidant ratio was altered from 0-3 at fixed operating

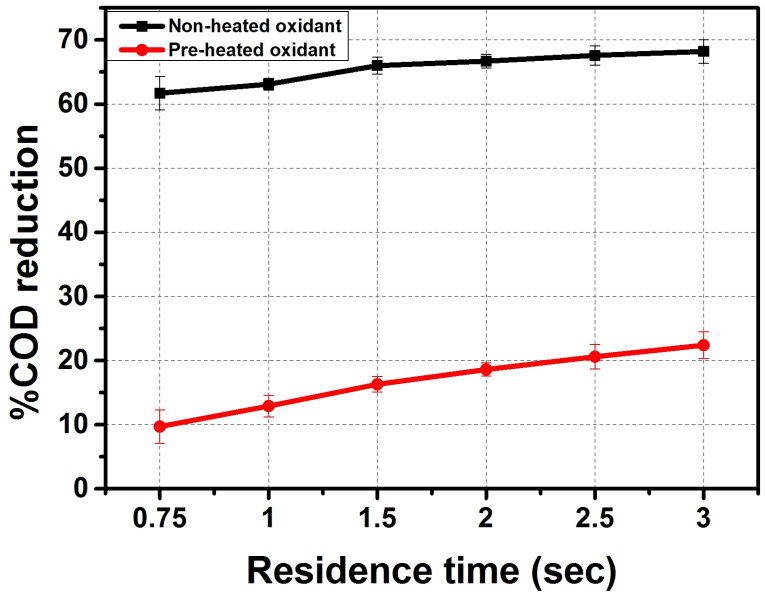


Figure 4.3: Experimental results for the effect of residence time on %COD removal at 380°C, 250 *bar*, an initial AA concentration of 10 mM and an oxidant ratio of 1.

conditions of 380°C and 250 *bar* with an initial concentration of 10 mM and 0.75 *sec* residence time. Figure 4.4 shows that COD removal rapidly increases with excess oxidant (Pinto et al., 2006). The reduction rate appears to plateau above an oxidant ratio of 2.0 which is in agreement with the findings of (Shin et al., 2009b) and although their residence times were significantly longer than 0.75 *sec*.

4.3.4 Effect of acrylic acid concentration

The effect of initial concentration in range of 5-20 mM on the SCWO of acrylic acid at 250 *bar*, 380°C, a 0.75 *sec* residence time and an oxidant ratio of 1 is presented in Figure 4.5. As shown in the figure, increasing AA concentration had a small effect on COD reduction in both preheated and non-preheated oxidant scenarios. However, in non-preheated oxidant scenario the effect is slightly more

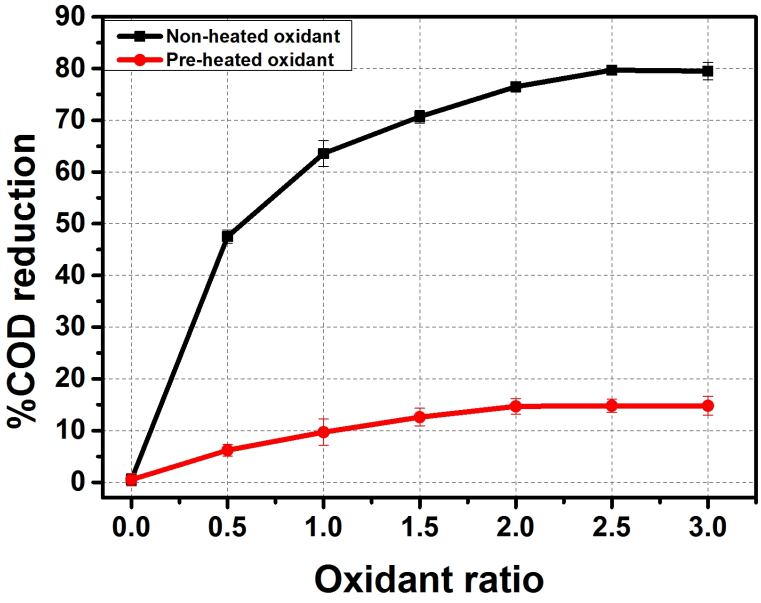


Figure 4.4: The effect of oxidant ratio on %COD removal efficiency at 380°C, 250 *bar* and 10 mM of AA.

obvious.

4.4 Effect of in-situ catalyst formation

A series of experiments were carried out to study the synergetic effect of various metal salt precursor and metal oxides nanoparticles as catalysts for the conversion of acrylic acid. These experiments used the same set up as described in Sections 4.2.1 and 4.2.2 but with controlled addition of different precursor salts (5, 10 and 20 mM) dissolved in 250 ml of 74.84 mM acrylic acid solution at ambient conditions. The effect of metal salt concentration on the catalytic SCWO of AA over two temperatures 340 and 380°C was studied at constant pressure of 250 *bar*. An initial AA concentration of 10 mM at reaction conditions was used for all the experiments, while the initial concentration of oxygen met a SR of 1.5.

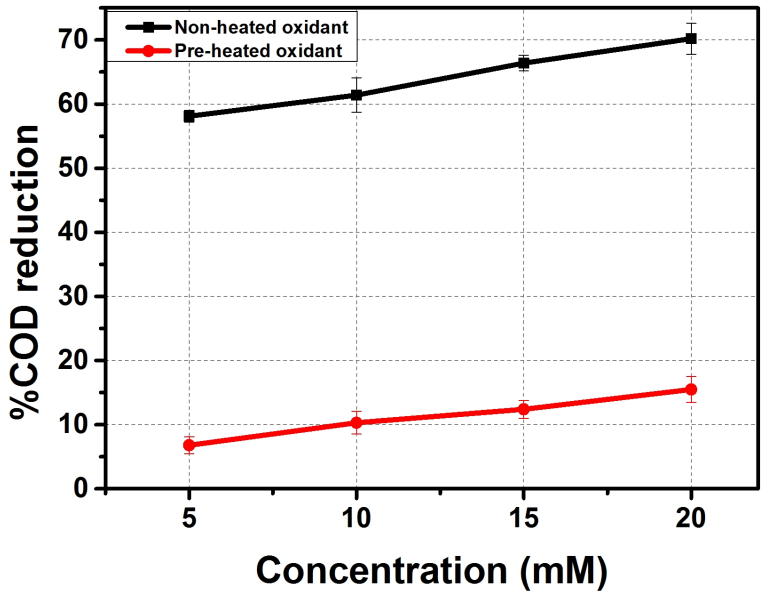


Figure 4.5: Experimental results for the effect of initial organic concentration on %COD removal efficiency at 380°C, 250 *bar* and oxidant ratio of 1.

4.4.1 Titania (TiO_2)

Titania or titanium dioxide (TiO_2) is one of the most used and studied compound due its unique chemical and physical characteristics, including nontoxicity, high thermal and chemical stability, and catalytic and photocatalytic activity (Cargnello et al., 2014). It is employed in variety of traditional applications such as medical implants, cosmetics, water purification, and pigments and paint industries (Chen and Selloni, 2014). Titania has three different crystalline forms, depending on the synthesis method. The most common form is anatase. Continuous-flow hydrothermal and solvothermal methods were used to produce anatase nanoparticles from a wide range of precursors (Caramazana-Gonzalez et al., 2017).

In this work, Titanium(IV) oxysulfate (TiOS) was used as precursor for titania production. A brief reaction schematic with flow arrows for both preheated

and non-preheated oxidant arrangements can be seen in Figure 4.6. Depending on the oxidant delivery method, a high pressure water pump supplied a H_2O_2 solution or deionised water through the preheater (2 kW) to enter the reactor from the top. Mixture of aqueous TiOS and AA solution as shown in Figure 4.6a for preheated oxidant arrangement or aqueous TiOS, AA and H_2O_2 solution as shown in Figure 4.6b for the non-preheated oxidant arrangement at ambient temperatures were fed to the reactor from the base and mixed counter-currently with the hot flow. The newly formed titania nanoparticles would act as catalysts during the decomposition of AA. Figure 4.7 shows the catalytic effect of titania

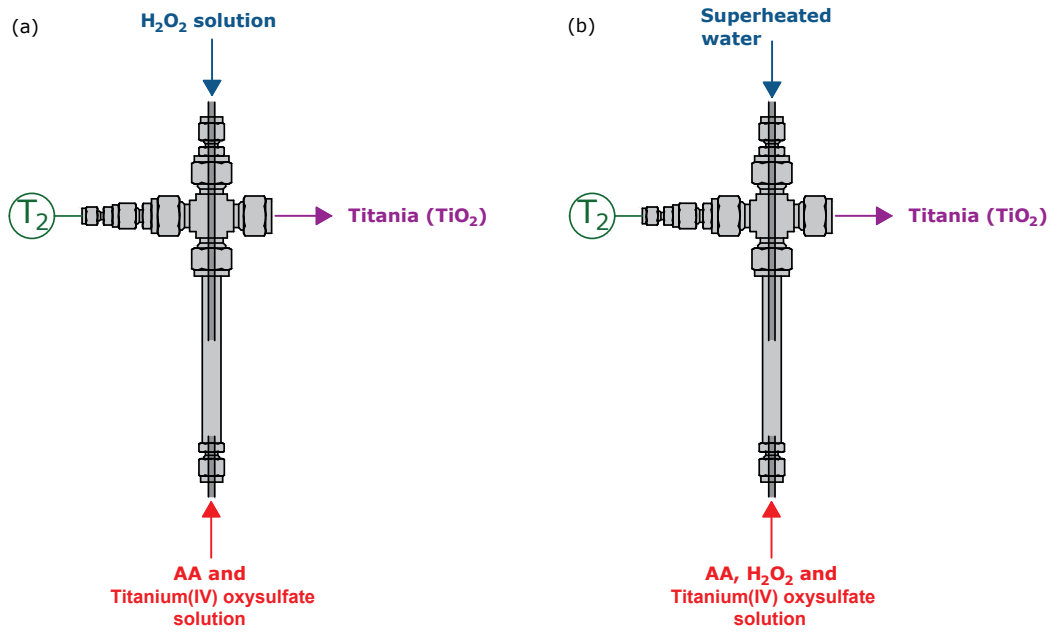


Figure 4.6: A schematic diagram showing the reaction arrangement for synthesis of TiO_2. (a) Preheated oxidant and (b) Non-preheated oxidant scenario

on COD removal compared to the catalyst free reactions at both sub and supercritical temperatures. As can be seen from Figure 4.7, titania has no activity on COD removal at subcritical temperatures for both oxidant delivery configurations. However, when the temperatures increase to 380°C, titania show a moder-

ate effect on COD reduction at preheated oxidant scenario. The reaction was not particularly efficient since at 20 mM of TiOS only 50% of COD was removed. The activity TiO_2 was demonstrated previously during the catalytic SCWO of phenol, which showed that the experimental conversion was always higher and nearly reached 50% compare to less than 25% phenol conversion obtained by noncatalytic SCWO (Yu and Savage, 2000a). At non-preheated oxidant configuration, although, a small enhancement was achieved compare to catalytic free reaction, the catalyst enhanced the removal of the AA in term of COD by 73%. Consequently, higher operating conditions or longer residence time are required to reach complete elimination.

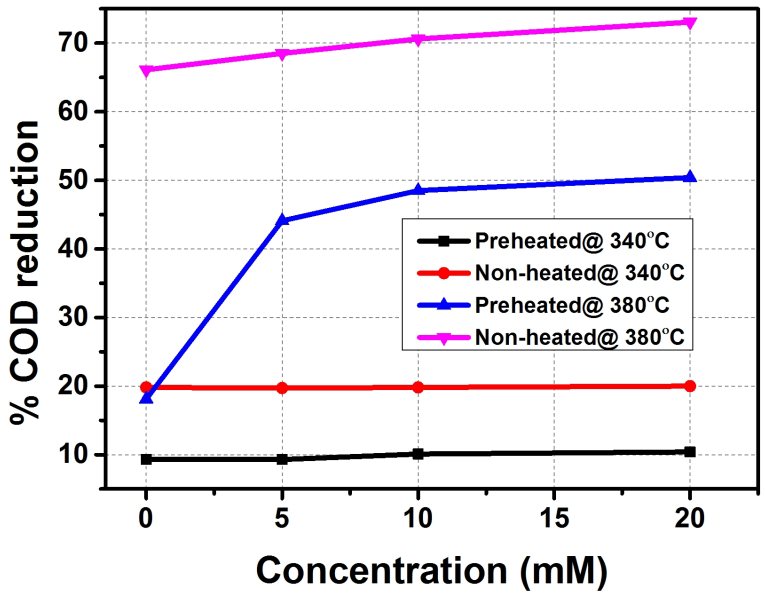


Figure 4.7: Catalytic effect of titania nanoparticles on %COD removal at 380°C, 250 *bar*, oxidant ratio of 1.5, and initial acrylic acid concentration of 10 mM

The XRD profiles for titania samples obtained from supercritical preheated and non-preheated oxidant scenarios are given in Figure 4.8, along with the expected peak positions for anatase. All the peaks corresponding to the reference

phase are present in both samples, confirming that anatase is the predominant crystal structure for both preheated and non-preheated samples. The crystallite diameters of the pure anatase as calculated using the Scherrer equation for the preheated and non-preheated oxidant scenarios were 7.74 and 7.49 nm, respectively.

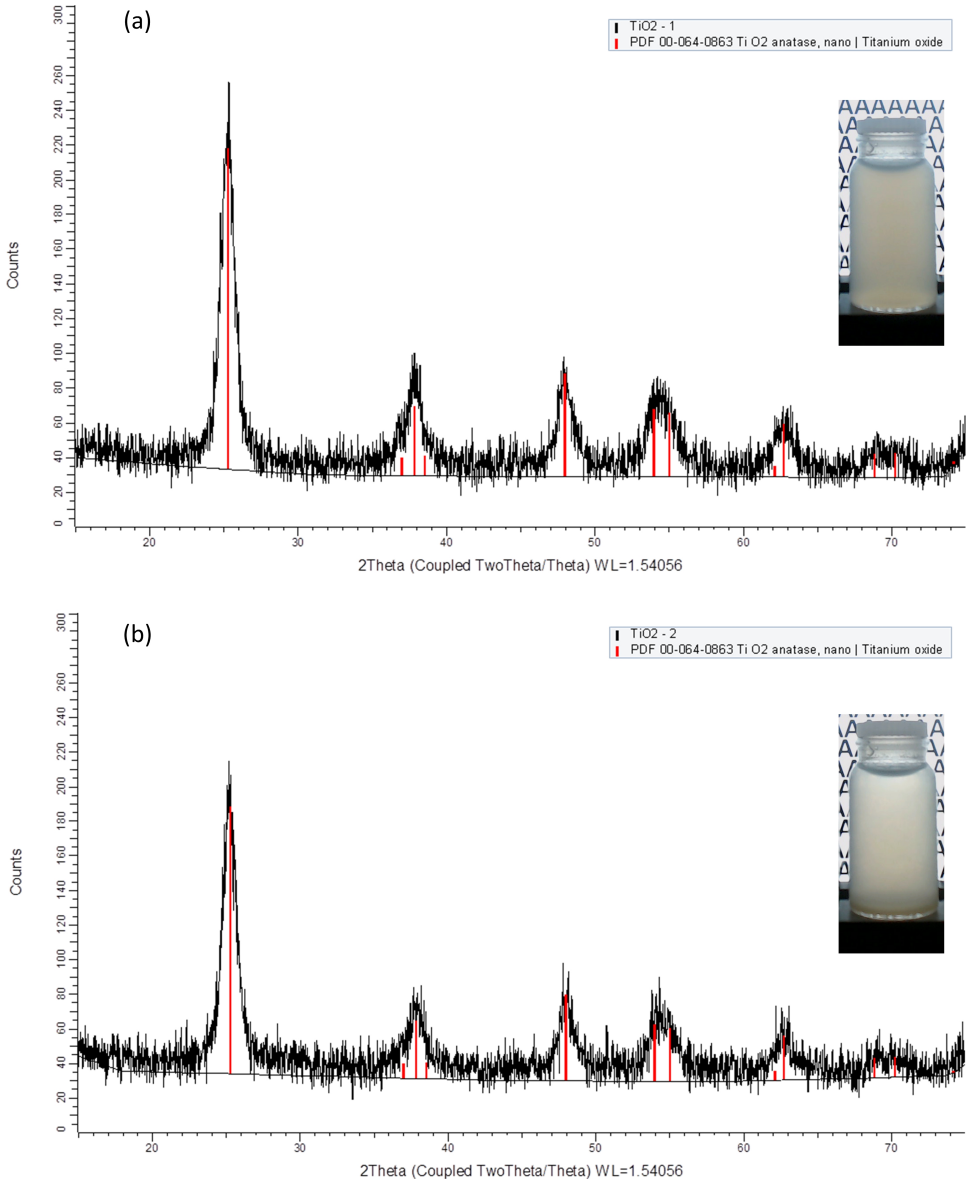


Figure 4.8: XRD patterns of TiO_2 nanoparticles obtained obtained at 380°C, 250 bar, oxidant ratio of 1.5 and 20 mM of metal salt concentration. The red lines at the bottom are the expected peak positions for anatase (PDF 00-064-0863). (a) Preheated oxidant and (b) Non-preheated oxidant scenario.

The images of titania samples collected using TEM analysis are shown in Figure 4.9. For both oxidant delivery methods, the particles are spherical in morphology with detectable edges and crystallinity. ImageJ software was used to give the sizing data from TEM analysis and over 100 measurements. Particle size for the preheated and non-preheated oxidant scenarios were found to be 8.02 and 8.97 nm, respectively.

4.4.2 Cobalt oxide (Co_3O_4)

Nanometer scale of cobalt oxide (Co_3O_4) have interesting magnetic, electrochemical, optical and catalytic properties (Salavati-Niasari et al., 2009). Co_3O_4 has been studied widely for applications in energy storage, chemical sensors, electrochemistry, magnetism, photocatalysis and heterogeneous catalysis. Co_3O_4 shows high-catalytic activity for the oxidation of carbon monoxide, and the catalytic decomposition of hydrocarbons (Li and Shen, 2012). Most of the properties of Co_3O_4 nanoparticles are depended on particle size and morphology (Lester et al., 2012). Thus, tremendous efforts have been directed in recent years to the synthesis and investigation of properties of Co_3O_4 nanostructures.

In this work, cobalt(II) nitrate hexahydrate ($Co(NO_3)_2.6H_2O$) was used as precursor for Co_3O_4 production. Figure 4.10 shows a simple reaction schematic of the flow orientations for both preheated and non-preheated oxidant configuration. For the preheated oxidant configuration, a superheated H_2O_2 solution flowed downward in the inner tube of the reactor are mixed with a mixture of AA and $Co(NO_3)_2.6H_2O$ solution flowed upward in the outer tube. Whereas, in non-preheated oxidant configuration, H_2O_2 solution is flowed upward along with

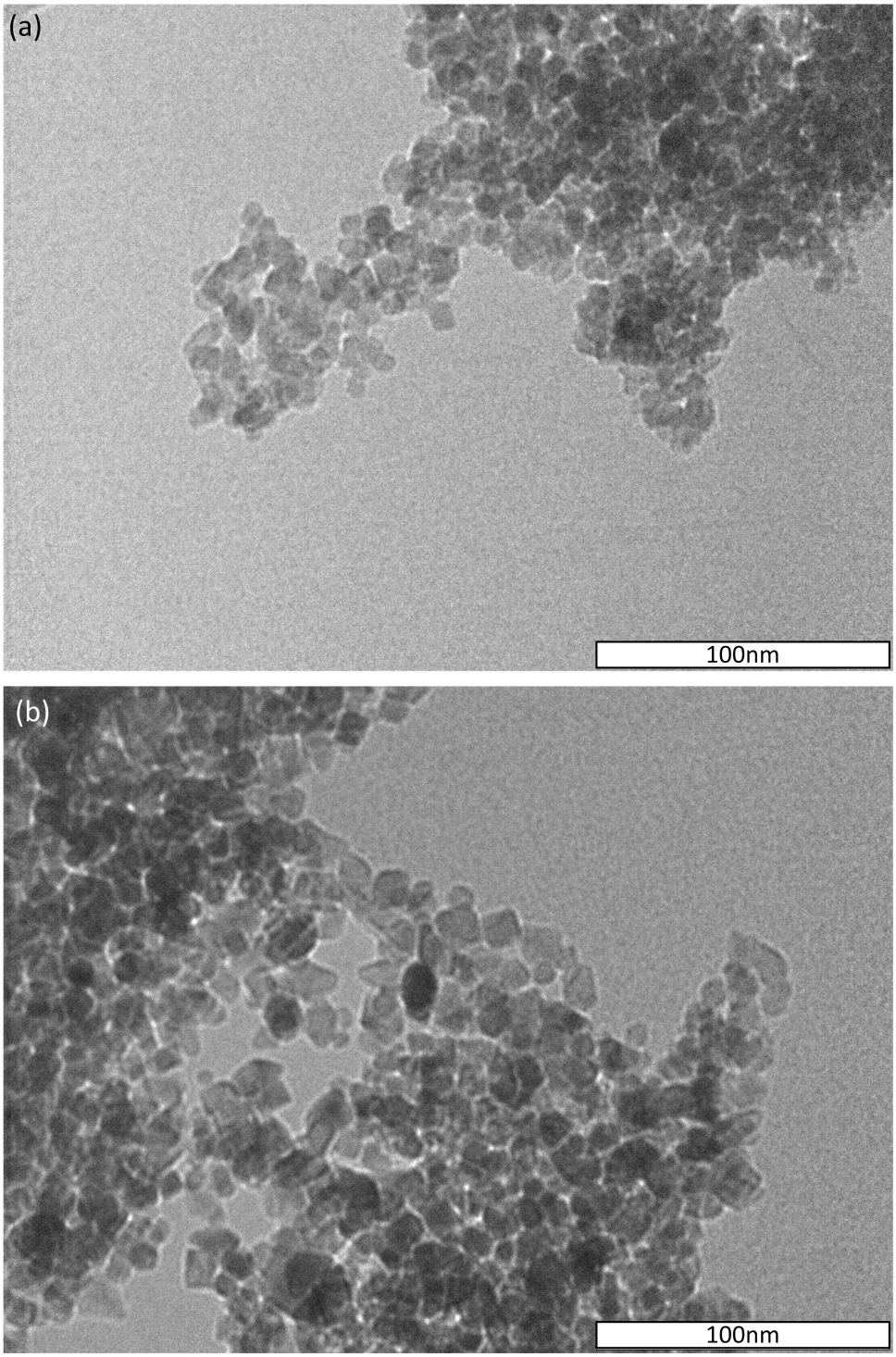


Figure 4.9: TEM images of TiO_2 nanoparticles obtained from (a)Preheated oxidant and (b) Non-preheated oxidant scenario

organic and inorganic solution. The downward flow is contained a clean superheated water. Co_3O_4 nanoparticles produced at the interface could enhance the oxidation reaction due to its catalytic activity. Figure 4.11 reveals that the addition of $Co(NO_3)_2.6H_2O$ dramatically improved the degradation of the organic content. Cobalt oxide produced in situ shows a high catalytic activity with a more than 60% increase over the non-catalysed reaction especially in the preheated oxidant arrangement where its activity is surprisingly higher compared with the non-preheated oxidant scenario. To illustrate, at a temperature of 380°C, the COD removal efficiencies for noncatalytic preheated and non-preheated oxidant configurations were 19.4% and 67.7%, respectively, whereas the values reached 79.7% and 77.04% with Co_3O_4. However, like titania, it has no effect at subcritical temperatures. The catalytic oxidation of Lurgi coal-gasification wastewater over Co_3O_4 was preformed in a batch reactor at 380°C and oxidant ratio of 2.5 (Wang et al., 2012). TOC removal efficiencies increased from 95.5% to 99% when catalyst employed. However, exposure of the Co_3O_4 catalyst to the SCWO environment resulted in morphology change and Co ion leaching which intensified with increasing temperatures.

The powder X-ray diffraction patterns of the in situ produced Co_3O_4 and the black suspension containing Co_3O_4 nanoparticles in 30 *ml* bottles are shown in Figure 4.12. It is clear from these patterns that Co_3O_4 is produced as the patterns display peaks matching the expected Co_3O_4 pattern for the preheated and non-preheated oxidant arrangement. The crystallite diameters of the Co_3O_4 as calculated using the Scherrer equation for the preheated and non-preheated

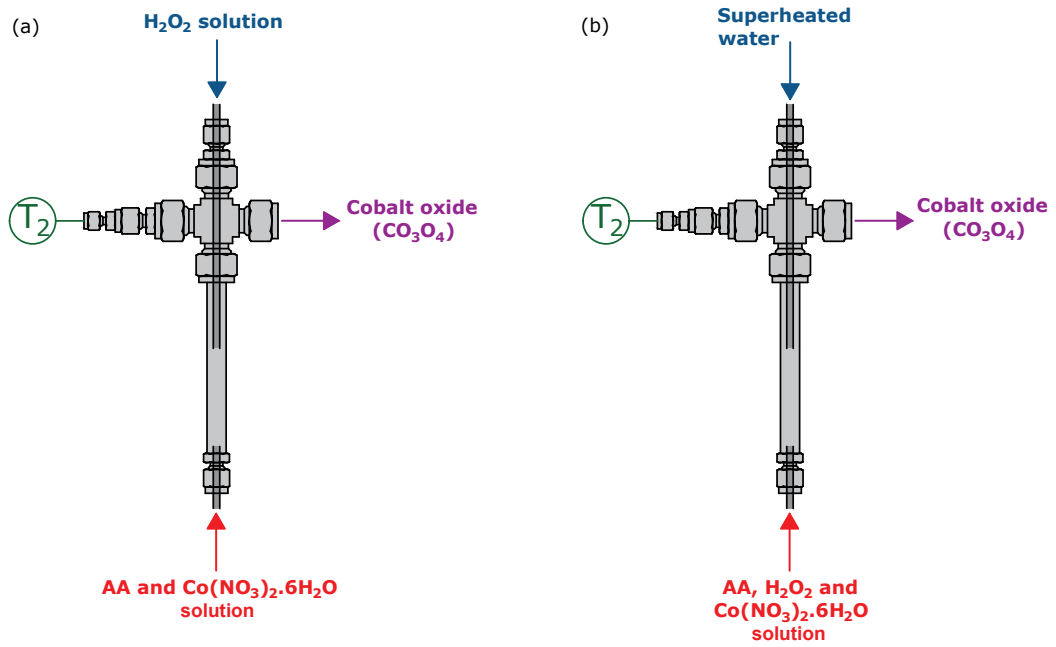


Figure 4.10: A schematic diagram showing the reaction arrangement for synthesis of Co_3O_4. (a) Preheated oxidant and (b) Non-preheated oxidant scenario

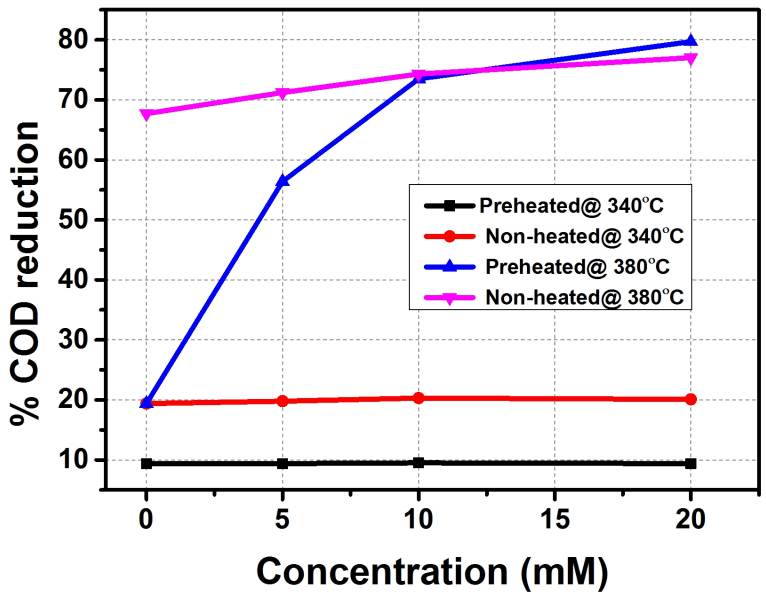


Figure 4.11: Catalytic effect of cobalt oxide nanoparticles on %COD removal at 380°C, 250 *bar*, oxidant ratio of 1.5, and initial acrylic acid concentration of 10 mM

oxidant arrangement were 23.27 and 20.39 nm, respectively.

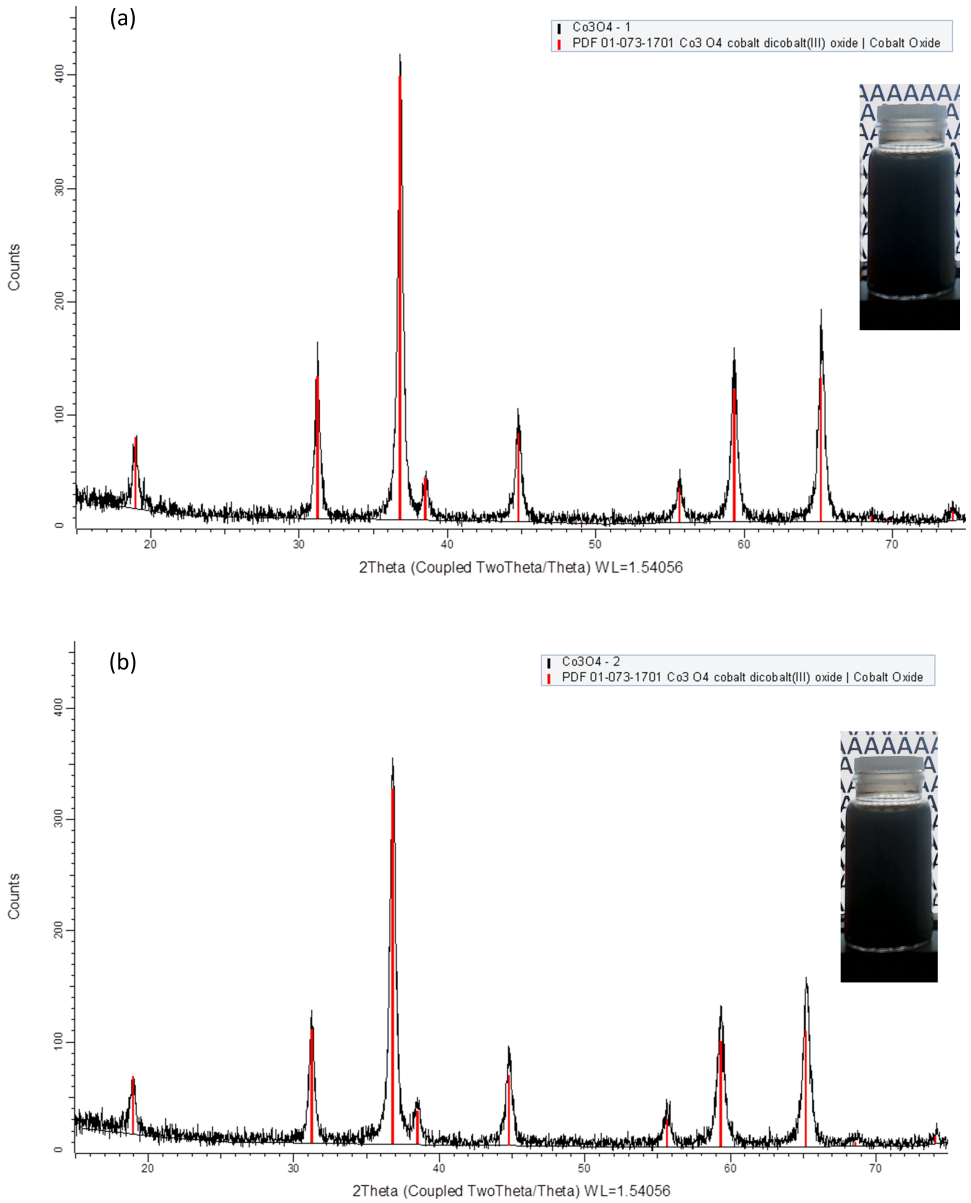


Figure 4.12: XRD patterns of Co_3O_4 nanoparticles obtained obtained at 380°C, 250 bar, oxidant ratio of 1.5 and 20 mM of metal salt concentration. The red lines at the bottom are the expected peak positions for Co_3O_4 (PDF 01-073-1701). (a) Preheated oxidant and (b) Non-preheated oxidant scenario.

Figure 4.13 shows the TEM images of Co_3O_4 nanoparticles made at 380°C with a precursor solution of 20 mM. From these images, it can be observed that most of Co_3O_4 nanoparticles were cubic in shape. More than 100 particles from each TEM images were measured by ImageJ software and the particle size were

found to be 35.43 and 15.78 *nm* for the preheated and non-preheated oxidant arrangement, respectively.

4.4.3 Hematite (Fe_2O_3)

Hematite has attracted plenty interests for its diverse application, such as pigments, catalyst, gas sensing materials and photoelectric devices (Zboril et al., 2002). Hematite nanoparticles had been previously produced in Nottingham using counter current mixing reactor (Dunne et al., 2015).

In this work, Iron(III) nitrate nonahydrate ($Fe(NO_3)_3.9H_2O$) was used as precursor for hematite production. The catalytic oxidation reactions were performed as shown in Figure 4.14. As can be seen, preheated H_2O_2 solution was mixed counter currently with a mixture of AA and $Fe(NO_3)_3.9H_2O$ solution. In non-preheated oxidant configuration supercritical water was mixed with a mixture of AA, $Fe(NO_3)_3.9H_2O$ and H_2O_2 solution. The in-situ formed Fe_2O_3 catalyst could enhance the oxidation of organic materials. Figure 4.15 shows that hematite significantly improves the removal rate of acrylic acid at both sub and supercritical temperatures. Nearly complete degradation of organic content of AA to CO_2 and H_2O was obtained at 380°C in the non-preheated oxidant configuration. It is worth mentioning that part of the high COD removal is also due to the Fenton reaction between H_2O_2 and the iron(III) present in the solution (Dunford, 2002).

The XRD data collected from hematite powder and photos of hematite suspension for the preheated and non-preheated oxidant configuration is shown in Figure 4.16. As it can be seen from the XRD patterns, the crystalline phase of hematite was present. Crystallite diameters were calculated using the Scher-

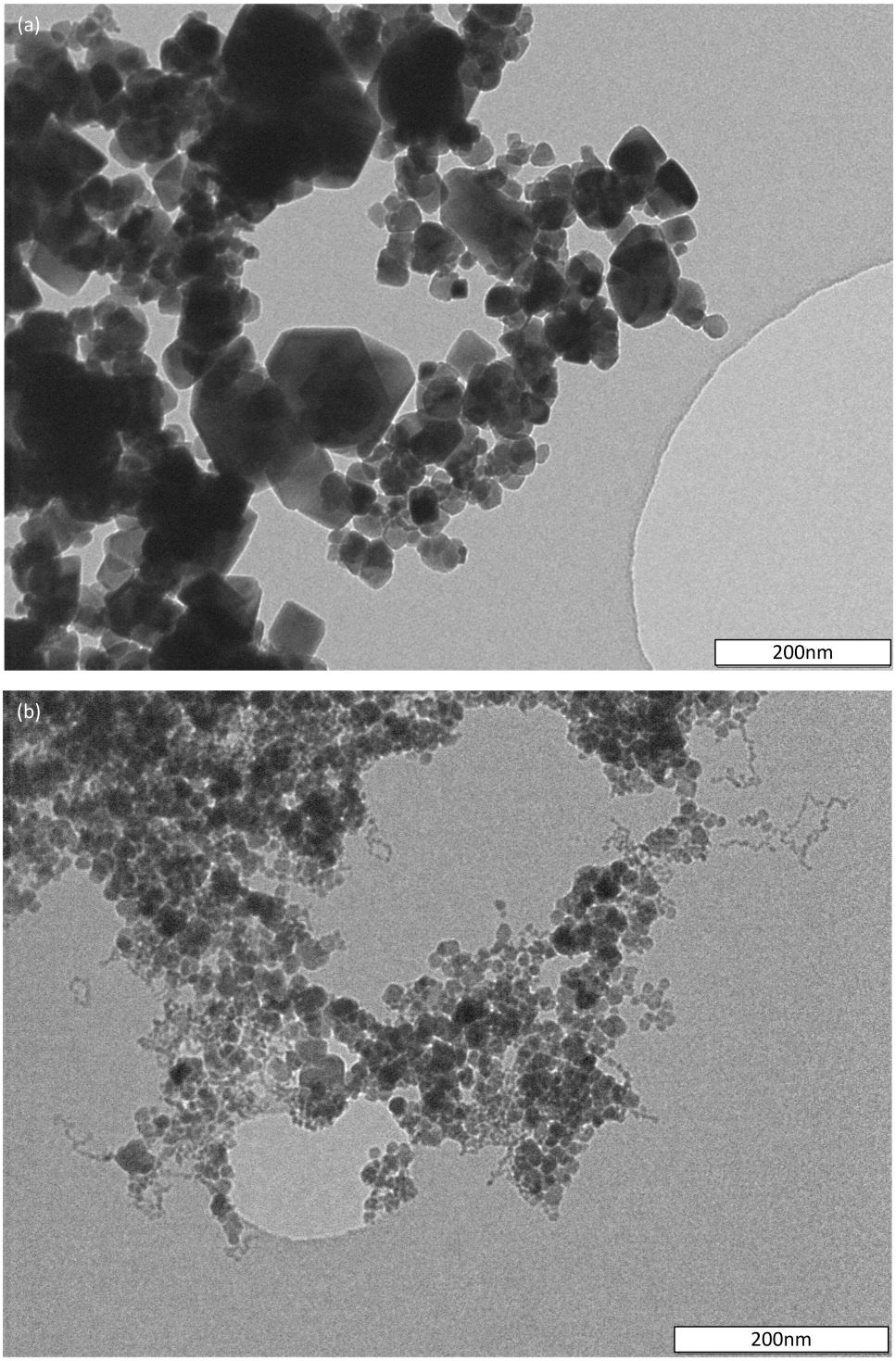


Figure 4.13: TEM images of Co_3O_4 nanoparticles obtained from (a)Preheated oxidant and (b) Non-preheated oxidant scenario

rer equation as 25.5 and 21.8 nm for the preheated and non-preheated oxidant configuration, respectively.

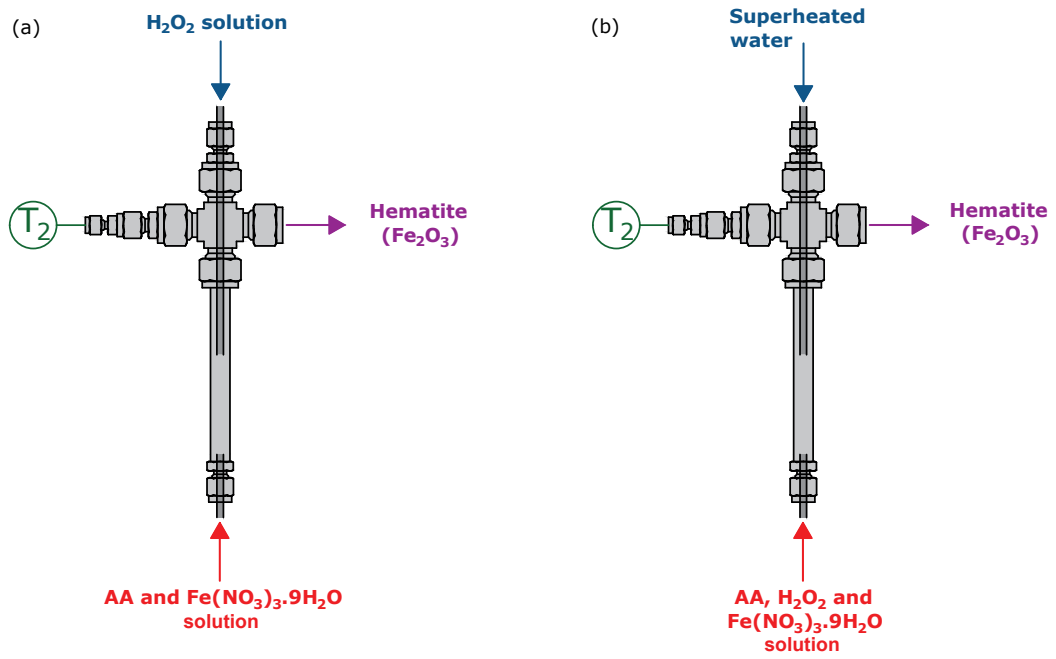


Figure 4.14: A schematic diagram showing the reaction arrangement for synthesis of Fe_2O_3. (a) Preheated oxidant and (b) Non-preheated oxidant scenario

Figure 4.17 shows the TEM images of Fe_2O_3 samples made at appears to show and precursor concentration of 20 mM. The morphology appears to be spherical with detectable edges. The average particle size using ImageJ software was 26.48 and 16.05 nm for the preheated and non-preheated oxidant configuration, respectively.

4.4.4 Chromium based particles

Nanostructured Cr_2O_3 have attracted considerable attention in variety of applications such as hydrogen sorption materials, catalysts, solar energy application, wear resistance materials, drug delivery, and dye and pigment (El-Sheikh et al.,

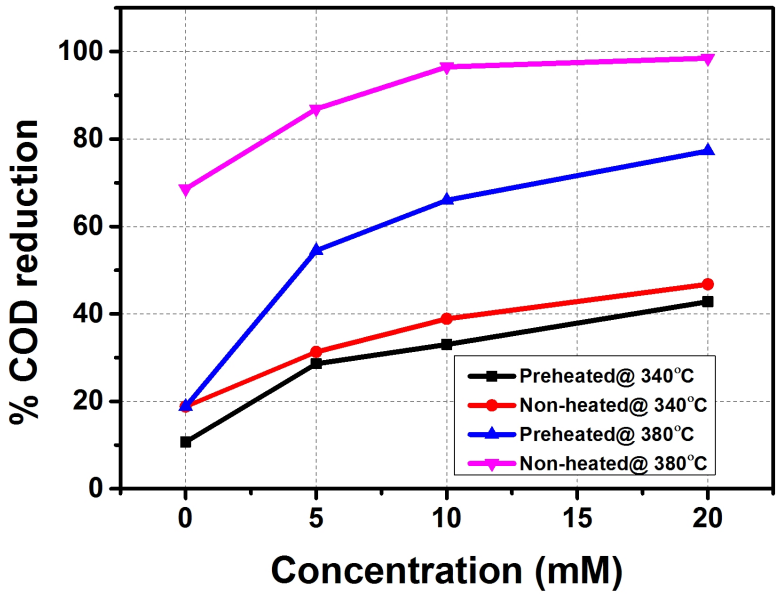


Figure 4.15: Catalytic effect of hematite nanoparticles on %COD removal at 380°C, 250bar, oxidant ratio of 1.5, and initial acrylic acid concentration of 10 mM

2009). In catalysis, both chromium oxide and supported chromium have been used in many reactions such as decomposition of ammonia (Choudhary et al., 2001), benzene and dichlorobenzene (Ding et al., 1995) and phenol (Ding et al., 1995). Hydrothermal technique has been developed to synthesize Cr_2O_3 nanoparticles (Pei et al., 2009).

Chromium based particles was produced in-situ during the oxidation of AA by mixing superheated H_2O_2 solution with chromium(III) nitrate nonahydrate ($Cr(NO_3)_3.9H_2O$) and AA solution as shown in Figure 4.18a or by mixing a supercritical water with a mixture of $Cr(NO_3)_3.9H_2O$, AA and H_2O_2 solution in counter current reactor as shown in Figure 4.18b. Figure 4.19 shows the catalytic effect of chromium based particles on COD removal compared to the catalyst free reactions at both sub and supercritical temperatures. Among all tested metal oxides, chromium based particles appears to show the most significant improvement

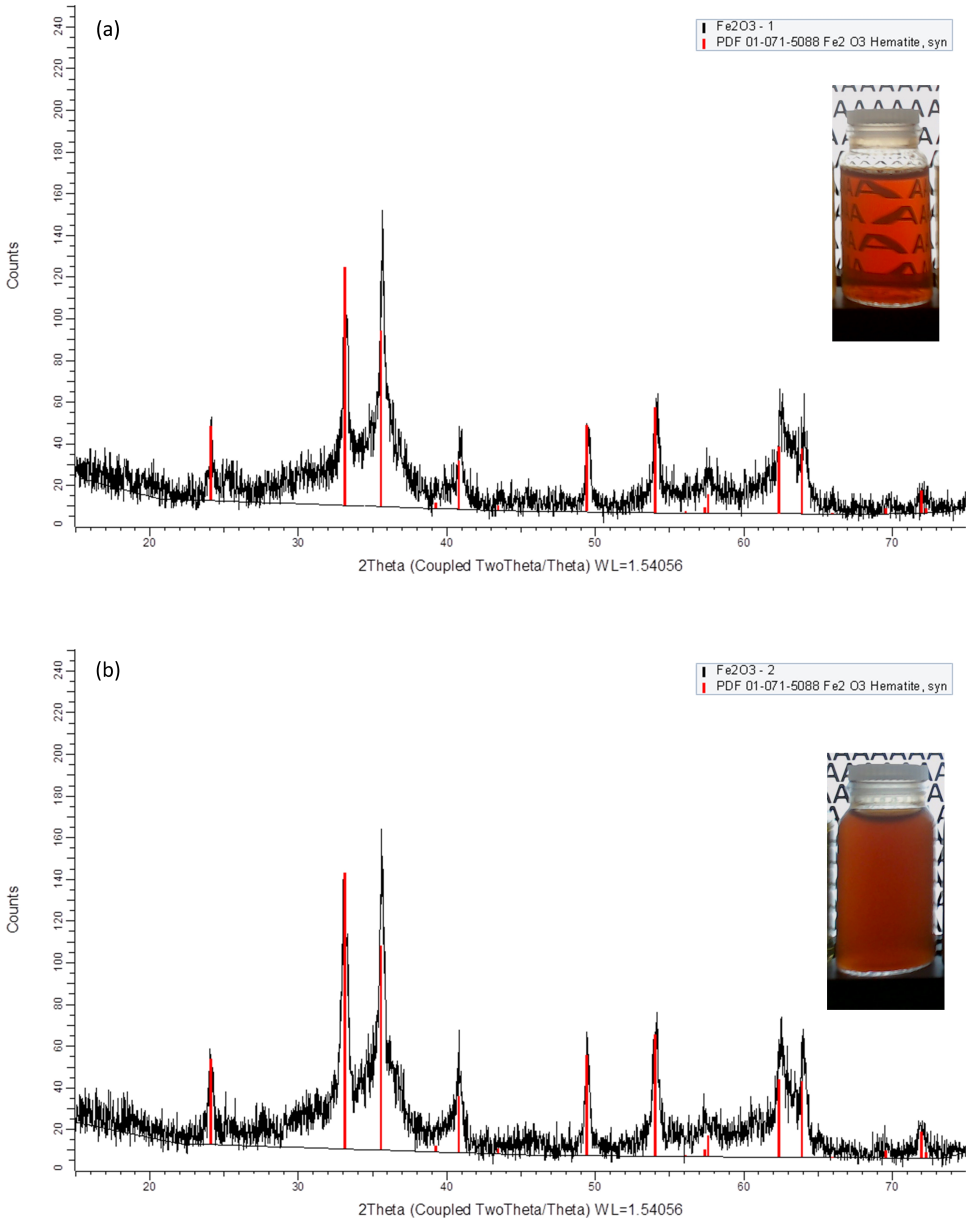


Figure 4.16: XRD patterns of hematite nanoparticles obtained obtained at 380°C, 250 *bar*, oxidant ratio of 1.5 and 20 *mM* of metal salt concentration. The red lines at the bottom are the expected peak positions for Co_3O_4 (PDF 01-071-5088). (a) Preheated oxidant and (b) Non-preheated oxidant scenario.

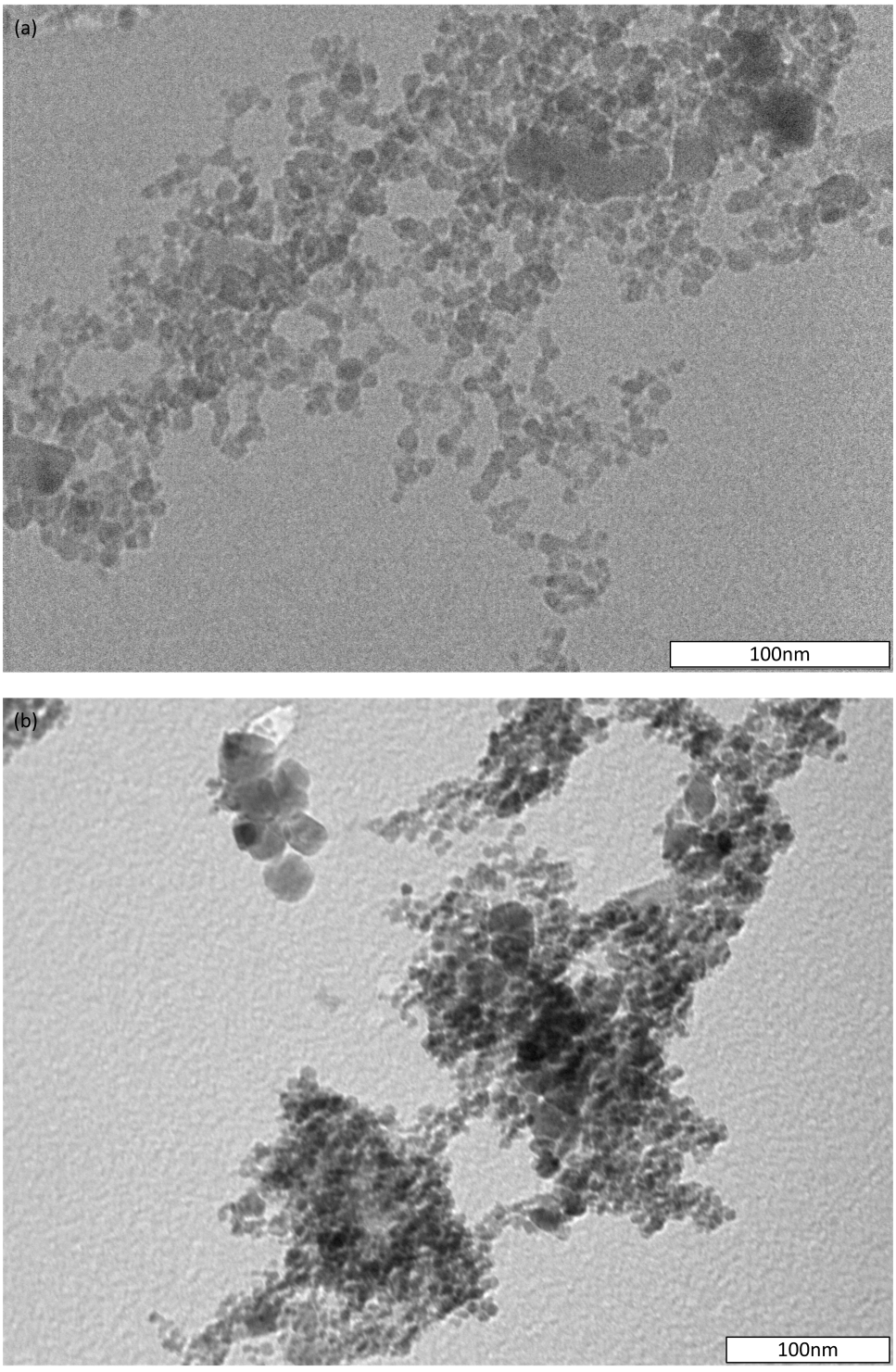


Figure 4.17: TEM images of Fe_2O_3 nanoparticles obtained from (a)Preheated oxidant and (b) Non-preheated oxidant scenario

in COD reduction at sub and supercritical temperatures, with both the preheated and non-preheated scenarios. Almost complete reduction of the organic content can be obtained at 380°C in both oxidant delivery arrangements. It was reported that oxide of Cr is more active single metal oxide catalyst than oxides of Mn, Fe, Co Ti and Cu for complete oxidation for variety of oxidation reactions (Ferrandon, 2001).

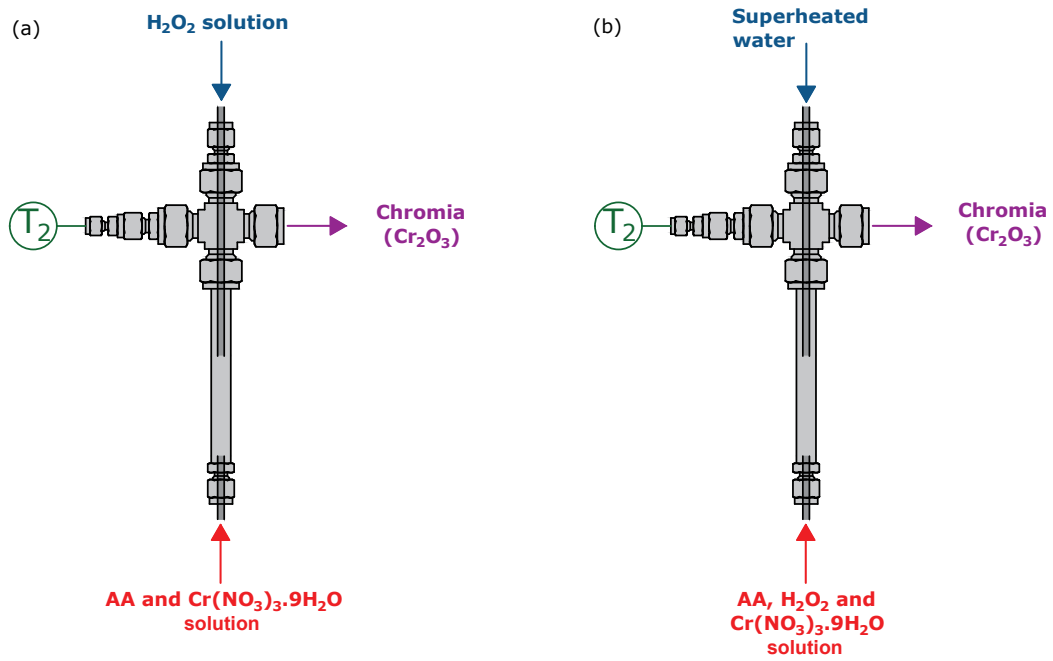


Figure 4.18: A schematic diagram showing the reaction arrangement for synthesis of chromium based particles. (a) Preheated oxidant and (b) Non-preheated oxidant scenario

The collected samples from catalytic SCWO with chromium based particles were transparent green, when tested with a laser pointer, showed a positive beam path which normally indicates the presence of nanoparticles (see Figure 4.20). However, the XRD patterns in Figure 4.21 show no crystalline or amorphous phase of chromium oxide. TEM analysis shown in Figure 4.22, combined with ImageJ software of chromium based particles showed very small nanoparticles

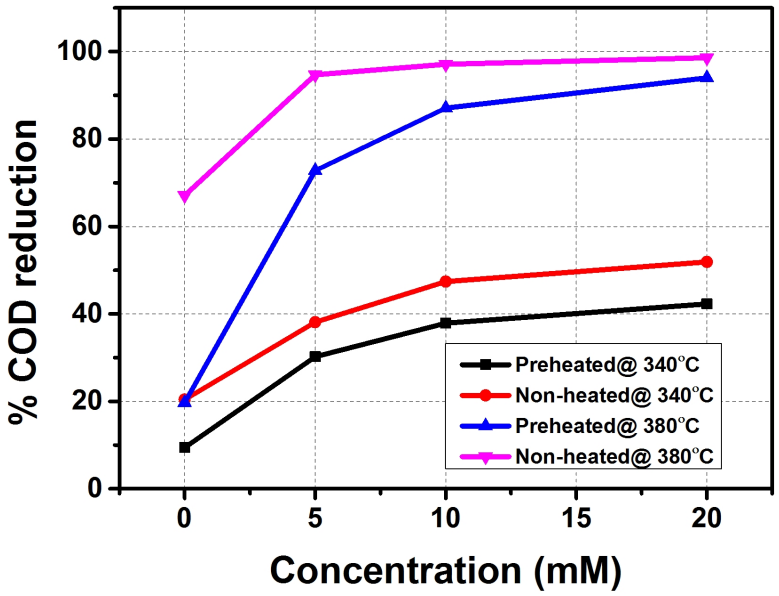


Figure 4.19: Catalytic effect of chromium based nanoparticles on %COD removal at 380°C, 250 *bar*, oxidant ratio of 1.5, and initial acrylic acid concentration of 10 *mM*

of 4.99 and 5.96 *nm* for the preheated and non-preheated oxidant scenario, respectively and that is one the most important factors that increase the catalytic activity of metal nanoparticles. Cr_2O_3 has been synthesised hydrothermally at milder conditions i.e. 180°C in batch, but only in the presence of urea (Rajagopal et al., 2016), so it is more likely that these particles observed using TEM were either CrOOH or $Cr(OH)_3$ particles. There are other papers to support the assumption that this greenish suspension is the Cr equivalent of boehmite (AlOOH). Most researchers conclude that a minimum of 450°C is required to convert the CrOOH to Cr_2O_3 (Gibot and Vidal, 2010; Pardo et al., 2017) which is higher than the experiments in this work. However, the CrOOH clearly provided a very high activity in AA decomposition.

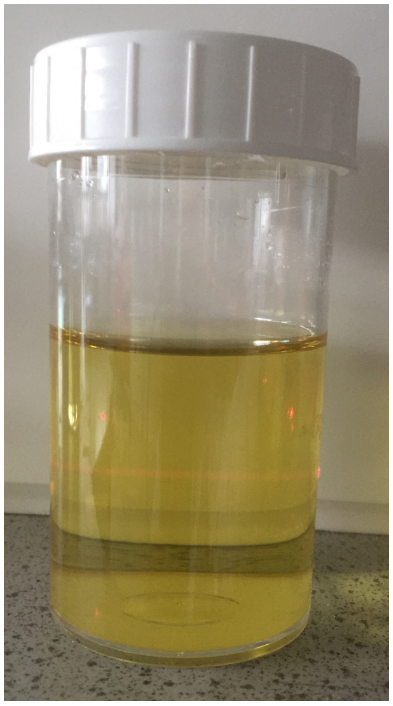


Figure 4.20: Photo showing a beam path of laser light passing through the chromium based particles sample- indicative of particles being present in sample.

4.4.5 Mixed catalyst

Reports in literature claim some combinations of metal oxides have high catalytic performance as compared to single components (Ferrandon, 2001). Dong et al. (2015) found that supported $Mn_2O_3/Ti-Al$ oxide composite catalyst has more activity for SCWO of p-nitrophenol than non-supported catalyst MnO_2 or Mn_2O_3. A combine catalyst containing $MnO_2/Al_2O_3/CuO$ was found to perform better in SCWO of terephthalic acid than single $\gamma-Al_2O_3$ (Park et al., 2003). Therefore, there are other interesting possibilities with the combination of catalysts.

The catalytic activity of the resultant metal oxide nanoparticles, was ranked in the following order: $CrOOH>Fe_2O_3>Co_3O_4>TiO_2$. Although the high activity of CrOOH in decomposition of AA, the target was to synthesis Cr_2O_3. Therefore, chromium based particles have been excluded. TiO_2 appeared to have relatively

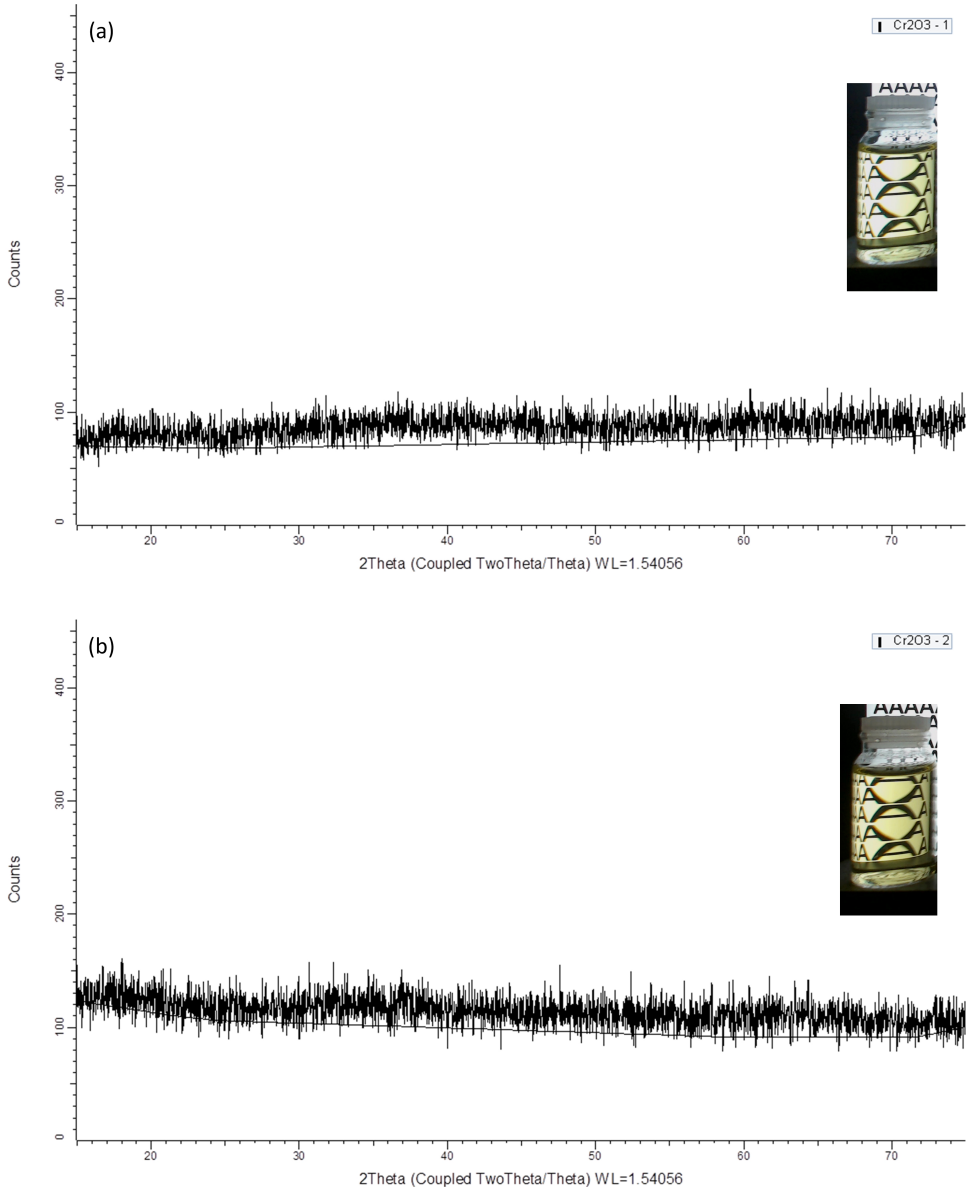


Figure 4.21: XRD of chromium based nanoparticles obtained at 380°C, 250 bar, oxidant ratio of 1.5 and 20 mM of metal salt concentration. (a) Preheated oxidant and (b) Non-preheated oxidant scenario.

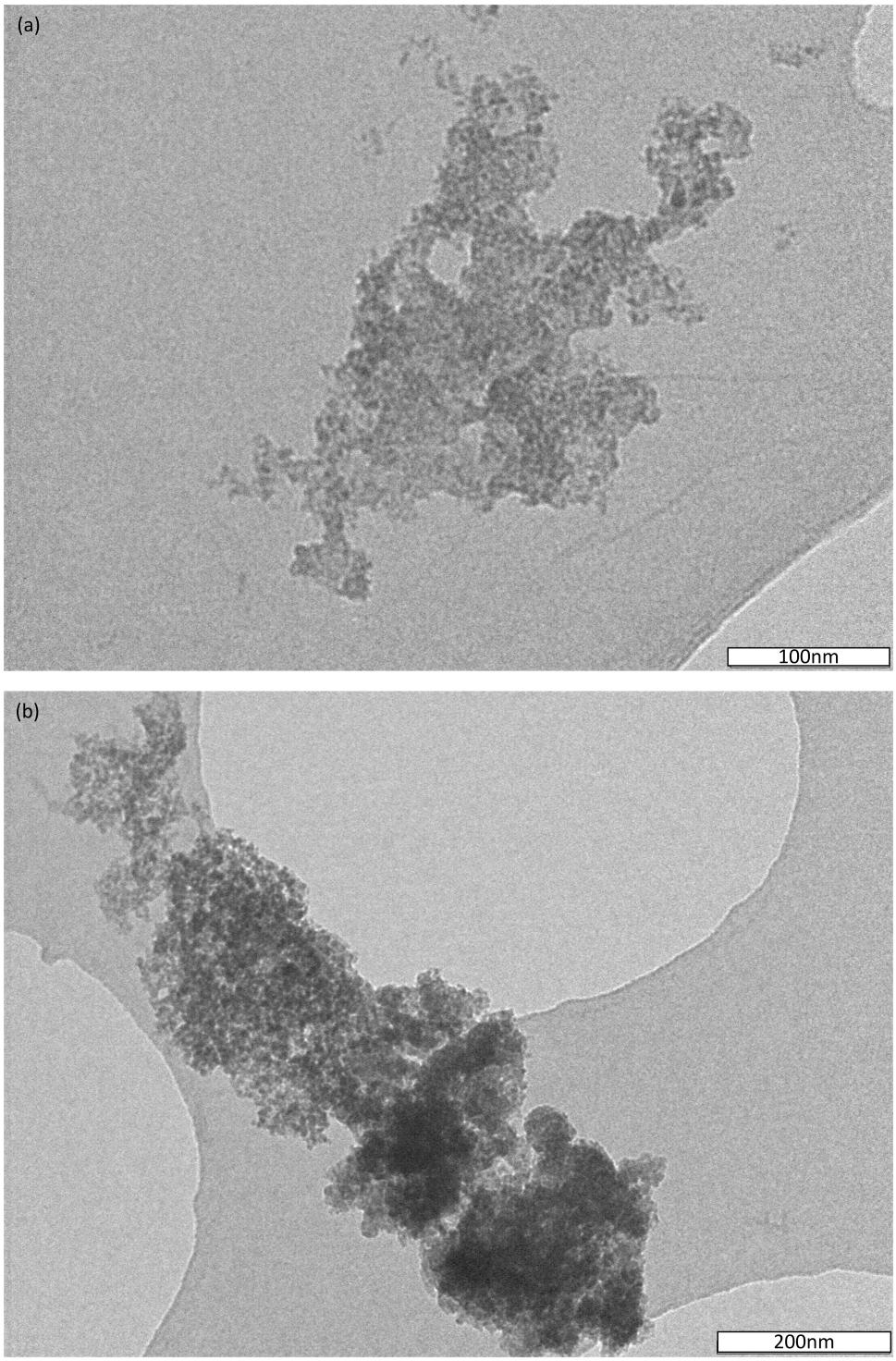


Figure 4.22: TEM images of chromium based nanoparticles obtained from (a)Preheated oxidant and (b) Non-preheated oxidant scenario

low catalytic affect. Hence, its combination with Fe_2O_3 could enhanced the final catalytic performance on organic material decomposition.

The experimental set up for for the preheated and non-preheated oxidant scenarios are given in Figure 4.23. Metal salt solutions of TiOS and $Fe(NO_3)_3.9H_2O$ were mixed in ratio of (1:1) in molar basis. The catalytic activity of mixed catalyst are shown in Figure 4.24. The catalytic performance of single TiO_2 enhanced by adding Fe_2O_3. %COD reduction was increased from 73.05 with single TiO_2 to 83.1 with mixed catalyst of TiO_2 and Fe_2O_3 in supercritical non-preheated oxidant configuration.

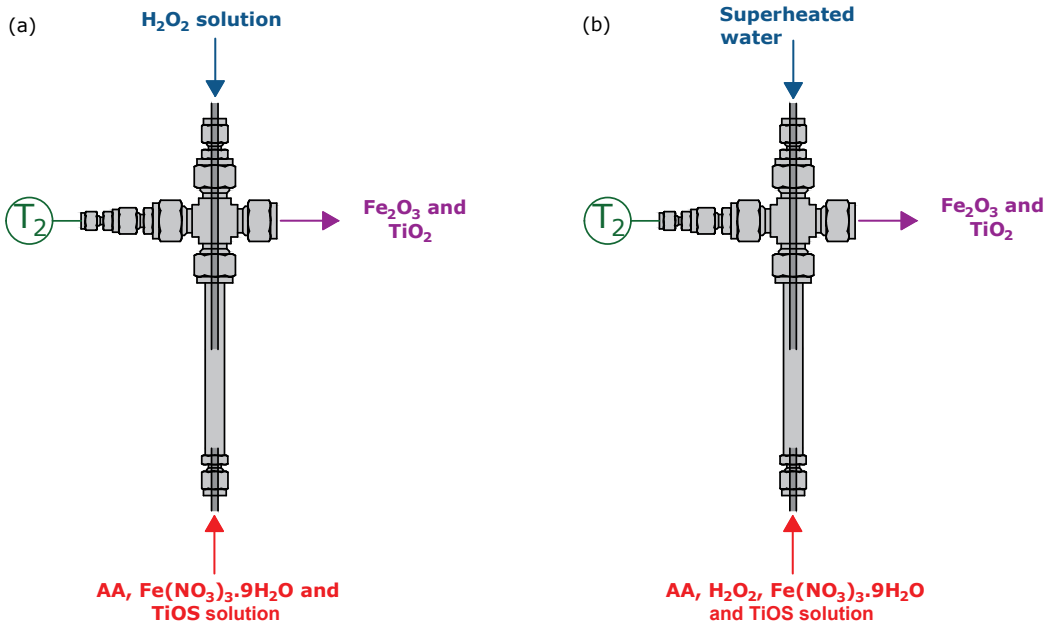


Figure 4.23: A schematic diagram showing the reaction arrangement for synthesis of TiO_2 and Fe_2O_3. (a) Preheated oxidant and (b) Non-preheated oxidant scenario

Another advantage of mixed catalyst is that the combination of TiO_2 with Fe_2O_3 enhanced the final settling rate in the effluent. In preheated oxidant scenario, Hematite, when on its own, was relatively stable in the effluent which would present practical issues with scale up of the process. Figure 4.25 shows the drop

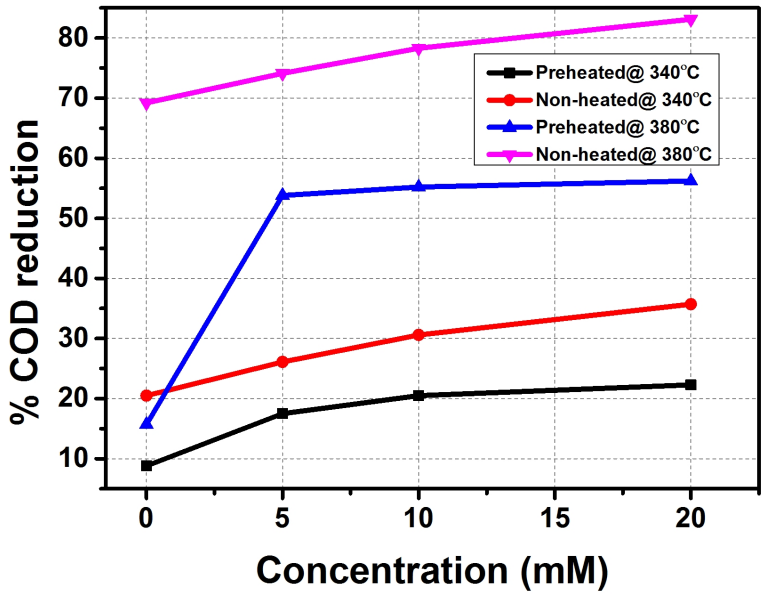


Figure 4.24: Catalytic effect of mixed catalyst of TiO_2 and Fe_2O_3 nanoparticles on %COD removal at 380°C, 250 *bar*, oxidant ratio of 1.5, and initial acrylic acid concentration of 10 mM

test of samples of hematite and mixed catalyst at concentrations of (5, 10, and 20 mM) for 24 hours.

TEM images of the mixed nanocatalyst are given in Figure 4.26. The morphology appears to be combination of spherical and rod with detectable edges. The particle size using ImageJ software were found to be 13.04 and 14.62 nm for the preheated and non-preheated oxidant configuration, respectively.

For all nanocatalysts, The catalytic preheated oxidant configuration showed highest activity when operating at supercritical temperatures. As discussed previously, O_2 is a weak oxidant at moderate temperatures (e.g. < 400°C), so the addition of catalyst clearly improves the overall reduction rate. For the catalytic preheated oxidation, the oxidation is most probably initiated by the adsorption of reactant species on the catalyst surface. Oxygen adsorbed at the catalyst surface



Figure 4.25: The effect of adding TiO_2 on the settlement of Fe_2O_3 for effluent taken from supercritical preheated oxidant experiments

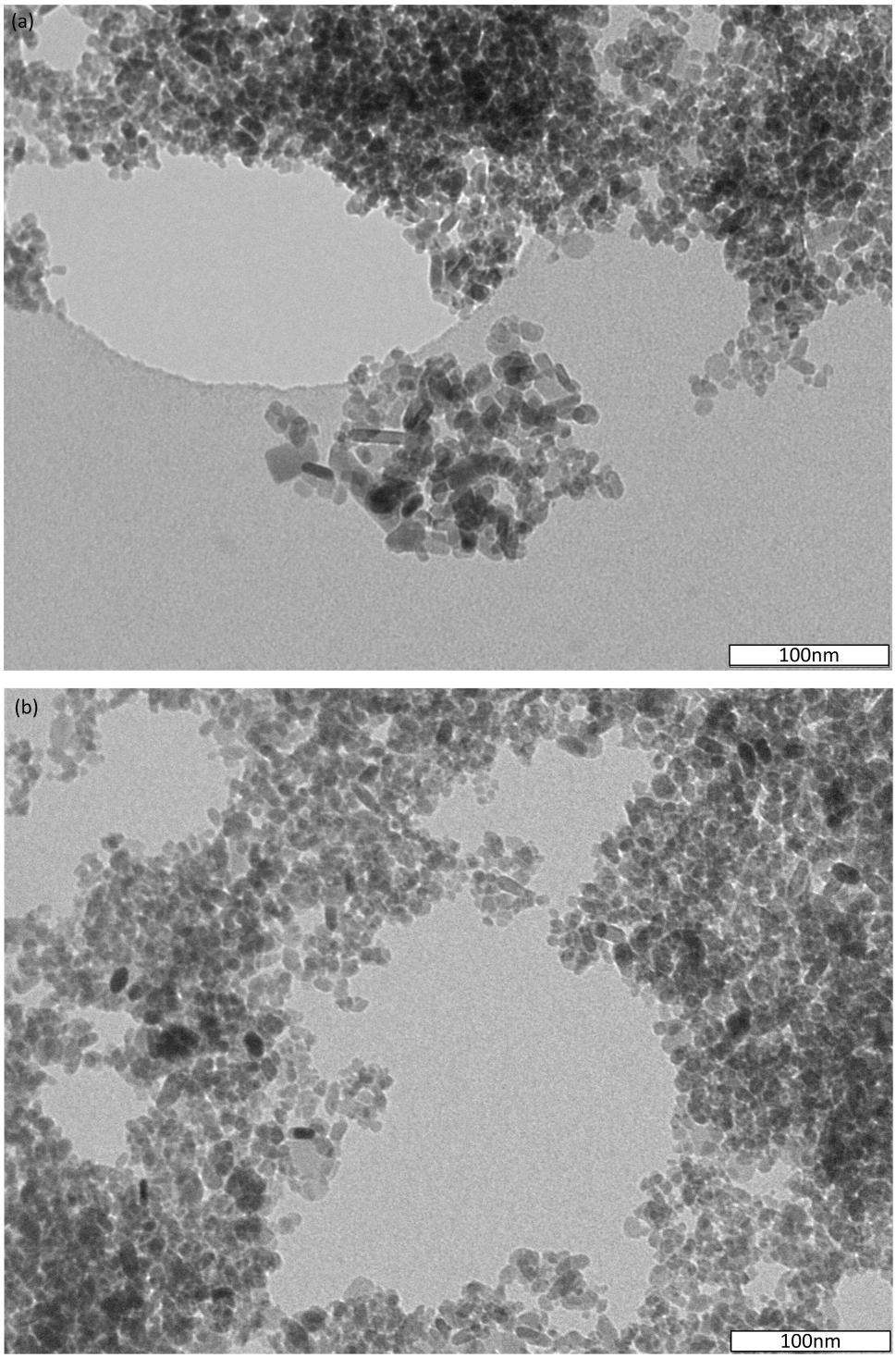


Figure 4.26: TEM images of mixed catalyst of TiO_2 and Fe_2O_3 nanoparticles obtained from (a)Preheated oxidant and (b) Non-preheated oxidant scenario

is present mainly as the superoxide ion O^{-2} which may decompose further with the formation of the O^{-} ion (Krajnc and Levec, 1997). The radical ion forms O^{-} and O^{-2} which possess even higher oxidative activities than $HO^{\bullet}$ radicals (Wang et al., 2012). As such, this combined approach with catalysts in-situ presents a new approach to enhanced COD reduction although more work is necessary to understand the kinetic mechanisms at work. Homogeneous and heterogeneous catalysis reactions may well create the synergetic effects where the metal salts and subsequent metal oxide products both act as catalysts during the destruction of acrylic acid at supercritical conditions.

4.5 Initial economic considerations

Work in this section was achieved as a research collaboration between the researcher and the Department of Chemical Engineering, University of Valladolid, Spain.

An initial simulation and economic study was carried out on the combined SCWO/SCWHS process to better understand the advantages that might be presented at industrial scale. These studies were based on an actual industrial scale plant, which was designed and constructed during the SHYMAN project (Stieberova et al., 2017). An Aspen Plus® simulation used the flow rates of 3:1.5 m^3h^{-1} (downflow of supercritical water: upflow of acrylic acid in water) and the reaction pressure at 25.0 MPa.

Three different scenarios are modelled using Aspen Plus® software to achieve a COD removal of 98%: pre-heated, non-preheated and catalytic non-preheated oxidant configuration (using $Fe(NO_3)_3 \cdot {}_9H_2O$). Whilst CrOOH was the better cat-

alyst, the iron nitrate precursor is significantly cheaper and Fe_2O_3 is more environmentally benign (Murugesan et al., 2018).

For calculating the necessary temperature to get 98% of conversion, the experimental results shown in Figure 4.2 were extrapolated with polynomial equations and the temperatures for the preheated and non-preheated oxidant process found to be 498°C and 401°C, respectively. These conditions were chosen because the catalytic non-preheated oxidant configuration, already showed that a 98% reduction of COD was possible at 380°C (see Figure 4.15).

Figure 4.27 shows the main simulated process using Aspen Plus® software. In preheated oxidant configuration, the organic solution is fed in via stream 1 and enters at the bottom end of the reactor via stream 2. The oxidant solution is introduced in the reactor by stream 3 at the top end. This stream is heated in a heat exchanger followed by a gas-fired boiler using natural gas (NG). Regarding non-preheated oxidant configuration the flow diagram is the same but in this case, the oxidant is fed by stream 1 and stream 3 consists of process water. Finally, using catalytic configuration, the metal salt is supplied from stream 1.

With the objective of studying the economic feasibility of each configuration in the industrial plant, the energy requirements are compared in Figure 4.28. The capital expenditure (CAPEX) is effectively the same in three configurations with the same number of pumps, heaters etc and the assumption is that none of the configurations will cause specific long term issues with operation. From Figure 4.28, the electricity requirement by the pumps are essentially equivalent in all three configurations. However, the natural gas requirement is dependent on the temperature required to achieve 98% conversion. Therefore, in preheated

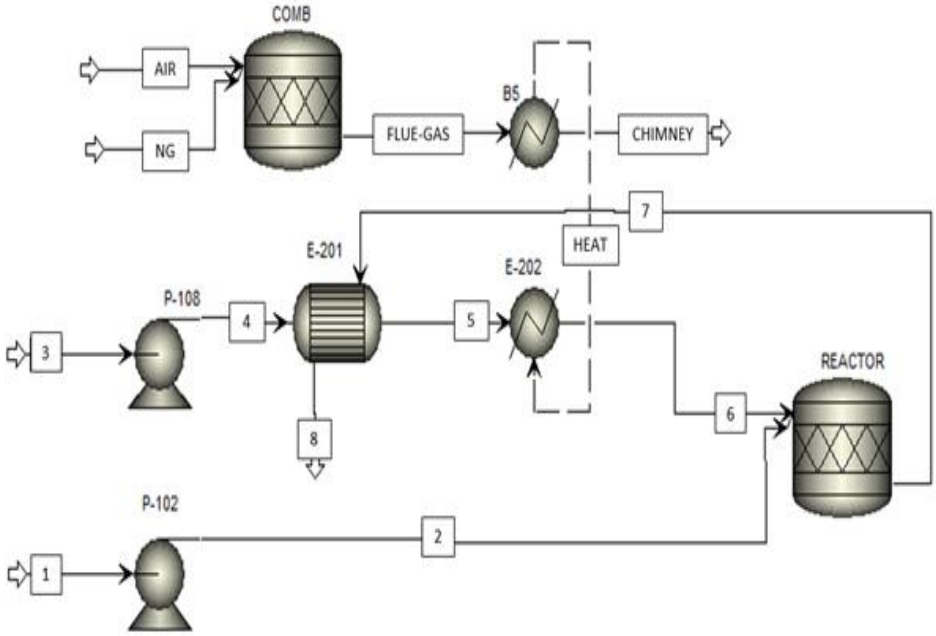


Figure 4.27: Flow diagram of the industrial scale process (Aspen Plus® software)

oxidant configuration the natural gas requirement is the highest, at about 1160 kW.

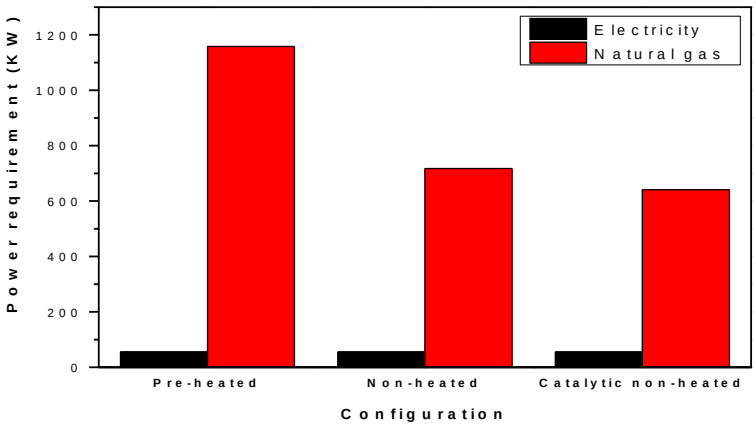


Figure 4.28: Energy calculation for energy demand for the three scenarios

Water costs £1.92/m^3, and hydrogen peroxide is £0.32/kg. In the United Kingdom electricity is costed at £0.12/kW and natural gas is £0.055/kW. Thus, the costs calculated for preheated and non-preheated oxidant configuration on



an industrial scale plant are about £85/h and £61/h, respectively, as shown in Tab 4.4. With the catalytic configuration, it must be noted the iron nitrate precursor price is £0.84/kg (from molbase.com) bringing the total cost to £67/h. This is more than the non-preheated case. However, in this case, Fe_2O_3 nanoparticles are also produced. Economic calculations should therefore take into account the value of this nanomaterial which, at almost 2.0 kgh^{-1} and a relatively conservative value of £30/kg would certainly negate any basic operating expenditure.

Table 4.4: Cost of preheated, non-preheated and catalytic non-preheated oxidant configurations

Preheated oxidant configuration						
	H_2O(l/h)	H_2O_2(kg/h)	Natural Gas (kW)	Metal Salt (kg/h)	Electricity(kW)	Total cost(£/h)
Flow	3807	22.95	1158.0	0	55.6	85.01
Cost(£/h)	7.31	7.34	63.7	0	6.7	
Total cost (£/kg contaminated water)				0.067		
Non-preheated oxidant configuration						
	H_2O(l/h)	H_2O_2(kg/h)	Natural Gas (kW)	Metal Salt (kg/h)	Electricity(kW)	Total cost(£/h)
Flow	3807	22.95	717.4	0	55.6	60.78
Cost(£/h)	7.31	7.34	39.5	0	6.7	
Total cost (£/kg contaminated water)				0.048		
Catalytic non-preheated oxidant configuration						
	H_2O(l/h)	H_2O_2(kg/h)	Natural Gas (kW)	Metal Salt (kg/h)	Electricity(kW)	Total cost(£/h)
Flow	3803.39	22.95	640.93	12.12	55.59	66.80
Cost(£/h)	7.30	7.34	35.25	10.23	6.67	
Total cost (£/kg contaminated water)				0.053		



4.6 Conclusions

The counter current reactor was designed to produce short residence times and rapid mixing of two different fluids and (whilst most SCWO reactors use substantial residence times and high temperatures) COD reduction was shown to be relatively high (up to 80%).

The oxidant (H_2O_2) delivery method was found to have a large impact on removal efficiency and reaction temperature was also a key variable. At 380°C and 25.0 MPa, the non-preheated oxidant configuration with a residence time of 0.75 *sec* resulted in an 80% COD removal as opposed to a 15% COD removal with the equivalent preheated oxidant experiment. The difference between the efficiency for the two methods is linked to the availability of $HO^{\bullet}$ radicals and/or molecular oxygen, respectively. The addition of small amounts of metal salts in the upflow also led to a reduction in COD levels. These precursors created metal oxide or oxyhydroxide nanoparticles in situ which enhanced the oxidation efficiency. Fe_2O_3 and CrOOH were the most significant catalysts, increasing COD reduction to more than 98% at a temperature of 380°C and a residence time of less than 1 *sec*.

From a basic OPEX analysis, the best option is the non-preheated catalytic configuration because the temperatures required to achieve high levels of COD reduction were much lower than the other configurations. The basic economic impact of catalyst addition was also assessed to be favourable. The secondary value of any nano-catalyst by-product could potentially outweigh any OPEX costs for the SCWO process itself. There is also a clear opportunity to increase the

metal precursor concentration, which would not impact on removal rates of the contaminant but would increase the quantity of the nano by-product, further increasing the financial viability of the combined process.

5

CATALYTIC SUPERCRITICAL WATER OXIDATION OF PHENOL IN COUNTER CURRENT REACTOR

Highlights

- A combined oxidation/ synthesis process for phenol removal was firstly reported.
- Lower temperature requirements for complete removal of contaminant compared to other research work.
- Oxidant delivery method greatly enhanced phenol and COD removal.

5.1 Introduction

As described in Chapter one, different reactor configurations had been utilised in oxidation of variety of model and industrial waste. These reactors are generally expensive and heavy due to the needs of a considerable thickness reactor wall and expensive material (such as nickel alloys) to make it possible to resist the high temperatures and pressures ($>$ 500°C and 25 Mpa) present inside the reactor. The relative merits of counter current mixing reactor geometry have not yet been identified to use for continuous supercritical water oxidation process. Therefore,

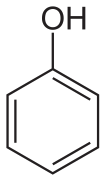
an analysis of the SCWO of different model compounds would be valuable to the field. Furthermore, an analysis of the SCWO of such compounds in differing oxidant delivery configurations with in-situ catalyst formation would be of even greater novelty, being that such research was even less common.

Owing to the capability of the combined process of supercritical water oxidation and in-situ catalyst formation in destruction of acrylic acid, this Chapter was devoted to study the destruction of phenol.

5.2 Phenol

Phenol and substituted phenols are frequently present in the effluent of major processing and refining plants. It is one of the most common organic pollutant in wastewater, because it is extremely toxic even at low concentrations. Phenol is also relevant in the field of environmental research, because it has been chosen frequently as a model pollutant and many data are available on its removal and destruction in particular with respect to wastewater treatments. This section presents a study of the destruction of phenol by a combined process of SCWO and SCWHS. Some chemical and physical properties of phenol are reported in Table 5.1. As an aromatic organic compound, phenol require operating conditions ranging from $400 - 650$°C and 25-35 MPa to be efficiently removed by non-catalytic SCWO (Thornton and Savage, 1990). It is believed that in the presence of a catalyst these conditions can be lowered. The range of the concentration of phenol in wastewater of various industries are given in Table 5.2 (Busca et al., 2008). Phenol-containing wastewater may not be disposed into open water without treatment because of its toxicity. Toxic levels usually range between the

Table 5.1: Properties of phenol.

Structure	
Formula	C_6H_6O
Molar mass	94.11 $gmol^{-1}$
Boiling point	181.7°C
Density	1.07 gcm^{-3}
Solubility in water	8.3 $g100mL^{-1}$

concentrations of 10-24 mgL^{-1} for human. Internally, phenol affects the liver, kidneys, lungs, and vascular system (Kulkarni and Kaware, 2013).

The stoichiometric reaction that represents the complete oxidation of phenol is given by

$$C_6H_6O + 7O_2 \longrightarrow 6CO_2 + 3H_2O \tag{5.1}$$

The efficiency of the process is given in terms of the remaining phenol compound and COD according to

$$\%COD\,reduction = \frac{COD_{initial} - COD_{\circ}}{COD_{initial}} \times 100 \tag{5.2}$$

$$\%Phenol\,reduction = \frac{Phenol_{initial} - Phenol_{\circ}}{Phenol_{initial}} \times 100 \tag{5.3}$$

initial and $\circ$ subscripts are the initial and final concentrations of COD and phe-

Table 5.2: The range of concentration of phenol in wastewater of different industries.

Industry	Phenol concentration, mgL^{-1}
Refineries	6-500
Coking operations	28-3900
Coal processing	9-6800
Petrochemicals	2.8-1220
Pharmaceutical	0.1-1600
Pulp and paper	0.1-1600

nol.

5.2.1 Initial experiments and configurations assessment

Initials trails have been made to assess whether or not the reactor configuration was suitable for complete degradation of organic content of phenol in supercritical water in terms of oxidative efficiency, e.g., a COD reduction approaching 99.99%. Both uncatalysed and catalysed reactions for preheated and non-preheated oxidant configurations were performed. The experimental set up for the preheated and non-preheated oxidant configurations is given in Figure 5.1. The catalytic reactions were obtained by injecting iron nitrate to the reactor as an up flow along with phenol solution. The initial experiments were conducted under the conditions shown in Table 5.3

The reaction temperature was set to excess the critical point of water which are governed by heater limitation. A short residence time was chosen because it

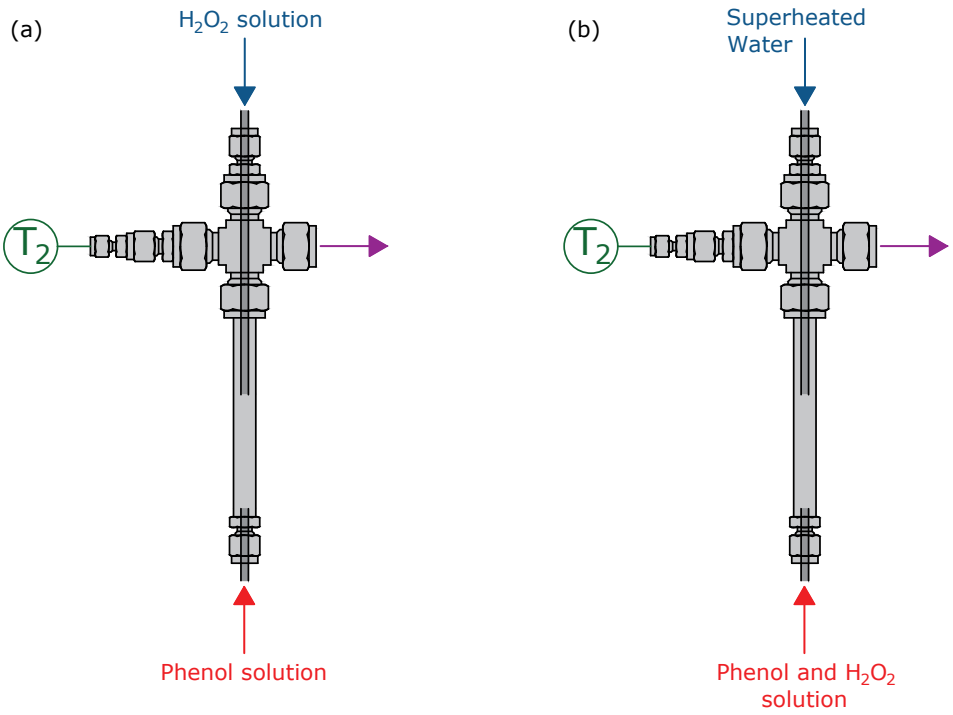


Figure 5.1: Experimental set up for phenol oxidation. (a) preheated oxidant scenario and (b) Non-preheated oxidant scenario

Table 5.3: Initial experimental conditions for phenol oxidation.

Temperature, °C	Pressure, Mpa	Feed COD, gL^{-1}	oxidant Ratio	Residence Time, s	Catalyst, mM
380	25	6.6-7.4	1.5	0.75	20

was shown to have a very little effect on the oxidation of acrylic acid. Oxidant ratio was taken to be 1.5 because work by other researchers show there was no apparent effect of the amount of excess oxygen so long as it was over 10% (Pérez et al., 2004). The results of the preliminary experiments in terms of the removal of phenol and COD are shown in Table 5.4. The GC-MS analysis of phenol samples treated by different configurations are given in Appendix B.

Table 5.4: Preliminary test results for phenol oxidation.

Scenario	%Phenol removal	%COD removal
Preheated	67.4	26
Catalysed preheated	99.999	34
Non-preheated	99.999	93.5
Catalysed non-preheated	99.999	99.7

Although a high phenol conversion was obtained in catalytic reaction, the COD removal of uncatalyed and catalysed preheated oxidant scenarios at excess oxygen were 26 and 34% respectively. Therefore, it was decided that these configurations are not suitable for the complete oxidation of phenol. Consequently all subsequent experiments were conducted using the uncatalysed and catalysed non-preheated oxidant configurations.

5.2.2 Non-preheated oxidant configuration

The behaviour of the reaction under the presence of different oxidant concentration was studied by varying the oxidant supplied from an oxidant ratio of

(0.0-2.0). The phenol was supplied at a constant concentration of 5 mM at reaction condition which correspond to (112.2 mM or COD of 6.6-7.4 at the feed stock). The operating conditions were maintained at 380°C, 25.0MPa and a residence time of 0.75 *sec*. The results of the effect of oxidant concentration in the non-preheated oxidant configuration for phenol and COD are given in Figure 5.2. The hydrolysis reaction has no effect on phenol degradation, however, when the concentration of oxidant increased to stoichiometric amount, a complete elimination of phenol was obtained. COD reduction increased approximately of 94%, at oxidant ratio of 2.0, which showed a strong dependence of the reaction on the $HO^{\bullet}$ concentration. At highest oxidant ratio, the close values of phenol and COD removal indicate that the free radicals $HO^{\bullet}$ reduced the formation of undesirable intermediates. The total ion current traces (TIC) for phenol samples treated at oxidant ratio of 1.0 and 1.5 are given in Figure 5.3.

Compare to other research works on the oxidation of phenol in supercritical water, the non-preheated oxidant configuration exhibits a high reduction of organic content at relatively mild temperature and short reaction time. This may attribute to the features of counter current mixing reactor which offer an immediate and rapid heating to the organic compounds and oxidant. This fast heating of the organic compounds could avoid the formation of organic pyrolysis intermediates which are more difficult to oxidize in the reaction zone (Kronholm et al., 2000). The operating conditions and corresponding phenol conversions from the literature are given in Table 5.5.

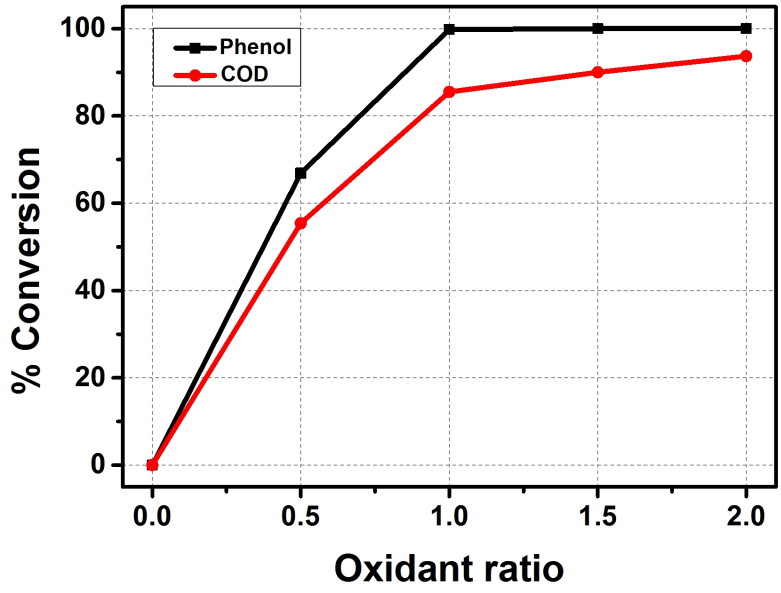


Figure 5.2: The effect oxidant ratio on phenol and COD removal. All experiments were carried out at 380°C, 250bar, a residence time of 0.75 sec and an initial phenol concentration of 5 mM.

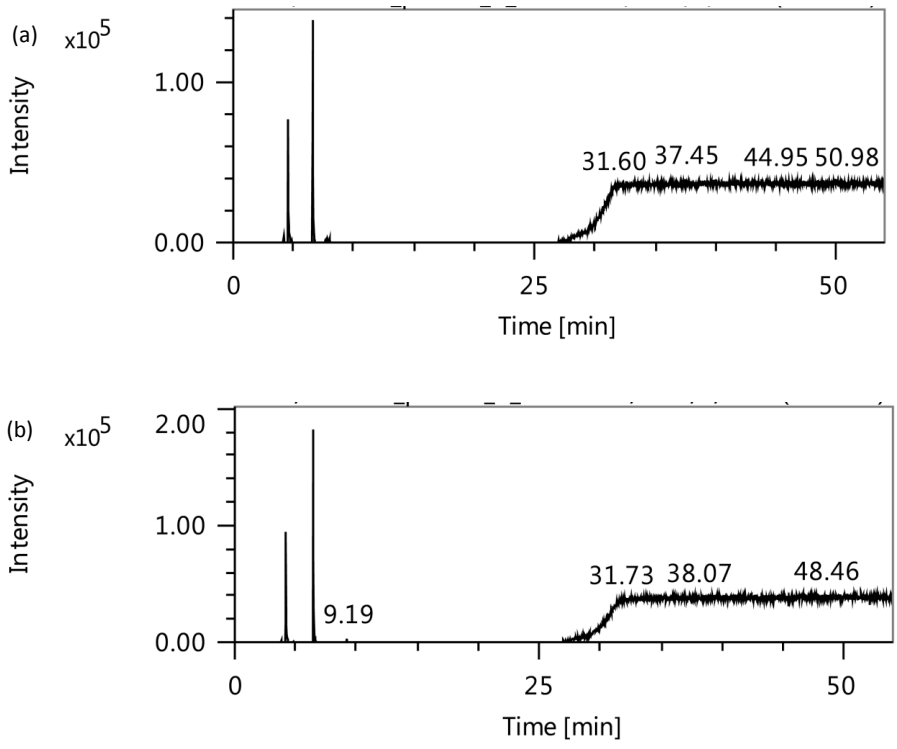


Figure 5.3: Total ion current traces (TIC) for phenol samples treated non-preheated oxidant configuration at oxidant ratio of (a) 1.0 and (b) 1.5.

Table 5.5: Operational conditions and conversions for various phenol oxidation experiments.

Temperature, °C	Pressure, *Mpa*	Time, sec	Oxidant,	Oxidant Ratio	X_{phenol}, %	X_{TOC}, %	Ref
380	23.6	8.5	O_2	1.03	14.8	-	(Thornton and Savage, 1990)
420	28.1	300	O_2	3.63	94.0	-	(Thornton et al., 1991)
380	28.1	3.5	O_2	11	15.5	-	(Thornton and Savage, 1992)
390	28.0	12	Preheated H_2O_2	11	83.5	-	(Kronholm et al., 2000)
390	25.0	104	Air	4.8	71.0	-	(García Jarana et al., 2010)
500	25.0	14.9	Preheated H_2O_2	4	53.0	34.7	(Portela et al., 2001a)
420	25.7	58.3	O_2	1.3	97.7	85.8	(Pérez et al., 2004)
380	25.0	0.75	Non-heated H_2O_2	1.5	100.0	93.5 (COD)	This work

5.2.3 Catalytic non-preheated oxidant configuration

It has been demonstrated in Chapter 4, that organic content of acrylic acid can be completely eliminated by the action of in-situ formation of CrOOH and Fe_2O_3 nanocatalyst. However, the XRD patterns show no crystalline or amorphous phase of chromium oxide. Therefore, hematite was chosen as a nanocatalyst in the oxidation of phenol in supercritical water. Like the non-preheated oxidant configuration, the effect of oxidant ratio on the phenol and COD removal was investigated at 25 MPa, 380°C and $Fe(NO_3)_3.9H_2O$ concentration of 10 mM. At the absence of oxidant, the % elimination of phenol and COD was 67.4 and 29.8, respectively. By increasing the concentration of oxidant to stoichiometric amount, the reaction approaches completion for phenol and COD (see Figure 5.4). The effect of the oxidant on organic content removal becomes less important at a SR above 1. The findings of (Yu and Savage, 1999) also proved that increasing the concentration of oxygen in the catalytic reaction promoted the oxidation of phenol. In their study oxygen concentrations above the stoichiometric value were used and phenol oxidation improved at higher oxygen concentrations. Close values of phenol and COD removal were found during the experiments, this indicates that the catalyst reduced the production of undesirable intermediates. The total ion current traces (TIC) for phenol samples treated by catalytic oxidation are given in Figure 5.5. The COD results, together with those obtained by GC-MS, indicate that, under optimized conditions, only minor amounts of side products were formed; i.e., the oxidation was almost complete.

The effect of $Fe(NO_3)_3.9H_2O$ concentration on the removal of COD are shown

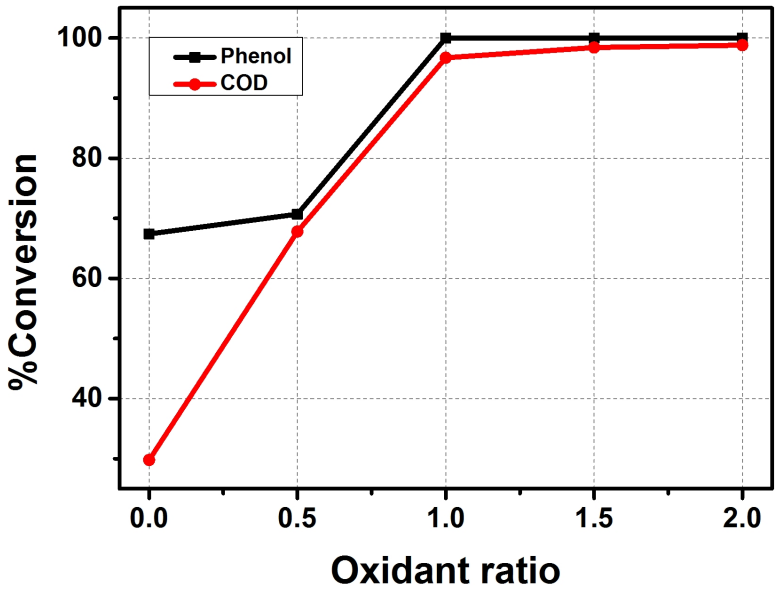


Figure 5.4: The effect oxidant ratio on phenol and COD removal. All experiments were carried out at 380°C, 250*bar*, a residence time of 0.75 *sec*, an initial phenol concentration of 5 mM and $Fe(NO_3)_3.9H_2O$ concentration of 10 mM.

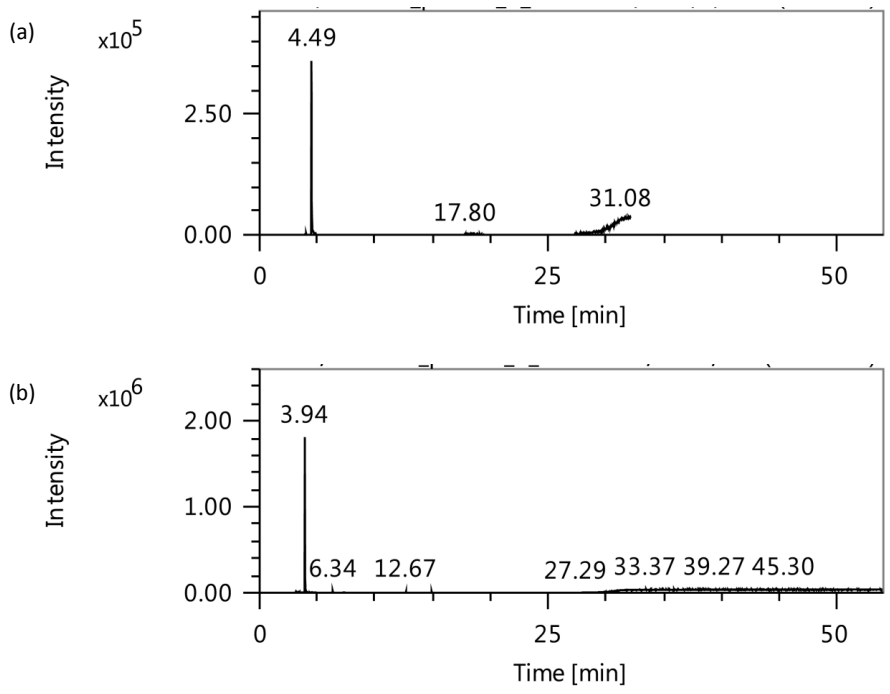


Figure 5.5: Total ion current traces (TIC) for phenol samples treated catalytic non-preheated oxidant configuration at oxidant ratio of (a) 1.0 and (b) 1.5.

in Figure 5.6. The operating pressure and temperature and phenol concentration were the same as for the evaluation of oxidant ratio gradients. The oxidant ratio was kept constant at 1.0. COD removal enhanced constantly with catalyst addition until the concentration of 20 mM. The addition of high amounts of catalyst did not appreciably affect the removal of the organic compound. Catalyst evidently can be used to accelerate the reaction, however its improvement is limited to a certain range of concentrations. When comparing the catalytic oxidation rates of phenol of various researchers (see Table 5.6) to those obtained in the presence of in-situ formed catalyst, a significant rate enhancement is observed in the latter case. A conversion greater than 99% is achieved in preheated and non-preheated oxidant scenarios in 1 order of magnitude shorter residence time compared to other catalytic oxidation works. Moreover, in the presence of the catalyst, a considerably smaller number of different organic acid species is formed, indicating that the catalyst is very effective in the ring-opening process (Krajnc and Levec, 1997). Consequently, higher pollutant destruction efficiency can be achieved at lower temperatures when employing a catalyst in the supercritical reactor system.

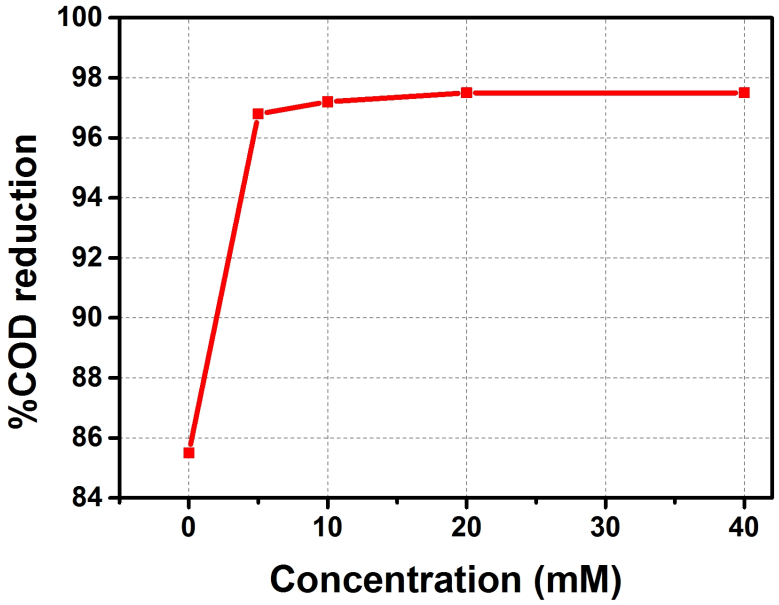


Figure 5.6: The effect in-situ formed catalyst on COD removal. All experiments were carried out at 380°C, 250 *bar*, a residence time of 0.75 *sec*, an initial phenol concentration of 5 mM and oxidant ratio of 1.0.

Table 5.6: Operational conditions and conversions for various phenol catalytic oxidation experiments.

Catalyst	Temperature, °C	Pressure, Mpa	Time, sec	Oxidant,	Oxidant Ratio	X_{phenol}, %	Ref
MnO_2	425	22.7	0.1	Preheated H_2O_2	-	88.0	(Tomita and Oshima, 2004)
TiO_2	380	25.3	8	Preheated H_2O_2	-	53.0	(Yu and Savage, 2000a)
V_2O_5	390	25.0	5.4	Air	4	99.5	(Ding et al., 1995)
$CuO/ZnO/Co_2O_3$	400	24.0	1.82	Preheated H_2O_2	-	90.0	(Krajnc and Levec, 1997)
Cr_2O_3–Al_2O_3	390	25.0	11.4	Air	4	99.5	(García Jarana et al., 2010)
In-situ formed Fe_2O_3	380	25.0	0.75	Preheated H_2O_2	1.5	100.0	This work
In-situ formed Fe_2O_3	380	25.0	0.75	Non-heated H_2O_2	1.5	100.0	This work

5.3 Conclusions

The uncatalysed and catalysed non-preheated oxidant configuration was chosen to perform the SCWO of phenol. Experiments were conducted at a variety of oxidant ratios and iron nitrate concentration. Complete removals of phenol were observed at 380°C for residence time less than 1 s in both configurations. Reductions in COD in excess of 94% were obtained in the non-preheated oxidant scenario. Near complete COD removals were achieved at the catalytic SCWO reactions. Chromatographic information showed that only acetic acid was produced as an intermediate compound. It was determined that SCWO combined with in-situ catalyst formation in counter current mixing reactor resulted in COD and phenol removal efficiencies greater that those seen for other researcher works.

6

SUPERCRITICAL WATER OXIDATION OF 2,4-DCP IN PROTECTED WALL REACTOR

- A new laboratory-scale SCWO rig was designed, constructed, tested, and operated.
- Two different scale layers are formed on protected wall reactor during SCWO of 2,4-DCP.
- Near-complete removal of organic content was obtained.

6.1 Introduction

As noted in Chapter 1, one of the biggest criticisms of SCWO is the rigorous reaction conditions required for oxidation reactions to take place. These conditions of high temperatures and pressures and highly oxidizing environment coupled with presence of heteroatoms cause corrosion and salt deposition problems to be inevitable in the absence of any control approaches (Vadillo et al., 2013). These issues have all hindered general industrial commercializing of the SCWO process (Marrone, 2013). Therefore, some mitigation actions are usually essential for safely and effectively facilitate the oxidation of waste materials in supercritical

water at a range of operational conditions.

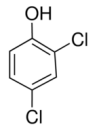
A considerable amount of research has been published on the reduction of corrosion in SCWO reactors (Marrone and Hong, 2009). These corrosion mitigation studies include use of high corrosion resistance materials (Ma et al., 2014), applying of liners/coatings (Marrone et al., 2005), employing transpiring/cooled wall reactors (Xu et al., 2014; Cabeza et al., 2015), pre-neutralization (Hazlebeck et al., 2000), and optimization of process operating conditions (Kritzer, 2004). However, it has been difficult to control the corrosion of the reactor itself when halogenated hydrocarbon is oxidized at supercritical condition. Wellig et al. (2009) claimed that the development of a sophisticated reactor design may be able to solve problems that arise during SCWO processes. Hodes et al. (2004) also discussed how an appropriate reactor design and/or operational procedures would be the most effective approach to overcoming such problems.

Clearly knowledge of the fluid dynamics and mixing regimes inside the reactor are fundamentally important (Chen et al., 2014). Supercritical water cannot be directly visualized easily, because the process conditions do not easily permit transparent reactors. Pseudo fluid modelling (Chapter 3) was conducted to recreate the mixing patterns inside three different reactor geometries at supercritical fluid conditions. A pseudo co-current protected wall reactor provided the best configuration in minimizing corrosion of the reactor by preventing corrosive species from reaching the surface of the reactor inner wall by enveloping the reaction zone with a clean supercritical water.

This Chapter involve empirical experiments under supercritical conditions to validate the pseudo fluid modelling for application to SCWO. Validation of this

modelling approach is crucial step before proceeding to potential more complex and intricate reactor designs which may extend beyond requirements for stock high pressure fittings. The performance of the reactor system was evaluated through oxidizing of 2,4-dichlorophenol (Table 6.1) which is usually used as a model halogenated organic compound in investigating an anti-corrosion/anti-fouling SCWO system (Lee et al., 2005).

Table 6.1: Properties of 2,4-DCP.

Structure	
Formula	$C_6H_4Cl_2O$
Molar mass	163 $gmol^{-1}$
Boiling point	209°C
Density	1.38 gcm^{-3}
Solubility in water	5 $g100mL^{-1}$

6.2 Protected wall reactor rig

A simplified scheme of the protected wall reactor system is shown in Figure 6.1. A full flow diagram of the reactor system was given in Chapter 2. Contrary to the previous counter current reactor used in this study, the protected wall reactor configuration creates a co-current mixing regime. Here, the halogenated organic stream (at ambient temperature) is pumped through the inner tube (1/8" outer

diameter), as an upflow, into the bottom of the reactor. Simultaneously, the superheated water stream is pumped into the sides of the reactor cross piece, entering below the outlet of the organic stream via the outer tube (1/4" outer diameter). The density difference between the two streams prevent the organic material from reaching the reactor walls. The mixture then flows upward to the reactor outlet. Upon leaving the reactor, the oxidation product is quenched and neutralized by a diluted NaOH stream.

The outer tube diameter was decreased in order to increase the velocity of the supercritical water flow and preventing any chance of back mixing. Non-heated oxidant configuration, where the H_2O_2 is premixed with organic solution was used in this study. The length of the inner tube was reduced to the minimum point to avoid any reaction between the organic content and oxidant before the mixing point. The reactor volume was 11.7 cm^3 and was one meter in length. The reactor, all valves, and connecting parts were made of stainless steel 316L. Table 6.2 shows the elemental composition (wt%) of the SS316L reactor tubing material.

Pseudo fluid modelling results showed that a high superheated flow (turbulent flow regime) relative to the cold flow is required to control mixing and keep corrosive species away from the reactor wall. Therefore the hot flow was introduced to the system at flow rate of 50 $mLmin^{-1}$ using two Gilson HPLC pumps (Model 305 equipped with a 25 SC pump head) while the cold flow was injected at 10 $mLmin^{-1}$ using the same Gilson HPLC pump model.

Table 6.2: Chemical composition of the SS316L reactor tubing.

Element	Percent by Weight
Carbon	0.03
Manganese	2.00
Silicon	0.75
Chromium	17.00
Nickel	12.00
Molybdenum	2.50
Phosphorus	0.05
Sulfur	0.03
Nitrogen	0.10
Iron	Bal.

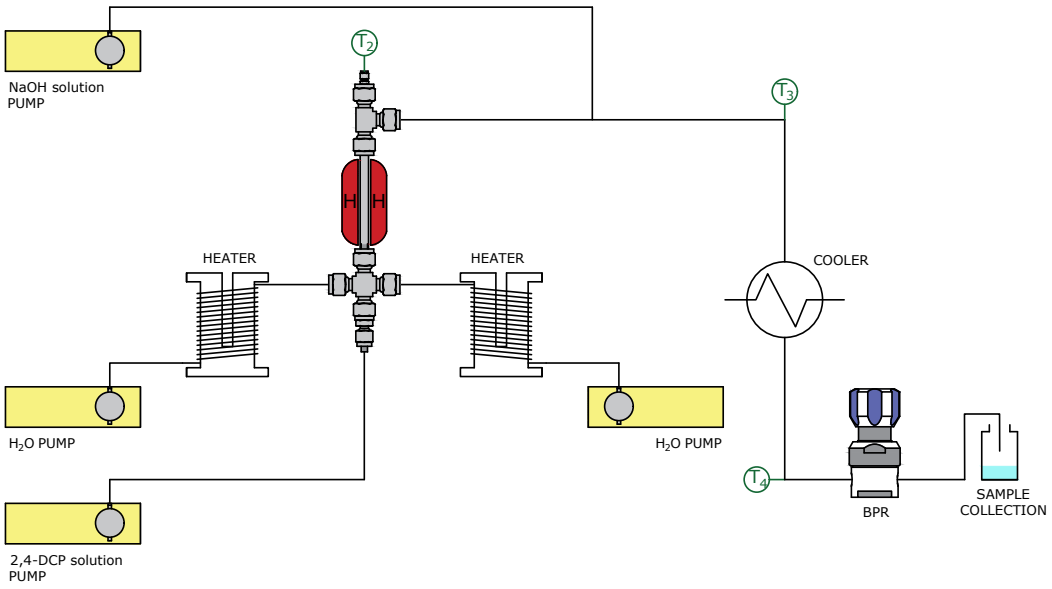


Figure 6.1: Schematic diagram of protected wall reactor system

6.3 Protected wall reactor results

After the heating up period, the halogenated feed stream was switched from distilled water to the 2,4-DCP and hydrogen peroxide mixture. Within approximately 2 min the reactor effluent became light brown in color. The experiment was terminated after 1 h of exposing to the oxidation reaction at supercritical (250 *bar* and 380°C) condition and the system was flushed with distilled water and allowed to cool. The reaction product was collected and analysed by COD test and reactor tubing was disassembled and the internal surface was examined with SEM and SEM/EDS analysis to investigate the oxide layer composition, thickness and integrity.

The reactor tubing was manually cut, into small pieces of approximately 5 *cm*, using Swagelok® TC72 tube cutter. These small reactor tube pieces were labelled and then cut vertically into two sections, as shown in Figure 6.2, using a hand saw coupled with a cutting blade. As shown in Figure 6.3, direct observation showed that internal surface of reactor tubing was divided into two regions based on the color. Region one from reactor entrance at piece one to mid of piece number five and region two from the end of region one to the outlet of reactor. This implies that corrosion mechanisms at the region one and two are different, a phenomenon probably due to the variation of solution that in contact to the wall. Therefore, two reactor tubing pieces (pieces number 2 and 7) were chosen as representatives for two identified regions. Small portion (1 *cm*) of each representative tube was cut and hot mounted with carbon for EDS analysis. The second part of the samples was kept for SEM surface imaging analysis. Hot mounted

samples were grinded to 1200 grit surface finish using SiC abrasive papers with H_2O as a lubricant.

The surface morphologies of both reactor pieces exposed to SCWO environment at 380°C and different oxygenation levels are shown in Figure 6.4 and Figure 6.5. For region one, the reactor tubing surface composed of compact grain structures. However, the surface structure of region two showed a smaller grain size than that of the region one. As temperature increase, the solubility of oxygen in water and consequently the oxidizing and solvating power of the solution increases (Kritzer et al., 2000). At the same time, the solubility of metal oxide are likely to increase (Hayashi and Hakuta, 2010) leading to much finer grain size and smoother oxide surface. This can be explained by decrease the resistance of protective oxide layer which lead to a continuous dissolution and general attack of the alloy (Choudhry et al., 2015).

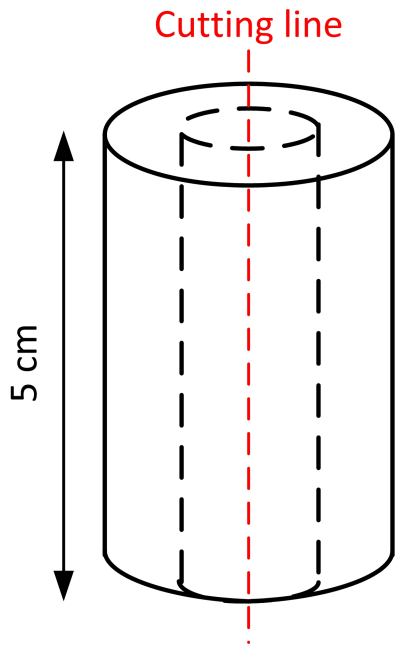


Figure 6.2: Diagram of a reactor tube

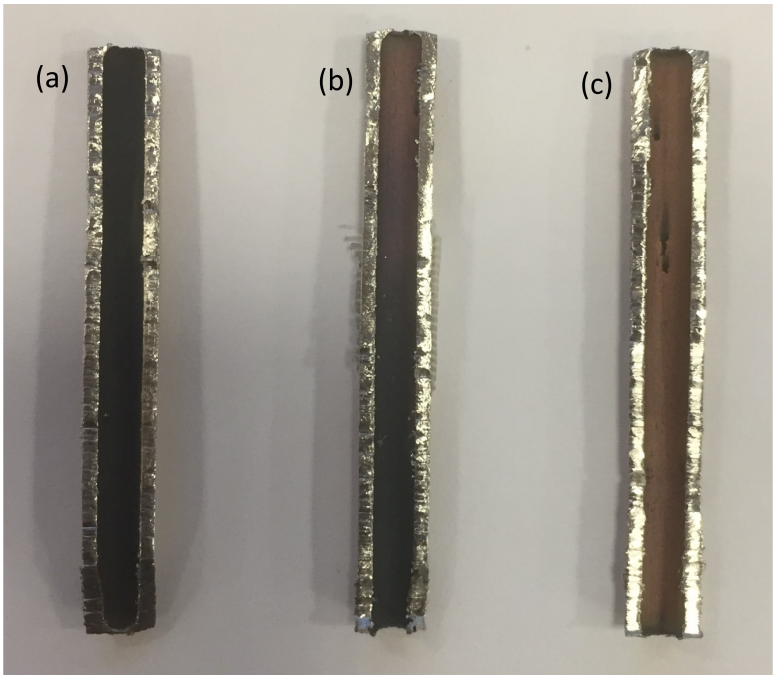


Figure 6.3: Cross-sectional photographs of reactor tube pieces. (a) piece number (2) representing region one in the reactor tubing, (b) piece number (5) showing the end of region one and beginning of region two and (c) piece number (7) representing region two in the reactor tubing.

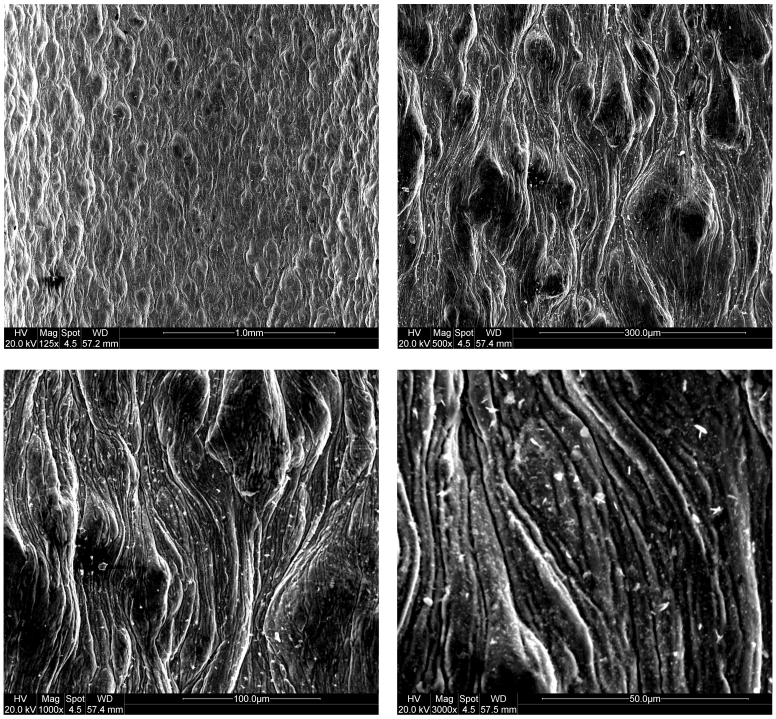


Figure 6.4: Surface morphologies of the oxide layer grown on region one of the reactor tubing.

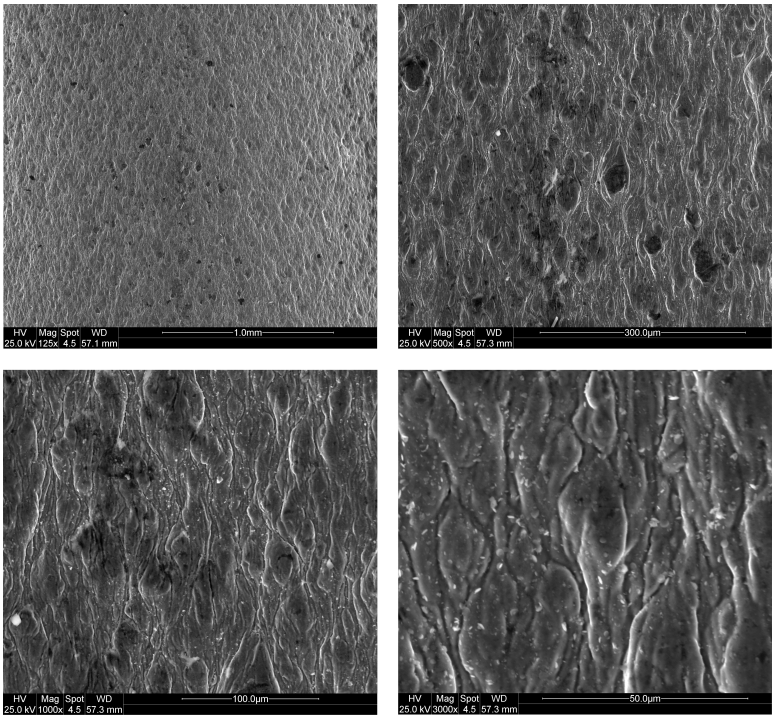


Figure 6.5: Surface morphologies of the oxide layer grown on region two of the reactor tubing.

The cross-sections of the reactor tube pieces are analysed by SEM/EDS to characterize the degradation behaviour. Figure 6.6 shows the cross-section of the oxide layers formed on pieces number 2 and 7 of the SS316L reactor tubing at 380°C and 25 MPa. It shows that the thickness of the oxide layer formed on the surface of the reactor tubing was about 2 μm and 1.2 μm for region one and region two, respectively. In SCWO of halogenated organic compounds, chlorinated organic materials are converted to carbon dioxide (CO_2), H_2O, and hydrochloric acid (HCl). As a high concentration of these mineral acids come in contact with reactor wall, extensive spallation of the oxide layer from the surface of region two reactor tubing was seen, as a very thin layer was found during the SEM analysis.

Figure 6.7 shows the EDS line scan results of the oxide layer grown on region

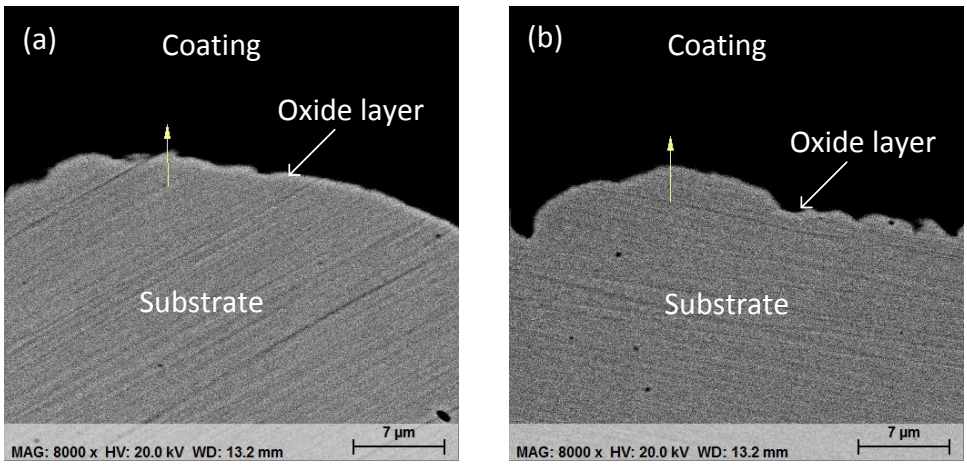


Figure 6.6: Cross-sectional view of the oxide film layer formed on (a) region one and (b) region two of SS316L reactor tubing during SCWO process (380°C and 25 MPa).

one and region two samples exposed to SCWO at 380°C and 25 MPa. A thin oxide layer was form on both reactor tube samples. Line scan shows gradual decreases in concentration of Fe and Cr, while the concentration of O is slightly increase in oxide layer formed on region one. In region 2, the concentrations of Fe and Cr are sharply decrease but there is an obvious increase in concentration of C. This is indicated that part of oxidation reaction took place at the reactor wall of region two.

The XRD analysis of the oxide layer formed on the surface of reactor tubing pieces during SCWO process are shown in Figure 6.8. The surface oxide formed on region one tubing was mainly composed of metallic oxide phase $FeO_{0\cdot 64}NiO_{0\cdot 36}$. Metallic, Fe and Ni, phases have been formed on stainless steel SS316 subjected to pure supercritical water at different oxygenation levels (Stroosnijder et al., 1990; Choudhry et al., 2015). For region two, XRD results showed the outer metallic layer composition was a mixture of $Cr_{12}Fe_{22}Mo_4Ni_{10}Si_9$ on the SS316L tubing surface. Line scans and XRD analysis results suggested the reactor tubing subjected to two different solutions. Region one subjected to clean supercritical

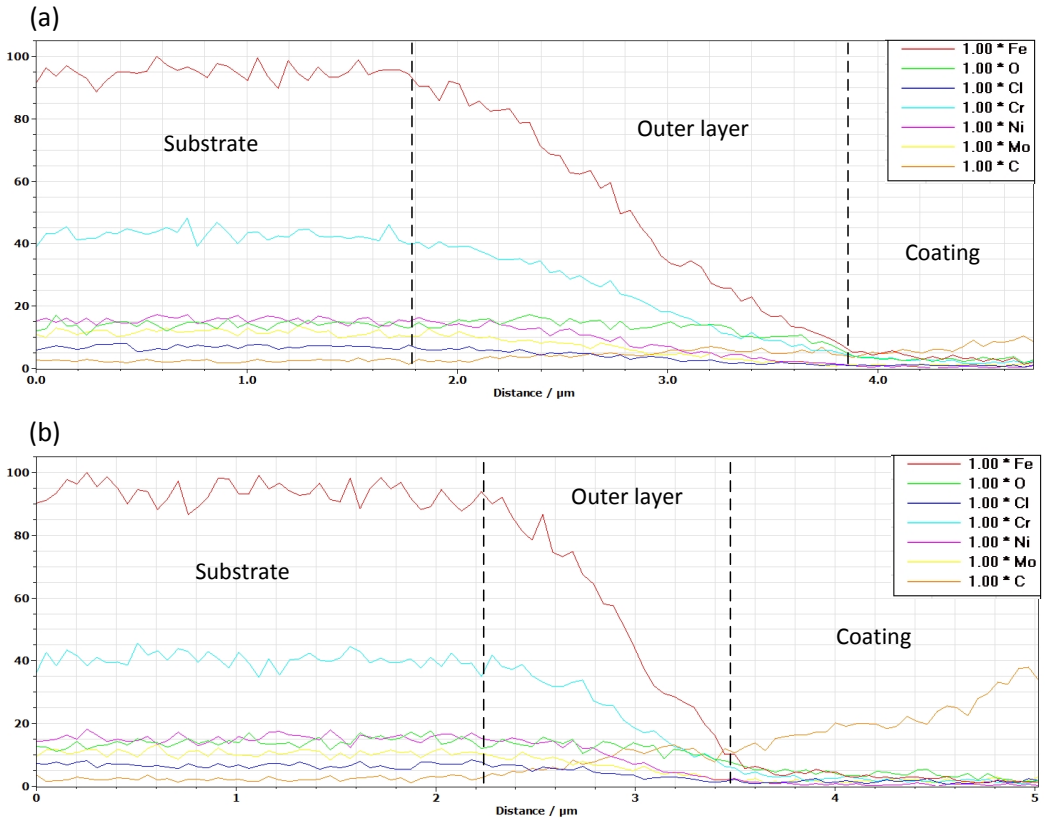


Figure 6.7: EDS line scans of oxide film layer formed on (a) region one and (b) region two of SS316L reactor tubing during SCWO process (380°C and 25 MPa).



water whereas region two come in contact with corrosive solution. As a result, the safe zone in protected wall reactor proceed for 25 *cm* at the flow rate ratio of 50:10.

Figure 6.9 shows the destruction efficiencies of 2,4-DCP at supercritical conditions and different oxygenation levels in co-current protected wall reactor. Oxidant ratio was altered from 0-2 at fixed operating conditions of 380°C and 25 MPa with an initial concentration of 1 mM and 4.7 *sec* residence time. The total oxidation reaction of 2,4-DCP to H_2O, CO_2 and HCl is given below:

$$Cl_2C_6H_3OH + 6O_2 \longrightarrow 6CO_2 + H_2O + 2HCl \tag{6.1}$$

Nearly complete removal of organic content was obtained at oxidant ratio of 1.5. However, the increment in the conversion was gradually diminished, and little effect was observed in COD removal as the oxidant ratio increased above the stoichiometric demand.

6.4 Conclusions

In this Chapter, corrosion tests of SS316L reactor tubing were performed in SCW (380°C and 25 MPa) containing 2,4-DCP and H_2O_2. Two different regions were observed depending on the morphology of the scale layer formed on the reactor tubing. Scale layers were analysed using SEM, SEM/EDS and XRD methods. For region one, a large compact grain structure were found. The thickness of the oxide layer was about 2 μm and it was composed of $FeO_{0\cdot 64}NiO_{0\cdot 36}$. For region two, the morphology of the scale surface showed a smaller grain size.

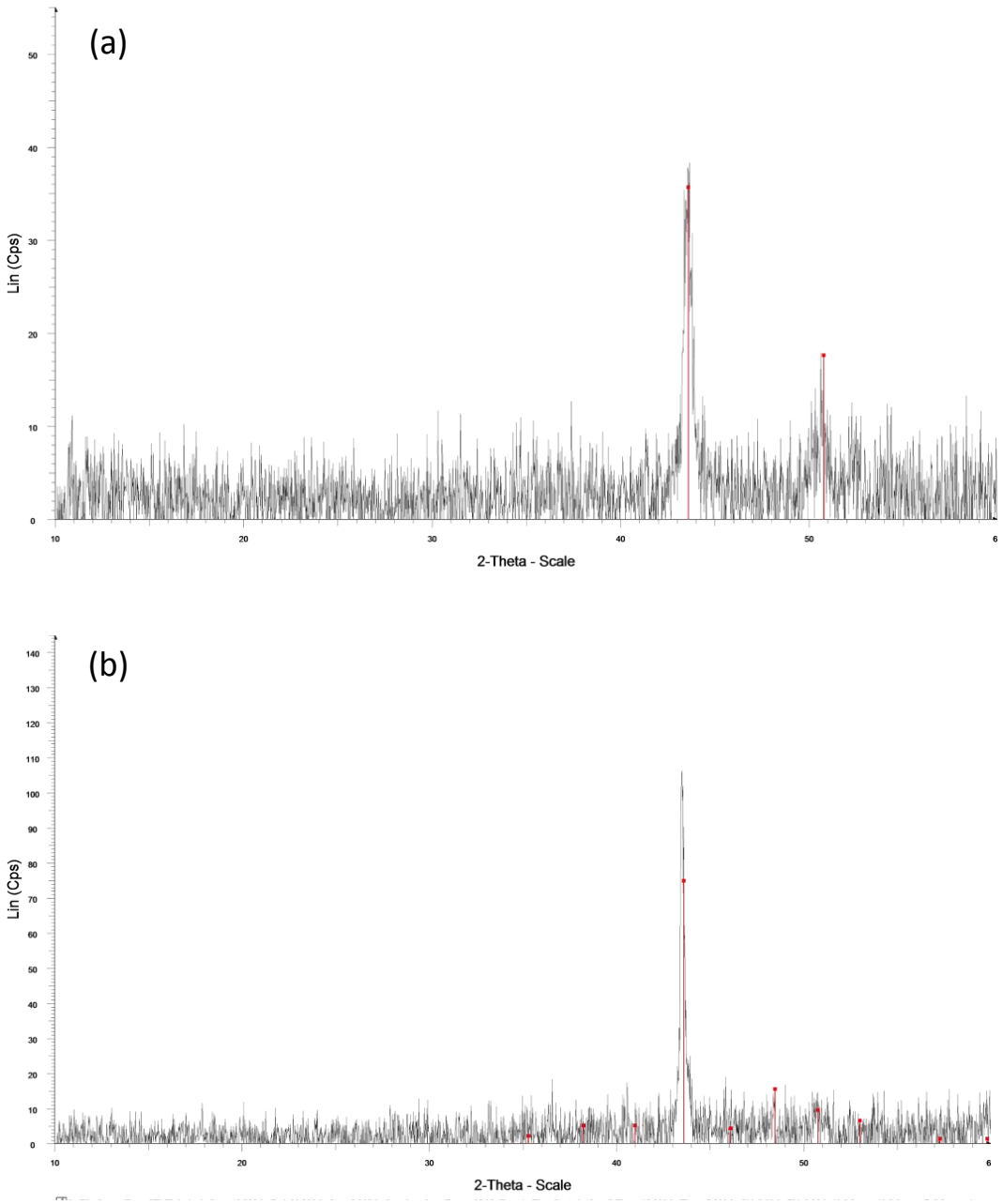


Figure 6.8: XRD patterns of scales form on SS316L tubing through SCWO process (380°C and 25 MPa): (a) $FeO_{0\cdot 64}NiO_{0\cdot 36}$ oxide scale on region one and (b) $Cr_{12}Fe_{22}Mo_4Ni_{10}Si_9$ mixture on region two.

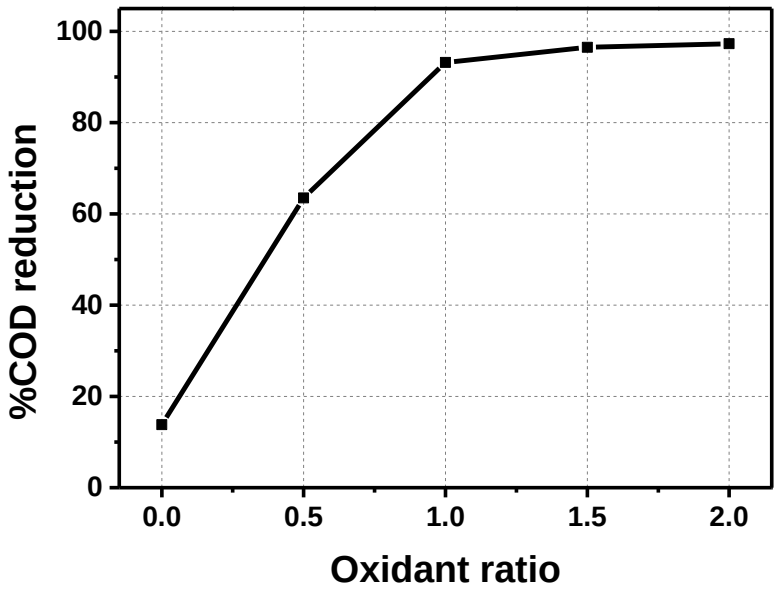


Figure 6.9: The effect of oxidant ratio on COD removal efficiency at 380°C and 25 MPa and 1 mM 2,4-DCP.

The thickness of the scale layer was found to be 1.2 μm and it was composed of $Cr_{12}Fe_{22}Mo_4Ni_{10}Si_9$. Corrosion test results suggested that reactor tubing was subjected to two different solutions and the clean SCW protected the reactor tubing for region one. Complete oxidation of organic content of 2,4-DCP was obtained at 380°C and 25 MPa.

7 CONCLUSIONS AND FUTURE WORK

7.1 Conclusions

The work presented in this thesis was carried out with the aim of designing an innovative anti-corrosive reactor that can account for SCWO of hazardous organic waste. Additionally, a counter current mixing reactor was used in combining two processes; SCWO and SCWHS in one stage reactor. This work and the associated publications have achieved these goals to some extent. Some concluding remarks of this study are summarized below.

In Chapter 3, a visualization technique using pseudo fluids has been advanced to simulate the general flow patterns and mixing regimes of two very different fluids at ambient conditions. This technique was successfully exploited to model the condition of SCWO process and to evaluate three different reactor geometries, all of which can be easily constructed using off the shelf high pressure fittings. The approach allows different flow conditions to be tested and quantified. Furthermore, a simplification of the concentration mapping can be made to create a traffic light system and efficiency rating analysis were used to represent the performance of reactor in terms of degree of mixedness inside the flow and around

the walls.

From the perspective of corrosion prevention, the modelling results show that each design appears to have optimal flow conditions that reduce or avoid re-circulation and wall contact. However, the third reactor or co-current protected wall design seems to provide the best opportunity for avoiding corrosion and salt accumulation. The protecting flow of superheated stream at the reactor wall could control mixing of reagent in a safe zone and away from the reactor wall. This is the first time that such an approach, with the use of pseudo fluids, has been used to quantify mixing inside a SCWO reactor.

Chapters 4 and 5 were devoted to study the SCWO of different model organic compounds combined with SCWHS of different metal oxide nanoparticles in counter current mixing reactor.

In Chapter 4, experiments were performed using acrylic acid as model compound for unsaturated carboxylic acid. Two different experimental configurations for oxidant delivery were conducted; Pre-heated and non-preheated oxidant configuration. In all cases, the non-preheated oxidant scenario where the hydrogen peroxide and organic solution streams were pressurised, mixed and fed cool to the reactor without any preheating showed better result as COD removal than preheated oxidant scenario. As expected, COD removal displayed positive dependence on the reaction temperature and oxidant ratio. However, the impacts of increasing residence time and organic concentration were found to be minimal on COD reduction. 80 and 15% of COD reduction was achieved for non-preheated and preheated oxidant configurations respectively in residence time of (0.75 sec) and 100% excess of oxygen. The catalytic SCWO of AA was a novel investigation

into the combination of two opposed chemical processes; destruction and synthesis in one reactor system. Adding a small amount of various soluble metal salts as precursor in the organic feed resulted in nanoparticles forming which accelerated the reaction rate and enhanced the hydrothermal oxidation efficiency. The catalytic activity of the produced metal oxide nanoparticles was in the following order: CrOOH> Fe_2O_3> mixed Fe_2O_3 and TiO_2> Co_3O_4> TiO_2. For catalytic process, near-complete reduction in COD was observed at temperature below than 400°C and residence time less than 1 *sec*.

In Chapter 5, the SCWO of a more recalcitrant compound, namely phenol, was conducted with in-situ hematite formation. It was found that there are several configurations that provide superior performance to a conventional SCWO process in term of COD removal. However, the catalysed non-preheated oxidant configuration was chosen as the best. It was demonstrated experimentally that near complete conversion of the organic content of phenol was obtained in both non-preheated and catalytic non-preheated oxidant configurations. The catalytic supercritical water oxidation process oxidised faster and produced less intermediates than the non-catalytic process. Compared to other research works, a conversion greater than 99% of phenol is obtained in different oxidant delivery configurations in 1 order of magnitude shorter residence time.

In Chapter 6, corrosion tests of co-current protected wall reactor were examined during the SCWO of 2,4-DCP. Two regions have been identified based on surface morphology, grain size, scale layer thickness and XRD results. The first 'protected' region proceeded for 25 *cm* and identified by larger grain size and thicker oxide layer. Whereas the second 'unprotected' region length was



about 75 *cm* and identified by smaller grain size and a thin metallic scale layer. Under supercritical conditions (380°C and 25 *Mpa*), 2,4-DCP was successfully decomposed in protected wall reactor.

7.2 Future work

During the research some areas were identified that required of further study to provide more evidence to support the development of the process at industrial scale as an available technology for the destruction of organic compounds.

Following on from the work on the pseudo fluid modelling reported in Chapter 3, It would be of interest to develop the protected wall reactor design by reducing the amount of protecting water consumption. Protected water can be recycled in one reactor compact unit.

After proving its ability as a cheap, rapid and effective approach to visual observation for a continuous flow supercritical hydrothermal processes, more complex and intricate reactor configurations can be tested by pseudo fluid modelling technique.

Chapter 6 showed that the protecting zone in protecting wall reactor proceed for 25 *cm*. A new supercritical water oxidation system equipped with protected wall reactor should be built and tested with different halogenated organic content to ensure the capability of this reactor design in handling such corrosive hazardous waste.

The work described in Chapter 4 and 5 demonstrated the ability of the counter-current mixing reactor and SCWO and SCWHS as a whole, to be a powerful, flexible and scalable treatment and synthesis tool. The work began

to look at the use of in-situ formed catalyst to enhance the SCWO of different organic compounds. However, the performance of catalysts in term of activity differed from one to each other and from one organic compound to another. Implementation of different (metal oxides, mixed metal oxides or metal/metal oxides combinations) catalysts will be useful for the proper selection of the best catalyst for specific types of organic waste.

Although acrylic acid and phenol are completely oxidized in different configurations, Some recalcitrant compounds like ammonia may require rigorous reaction conditions. Therefore, two stage operations will be useful to increase the residence time and hence the destruction efficiency of the process. A counter current mixer stage (for catalyst synthesis) followed by an additional heating stage can eliminate high concentrations of any contaminants (which are easily oxidised) during the first step leaving the second stage for recalcitrant by-products and molecules hard to oxidise. In this way, the energy input for the first process is integrated in to the second stage.

The aim of the research was to conduct a combined process of organic materials oxidation and metal oxides production in the novel counter current mixing reactor. Any future research should consider the identification and quantification in detail of the products and the remaining by-products in order to build a proper reaction mechanism.

So far, the implementations of detailed kinetic mechanisms that have been extrapolated from the oxidation of organic compounds have been produced good results in the prediction of product distributions for SCWO and catalytic SCWO. There is however, no kinetic information for catalytic oxidations in counter cur-



rent mixing reactor that can be used to model homogeneous and heterogeneous catalysis reactions. A kinetic study of catalytic reactions in a counter current mixing reactor would help to understand how the reactions proceed above the critical point of water.

BIBLIOGRAPHY

J. Abelleira, J. Sánchez-Oneto, J. Portela, and E. M. de la Ossa. Kinetics of supercritical water oxidation of isopropanol as an auxiliary fuel and co-fuel. *Fuel*, 111:574–583, 2013.

T. Adschiri, K. Kanazawa, and K. Arai. Rapid and continuous hydrothermal crystallization of metal oxide particles in supercritical water. *Journal of the American Ceramic Society*, 75(4):1019–1022, 1992.

T. Adschiri, S. Takami, M. Umetsu, and T. Tsukada. Hydrothermal synthesis at supercritical conditions: experiments and simulation. In *Sixth International Symposium on Supercritical Fluids, Versailles, France*, volume 28, page 30, 2003.

T. Aizawa, Y. Masuda, K. Minami, M. Kanakubo, H. Nanjo, and R. L. Smith. Direct observation of channel-tee mixing of high-temperature and high-pressure water. *The Journal of Supercritical Fluids*, 43(2):222–227, 2007.

G. Aksomaityte, M. Poliakoff, and E. Lester. The production and formulation of silver nanoparticles using continuous hydrothermal synthesis. *Chemical engineering science*, 85:2–10, 2013.

B. Al-Duri and F. Alsoqyani. Supercritical water oxidation (scwo) for the removal of ncontaining heterocyclic hydrocarbon wastes; part ii: System kinetics. *The Journal*



of Supercritical Fluids, 2017.

B. Al-Duri, L. Pinto, N. Ashraf-Ball, and R. Santos. Thermal abatement of nitrogen-containing hydrocarbons by non-catalytic supercritical water oxidation (scwo). *Journal of Materials Science*, 43(4):1421–1428, 2008.

B. Al-Duri, F. Alsoqyani, and I. Kings. Supercritical water oxidation for the destruction of hazardous waste: better than incineration. *Phil. Trans. R. Soc. A*, 373(2057): 20150013, 2015.

B. Al-Duri, F. Alsoqyiani, and I. Kings. Supercritical water oxidation (scwo) for the removal of n-containing heterocyclic hydrocarbon wastes. part i: Process enhancement by addition of isopropyl alcohol. *The Journal of Supercritical Fluids*, 116:155–163, 2016.

M. J. Angeles-Hernández, G. A. Leeke, and R. C. Santos. Catalytic supercritical water oxidation for the destruction of quinoline over mno2/cuo mixed catalyst. *Industrial & Engineering Chemistry Research*, 48(3):1208–1214, 2008.

F. J. Armellini, J. W. Tester, and G. T. Hong. Precipitation of sodium chloride and sodium sulfate in water from sub-to supercritical conditions: 150 to 550 c, 100 to 300 bar. *The Journal of Supercritical Fluids*, 7(3):147–158, 1994.

I. Arslan-Alaton and J. L. Ferry. H 4 siw 12 o 40-catalyzed oxidation of nitrobenzene in supercritical water: kinetic and mechanistic aspects. *Applied Catalysis B: Environmental*, 38(4):283–293, 2002.

J. Benjumea, J. Sánchez-Oneto, J. Portela, F. Jiménez-Espadafor, and E. M. de la Ossa. Simulation of supercritical water oxidation reactor in transitory state: Application to time-dependent processes. *The Journal of Supercritical Fluids*, 117:219–229, 2016.

M. Bermejo and M. Cocero. Destruction of an industrial wastewater by supercritical water oxidation in a transpiring wall reactor. *Journal of hazardous materials*, 137



(2):965–971, 2006a.

M. Bermejo and M. Cocero. Supercritical water oxidation: a technical review. *AIChE Journal*, 52(11):3933–3951, 2006b.

M. Bermejo, F. Cantero, and M. Cocero. Supercritical water oxidation of feeds with high ammonia concentrations: Pilot plant experimental results and modeling. *Chemical Engineering Journal*, 137(3):542–549, 2008.

M. Bermejo, C. Jimenez, P. Cabeza, A. Matías-Gago, and M. Cocero. Experimental study of hydrothermal flames formation using a tubular injector in a refrigerated reaction chamber. influence of the operational and geometrical parameters. *The Journal of Supercritical Fluids*, 59:140–148, 2011.

M. D. Bermejo, D. Rincon, A. Martin, and M. J. Cocero. Experimental performance and modeling of a new cooled-wall reactor for the supercritical water oxidation. *Industrial & Engineering Chemistry Research*, 48(13):6262–6272, 2009.

P. J. Blood, J. P. Denyer, B. J. Azzopardi, M. Poliakoff, and E. Lester. A versatile flow visualisation technique for quantifying mixing in a binary system: application to continuous supercritical water hydrothermal synthesis (swhs). *Chemical engineering science*, 59(14):2853–2861, 2004.

V. Bolla, W. Hauschild, O. Hoffmeister, et al. Sustainable development in the european union: 2009 monitoring report of the eu sustainable development strategy. 2009.

G. Busca, S. Berardinelli, C. Resini, and L. Arrighi. Technologies for the removal of phenol from fluid streams: a short review of recent developments. *Journal of Hazardous Materials*, 160(2):265–288, 2008.

K. Byrappa and T. Adschiri. Hydrothermal technology for nanotechnology. *Progress in Crystal Growth and Characterization of Materials*, 53(2):117–166, 2007.

P. Cabeza, J. Queiroz, S. Arca, C. Jiménez, A. Gutiérrez, M. Bermejo, and M. Cocero.



Sludge destruction by means of a hydrothermal flame. optimization of ammonia destruction conditions. *Chemical engineering journal*, 232:1–9, 2013.

P. Cabeza, B. Al-Duri, M. Bermejo, and M. Cocero. Co-oxidation of ammonia and isopropanol in supercritical water in a tubular reactor. *Chemical Engineering Research and Design*, 92(11):2568–2574, 2014.

P. Cabeza, J. P. S. Queiroz, M. Criado, C. Jiménez, M. D. Bermejo, F. Mato, and M. J. Cocero. Supercritical water oxidation for energy production by hydrothermal flame as internal heat source. experimental results and energetic study. *Energy*, 90: 1584–1594, 2015.

F. Cansell. Method for treating waste by hydrothermal oxidation, Aug. 16 2005. US Patent 6,929,752.

P. Caramazana-Gonzalez, P. W. Dunne, M. Gimeno-Fabra, M. Zilka, M. Ticha, B. Stieberova, F. Freiberg, J. McKechnie, and E. Lester. Assessing the life cycle environmental impacts of titania nanoparticle production by continuous flow solvo/hydrothermal syntheses. *Green Chemistry*, 19(6):1536–1547, 2017.

M. Cargnello, T. R. Gordon, and C. B. Murray. Solution-phase synthesis of titanium dioxide nanoparticles and nanocrystals. *Chemical reviews*, 114(19):9319–9345, 2014.

S. Chaturvedi, P. N. Dave, and N. Shah. Applications of nano-catalyst in new era. *Journal of Saudi Chemical Society*, 16(3):307–325, 2012.

H. Chen, G. Wang, Y. Xu, Z. Chen, and F. Yin. Application of red mud as both neutralizer and catalyst in supercritical water oxidation (scwo) disposal of sewage sludge. *RSC Advances*, 6(59):54202–54214, 2016.

X. Chen and A. Selloni. Introduction: titanium dioxide (tio2) nanomaterials, 2014.

Z. Chen, G. Wang, Z. A. Mirza, S. Yang, and Y. Xu. Study of transpiring fluid dynamics in supercritical water oxidation using a transparent reactor. *The Journal*



of Supercritical Fluids, 88:117–125, 2014.

Z. Chen, G. Wang, F. Yin, H. Chen, and Y. Xu. A new system design for supercritical water oxidation. *Chemical Engineering Journal*, 269:343–351, 2015.

T. Choudhary, C. Sivadinarayana, and D. Goodman. Catalytic ammonia decomposition: Cox-free hydrogen production for fuel cell applications. *Catalysis Letters*, 72 (3):197–201, 2001.

K. I. Choudhry, S. Mahboubi, G. A. Botton, J. R. Kish, and I. M. Svishchev. Corrosion of engineering materials in a supercritical water cooled reactor: Characterization of oxide scales on alloy 800h and stainless steel 316. *Corrosion Science*, 100:222–230, 2015.

H. Cochran, P. Cummings, and S. Karaborni. Solvation in supercritical water. *Fluid phase equilibria*, 71(1-2):1–16, 1992.

Z.-Y. Ding, S. N. Aki, and M. A. Abraham. Catalytic supercritical water oxidation: phenol conversion and product selectivity. *Environmental science & technology*, 29 (11):2748–2753, 1995.

Z. Y. Ding, M. A. Frisch, L. Li, and E. F. Gloyna. Catalytic oxidation in supercritical water. *Industrial & engineering chemistry research*, 35(10):3257–3279, 1996.

X. Dong, Y. Wang, X. Li, Y. Yu, and M. Zhang. Process simulation of laboratory wastewater treatment via supercritical water oxidation. *Industrial & Engineering Chemistry Research*, 53(18):7723–7729, 2014.

X. Dong, Z. Gan, X. Lu, W. Jin, Y. Yu, and M. Zhang. Study on catalytic and non-catalytic supercritical water oxidation of p-nitrophenol wastewater. *Chemical Engineering Journal*, 277:30–39, 2015.

X. Du, R. Zhang, Z. Gan, and J. Bi. Treatment of high strength coking wastewater by supercritical water oxidation. *Fuel*, 104:77–82, 2013.



H. B. Dunford. Oxidations of iron (ii)/(iii) by hydrogen peroxide: from aquo to enzyme. *Coordination Chemistry Reviews*, 233:311–318, 2002.

P. W. Dunne, A. S. Munn, C. L. Starkey, T. A. Huddle, and E. H. Lester. Continuous-flow hydrothermal synthesis for the production of inorganic nanomaterials. *Phil. Trans. R. Soc. A*, 373(2057):20150015, 2015.

S. El-Sheikh, R. Mohamed, and O. Fouad. Synthesis and structure screening of nanostructured chromium oxide powders. *Journal of Alloys and Compounds*, 482(1):302–307, 2009.

J. M. Eller, R. N. McBrayer, and J. G. Swan. Method for controlling reaction temperature, June 23 1998. US Patent 5,770,174.

H. Erkonak, O. Ö. Söğüt, and M. Akgün. Treatment of olive mill wastewater by supercritical water oxidation. *The Journal of Supercritical Fluids*, 46(2):142–148, 2008.

S. Falamarzian, O. Tavakoli, R. Zarghami, and M. A. Faramarzi. Catalytic hydrothermal treatment of pharmaceutical wastewater using sub-and supercritical water reactions. *The Journal of Supercritical Fluids*, 95:265–272, 2014.

Z. Fang. *Near-critical and supercritical water and their applications for biorefineries*. PhD thesis, Springer, 2014.

M. Ferrandon. *Mixed metal oxide-noble metal catalysts for total oxidation of volatile organic compounds and carbon monoxide*. PhD thesis, Kemiteknik, 2001.

K. Foo and B. Hameed. An overview of landfill leachate treatment via activated carbon adsorption process. *Journal of hazardous materials*, 171(1):54–60, 2009.

T. Funazukuri and M. Takahashi. Decomposition of 2-aminoethanol in sub-and supercritical water with/without hydrogen peroxide. *Fuel*, 78(9):1117–1119, 1999.

B. García Jarana, J. Sánchez Oneto, J. R. Portela Miguélez, E. Nebot Sanz, and E. J.



Martínez de la Ossa. Simulation of supercritical water oxidation with air at pilot plant scale. *International Journal of Chemical Reactor Engineering*, 8(1), 2010.

M. García-Jarana, I. Kings, J. Sánchez-Oneto, J. R. Portela, and B. Al-Duri. Supercritical water oxidation of nitrogen compounds with multi-injection of oxygen. *The Journal of Supercritical Fluids*, 80:23–29, 2013.

E. Garcia-Verdugo, E. Venardou, W. B. Thomas, K. Whiston, W. Partenheimer, P. A. Hamley, and M. Poliakoff. Is it possible to achieve highly selective oxidations in supercritical water? aerobic oxidation of methylaromatic compounds. *Advanced Synthesis & Catalysis*, 346(2-3):307–316, 2004.

P. Gibot and L. Vidal. Original synthesis of chromium (iii) oxide nanoparticles. *Journal of the European Ceramic Society*, 30(4):911–915, 2010.

A. Gidner and L. Stenmark. Supercritical water oxidation of sewage sludge–state of the art. In *Proceedings of the IBCs Conference on Sewage Sludge and Disposal Options*, 2001.

A. M. Gizir, A. A. Clifford, and K. D. Bartle. The catalytic role of transition metal salts on supercritical water oxidation of phenol and chlorophenols in a titanium reactor. *Reaction Kinetics and Catalysis Letters*, 78(1):175–182, 2003.

W. Gong and X. Duan. Degradation of landfill leachate using transpiring-wall supercritical water oxidation (scwo) reactor. *Waste Management*, 30(11):2103–2107, 2010.

W.-J. Gong, F. Li, and D.-L. Xi. Supercritical water oxidation of acrylic acid production wastewater in transpiring wall reactor. *Environmental Engineering Science*, 26(1): 131–136, 2009.

S. Gopalan and P. E. Savage. Reaction mechanism for phenol oxidation in supercritical water. *The Journal of Physical Chemistry*, 98(48):12646–12652, 1994.



Y. Hao and A. S. Teja. Continuous hydrothermal crystallization of α–fe2o3 and co3o4 nanoparticles. *Journal of Materials Research*, 18(2):415–422, 2003.

M. Hashimoto, S. Taniguchi, R. Takanami, R. Giri, and H. Ozaki. Oxidative degradation of 2, 4-dichlorophenoxyacetic acid (2, 4-d) in subcritical and supercritical waters. *Water Science and Technology*, 62(3):484–490, 2010.

K. Hatakeda, Y. Ikushima, O. Sato, T. Aizawa, and N. Saito. Supercritical water oxidation of polychlorinated biphenyls using hydrogen peroxide. *Chemical Engineering Science*, 54(15-16):3079–3084, 1999.

H. Hayashi and Y. Hakuta. Hydrothermal synthesis of metal oxide nanoparticles in supercritical water. *Materials*, 3(7):3794–3817, 2010.

T. M. Hayward, I. M. Svishchev, and R. C. Makhija. Stainless steel flow reactor for supercritical water oxidation: corrosion tests. *The Journal of supercritical fluids*, 27 (3):275–281, 2003.

D. A. Hazlebeck, K. W. Downey, and M. H. Spritzer. Downflow hydrothermal treatment, Apr. 25 2000. US Patent 6,054,057.

J. A. Heimbuch and A. R. Wilhelmi. Wet air oxidationa treatment means for aqueous hazardous waste streams. *Journal of hazardous materials*, 12(2):187–200, 1985.

H. Hobbs, S. Briddon, and E. Lester. The synthesis and fluorescent properties of nanoparticulate zro 2 doped with eu using continuous hydrothermal synthesis. *Green Chemistry*, 11(4):484–491, 2009.

M. Hodes, P. A. Marrone, G. T. Hong, K. A. Smith, and J. W. Tester. Salt precipitation and scale control in supercritical water oxidationpart a: fundamentals and research. *The Journal of Supercritical Fluids*, 29(3):265–288, 2004.

J. Kamler and J. A. Soria. Supercritical water gasification of municipal sludge: a novel approach to waste treatment and energy recovery. In *Gasification for practical*



applications. InTech, 2012.

S.-I. Kawasaki, T. Oe, N. Anjoh, T. Nakamori, A. Suzuki, and K. Arai. Practical supercritical water reactor for destruction of high concentration polychlorinated biphenyls (pcb) and dioxin waste streams. *Process Safety and Environmental Protection*, 84 (4):317–324, 2006.

S.-i. Kawasaki, Y. Xiuyi, K. Sue, Y. Hakuta, A. Suzuki, and K. Arai. Continuous supercritical hydrothermal synthesis of controlled size and highly crystalline anatase tio 2 nanoparticles. *The Journal of Supercritical Fluids*, 50(3):276–282, 2009.

S. Kolaczkowski, F. Beltran, D. McLurgh, and F. Rivas. Wet air oxidation of phenol: factors that may influence global kinetics. *Process safety and environmental protection*, 75(4):257–265, 1997.

S. Kolaczkowski, P. Plucinski, F. Beltran, F. Rivas, and D. McLurgh. Wet air oxidation: a review of process technologies and aspects in reactor design. *Chemical Engineering Journal*, 73(2):143–160, 1999.

M. Koo, W. K. Lee, and C. H. Lee. New reactor system for supercritical water oxidation and its application on phenol destruction. *Chemical engineering science*, 52(7):1201–1214, 1997.

M. Krajnc and J. Levec. Oxidation of phenol over a transition-metal oxide catalyst in supercritical water. *Industrial & engineering chemistry research*, 36(9):3439–3445, 1997.

P. Kritzer. Corrosion in high-temperature and supercritical water and aqueous solutions: a review. *The Journal of Supercritical Fluids*, 29(1):1–29, 2004.

P. Kritzer and E. Dinjus. An assessment of supercritical water oxidation (scwo): existing problems, possible solutions and new reactor concepts. *Chemical Engineering Journal*, 83(3):207–214, 2001.



P. Kritzer, N. Boukis, and E. Dinjus. Factors controlling corrosion in high-temperature aqueous solutions: a contribution to the dissociation and solubility data influencing corrosion processes. *The Journal of supercritical fluids*, 15(3):205–227, 1999.

P. Kritzer, N. Boukis, and E. Dinjus. Review of the corrosion of nickel-based alloys and stainless steels in strongly oxidizing pressurized high-temperature solutions at subcritical and supercritical temperatures. *Corrosion*, 56(11):1093–1104, 2000.

J. Kronholm, P. Jyske, and M.-L. Riekkola. Oxidation efficiencies of potassium persulfate and hydrogen peroxide in pressurized hot water with and without preheating. *Industrial & engineering chemistry research*, 39(7):2207–2213, 2000.

S. J. Kulkarni and J. P. Kaware. Review on research for removal of phenol from wastewater. *International journal of scientific and research publications*, 3(4):1–5, 2013.

P. Kumar, P. Raghavendra, and S. Chand. Catalytic wet air oxidation of carboxylic acid present in wastewater. 2006.

M. D. LaGrega, P. L. Buckingham, and J. C. Evans. *Hazardous waste management*. Waveland Press, 2010.

D.-S. Lee, E. F. Gloyna, and L. Li. Efficiency of h2o2 and o2 in supercritical water oxidation of 2, 4-dichlorophenol and acetic acid. *The Journal of Supercritical Fluids*, 3(4):249–255, 1990.

E. Lee, H. Lee, Y. Kim, K. Sohn, and K. Lee. Hydrogen peroxide interference in chemical oxygen demand during ozone based advanced oxidation of anaerobically digested livestock wastewater. *International Journal of Environmental Science & Technology*, 8(2):381–388, 2011.

H.-C. Lee, J.-H. In, S.-Y. Lee, J.-H. Kim, and C.-H. Lee. An anti-corrosive reactor for the decomposition of halogenated hydrocarbons with supercritical water oxidation.

The Journal of supercritical fluids, 36(1):59–69, 2005.

E. Lester, P. Blood, J. Denyer, D. Giddings, B. Azzopardi, and M. Poliakoff. Reaction engineering: The supercritical water hydrothermal synthesis of nano-particles. *The Journal of Supercritical Fluids*, 37(2):209–214, 2006.

E. Lester, G. Aksomaityte, J. Li, S. Gomez, J. Gonzalez-Gonzalez, and M. Poliakoff. Controlled continuous hydrothermal synthesis of cobalt oxide (co 3 o 4) nanoparticles. *Progress in Crystal Growth and Characterization of Materials*, 58(1):3–13, 2012.

E. Lester, S. V. Tang, A. Khlobystov, V. L. Rose, L. Buttery, and C. J. Roberts. Producing nanotubes of biocompatible hydroxyapatite by continuous hydrothermal synthesis. *CrystEngComm*, 15(17):3256–3260, 2013.

E. H. Lester and B. J. Azzopardi. Counter current mixing reactor, July 28 2005. US Patent 7,566,436.

A. Leybros, A. Roubaud, P. Guichardon, and O. Boutin. Ion exchange resins destruction in a stirred supercritical water oxidation reactor. *The Journal of Supercritical Fluids*, 51(3):369–375, 2010.

Y. Li and W. Shen. Morphology-dependent nanocatalysis on metal oxides. *Science China Chemistry*, 55(12):2485–2496, 2012.

H. Lin and X. Ma. Simulation of co-incineration of sewage sludge with municipal solid waste in a grate furnace incinerator. *Waste management*, 32(3):561–567, 2012.

V. Loryuenyong, A. Buasri, J. Pochana, S. Hosawangwong, S. Thaisaung, and P. Sooksaen. Synthesis of anatase tio2 nanoparticles by template sol–gel method and its application in photocatalytic degradation of organic pollutants. *Advanced Science Letters*, 19(10):2919–2922, 2013.

F. Luck. Wet air oxidation: past, present and future. *Catalysis today*, 53(1):81–91, 1999.



H. Ma, S. Wang, L. Zhou, Y. Gong, D. Xu, Y. Wang, and Y. Guo. Abatement of aniline in supercritical water using oxygen as the oxidant. *Industrial & Engineering Chemistry Research*, 51(28):9475–9482, 2012.

H. Ma, S. Z. Wang, M. Gao, and S. Wen. Research on the corrosion behavior of nickel base alloy in municipal sludge treated by supercritical water oxidation. In *Advanced Materials Research*, volume 1010, pages 220–224. Trans Tech Publ, 2014.

P. A. Marrone. Supercritical water oxidationcurrent status of full-scale commercial activity for waste destruction. *The Journal of Supercritical Fluids*, 79:283–288, 2013.

P. A. Marrone and G. T. Hong. Corrosion control methods in supercritical water oxidation and gasification processes. *The Journal of Supercritical Fluids*, 51(2):83–103, 2009.

P. A. Marrone, S. D. Cantwell, and D. W. Dalton. Scwo system designs for waste treatment: application to chemical weapons destruction. *Industrial & engineering chemistry research*, 44(24):9030–9039, 2005.

C. J. Martino and P. E. Savage. Supercritical water oxidation kinetics, products, and pathways for ch3-and cho-substituted phenols. *Industrial & engineering chemistry research*, 36(5):1391–1400, 1997.

C. J. Martino and P. E. Savage. Supercritical water oxidation kinetics and pathways for ethylphenols, hydroxyacetophenones, and other monosubstituted phenols. *Industrial & engineering chemistry research*, 38(5):1775–1783, 1999a.

C. J. Martino and P. E. Savage. Total organic carbon disappearance kinetics for the supercritical water oxidation of monosubstituted phenols. *Environmental science & technology*, 33(11):1911–1915, 1999b.

V. Marulanda and G. Bolaños. Supercritical water oxidation of a heavily pcb-contaminated mineral transformer oil: Laboratory-scale data and economic assess-

ment. *The journal of supercritical fluids*, 54(2):258–265, 2010.

Y. Matsumura, T. Urase, K. Yamamoto, and T. Nunoura. Carbon catalyzed supercritical water oxidation of phenol. *The Journal of supercritical fluids*, 22(2):149–156, 2002.

T. McGuinness. Supercritical oxidation reactor apparatus and method. *Patent WO*, 9418128, 1994.

A. Miller, R. Espanani, A. Junker, D. Hendry, N. Wilkinson, D. Bollinger, J. Abelleira-Pereira, M. Deshusses, E. Inniss, and W. Jacoby. Supercritical water oxidation of a model fecal sludge without the use of a co-fuel. *Chemosphere*, 141:189–196, 2015.

M. Modell, J. Larson, and S. Sobczynski. Supercritical water oxidation of pulp mill sludges. *Tappi journal*, 75(6):195–202, 1992.

A. Munn, P. W. Dunne, S. Tang, and E. Lester. Large-scale continuous hydrothermal production and activation of zif-8. *Chemical Communications*, 51(64):12811–12814, 2015.

K. Murugesan, T. Senthamarai, M. Sohail, M. Sharif, N. V. Kalevaru, and R. V. Jagadeesh. Stable and reusable nanoscale fe 2 o 3-catalyzed aerobic oxidation process for the selective synthesis of nitriles and primary amides. *Green Chemistry*, 20(1): 266–273, 2018.

A. Nugroho and J. Kim. Effect of koh on the continuous synthesis of cobalt oxide and manganese oxide nanoparticles in supercritical water. *Journal of Industrial and Engineering Chemistry*, 20(6):4443–4446, 2014.

T. Oe, H. Suzugaki, I. Naruse, A. T. Quitain, H. Daimon, and K. Fujie. Role of methanol in supercritical water oxidation of ammonia. *Industrial & engineering chemistry research*, 46(11):3566–3573, 2007.

P. Pardo, J. M. Calatayud, and J. Alarcón. Chromium oxide nanoparticles with con-



trolled size prepared from hydrothermal chromium oxyhydroxide precursors. *Ceramics International*, 43(2):2756–2764, 2017.

T.-J. Park, J. S. Lim, Y.-W. Lee, and S.-H. Kim. Catalytic supercritical water oxidation of wastewater from terephthalic acid manufacturing process. *The Journal of supercritical fluids*, 26(3):201–213, 2003.

Z. Pei, H. Xu, and Y. Zhang. Preparation of cr 2 o 3 nanoparticles via c 2 h 5 oh hydrothermal reduction. *Journal of Alloys and Compounds*, 468(1):L5–L8, 2009.

E. Pérez, M. L. Thomas, D. Housley, P. A. Hamley, J. Fraga-Dubreuil, J. Li, E. Lester, and M. Poliakoff. Selective aerobic oxidation of para-xylene in sub-and supercritical water. part 3: effects of geometry and mixing in laboratory scale continuous reactors. *RSC Advances*, 6(14):11289–11294, 2016.

I. V. Pérez, S. Rogak, and R. Branion. Supercritical water oxidation of phenol and 2, 4-dinitrophenol. *The Journal of supercritical fluids*, 30(1):71–87, 2004.

B. D. Phenix, J. L. DiNaro, J. W. Tester, J. B. Howard, and K. A. Smith. The effects of mixing and oxidant choice on laboratory-scale measurements of supercritical water oxidation kinetics. *Industrial & engineering chemistry research*, 41(3):624–631, 2002.

R. Piñero-Hernanz, C. Dodds, J. Hyde, J. García-Serna, M. Poliakoff, E. Lester, M. J. Cocero, S. Kingman, S. Pickering, and K. H. Wong. Chemical recycling of carbon fibre reinforced composites in nearcritical and supercritical water. *Composites Part A: Applied Science and Manufacturing*, 39(3):454–461, 2008.

L. D. Pinto, L. M. F. dos Santos, B. Al-Duri, and R. C. Santos. Supercritical water oxidation of quinoline in a continuous plug flow reactorpart 1: effect of key operating parameters. *Journal of Chemical Technology and Biotechnology*, 81(6):912–918, 2006.

S. A. Pisharody, J. W. Fisher, and M. A. Abraham. Supercritical water oxidation of solid particulates. *Industrial & engineering chemistry research*, 35(12):4471–4478,

1996.

J. M. Ploeger, M. A. Mock, and J. W. Tester. Cooxidation of ammonia and ethanol in supercritical water, part 1: Experimental results. *AIChE journal*, 53(4):941–947, 2007.

A. Plugatyr, T. M. Hayward, and I. M. Svishchev. Thermal decomposition of hydrazine in sub-and supercritical water at 25mpa. *The Journal of Supercritical Fluids*, 55(3): 1014–1018, 2011.

J. Portela, E. Nebot, and E. M. de la Ossa. Kinetic comparison between subcritical and supercritical water oxidation of phenol. *Chemical Engineering Journal*, 81(1): 287–299, 2001a.

J. R. Portela, J. Lopez, E. Nebot, and E. M. de la Ossa. Elimination of cutting oil wastes by promoted hydrothermal oxidation. *Journal of hazardous materials*, 88(1): 95–106, 2001b.

J. Portella, D. Mateos, F. Mancini, C. Marraud, and F. Cansell. Hydrothermal oxidation with multi-injection of oxygen: Simulation and experimental data. *The Journal of supercritical fluids*, 40(2):258–262, 2007.

M. T. Postek, K. S. Howard, A. H. Johnson, and K. L. McMichael. Scanning electron microscopy: A students handbook. ladd research industries. *Inc, Burlington, VT*, 1980.

X.-H. Qi, Y.-Y. Zhuang, Y.-C. Yuan, and W.-X. Gu. Decomposition of aniline in supercritical water. *Journal of hazardous materials*, 90(1):51–62, 2002.

A. Quintanilla, J. Casas, and J. Rodriguez. Hydrogen peroxide-promoted-cwao of phenol with activated carbon. *Applied Catalysis B: Environmental*, 93(3):339–345, 2010.

S. Rajagopal, M. Bharaneswari, D. Nataraj, O. Khyzhun, and Y. Djaoued. Crystal structure and electronic properties of facile synthesized cr2o3 nanoparticles. *Mate-*

rials Research Express, 3(9):095019, 2016.

J. Remón, J. Arauzo, L. García, P. Arcelus-Arrillaga, M. Millan, I. Suelves, and J. Pinilla. Bio-oil upgrading in supercritical water using ni-co catalysts supported on carbon nanofibres. *Fuel Processing Technology*, 154:178–187, 2016.

S. Renou, J. Givaudan, S. Poulain, F. Dirassouyan, and P. Moulin. Landfill leachate treatment: review and opportunity. *Journal of hazardous materials*, 150(3):468–493, 2008.

J. Richardson and J. Harker. Chemical engineering-volume 2: Particle technology and separation processes, 2002.

F. J. Rivas, S. T. Kolaczkowski, F. J. Beltran, and D. B. McLurgh. Hydrogen peroxide promoted wet air oxidation of phenol: influence of operating conditions and homogeneous metal catalysts. *Journal of Chemical Technology and Biotechnology*, 74(5): 390–398, 1999.

A. Rubalcaba, M. E. Suárez-Ojeda, J. Carrera, J. Font, F. Stüber, C. Bengoa, A. Fortuny, and A. Fabregat. Biodegradability enhancement of phenolic compounds by hydrogen peroxide promoted catalytic wet air oxidation. *Catalysis Today*, 124(3): 191–197, 2007.

M. Salavati-Niasari, A. Khansari, and F. Davar. Synthesis and characterization of cobalt oxide nanoparticles by thermal treatment process. *Inorganica Chimica Acta*, 362(14):4937–4942, 2009.

P. E. Savage. A perspective on catalysis in sub-and supercritical water. *The Journal of Supercritical Fluids*, 47(3):407–414, 2009.

P. E. SAVAGE*, J. B. DUNN, and J. Yu. Recent advances in catalytic oxidation in supercritical water. *Combustion science and technology*, 178(1-3):443–465, 2006.

R. V. Shende and J. Levec. Subcritical aqueous-phase oxidation kinetics of acrylic,

maleic, fumaric, and muconic acids. *Industrial & engineering chemistry research*, 39 (1):40–47, 2000.

Y. H. Shin, H.-s. Lee, Y.-H. Lee, J. Kim, J.-D. Kim, and Y.-W. Lee. Synergetic effect of copper-plating wastewater as a catalyst for the destruction of acrylonitrile wastewater in supercritical water oxidation. *Journal of hazardous materials*, 167(1): 824–829, 2009a.

Y. H. Shin, N. C. Shin, B. Veriansyah, J. Kim, and Y.-W. Lee. Supercritical water oxidation of wastewater from acrylonitrile manufacturing plant. *Journal of hazardous materials*, 163(2):1142–1147, 2009b.

J. Sierra-Pallares, D. L. Marchisio, E. Alonso, M. T. Parra-Santos, F. Castro, and M. J. Cocero. Quantification of mixing efficiency in turbulent supercritical water hydrothermal reactors. *Chemical engineering science*, 2011.

J. Sierra-Pallares, T. Huddle, E. Alonso, F. A. Mato, J. García-Serna, M. J. Cocero, and E. Lester. Prediction of residence time distributions in supercritical hydrothermal reactors working at low reynolds numbers. *Chemical Engineering Journal*, 299:373–385, 2016a.

J. Sierra-Pallares, T. Huddle, J. García-Serna, E. Alonso, F. Mato, I. Shvets, O. Luebben, M. J. Cocero, and E. Lester. Understanding bottom-up continuous hydrothermal synthesis of nanoparticles using empirical measurement and computational simulation. *Nano Research*, 9(11):3377–3387, 2016b.

D. S. Sloan, R. A. Pelletier, and M. Modell. Sludge management in the city of orlando it's supercritical! *Proceedings of the Water Environment Federation*, 2008(7):7762–7774, 2008.

S. Stavbar, M. K. Hrnčič, K. Premzl, M. Kolar, and S. Š. Turk. Sub-and super-critical water oxidation of wastewater containing amoxicillin and ciprofloxacin. *The Journal*



of Supercritical Fluids, 2017.

B. Stieberova, M. Zilka, M. Ticha, F. Freiberg, P. Caramazana-Gonzalez, J. McKechnie, and E. Lester. Application of zno nanoparticles in a self-cleaning coating on a metal panel: an assessment of environmental benefits. *ACS Sustainable Chemistry & Engineering*, 5(3):2493–2500, 2017.

M. Stroosnijder, V. Guttmann, T. Fransen, and J. De Wit. Corrosion of alloy 800h and the effect of surface-applied ceo 2 in a sulphidizing/oxidizing/carburizing environment at 700 c. *Oxidation of metals*, 33(5-6):371–397, 1990.

K.-i. Sugioka, K. Ozawa, T. Tsukada, S. Takami, T. Adschiri, K. Sugimoto, N. Takenaka, and Y. Saito. Neutron radiography and numerical simulation of mixing behavior in a reactor for supercritical hydrothermal synthesis. *AIChE Journal*, 60(3): 1168–1175, 2014.

M. Sun, X. Wu, Z. Zhang, and E.-H. Han. Oxidation of 316 stainless steel in supercritical water. *Corrosion science*, 51(5):1069–1072, 2009.

Z. Sun, F. Takahashi, Y. Odaka, K. Fukushi, Y. Oshima, and K. Yamamoto. Effects of potassium alkalis and sodium alkalis on the dechlorination of o-chlorophenol in supercritical water. *Chemosphere*, 66(1):151–157, 2007.

S. Takami, K.-i. Sugioka, T. Tsukada, T. Adschiri, K. Sugimoto, N. Takenaka, and Y. Saito. Neutron radiography on tubular flow reactor for hydrothermal synthesis: In situ monitoring of mixing behavior of supercritical water and room-temperature water. *The Journal of Supercritical Fluids*, 63:46–51, 2012.

S. V. Y. Tang. *Synthesis of nanomaterials for biomedical applications*. PhD thesis, University of Nottingham, 2014.

T. D. Thornton and P. E. Savage. Phenol oxidation in supercritical water. *The Journal of Supercritical Fluids*, 3(4):240–248, 1990.

T. D. Thornton and P. E. Savage. Phenol oxidation pathways in supercritical water. *Industrial & engineering chemistry research*, 31(11):2451–2456, 1992.

T. D. Thornton, D. E. LaDue III, and P. E. Savage. Phenol oxidation in supercritical water: formation of dibenzofuran, dibenzo-p-dioxin, and related compounds. *Environmental science & technology*, 25(8):1507–1510, 1991.

C. J. Tighe, R. I. Gruar, C. Y. Ma, T. Mahmud, X. Z. Wang, and J. A. Darr. Investigation of counter-current mixing in a continuous hydrothermal flow reactor. *The Journal of Supercritical Fluids*, 62:165–172, 2012.

K. Tomita and Y. Oshima. Stability of manganese oxide in catalytic supercritical water oxidation of phenol. *Industrial & engineering chemistry research*, 43(24):7740–7743, 2004.

V. Vadillo, J. Sanchez-Oneto, J. R. Portela, and E. J. Martinez de la Ossa. Problems in supercritical water oxidation process and proposed solutions. *Industrial & Engineering Chemistry Research*, 52(23):7617–7629, 2013.

B. Veriansyah, J.-D. Kim, and J.-C. Lee. Supercritical water oxidation of thiodiglycol. *Industrial & engineering chemistry research*, 44(24):9014–9019, 2005.

B. Veriansyah, J.-D. Kim, and J.-C. Lee. Destruction of chemical agent simulants in a supercritical water oxidation bench-scale reactor. *Journal of hazardous materials*, 147(1):8–14, 2007.

F. Vogel, J. Harf, A. Hug, and P. R. Von Rohr. Promoted oxidation of phenol in aqueous solution using molecular oxygen at mild conditions. *Environmental Progress & Sustainable Energy*, 18(1):7–13, 1999.

L. Wang, S. Wang, Y. Li, T. Zhang, J. Yang, and M. Wang. Supercritical water oxidation of acrylic acid wastewater and sludge. In *Resources, Environment and Engineering II: Proceedings of the 2nd Technical Congress on Resources, Environment*



and Engineering (CREE 2015, Hong Kong, 25-26 September 2015), page 459. CRC Press, 2015.

S. Wang, Y. Guo, L. Wang, Y. Wang, D. Xu, and H. Ma. Supercritical water oxidation of coal: Investigation of operating parameters' effects, reaction kinetics and mechanism. *Fuel Processing Technology*, 92(3):291–297, 2011.

Y. Wang, S. Wang, Y. Guo, D. Xu, Y. Gong, X. Tang, and H. Ma. Oxidative degradation of lurgi coal-gasification wastewater with mn2o3, co2o3, and cuo catalysts in supercritical water. *Industrial & Engineering Chemistry Research*, 51(51):16573–16579, 2012.

R. Weber, A. Watson, M. Forter, and F. Oliaei. Review article: Persistent organic pollutants and landfills-a review of past experiences and future challenges. *Waste Management & Research*, 29(1):107–121, 2011.

B. Wellig, M. Weber, K. Lieball, K. Príkopskỳ, and P. R. von Rohr. Hydrothermal methanol diffusion flame as internal heat source in a scwo reactor. *The Journal of Supercritical Fluids*, 49(1):59–70, 2009.

T. Wu and J. D. Englehardt. A new method for removal of hydrogen peroxide interference in the analysis of chemical oxygen demand. *Environmental science & technology*, 46(4):2291–2298, 2012.

D. Xu, S. Wang, C. Huang, X. Tang, and Y. Guo. Transpiring wall reactor in supercritical water oxidation. *Chemical Engineering Research and Design*, 92(11):2626–2639, 2014.

D. Xu, C. Huang, S. Wang, G. Lin, and Y. Guo. Salt deposition problems in supercritical water oxidation. *Chemical Engineering Journal*, 279:1010–1022, 2015a.

D. Xu, S. Wang, J. Zhang, X. Tang, Y. Guo, and C. Huang. Supercritical water oxidation of a pesticide wastewater. *Chemical Engineering Research and Design*, 94:

396–406, 2015b.

D. H. Xu, S. Z. Wang, Y. M. Gong, Y. Guo, X. Y. Tang, and H. H. Ma. A novel concept reactor design for preventing salt deposition in supercritical water. *Chemical Engineering Research and Design*, 88(11):1515–1522, 2010.

H. H. Yang and C. A. Eckert. Homogeneous catalysis in the oxidation of p-chlorophenol in supercritical water. *Industrial & engineering chemistry research*, 27(11):2009–2014, 1988.

S. Yesodharan et al. Supercritical water oxidation: an environmentally safe method for the disposal of organic wastes. *CURRENT SCIENCE-BANGALORE-*, 82(9): 1112–1122, 2002.

B. Youngprasert, K. Poochinda, and S. Ngamprasertsith. Treatment of acetonitrile by catalytic supercritical water oxidation in compact-sized reactor. *Journal of Water Resource and Protection*, 2(03):222, 2010.

J. Yu and P. E. Savage. Catalytic oxidation of phenol over mno2 in supercritical water. *Industrial & engineering chemistry research*, 38(10):3793–3801, 1999.

J. Yu and P. E. Savage. Kinetics of catalytic supercritical water oxidation of phenol over tio2. *Environmental science & technology*, 34(15):3191–3198, 2000a.

J. Yu and P. E. Savage. Phenol oxidation over cuo/al 2 o 3 in supercritical water. *Applied Catalysis B: Environmental*, 28(3):275–288, 2000b.

J. Yu and P. E. Savage. Catalyst activity, stability, and transformations during oxidation in supercritical water. *Applied Catalysis B: Environmental*, 31(2):123–132, 2001.

R. Zboril, M. Mashlan, and D. Petridis. Iron (iii) oxides from thermal processes synthesis, structural and magnetic properties, mössbauer spectroscopy characterization, and applications. *Chemistry of Materials*, 14(3):969–982, 2002.

P. Zielke, Y. Xu, S. B. Simonsen, P. Norby, and R. Kiebach. Simulation, design and proof-of-concept of a two-stage continuous hydrothermal flow synthesis reactor for synthesis of functionalized nano-sized inorganic composite materials. *The Journal of Supercritical Fluids*, 117:1–12, 2016.

D. Zou, Y. Chi, C. Fu, J. Dong, F. Wang, and M. Ni. Co-destruction of organic pollutants in municipal solid waste leachate and dioxins in fly ash under supercritical water using h 2 o 2 as oxidant. *Journal of hazardous materials*, 248:177–184, 2013.

A

Pseudo fluid calculator

Table A.1: summarised stream properties for counter current reactor system and pseudo fluid modelling.

SCWO Reactor		**Pseudo Reactor**	
Stainless Steel Reactor dimensions		**Flat plate (half) cross-sectional reactor dimensions**	
Outer tube OD	0.375 in	Outer Across	5 cm
	0.009525 m		0.05 m
OT wall thickness	0.065 in		
	0.001651 m		
Outer tube ID	0.006223 m		
Inner tube OD	0.125 in	Inner Across	1 cm
	0.003175 m		0.01 m
IT wall thickness	0.028 in	IA tube thickness	1 cm
	0.0007112 m		0.01 m
Inner tube ID	0.0017526 m	Depth	0.006 m
Wastewater Feed		**Pseudo Wastewater Feed**	
C.S wetted area	3.04E-5 m^2	C.S wetted area	0.0003 m^2
		Wetted perimeter	0.112 m
Hydraulic Diameter	0.006223 m	Hydraulic Diameter	0.0107 m
Flow rate	10 ml/min	Flow rate	305 ml/min
Flow rate	0.000166 l/s	Flow rate	0.00508 l/s
Density of fluid	1008.9 kg/m^3	Density of fluid	1176.4 kg/m^3
Viscocity of fluid	9.9E-4 kg/m.s	Viscocity of fluid	6.2E-3 kg/m.s
Volumetric flow	1.6E-07 m^3/s	Volumetric flow	5.1E-06 m^3/s
Average velocity	0.0055 m/s	Average velocity	0.0169 m/s
Reynolds number	34.637	Reynolds number	34.637
Superheated Downward Feed		**Pseudo Superheated Downward Feed**	
C.S wetted area	2.4E-06 m^2	C.S wetted area	0.00006 m^2
		Wetted perimeter	0.032 m
Hydraulic Diameter	0.0017526 m	Hydraulic Diameter	0.0075 m
Flow rate	20 ml/min	Flow rate	3983 ml/min
Flow rate	0.001846 l/s	Flow rate	0.06638 l/s
Density of fluid	182.14 kg/m^3	Density of fluid	998.2 kg/m^3
Viscocity of fluid	2.9E-5 kg/m.s	Viscocity of fluid	1E-3 kg/m.s
Volumetric flow	1.8E-06 m^3/s	Volumetric flow	6.6E-5 m^3/s
Average velocity	0.76536 m/s	Average velocity	1.1063 m/s
Reynolds number	8269.607	Reynolds number	8269.6

Table A.2: summarised stream properties for co-current reactor system and pseudo fluid modelling.

SCWO Reactor		**Pseudo Reactor**	
Stainless Steel Reactor dimensions		**Flat plate (half) cross-sectional reactor dimensions**	
Outer tube OD	0.375 in	Outer Across	8.9 cm
	0.009525 m		0.089 m
OT wall thickness	0.065 in		
	0.001651 m		
Outer tube ID	0.006223 m		
Inner tube OD	0.125 in	Inner Across	1 cm
	0.003175 m		0.01 m
IT wall thickness	0.028 in	IA tube thickness	0.7 cm
	0.0007112 m		0.007 m
Inner tube ID	0.0017526 m	Depth	0.006 m
Wastewater Feed		**Pseudo Wastewater Feed**	
C.S wetted area	2.25E-5 m^2	C.S wetted area	0.00039 m^2
Wetted perimeter	0.0295247 m	Wetted perimeter	0.142 m
Hydraulic Diameter	0.003048 m	Hydraulic Diameter	0.011 m
Flow rate	5 ml/min	Flow rate	128 ml/min
Flow rate	8.33E-05 l/s	Flow rate	0.00213 l/s
Density of fluid	1008.9 kg/m^3	Density of fluid	1176.4 kg/m^3
Viscocity of fluid	9.9E-4 kg/m.s	Viscocity of fluid	6.2E-3 kg/m.s
Volumetric flow	8.33E-08 m^3/s	Volumetric flow	2.134E-06 m^3/s
Average velocity	0.0037 m/s	Average velocity	0.0054 m/s
Reynolds number	11.46	Reynolds number	11.46
Superheated Downward Feed		**Pseudo Superheated Downward Feed**	
C.S wetted area	2.4E-06 m^2	C.S wetted area	0.00006 m^2
		Wetted perimeter	0.032 m
Hydraulic Diameter	0.0017526 m	Hydraulic Diameter	0.0075 m
Flow rate	5 ml/min	Flow rate	995.72 ml/min
Flow rate	0.000461 l/s	Flow rate	0.0166 l/s
Density of fluid	182.14 kg/m^3	Density of fluid	998.2 kg/m^3
Viscocity of fluid	2.9E-5 kg/m.s	Viscocity of fluid	1E-3 kg/m.s
Volumetric flow	4.6E-07 m^3/s	Volumetric flow	1.6E-5 m^3/s
Average velocity	0.1913 m/s	Average velocity	0.2765 m/s
Reynolds number	2067.4	Reynolds number	2067.4

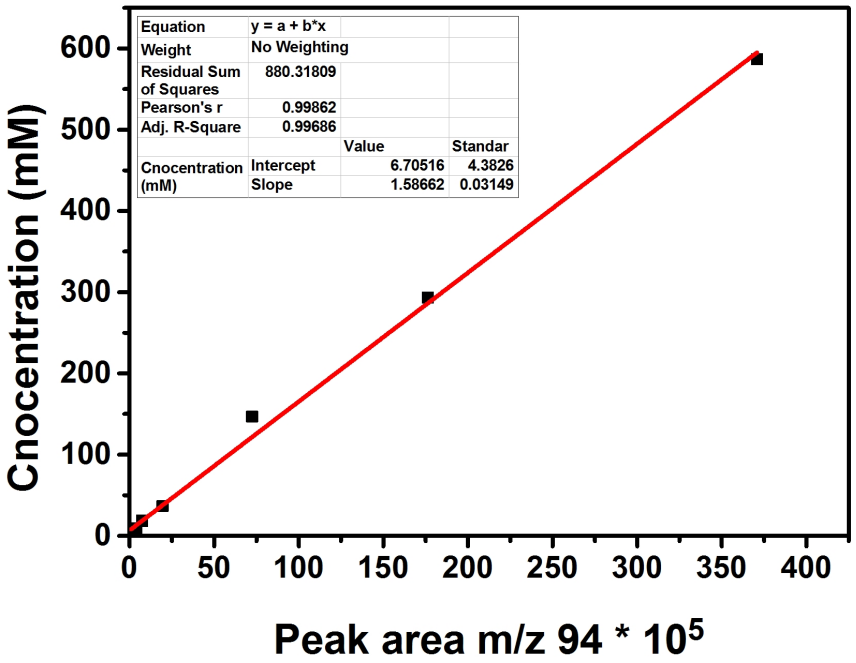
Table A.3: summarised stream properties for co-current protected wall reactor system and pseudo fluid modelling.

SCWO Reactor		**Pseudo Reactor**	
Stainless Steel Reactor dimensions		**Flat plate (half) cross-sectional reactor dimensions**	
Outer tube OD	0.25 in	Outer Across	7.5 cm
	0.00635 m		0.075 m
OT wall thickness	0.049 in		
	0.0012446 m		
Outer tube ID	0.0038608 m		
Inner tube OD	0.125 in	Inner Across	4 cm
	0.003175 m		0.04 m
IT wall thickness	0.014 in	IA tube thickness	1.0 cm
	0.0003556 m		0.01 m
Inner tube ID	0.0024638 m	Depth	0.006 m
Wastewater Feed		**Pseudo Wastewater Feed**	
C.S wetted area	4.77E-6 m^2	C.S wetted area	0.00024 m^2
		Wetted perimeter	0.092 m
Hydraulic Diameter	0.002464 m	Hydraulic Diameter	0.0104 m
Flow rate	10 ml/min	Flow rate	632 ml/min
Flow rate	0.000166 l/s	Flow rate	0.01053 l/s
Density of fluid	1008.9 kg/m^3	Density of fluid	1176.4 kg/m^3
Viscocity of fluid	9.9E-4 kg/m.s	Viscocity of fluid	6.2E-3 kg/m.s
Volumetric flow	1.66E-07 m^3/s	Volumetric flow	1.053E-05 m^3/s
Average velocity	0.0349 m/s	Average velocity	0.0439 m/s
Reynolds number	87.5	Reynolds number	87.5
Superheated Downward Feed		**Pseudo Superheated Downward Feed**	
C.S wetted area	3.79E-06 m^2	C.S wetted area	0.00009 m^2
Wetted perimeter	0.0221 m	Wetted perimeter	0.054 m
Hydraulic Diameter	0.000686 m	Hydraulic Diameter	0.00667 m
Flow rate	40 ml/min	Flow rate	3348 ml/min
Flow rate	0.0037 l/s	Flow rate	0.0558 l/s
Density of fluid	182.14 kg/m^3	Density of fluid	998.2 kg/m^3
Viscocity of fluid	2.9E-5 kg/m.s	Viscocity of fluid	1E-3 kg/m.s
Volumetric flow	3.692E-06 m^3/s	Volumetric flow	5.58E-5 m^3/s
Average velocity	0.9744 m/s	Average velocity	0.62 m/s
Reynolds number	4120	Reynolds number	4120

B

Chromatographic information of phenol samples

(a)



(b)

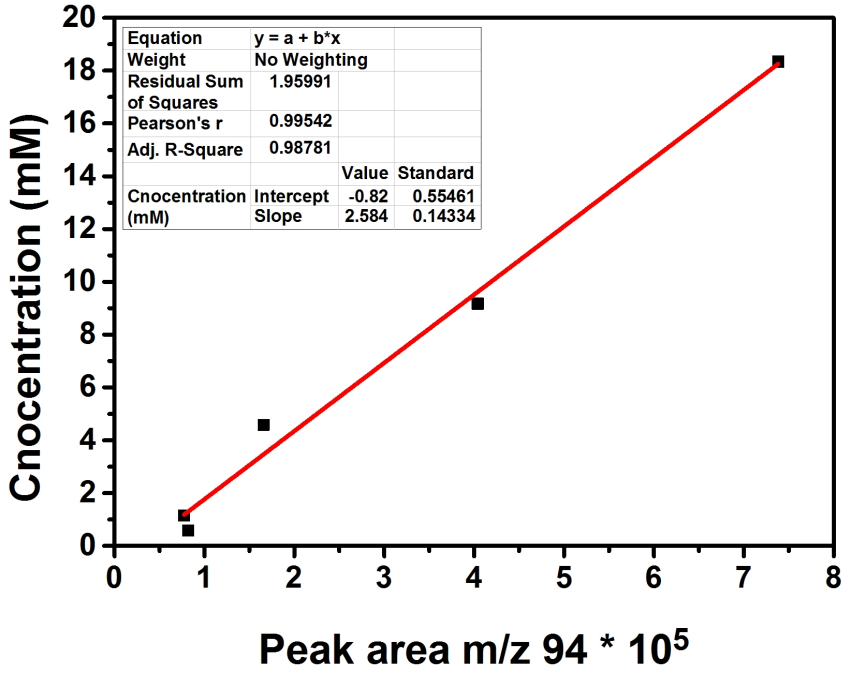


Figure B.1: Calibration curves for phenol (a) entire dataset and (b) lower phenol concentrations.

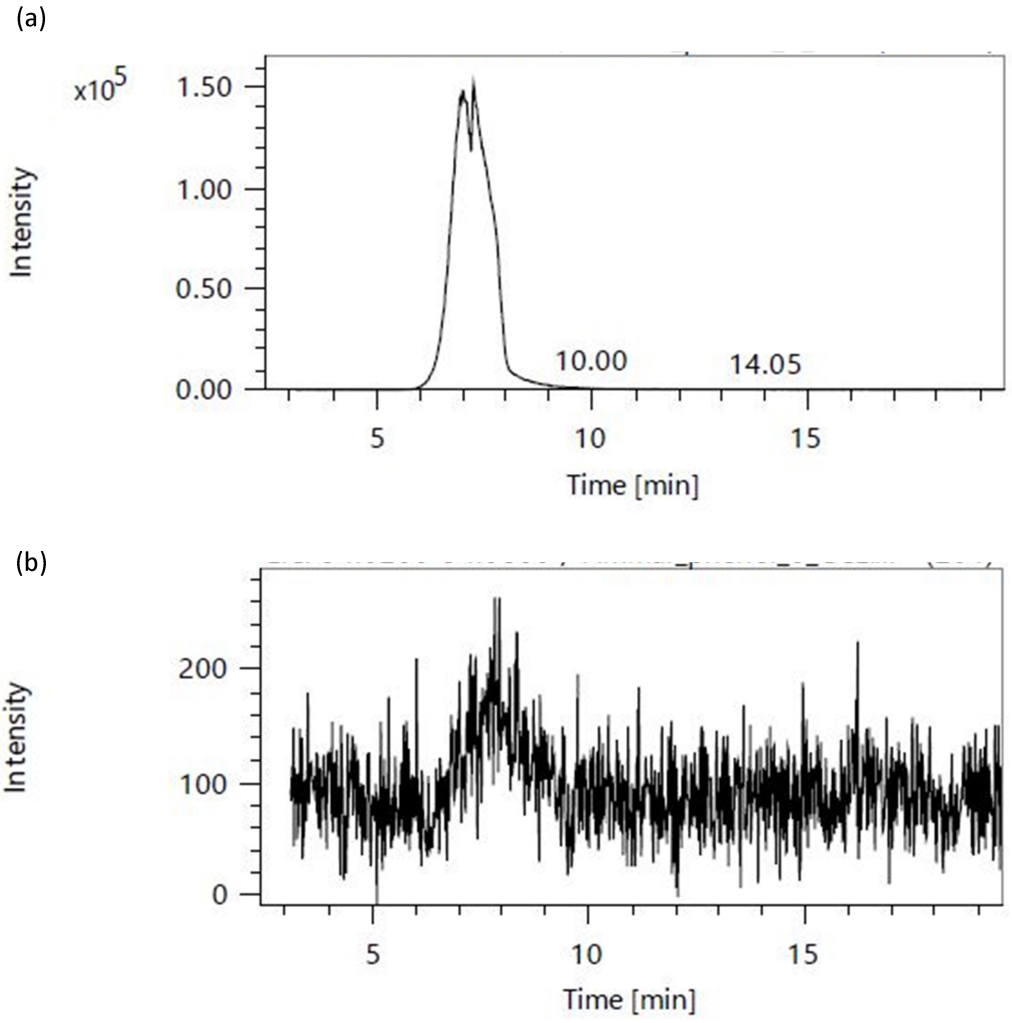


Figure B.2: Extracted ion current traces (EIC) for target m/z 94.06 - molecular ion of phenol. (a) Preheated oxidant and (b) Catalytic preheated oxidant scenario